FACULDADE DE ENGENHARIA DA UNIVERSIDADE DO PORTO

Mechanical behavior of printed upcycled powders produced by Direct Energy Deposition

Vasco José Campinho Araújo



Master in Mechanical Engineering

FEUP Supervisor: Prof. Dr. Ana Reis

INEGI Supervisor: Dr. Omid Emadinia

June 21, 2024

Mechanical behavior of printed upcycled powders produced by Direct Energy Deposition

Vasco José Campinho Araújo

Master in Mechanical Engineering

June 21, 2024

Abstract

Machining chips represent a significant portion of the waste generated by the metalworking industry. Usually, this waste is remelted in foundry industries. However, there are alternatives that not only recycle chips but also add value and utility to this waste, which represent solutions known as Upcycling. This dissertation tests the feasibility of one of these alternatives: transforming metal scraps into powder for additive manufacturing processes, more specifically Direct Energy Deposition (DED).

Thus, this study investigates the processing of one austenitic stainless steel chips into powder particles for DED through mechanical milling. The powder production process involves two different methods: milling by a vibrating disc mill (DM) and milling by a planetary ball mill (PBM). Various milling procedures have been tested in order to study the productivity of the process, quantified by the amount (in mass percent) of final powder that is within the particle size range intended for DED processing.

The resulting powder particles were firstly separated by sieving according to particle size ranges. Then, the particles with appropriate sizes for DED were analyzed in a scanning electron microscope in order to assess their size distribution, aspect ratio and morphology. Powder properties such as tap density, loose density and flowability were also measured.

Then, the parametrization of the DED powder depositions was carried out in order to choose the optimum set of parameters (laser power, scanning speed and powder feeding rate). The printed lines were analysed visually and metallographically in order to select the optimal set of parameters. Subsequently, vertical DED depositions of several single lines (often known as thin walls) were carried out, after a study of the parameters involved in DED height construction. The thin walls were then analysed metallographically (to study the presence of defects, the microstructure and the resulting chemical composition) and mechanically (through microhardness measurements and tensile tests).

The PBM milling process proved to be efficient due to its good productivity, and production of particles with desirable morphology, size distribution and aspect ratio as well as favorable densities and flowability, coming close to the commercial powders produced by atomization. However, the printing of PBM milled powders lead to a considerable amount of oxides in the printings, which is undesired since it worsens the mechanical properties and corrosion resistance. On the other side, DM milled powders have considerably weaker characteristics and properties but are less prone to oxide formation in the printings.

The results of the printings analyses indicated that deposition of the powder in question is feasible since the mechanical properties obtained were satisfactory and the wall was uniform along its height. However, the presence of oxides in the printed material still needs to be optimized.

Keywords: Direct Energy Deposition, Mechanical Milling, Upcycling, Metallic Powder, Powder Characteristics and Properties, Mechanical Characterization.

Resumo

As aparas provenientes de processos de maquinagem representam uma signficativa porção dos resíduos gerados pela indústria metalúrgica. Por norma, estes resíduos são refundidos em indústrias de fundição. No entanto, há alternativas que não só reciclam as aparas como acrescentam valor e utilidade a estes resíduos, o que representam soluções conhecidas como *Upcycling*. Esta dissertação testa a viablidade de uma destas alternativas: transformar aparas metálicas em pó para processos de fabrico aditivo, mais concretamente *Direct Energy Deposition* (DED).

Posto isto, este estudo investiga o processamento de aparas de um aço inoxidável austenítico em partículas de pó para DED, através de moagem mecânica. O processo de produção envolve dois métodos diferentes: moagem num moinho vibratório de disco (MD) e moagem num moinho de bolas planetário (MBP). Vários procedimentos de moagem foram testados de modo a estudar a produtividade do processo, quantificada pela quantidade (em porção de massa) de pó final que se encontra no intervalo de tamanho de partículas destinado a processamento DED.

As partículas de pó resultantes foram, numa primeira instância, separadas por crivagem, de acordo com os intervalos de tamanhos de partículas. Depois, as partículas com tamanhos apropriados para DED foram analisadas num microscópio de varrimento eletrónico de modo a a analisar a distribuição de tamanhos, *aspect ratio* e morfologia das mesmas. As propriedades das partículas, como densidade compactada, densidade aparente e fluidez, foram também medidas.

De seguida, procedeu-se à parametrização das deposições DED do pó, de forma a escolher o conjunto otimizado de parametros (potência do laser, a velocidade de impressão, e a taxa de entrega de pó). As linhas impressas foram analisadas visualmente e metalograficamente de forma a poder selecionar-se o conjunto ideal de parâmetros. Posteriormente, procedeu-se a deposições DED verticais de várias linhas (frequentemente conhecidas como *thin walls*), após um estudo dos parâmetros envolvidos em construção em altura por DED. Posto isto, as *thin walls* foram analisadas metalograficamente (para estudar a presença de defeitos, a microestrutura e a composição química resultante) e mecânicamente (através de medições de microdureza e ensaios à tração).

O processo de moagem MBP mostrou-se mais eficiente devido à sua boa produtividade e à produção de partículas com morfologia, distribuição de tamanhos e *aspect ratio* desejáveis assim como densidades e fluidez favoráveis, assemelhando-se aos pós comerciais produzidos por atomização. No entanto, a deposição de pós moídos por MBP levou a uma quantidade considerável de óxidos nas impressões, o que é inadequado já que piora as propriedades mecânicas e a resistência à corrosão. Pelo outro lado, pós moídos por MD apresentaram consideravelmente piores caracteristicas e propriedades mas são menos susceptíveis à formação de óxidos nas impressões.

Os resultados das análises das impressões indicaram que a deposição do pó em causa é viável já que as propriedades mecânicas obtidas foram satisfatórias e a parede foi uniforme ao longo da sua altura. No entanto, a presença de óxidos no material impresso ainda precisa de ser otimizada.

Palavras-chave: *Direct Energy Deposition*, Moagem Mecânica, *Upcycling*, Pós Metálicos, Características e Propriedades do Pó, Caracterização Mecânica.

Acknowledgements

I would like to express my gratitude to Ph.D. Omid Omadinia for guiding me and transmitting to me all the valuable knowledge essential for this work. His notable expertise and clear proficiency in the field of metallurgy were crucial in laying the foundationS for this study.

To Engineer Lara Castanheira, for her constant availability, help and advice throughout this work, which was crucial.

To Ramiro Soares and the remaining DEMM staff as well as Engineer Fahad Zafar, for the availabilty and prompt assistance throughout the milling procedures.

To Armanda Teixeira for her kindness, patience and readiness for preparing and testing all the necessary samples.

To Tiago Santos for the technical support during the performance of DED at INEGI.

To José Bouças and José Teixeira for the help with the machining of the original block, the substrate and printings and the tensile specimens.

To Engineer Hélder Nunes for the help with the microstructure and chemical compositions analysis.

To Engineer Daniel Cruz for the kind help with the tensile testing.

Since this work marks the end of my Master's Degree, it becomes important to acknowledge those who accompanied me on this journey, which is now coming to an end.

I would like to thank my beloved parents for being a living example of courage and resilience and therefore my biggest inspiration. Also for always having done everything they could to make it possible for me to, firstly, enter FEUP and, now, leave FEUP.

To my godfather for showing me the worth and importance of education.

To my dearest "Tortos" for the friendship, the countless (good and bad) moments shared, the beautiful bonds created and the unforgettable memories that I will carry with me for life.

To Camila, for being my unconditional and strong haven.

To all those who, directly or indirectly, accompanied me at FEUP, from the Faculty staff to my colleagues, among others.

Last but definitely not least, and quoting Francisco Guimarães in his book *Convocatória*, "to God, who does not abandon my smallness and who wishes me greater and greater".

Institutional Acknowledgements

I gratefully acknowledge INEGI (Institute of Science and Innovation in Mechanical and Industrial Engineering) for their invaluable expertise and support in the field of Additive Manufacturing.

I also acknowledge CEMUP (Materials Center of the University of Porto) for expert assistance with SEM, and to the Department of Metallurgical and Materials Engineering for providing powder analysis and milling facilities.

Finally, I acknowledge the financial support from the IAPMEI - Plano de Recuperação e Resiliência through the program NextGenerationEU, under the project 02/C05-i01.01/2022.PC644936537-00000046 - New Space Portugal (PR192303).



"Doubt is such a strange thing.
There will be times when you succeed and times when you fail.
So wasting your time doubting if you'll be successful or not, is pointless.
Just put one foot in front of the other, control what you can control, and then see what the outcome is.
If you win, great, you're going to have to wake up the next day and do the journey all over again.
If you lose, sucks, but you'll have to wake up the next day and do the journey all over again anyway."

Kobe Bryant

Contents

1 Introduction **1**
- 1.1 Framework and Motivation . . . 1
- 1.2 Objectives . . . 1
- 1.3 Work Plan Timeline . . . 2
- 1.4 Structure . . . 2

2 Literature Review **5**
- 2.1 Recycling and Sustainability in Metalworking Industries . . . 5
  - 2.1.1 Steel Recycling . . . 5
    - 2.1.1.1 Advantages of steel recycling . . . 6
  - 2.1.2 Recycling of Machining Chips . . . 6
    - 2.1.2.1 Machining Chips Recycling Methods . . . 6
    - 2.1.2.2 Recycling, Downgrading and Upcycling . . . 7
- 2.2 Direct Energy Deposition (DED) . . . 9
  - 2.2.1 DED nomenclature and other AM processes . . . 9
  - 2.2.2 Process description . . . 9
  - 2.2.3 Advantages and Drawbacks . . . 12
  - 2.2.4 Applications . . . 13
  - 2.2.5 Process Parameters . . . 13
    - 2.2.5.1 Laser Power . . . 14
    - 2.2.5.2 Laser spot size . . . 15
    - 2.2.5.3 Powder Feed Rate . . . 15
    - 2.2.5.4 Scanning Speed . . . 15
    - 2.2.5.5 Carrying Gas . . . 16
    - 2.2.5.6 Shielding Gas . . . 16
    - 2.2.5.7 Tool path strategy . . . 16
    - 2.2.5.8 Hatch spacing and Overlapping . . . 17
    - 2.2.5.9 Key Formulae . . . 18
  - 2.2.6 Typical Defects in DED produced parts . . . 19
    - 2.2.6.1 Porosity . . . 19
    - 2.2.6.2 Residual Stresses . . . 21
    - 2.2.6.3 Delamination . . . 21
    - 2.2.6.4 Cracking . . . 21
  - 2.2.7 Printings Assessment . . . 22
    - 2.2.7.1 Bead analysis: shape and geometry . . . 22
    - 2.2.7.2 Porosity Assessment . . . 24
    - 2.2.7.3 Microstructure Assessment . . . 25
    - 2.2.7.4 Residual Stresses, Cracking and Delamination . . . 26

2.3 Directed Energy Deposition of austenitic stainless steel powder . . . 27
2.3.1 DED processing of AISI 316L powder . . . 27
2.3.1.1 Bead geometry . . . 27
2.3.1.2 Microstructure . . . 28
2.3.1.3 Mechanical properties . . . 30
2.3.1.4 Applications of DED processing with AISI 316L powder . . . 33
2.4 Powder Production for DED Processing . . . 37
2.4.1 Powder Production Processes . . . 37
2.4.2 Mechanical Milling Processes . . . 37
2.4.2.1 Milling parameters . . . 38
2.4.2.2 Disc Milling . . . 40
2.4.2.3 Planetary Ball Milling . . . 41
2.4.2.4 Mechanical Properties of powder produced through milling processes . . . 42
2.4.3 Quality and Requirements for DED powder feedstock . . . 42
2.4.3.1 Particle Shape . . . 42
2.4.3.2 Particle Size and Size Distribution . . . 43
2.4.3.3 Particle Structure . . . 44
2.4.3.4 Flowability . . . 44
2.4.3.5 Density . . . 45
2.4.4 Upcycling machining chips into powder for DED Processing . . . 46
2.4.4.1 Chips formation and morphology . . . 46
2.4.4.2 State-of-the-art of austenitic stainless steel chips upcycling into powder for DED Processing . . . 46

3 Materials and Methods 49
3.1 Materials . . . 49
3.1.1 AISI 301 . . . 50
3.1.2 Substrate Material . . . 51
3.2 Methods . . . 52
3.2.1 Powder Production . . . 52
3.2.1.1 Collection of chips . . . 52
3.2.1.2 Milling Procedure . . . 52
3.2.2 Powder Characterization . . . 56
3.2.2.1 Particle Size Distribution and Particle Shape . . . 56
3.2.2.2 Density and Flowability Measurements . . . 58
3.2.3 DED Printings . . . 60
3.2.3.1 DED Setup and Procedure . . . 60
3.2.3.2 Single line and Thin Wall depositions . . . 62
3.2.4 Printings Assessment . . . 65
3.2.4.1 Top view analysis . . . 65
3.2.4.2 Cross section Analysis . . . 65
3.2.4.3 Microstructural analysis . . . 66
3.2.4.4 Chemical analysis . . . 67
3.2.4.5 Microhardness measurements . . . 68
3.2.4.6 Tensile Tests . . . 69

4 Results and Discussion **73**
4.1 Powder Production and Characterization . . . 73
4.1.1 Milling Productivity . . . 73
4.1.1.1 Comparison of the same milling conditions for different materials 75
4.1.1.2 Milling conditions developed in this work . . . 77
4.1.1.3 Overall productivity of the milling process . . . 78
4.1.2 Particle Size Distribution . . . 79
4.1.2.1 Disc Milling results . . . 79
4.1.2.2 Ball Milling results . . . 80
4.1.3 Particles Aspect Ratio, Size and Shape . . . 83
4.1.3.1 Disc Milling results . . . 84
4.1.3.2 Ball milling results . . . 85
4.1.4 Density and Flowability Measurements . . . 88
4.1.4.1 Tap and Loose Densities . . . 89
4.1.4.2 Flowability . . . 91
4.1.4.3 Comparison with gas atomized powder . . . 91
4.2 Printings Assessment . . . 93
4.2.1 Top view and cross section analysis . . . 93
4.2.1.1 Parametrization . . . 93
4.2.1.2 Thin walls printings . . . 96
4.2.2 Microstructure Analysis . . . 101
4.2.3 Chemical analysis . . . 103
4.2.3.1 Comparison between the original and the DED printed materials 103
4.2.3.2 Measurements along the thin wall heights . . . 105
4.2.3.3 Analysis of inclusions . . . 106
4.2.4 Microhardness test . . . 108
4.2.5 Tensile Tests . . . 108
4.2.5.1 Observation of the fracture surfaces . . . 110

5 Conclusions and Future Works **113**
5.1 Conclusions . . . 113
5.2 Future Works . . . 116

References **119**

Annex A - Summary of the state-of-the-art of AISI 316L Powder DED Processing - Analysis, conclusions and obtained mechanical properties from recent studies **131**

Annex B - Summary of the state-of-the-art of AISI 316L Powder DED Processing - DED Processing Parameters used in recent studies **135**

Annex C - Technical Drawing of the specimen for tensile testing **139**

Annex D - Micrographs of the powder produced through disc and ball milling **141**

Annex E - Micrographs of the DED printed thin wall with upcycled powder **151**

Annex F - Semi-quantitative chemical composition of a thin wall printed with upcycled powder - Matrix measurements **161**

Annex G - Semi-quantitative chemical composition of the original block (as supplied) - Matrix measurements 163

Annex H - Semi-quantitative chemical composition measurements on a thin wall printed with upcycled powder 165

Annex I - Semi-quantitative chemical composition of inclusions observed in the DED printed thin wall (with upcycled powder) 167

Annex J - Micrographs of the original block (as supplied) 173

Annex K - Semi-quantitative chemical composition measurements of inclusions observed in the original block (as supplied) 175

Annex L - Microhardness measurements along the height of a DED printed thin wall with upcycled powder 179

Annex M - Engineering and true curves obtained from the tensile tests 181

Annex N - Images of the deformation field during the tensile tests obtained though DIC 185

Annex 0 - Tensile specimens dimensions measurements 187

Annex P - Micrographs of the tensile specimens fracture surfaces 189

List of Figures

2.1 Recycling, Ucycling and Downcycling Icons. 8
2.2 Schematic of a powder DED system with laser as energy source (Adapted from Cho et al. (2023)). 10
2.3 Common Nozzle Configurations: a) Lateral; b) Annular; c) Coaxial (Adapted from Nasiri and Movahhedy (2022)). 11
2.4 DED process parameters (Adapted from Dutta (2020) and Castanheira (2022)). . 14
2.5 Schematic of Laser Spot Size. 15
2.6 Common tool paths in DED systems: a) Raster, b) Zig-zag, c) Chessboard, d) Offset-Out, e) Offset-in, f) Fractal (Adapted from Ribeiro et al. (2020) and Hu and Cong (2018)). 17
2.7 Schematics of hatch spacing ad overlapping (Adapted from Kim et al. (2024)). . . 18
2.8 a) Linear Heat Input vs. Powder Feed Rate graph with the 3 processing zones which lead to porosity (Adapted from Dass and Moridi (2019)); b) Porosity occurence regarding global energy density (ω) (Adapted from Dass and Moridi (2019)). 20
2.9 Cross section view of a single line deposition and its geometrical parameters (Adapted from Sreekanth et al. (2020)). 22
2.10 Schematic of Marangoni effect of bead pool shape with variation of surface tension and temperature of the melt pool, with reference to DED systems. a) Melt pool shape for negative tension gradient, b) melt pool shape for positive tension gradient, and c) Melt pool shape in the case of a surface tension gradient change from positive to negative (Adapted from Dass and Moridi (2019)). 24
2.11 Influence of laser power and scanning speed on the bead geometry (Adapted from Ding et al. (2023)). 28
2.12 Observed microstructure from micrographs of the DED AISI 316L SS samples (Adapted from Saboori et al. (2019)). 29
2.13 AISI 316L printed in perpendicular and parallel direction and schematic for obtaining specimens for tensile tests (Adapted from Guo et al. (2017)). 32
2.14 Grinding bodies of disc mill (Adapted from Retsch GmbH Haan (2024)). 40
2.15 a) Overall layout of planetary disk (with multiple jars); b) Horizontal section of grinding jar; c) Ball Motion pattern in a jar during milling (Adapted from MTI Corp and Burmeister and Kwade (2013)). 41
2.16 a) Typical powder particle shapes (Adapted from ISO 3252:2023); b) Example of satellite particle (Adapted from Chu et al. (2021)). 43

3.1 Collected Chips. 52
3.2 Vibratory Disc Mill RS 1 and positioning of the grinding bodies. 53
3.3 Planetary Ball Mill Retsch PM 100 and detail of the jar positioning and counterweight. 54

3.4 Sieving apparatus: globe box, vibratory machine and standard sieves (38 and 212 μm). . . . 57
3.5 Particle size measurements on SEM results using the ImageJ software. . . . 57
3.6 Equipment used to measure the loose density of the powder. . . . 58
3.7 Equipment used to measure the tap density of the powder. . . . 59
3.8 Equipment used to measure the flowability of the powder. . . . 60
3.9 DED equipment used for the printings with details of the powder feeders (on the left) and the nozzle head (on the right). . . . 60
3.10 Linearization process in the Medicoat software: a) upcycled powder; b) commercial powder). . . . 61
3.11 Equipment used for sample preparation (a) and b) for cutting substrate and printings and c) for polish and grind the face to analyse) :a) Wire-cut EDM equipment; b) abrasive cut off machine; c) Grinding and polishing machines. . . . 66
3.12 Equipment used for sample preparation and microstruture analysis: a) Hot mounting press for resin samples preparation; b) SEM Equipment (Thermo Scientific Phenom XL G2 Desktop); c) Optical Microscope (Leica DM6 M). . . . 66
3.13 Inclusions measurements on printed wall micrograph using the ImageJ software. . 67
3.14 Equipment used for the chemical composition assessment: a) SPECTROMAXx with iCAL 2.0 (Quantitative analysis); b) and c) Thermo Scientific Phenom XL G2 Desktop SEM equipment (Semi-quantitative analysis). . . . 68
3.15 ZwickRoell microhardness tester. . . . 69
3.16 a) Schematic of the specimen obtained from the thin-walled structure; b) Tensile specimen dimensions 69
3.17 Tensile specimens: a) taken from the DED printed thin wall (the 3 on the left); taken from the as supplied AISI 301 cylinder block (the 3 on the right); b) tensile specimens after painting for DIC processing. . . . 70
3.18 Tensile testing apparatus. . . . 71

4.1 Resultant powder content in wt. % for each milling procedure 74
4.2 Elongation and Fracture Toughness of AISI 301, AISI 303 and AISI P20+Ni (Granta Design (2021)). . . . 75
4.3 Overused lid, jar and 30mm grinding balls. . . . 78
4.4 PSD of the powder produced through the PN5 disc milling conditions. . . . 80
4.5 PSD of the powder produced through the PN3 ball milling conditions. . . . 81
4.6 PSD of the powder produced through the NP2 ball milling conditions. . . . 81
4.7 PSD of the powder produced through the NP2 ball milling conditions with overused balls. . . . 82
4.8 PSD of the powder produced through the NP3 ball milling conditions. . . . 83
4.9 SEM micrograph of particles in the 38-212 μm size range produced in disc milling PN5 conditions. . . . 84
4.10 SEM micrograph of particles in the 38-212 μm size range produced in the ball milling PN3 conditions 85
4.11 Micrographs of: a) particles in the 38-212 μm size range produced in the ball milling NP2 conditions (SEM image); b) polished particles in the 38-212 μm size range produced in the ball milling NP conditions (observed in an optical microscope). 87
4.12 Micrographs of: a) particles in the 38-212 μm size range produced in the ball milling NP2 wigh overused balls conditions (SEM image); b) polished particles in the 38-212 μm size range produced in the ball milling NP2 with overused balls conditions (observed in an optical microscope). . . . 87

4.13 Micrographs of: a) particles in the 38-212 μm size range produced in the ball milling NP3 conditions (SEM image); b) polished particles in the 38-212 μm size range produced in the ball milling NP3 conditions (observed in an optical microscope). . . . 88
4.14 Tap Density, Loose Density and Flowability results in mean values. . . . 89
4.15 Evolution of the packaging density according to proportion between smaller and larger particles (adapted from Ddungu (2020)). . . . 90
4.16 Top views of printed lines 24 to 35. . . . 93
4.17 Cross section views of lines 2 to 12. . . . 94
4.18 a) Tool path employed; b) Warping and separation from substrate (adapted from Miedzinski). . . . 96
4.19 Single and multi layer printings performed with AISI 316L commercial powder. . . 96
4.20 1st printed wall. . . . 98
4.21 2nd and 3rd printed walls. . . . 99
4.22 2nd printed wall. . . . 99
4.23 3rd printed wall. . . . 100
4.24 Macrograph of the 1st printed wall (observed under an optical microscope). . . . 100
4.25 Macrograph of the 1st printed wall (observed under an optical microscope). . . . 101
4.26 Schematic of the 3 zones of the DED printed thin wall where the microstructure was assessed. . . . 101
4.27 Inclusions observed in the DED printed thin wall. . . . 102
4.28 Defect observed in Zone 3. . . . 102
4.29 Columnar dentritic structures observed. . . . 103
4.30 Inclusions observed on the DED printed thin wall. . . . 106
4.31 Inclusions observed on the original block (as supplied) in comparison with those observed in the DED printed thin wall. . . . 107
4.32 Microhardness along the height of a DED printed thin wall with upcycled powder. 108
4.33 Engineering curves of specimens DED printed with upcycled powder (U1, U2 and U3) and specimens taken from the original block (as supplied) (AS1, AS2 and AS3) 109
4.34 Observed fracture surfaces of AS2 and U1 specimens. . . . 111

5.1 Technical Drawing of the specimen for tensile testing. . . . 140
5.2 SEM micrographs of powder produced in the PN5 disc milling conditions. . . . 141
5.3 SEM micrographs of powder produced in the PN5 disc milling conditions. . . . 142
5.4 SEM micrographs of powder produced in the PN3 ball milling conditions. . . . 143
5.5 SEM micrographs of powder produced in the NP2 ball milling conditions. . . . 144
5.6 Micrographs of powder produced in the NP2 ball milling conditions (polished sample observed under optical microscopy). . . . 145
5.7 SEM micrographs of powder produced in the NP2 (with overused balls) ball milling conditions. . . . 146
5.8 Micrographs of powder produced in the NP2 (with overused balls) ball milling conditions (polished sample observed under optical microscopy). . . . 147
5.9 SEM micrographs of powder produced in the NP3 ball milling conditions. . . . 148
5.10 Micrographs of powder produced in the NP3 ball milling conditions (polished sample observed under optical microscopy). . . . 149
5.11 Micrographs of the DED printed thin wall with upcycled powder (observed under optical microscopy) and schematic of the 3 different zones observed. . . . 151
5.12 Micrographs of the DED printed thin wall with upcycled powder (observed under optical microscopy) - Zone 1 152

5.13 Micrographs of the DED printed thin wall with upcycled powder (observed in SEM) - Zone 1 . . . 153
5.14 Micrographs of the DED printed thin wall with upcycled powder (observed under optical microscopy) - Zone 1 . . . 154
5.15 Micrographs of the DED printed thin wall with upcycled powder (observed in SEM) - Zone 2 . . . 155
5.16 Micrographs of the DED printed thin wall with upcycled powder (observed in SEM) - Zone 2 . . . 156
5.17 Micrographs of the DED printed thin wall with upcycled powder (observed under optical microscopy) - Zone 1 . . . 157
5.18 Micrographs of the DED printed thin wall with upcycled powder (observed in SEM) - Zone 3 . . . 158
5.19 Micrographs of the DED printed thin wall with upcycled powder (observed in SEM) - Zone 3 . . . 159
5.20 Semi-quantitative chemical composition of a thin wall printed with upcycled powder - Matrix measurement. . . . 161
5.21 Semi-quantitative chemical composition of a thin wall printed with upcycled powder - Matrix measurement. . . . 162
5.22 Semi-quantitative chemical composition of a thin wall printed with upcycled powder - Matrix measurement. . . . 162
5.23 Semi-quantitative chemical composition of the original block (as supplied) - Matrix measurement. . . . 163
5.24 Semi-quantitative chemical composition of the original block (as supplied)r - Matrix measurement. . . . 164
5.25 Semi-quantitative chemical composition of the original block (as supplied) - Matrix measurement. . . . 164
5.26 Semi-quantitative chemical composition of a thin wall printed with upcycled powder. 165
5.27 Semi-quantitative chemical composition of a thin wall printed with upcycled powder (continuation). . . . 166
5.28 Semi-quantitative chemical composition of the inclusions numbered 3.1 and 3.2. . 168
5.29 Semi-quantitative chemical composition of the inclusions numbered 5.1, 5.2, 5.3, 5.4 and 5.5. . . . 169
5.30 Semi-quantitative chemical composition of the inclusions numbered 7.1, 7.2 and 7.3 170
5.31 Semi-quantitative chemical composition of the inclusions numbered 11.1, 11.2, 11.3, 11.4 and 11.5. . . . 171
5.32 Micrographs of the original block (as supplied) (observed under optical microscopy). 173
5.33 Micrographs of the original block (as supplied) (observed under optical microscopy). 174
5.34 Semi-quantitative chemical composition of the inclusions numbered 1.1, 1.2, 1.3, 1.4 and 1.5 . . . 176
5.35 Semi-quantitative chemical composition of the inclusions numbered 2.1, 2.2, 2.3, 2.4 and 2.5 . . . 177
5.36 Semi-quantitative chemical composition of the inclusions numbered 3.1, 4.2, 5.3, 5.4, 5.5 and 5.6 . . . 178
5.37 Microhardness measurements along the height of a DED printed thin wall with upcycled powder. . . . 179
5.38 Engineering curve obtained from the tensile testing of the specimens DED printed with upcycled powder. . . . 181

5.39 True curve obtained from the tensile testing of the specimens DED printed with upcycled powder. 182
5.40 Engineering curve obtained from the tensile testing of the specimens taken from the original block (as supplied). 182
5.41 True curve obtained from the tensile testing of the specimens taken from the original block (as supplied) 183
5.42 Images of the deformation field during the tensile tests obtained though DIC: specimen AS2; from the left to the right, 1st, 1000th, 2000th and 2557th (immediately prior to the fracture) images. 185
5.43 Images of the deformation field during the tensile tests obtained though DIC: specimen AS3; from the left to the right, 1st, 1000th, 2000th and 2515th (immediately prior to the fracture) images. 185
5.44 Images of the deformation field during the tensile tests obtained though DIC: specimen AS4; from the left to the right, 1st, 1000th, 2000th and 2619th (immediately prior to the fracture) images. 186
5.45 Images of the deformation field during the tensile tests obtained though DIC: specimen U1; from the left to the right, 1st, 850th and 1000th (immediately prior to the fracture) images. 186
5.46 Images of the deformation field during the tensile tests obtained though DIC: specimen U2; from the left to the right, 1st, 900th and 1313th (immediately prior to the fracture) images. 186
5.47 Images of the deformation field during the tensile tests obtained though DIC: specimen U3; from the left to the right, 1st, 1000th and 1300th (immediately prior to the fracture) images. 186
5.48 Schematic of the tensile specimens dimensions measured prior to the tensile testing. 187
5.49 Fracture surface micrographs of specimen AS2 (observed in SEM). 189
5.50 Fracture surface micrographs of specimen AS2 (observed in SEM). 190
5.51 Fracture surface micrographs of specimen U1 (observed in SEM). 191
5.52 Fracture surface micrographs of specimen U1 (observed in SEM). 191
5.53 Fracture surface micrographs of specimen U2 (observed in SEM). 192
5.54 Fracture surface micrographs of specimen U2 (observed in SEM). 193

List of Tables

1.1 Gantt chart for the thesis work plan. 2

2.1 Minimum, maximum and average values of mechanical properties obtained through DED processing of AISI 316L powder (Data gathered in the bibliographic review and presented in detail in Annex B). 30
2.2 Mechanical properties of AISI 316L parts obtained through conventional manufacturing methods. 31
2.3 Mechanical properties of AISI 316L Thin-walled structures. 34

3.1 Chemical composition (wt%) of the handled material obtained through OES analysis. 49
3.2 Chemical composition (wt%) of AISI 316L stainless steel (European Steel and Alloy Database). 50
3.3 Chemical composition (wt%) of possible stainless steels (European Steel and Alloy Database). 50
3.4 AISI 301 stainless steel properties (European Steel and Alloy Database). 51
3.5 Disc Milling procedure. 54
3.6 Planetary Ball Milling Procedures. 55
3.7 Fixed parameters for the AISI 316L depositions. 63
3.8 Printing parameters selected according to the literature review, combined considering the Taguchi L9 method - Upcycled Powder. 64
3.9 Printing parameters selected according to previous depositons - Upcycled Powder. 64
3.10 Printing parameters selected according to previous depositons - Upcycled Powder. 64

4.1 Powder content in wt (%) according to the size range - Comparison of the PN5 milling conditions for 3 different materials. 77
4.2 D10, D50 and D90 for powder produced according to different milling conditions. 79
4.3 D10, D50 and D90 for powder produced in the PN5 disc milling conditions - Comparison for 2 different materials. 80
4.4 Aspect Ratio and Average Particle Size results according to different milling conditions. 84
4.5 Average and standard deviation values from the tap density, loose density and flowability measurements. 89
4.6 Geometrical measurement results of the lines 3 to 12. 95
4.7 Calculation of the number of layers for each wall and measurements of the wall dimensions. 98
4.8 Quantitative chemical composition (wt%) of the original AISI 301 block (as supplied) and DED printed thin wall. 104
4.9 Semi-quantitative chemical composition (wt%) of the DED printed thin wall and original block matrices 104

4.10 Semi-quantitative chemical composition (wt%) of the DED printed thin wall (with upcycled powder). . . . 105
4.11 Yield strength, ultimate tensile strength and total elongation results from the tensile tests. . . . 109

5.1 Mechanical properties and other conclusions drawn in works regarding AISI 316L powder DED . . . 132
5.2 DED parameters applied in other studies regarding AISI 316L powder deposition. 136
5.3 DED parameters applied in other studies regarding AISI 316L powder deposition - continuation. . . . 137
5.4 Semi-quantitative chemical composition (wt%) of inclusions observed in the DED printed thin wall (with upcycled powder). . . . 167
5.5 Semi-quantitative chemical composition (wt%) of inclusions observed in the original block (as supplied). . . . 175
5.6 Microhardness measurements along the height of a DED printed thin wall with upcycled powder . . . 180
5.7 Tensile specimens measurements and parameters involved in the tensile testing and image acquisition. . . . 187

List of Abbreviations and Symbols

Abbreviations

AISI	American Iron and Steel Institute
AM	Additive Manufacturing
AR	Aspect Ratio
AS	As supplied
BM	Ball Milling
BPR	Ball to Powder Ratio
DED	Direct Energy Deposition
DIC	Digital Image Correlation
DoE	Design of Experiments
EBSD	Electron Backscatter Diffraction
EDM	Electrical discharge Machining
EDS	Energy Dispersive X-ray spectroscopy
EoL	End of Life
GED	Global Energy Density (or ω)
HAZ	Heat Affected Zone
INEGI	Institute of Science and Innovation in Mechanical and Industrial Engineering
LEL	Laser Energy Length (or Π)
LENS	Laser Engineered Net Shaping
OES	Optical Emission Spectrometry
PBF	Powder Bed Fusion
PBM	Planetary Ball Milling
PCA	Process Control Agents
PFL	Powder Feed Length (or Γ)
PSD	Particle Size Distribution
SEM	Scanning Electron Microscope
SPF	Speed per Feed
SS	Stainless Steel
U	Upcycled
UTS	Ultimate Tensile Strength
VED	Volumetric Energy Density
YS	Yield Strength
XRD	X-ray diffraction

Symbols

A_m	Melted Area
A_p	Printed Area
d	Melt Pool depth
d_i	Laser Beam Diameter
D	Dilution
D_{cut}	Depth of cut
F	Feed
h	Melt Pool height
h_{chip}	Chip height
L	Characteristic Length
m_p	Powder Feed Rate
M_a	Marangoni Number
N	Number of teeth
P	Laser Power
R	Cutting tool radius
t_{chip}	Chip Thickness
w_{chip}	Chip width
w	Melt Pool width
W_{cut}	Width of cut
ν	Scanning Speed
ϕ	Shear angle during cutting
φ	Spot Size
γ	Surface Tension
α	Thermal Diffusivity or Rake angle of the tool
η	Viscosity

Chapter 1

Introduction

1.1 Framework and Motivation

In the metalworking industries, tons of metallic wastes are generated on a daily basis. The chips resultant from machining processes represent a significant portion of those residues and are commonly recycled through re-melting and casting in foundry industries. However, there are other innovative and novel methodologies to recycle metallic chips such as the milling of machining swarf into metal powder for Additive Manufacturing processing. This strategy adds value to the residual chips while being a more sustainable powder production process in comparison with the conventional atomization processes (which require great amounts of energy and resources).

Therefore, this work aims to assess the feasibility of producing austenitic stainless steel powder through the upcycling of residual machining chips. The milling methods studied are disc milling and planetary ball milling. The upcycled powder is analyzed and its characteristics and properties are assessed. Moreover, this work studies the viability of printing these powders on a non-preheated dissimilar substrate, using Direct Energy Deposition technology. The resulting depositions were also characterized. Some possible applications of this methodology are (1) the production of clads/coatings in already existing components in order to increase the part's corrosion resistance, (2) repairing damaged components or (3) building of structural components with complex geometries.

1.2 Objectives

The primary objective of this dissertation is to transform austenitic stainless steel machining chips into powder for DED processing, deposit the resultant powder and access the printings through metallographic analysis and mechanical testing. The upcycled powder characteristics and properties are also compared to those of commercial gas atomized powder, in order to study the feasibility of producing DED powder feedstock through this strategy. Therefore, the most significant steps set for this work are detailed as follow:

- Literature review of: (1) Recycling and sustainability in Metalworking industries; (2) DED process (description, parameters, etc); (3) the state-of-the-art of DED processing of austenitic stainless steel powder (parameters influence, properties and applications); (4) milling processes and powder characteristics and properties; (5) state-of-the-art of upcycling of machining chips into powder.

- Transformation of machining chips into powder through disc and planetary ball milling. Assessment of the milling procedures productivity through sieving and weighing of the powder in the size range intended for DED processing.

- Characterization of the resultant powder according to its size, size distribution and shape through SEM analysis. Measurements of tap and loose densities and flowability.

- DED printings of the final powder on a dissimilar non-preheated substrate. Optimization of parameters (laser power, scanning speed and powder feed rate) according to a visual and micrographic evaluation of the depositions considering the top and cross section views.

- Printing of multiple-layered as thin-walled structure in order to obtain specimens for tensile tests.

- Tensile testing, microhardness testing, microstructure analysis and chemical analysis.

1.3 Work Plan Timeline

Table 1.1 presents a Gantt diagram of this work plan, highlighting the most significant tasks completed over the course of the several weeks allocated for the elaboration of this dissertation.

Table 1.1: Gantt chart for the thesis work plan.

Month	**February**					**March**					**April**					**May**					**June**		
Week nº	**1**	**2**	**3**	**4**	**5**	**1**	**2**	**3**	**4**	**5**	**1**	**2**	**3**	**4**	**5**	**1**	**2**	**3**	**4**	**5**	**1**	**2**	**3**
Bibliographic Review																							
Chips collection																							
Powder production (milling)																							
Powder analysis and characterization																							
Writing of the practical part																							
DED printings																							
Printings assessment and characterization																							

1.4 Structure

This report is divided into 5 chapters and the contents of those are presented below.

Chapter 1 corresponds to the introduction and presents, firstly, an explanation of the framework and the motivation for this work, and secondly the desired objectives and the programmed work plan.

Chapter 2 presents the literature review which works as the theoretical basis for the practical part of this dissertation. Therefore, the bibliographic review includes topics such as: (1) current state of recycling and sustainability in the metalworking industries; (2) DED process (description, advantages and drawbacks, parameters, etc); (3) state-of-the art of DED processing of austenitic stainless steel powders and (4) Powder production for DED processing (methods, powder characteristics and properties, etc).

Chapter 3 displays the materials and methods. In this section, the used equipment, followed procedures and performed tests are described in detail.

Chapter 4 presents the obtained results alongside the critical discussion regarding those.

Finally, Chapter 5 sums up the conclusions and future works. This section highlights the most important findings from this dissertation, according to its proposed goals and results. It is also suggested further studies that could be conducted to improve this work or to serve as starting point for other works.

Chapter 2

Literature Review

2.1 Recycling and Sustainability in Metalworking Industries

In recent years, it has been observed a global industrial growth due to the the increase in population and evolution of technology. This growth has led to undesirable environmental impacts. As the metalworking industry is one of the most important industries in today's world, it was responsible for growing and worsening environmental impacts. Therefore, when it comes to the metalworking industry, there are critical aspects that must be improved towards sustainability, namely the minerals consumption, energy generation and production and recycling of residue, among others (Batista et al. (2021)).

2.1.1 Steel Recycling

The recycling of metal residues has a pivotal role in the metalworking industries sustainability since it leads to the minimization of the environmental impacts due to the reduction of emissions and drop of energy and resource consumptions (Bendikiene et al. (2019)). Thanks to their unique properties, metals can be indefinitely recycled. At their end-of-life (EoL) stage, metal products can be re-processed via mechanical treatment and re-introduced into the production process to make new metals. Metal recycling closes the loop within the production process, therefore reducing the amount of waste that goes into landfill and the amount of required primary raw materials (EuRIC aisbl (2020)).

Regarding steel, its huge importance and application in engineering and construction is well known, being by far the most used metal globally. In addition, the global steel demand increased from 1046 million tons to 1500 million tons from 2005 to 2015 (Nidheesh and Kumar (2019)). Besides that, steel is 100% recyclable, being considered the most recycled material in the world and over 90% of EoL stainless steel is currently collected and recycled into new products (EuRIC aisbl (2020)).

2.1.1.1 Advantages of steel recycling

Steel recycling offers many advantages, both economically and environmentally. From the economic point of view, in 2018, it was projected that annual savings on environmental costs by using steel scrap in the EU could achieve up to 20 billion euros (EuRIC aisbl (2020)). Regarding the environmental benefits, it is stated that using steel scrap in the production process reduces CO_2 emissions by 58%. Besides that, recycling steel reduces the energy needed for primary production by 72%, air pollution by 86%, water use by 40%, and water pollution by 76%. The steel scrap availability has been increasing and nowadays, the amount of European steel scrap that is being collected and reprocessed is greater than the demand for steel scrap, therefore, there is no steel scrap shortage in the European Union (EuRIC aisbl (2020)).

2.1.2 Recycling of Machining Chips

Machining wastes such as chips or swarf are obtained by subtractive processes such as turning, facing, drilling, milling, and grinding. Until recently, chips were considered as waste, however, in the last years there have been multiple studies about metal chips reuse. At the moment, machining chips are estimated to represent a significant percentage of the metal scrap produced by all production processes worldwide (14.6% for steel and 13.7% for aluminum (Cullen and Allwood (2013)). Though Titanium is difficult to machine, it is estimated a 55% of chips left after machining. Titanium is commonly used to produced complex geometries parts therefore generating a large amount of waste. Besides that, the high cost of the material encourages the recycling of waste (Dhiman et al. (2021)). Thus, the importance of recycling titanium chips is highlighted.

Therefore, it is clear that metal chips recycling is an important subject to research since it can greatly reduce the environmental impacts present in the metalworking industry while reducing the production costs.

2.1.2.1 Machining Chips Recycling Methods

Firstly, the conventional method of chips recycling is the re-melting and casting in foundry industries. However, this process has a very high energy consumption and environmental impacts such as air contamination and gas emissions while representing high expenses and labor costs (Bendikiene et al. (2019)).

Secondly, and as stated above, in the previous years there have been various works which access different and novel methodologies to reuse metal chips. Those methodologies aim to overcome the shortcomings of the conventional recycling methods. Those innovative methods may be classified as either direct (when the chips are used as received) or indirect (when the chips suffer transformations before being reused).

Regarding the direct processes, some recently studied examples are: production of concrete by partially replacing sand with metal chips; use of steel chips in metal matrices as a reinforcement by infiltration and sintering of metal chips mixed with powders for the production of porous structures. However, all of these processes are highly influenced by the interactions between the

matrices and the chips, such as possible oxidation and poor bonding (Bendikiene et al. (2019), Batista et al. (2021)).

Another solution for the recycling of steel chips is the production of metal powders by milling processes, which represents an indirect process. This methodology is the focus of this study and is later detailed on this document in the Chapters 2.4.2 and 2.4.4. The majority of the literature available aims to access this method as an alternative to conventional powder production through atomization. Batista et al. (2021) reviewed the available studies about milling methods to produce powders from recycled chips. The authors concluded that those methods are feasible to obtain powder for composite production or additive manufacturing. The authors reviewed various studies regarding chips from different origins, different initial sizes and different materials (tool and stainless steels and aluminum, tin, titanium and nickel alloys).

Wei et al. (2023) reviewed the published studies regarding the transformation of machining chips into metal powder through ball milling. The authors concluded that this process is capable to produce large volumes of metal powder from discarded chips. However, the size and capacity of the ball mill utilized for processing the metal waste have an important effect on the amount of metal powder that may be produced. Large-scale ball milling methods can be energy-intensive and laborious, and the process may need to be adjusted for each metal type being milled. Furthermore, the cost of the equipment and the necessary maintenance can affect the economic viability of employing ball milling to manufacture large amounts of metal powder from metal waste. Besides that, there are other drawbacks such as contamination of metal powder due to excessive wear of the grinding equipment or issues related to the reactivity of some materials such as Ti and Al which require safety measures. The authors found some gaps in the literature regarding this theme and recommended those lacunae as foci of future works. Some of those mentioned gaps are: to understand the effects of ball jar and ball mill size and capacity on the process efficiency; to study the effects of additives and to investigate the environmental impact of ball milling on metal powder production (energy consumption, waste generated, etc). Nevertheless, those ball milling parameters and their influence are detailed later on this document on Chapters 2.4.2 and 2.4.4.

2.1.2.2 Recycling, Downgrading and Upcycling

So far, for simplicity purposes, only the term recycling has been used to describe the processes of reusing waste from the metalworking industry. However, in the realm of sustainability, three different terms often arise: recycling, downgrading and upcycling. Those terms are often represented by the icons presented in Figure 2.1. While they all involve repurposing materials, each approach has distinct characteristics and implications, particularly within the metalworking industry.

Recycling is perhaps the most familiar concept and involves collecting, processing, and converting waste materials into new products or raw materials for manufacturing.

In addition, downgrading involves converting materials into lower-grade products or materials. Therefore, downgrading does not attempt to maintain or enhance the original material quality. In the metalworking industry, a downgrading example is the shredding or breaking down of metal components into smaller pieces for use in less demanding applications. While downgrading can

prolong the lifespan of materials and reduce immediate waste, it ultimately leads to a loss of value and potential for reuse (Kucukvar and Kucukvar (2018)).

Finally, upcycling focuses on creatively transforming discarded materials into products of equal or higher value or quality than the original. Upcycling not only reduces waste but also adds aesthetic, functional or structural value, contributing to a more sustainable and innovative approach to production (Kucukvar and Kucukvar (2018)). A solution for adding value to metal wastes is to implement a a circular economy, using the wastes as “secondary” raw materials for new applications, reducing both costs and environmental impacts (EuRIC aisbl (2020)).

In this work, the transformation of chips into powders adds value to the swarf hence the common use of the upcycling terminology throughout this document. However, when addressing a broader context, as in Chapter 2.1.2, the term "recycling" is used.

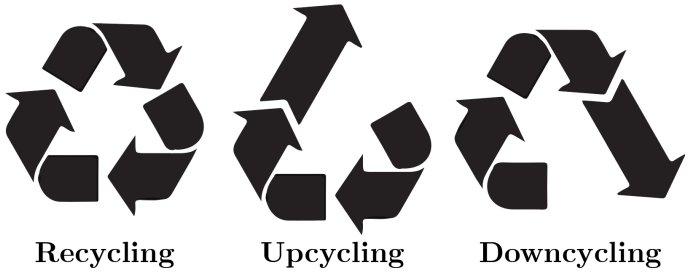

Figure 2.1: Recycling, Ucycling and Downcycling Icons.

2.2 Direct Energy Deposition (DED)

2.2.1 DED nomenclature and other AM processes

According to ASTM F2792-12a, Additive Manufacturing (AM) is described as a "process of joining materials to make objects from 3D model data, usually layer upon layer, as opposed to subtractive manufacturing technologies". The AM processes are classified into seven categories: Sheet Lamination, Vat Photopolymerization, Material Jetting, Material Extrusion, Binder Jetting, Powder Bed Fusion (PBF) and Directed Energy Deposition (ASTM F2792-12a).

From these range of processes, the last one will be reviewed due to its implications on these work. It should also be noted that, in the literature, different terminology is generally reported for the DED process such as: LENS (Laser Energy Net Shaping), LMD (Laser Metal Deposition), LC (Laser Cladding), DMD (Direct Metal Deposition), LAMP (Laser aided manufacturing process), DLF (Direct Laser Fabrication), LPF (Laser Powder Fusion) and others (Saboori et al. (2020a)).

2.2.2 Process description

Directed energy deposition (DED) is an additive manufacturing process in which focused thermal energy is used to fuse materials by melting them as they are being deposited on a substrate. Therefore, in DED, an energy source (e.g. laser, electron beam, or gas metal arc) is focused to melt the materials being deposited (Godec et al. (2022)). The most common heat source is a laser beam and it is also the case of the equipment used in this work. Therefore, this bibliographic review will focus its attention on laser based DED systems.

DED can use either powder or wire as feedstock. The use of powder as feedstock results in lower deposition efficiency compared with metal wire since only a portion of the total powder is melted and bonded to the substrate (Lee (2008)). In this document it will be reviewed the powder based systems since this is the system type used in this work. A schematic of a common powder DED system is presented in Figure 2.2.

Regarding the materials used in DED processing, the most common ones are are metals, metallic alloys, metal matrix composites, and refractory metals (Dutta (2020)).

The DED process share some similarities with Powder Bed Fusion (PBF), being the main difference the fact that, in DED the feedstock is not previously deposited on the substrate but is continuously supplied simultaneously alongside the heat input (Dutta (2020)).

Regarding the powder supply, these machines can have single or multiple nozzles to deposit the powder. Multiple nozzles have the advantage of allowing the mix of dissimilar materials to get functionally graded materials (FGM) (Li et al. (2017)). On the other hand, single nozzle feeding has a lower cost from its simplicity and enables printings in tight geometries and with a better powder capture efficiency. However, single nozzle feeding has the disadvantage of the geometry of the melt pool which tends to form in the direction of the nozzle (Gibson et al. (2015)).

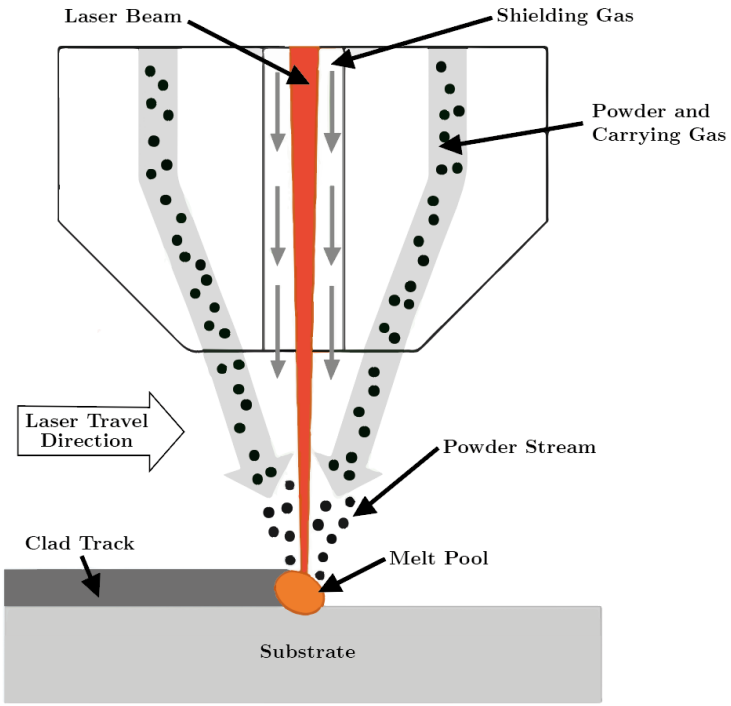

Figure 2.2: Schematic of a powder DED system with laser as energy source (Adapted from Cho et al. (2023)).

The configuration of the nozzle may also differ. The three most common configurations (lateral, annular and coaxial) are presented in Figure 2.3 (Nasiri and Movahhedy (2022)).

A lateral nozzle (Figure 2.3a)) uses a single nozzle that deposits powder into the melt pool created by laser. This type of nozzle is very suitable for simple processes due to its simple geometry and low price. However, the tool path dependency of the process hinders its application in manufacturing of complicated geometries. In annular nozzles (Figure 2.3b)) the powder is injected from the center of the nozzle and the laser radiates coaxially in a cone around the powder stream. This type of nozzle is the less common from the 3 since it is a recent technology and is relatively difficult to manufacture. Finally, the coaxial feeding (Figure 2.3c)) uses multiples powder injector (a minimum of three) arranged around the nozzle's axis, with the laser beam emitted from the center. In this situation, the powder is deposited at the laser beam's focus point. In these nozzles, the powder is injected from many directions, allowing it to deposit in all directions. (Nasiri and Movahhedy (2022)).

Before the deposition, the powder particles need to previously be fluidized by the application of an ultrasonic vibration, a rotating disc, or a gas flux. Afterwards, they can be stocked in hoppers. Then, a carrying gas (usually Ar) is turned on to to transfer the powder from the hoppers to the nozzle (Gibson et al. (2015)).

Usually, the nozzle head moves around a fixed object to deposit the material in specific locations (Shamsaei et al. (2015)). However, in some cases, it is the substrate which moves while the nozzle head stays still. Other systems combine the motion of the substrate and the printing head.

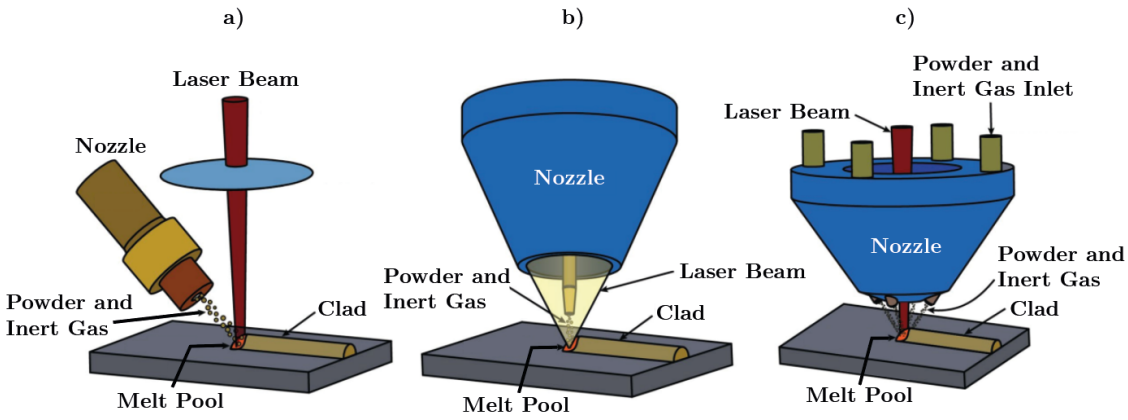

Figure 2.3: Common Nozzle Configurations: a) Lateral; b) Annular; c) Coaxial (Adapted from Nasiri and Movahhedy (2022)).

The most common are 3-axis systems although 4 and 5-axis may also be applied, where robotic arms and rotary tables are used which normally results in a greater freedom in the geometry to print. In multi-axial printing systems, the printings can be build following non vertical directions (Gibson et al. (2015)).

Therefore, the relative movement between the printing head and the substrate controls the process. In the most common case, where the printing head moves and the substrate is fixed, the the path taken by the nozzle is know as the toolpath. The toolpath is created directly from the CAD geometry. Therefore, DED systems work by repetitively producing lines every time the laser passes and, normally, more layers are deposited at the top of previous ones to form walls and to build parts (Oberg et al. (2020)).

The laser based DED systems work either in inert atmosphere chamber or under local shielding. The local shielding is provided through the supply of an inert gas, alongside the powder from the nozzles, which covers the melted region, reducing the oxidation rate (Gokuldoss et al. (2017)). In this case, the interactions among laser, powder and gas (normally Ar) create a controlled atmosphere for the powder melting and deposition on a substrate with proper prevention of oxidation on the melt pool. On the other hand, an inert atmosphere chamber is mandatory when depositing reactive metals such as Ti, Ta or Mo (Dutta (2020)).

Laser based DED machines may use different laser types, being the most commonly used the CO_2 lasers, the neodymium:yttrium-aluminum-garnet (Nd:YAG) lasers, the ytterbium fiber (Yb) lasers, and the high-power diode lasers (HPDL). The wavelength of these lasers range from 0.1 μm to 10 μm (Toyserkani et al. (2004)). The absorptivity of most metals increases with the decrease of the wavelength especially in the near-infrared region of the specter, which justifies the fact that most used lasers present wavelengths of 1 μm (more typical of diode or fiber lasers instead of CO_2 lasers), which leads to a more efficient melting of the metal. The laser selection must take into account the wavelength of the deposited material in order to decrease the energy reflection losses, the cost effectiveness, and the laser power while ensuring the desired printing rate, the melting of the particles and the pretended energy distribution (Toyserkani et al. (2004), d. A. Maciel (2021)).

Besides the laser based DED systems, this technology may also be applied using other heat sources such as Electron Beam or Gas Metal Arc. Regarding the Electron beam (EB-DED) systems, they require the use of a vacuum environment and are more expensive. In contrast, the EB-DED process results in lower residual stresses therefore those parts usually do not go under any stress relieving operation (Dutta (2020)).

2.2.3 Advantages and Drawbacks

As stated above, the functioning of the DED process share some similarities with the PBF process. The main advantages of DED, in comparison with PBF, are a higher printing rate (3-10 mm^3/s), elimination of scalability issues that occur in PBF and better utilization of the material since the feedstock is directly injected into the melt pool, in contrast with spread in a layer. DED systems, compared to PBF systems, tend to be larger and demand a higher energy density. (David L. Bourell and Seifi (2020a)).

In a more general view, DED stands out for its possibility of producing large and complex components with great quality and long service life, higher printing velocity and good metallurgical bonding. The DED process also allows the reduction of primary resources (Izdebska-Podsiadły (2022)). If integrated with CNC machining in a single hybrid machine, DED results in a powerful technology for achieving a precise finish on the manufactured product (Palmero and Bollero (2021)). This process also allows multiple material in single build and the building of FGM's. Besides that, DED has proven to be a qualified process to build parts with different type of metals such as tool steels, alloy steels, stainless steels, etc and even allows building parts with composite or ceramic feedstock materials. (Dutta (2020)).

There are also some economic benefits from the application of this process. DED allows an efficient short run production and reduced machining (DED parts are near net shape which reduces machining requirements for parts with high buy-to-fly ratio). The buy-to-fly ratio is defined as the weight of the initially purchased stock material compared to the weight of the final manufactured product. Aerospace components often have buy-to-fly ratios ranging from 10:1 to 40:1. DED also reduces time to market down to about 64% due to not being necessary tool fabrication (Coykendall et al. (2014)). Other benefit is material saving trough an efficient material utilization represented by an almost 1:1 buy-to-fly ratio. This characteristic becomes more important when working with costly metals (for example titanium, Inconel and refractory metals) which are very common in Aerospace, space and defense industry. The application of DED to repair, reconfiguration and re-manufacturing also is a very economically pleasant characteristic since it allows cost saving (Dutta (2020)).

The major drawback of the DED process is the poor accuracy (rough surface finish (60-100 μm) in comparison with other AM processes (Dutta (2020))), which leads to the need of post-process machining. On the other hand, defects such as residual stresses and porosity are common to appear, thus heat treatments and stress relief postprocesses are sometimes needed (David L. Bourell and Seifi (2020a)). In addition, tight tolerance parts are a difficult to achieve and large overhangs are not possible (Dutta (2020)). Another drawback is the feedstock losses, which can

go from 20% to 60%. Those losses happen when the powder is blown onto the surface and some of it escapes and is not melted. Therefore, it should be ensured that the lost powder is recaptured in a clean state to be recycled/reused (Oberg et al. (2020)).

2.2.4 Applications

The DED applications may be grouped into 4 categories: addition of features to already existing parts; repair of components; production of near net shape parts and cladding/coating.

Firstly, DED can be applied to add features such as flanges, ribs, connectors, or bosses to an existing part. This approach, in particular cases, may be more productive since it reduces machining time and waste materials (David L. Bourell and Seifi (2020a)).

Secondly, the DED process can be employed for the repair of damaged or worn out parts. This is the most used application and is due some DED unique characteristics. DED is versatile, practical and can operate in non-flat surfaces which makes it very suitable for repair, restoration and re-manufacturing. This applications leads to a decrease in lead time, production costs and environmental impacts (Gokuldoss et al. (2017)).

In addition, DED may be used to make almost net-shaped components with high levels of intricacy and very little waste material when compared to parts produced by traditional machining techniques (David L. Bourell and Seifi (2020a)). This application, sometimes referred to as "free form fabrication" makes use of additive manufacturing's tool-less capability, which makes low volume production very affordable.

Finally, the production of thick coatings to increase wear resistance and/or corrosion resistance is another application of the DED process. Since this application, also referred to as Cladding, is the primary focus of this work, it will be examined in greater detail throughout the document.

2.2.5 Process Parameters

The quality of DED products is mostly determined by the deposition parameters used in the process. A large number of parameters, which are detailed below, can be varied in DED in order to achieve the desired quality in the final part. The Figure 2.4 presents those parameters, divided into 4 main categories. The optimization of this parameters is pivotal to achieve the intended properties and mitigate or eliminate defects. It is established that those parameters influence the cooling rate, the thermal gradient and consequently the thermal history of the printed parts. The complex thermal history of DED deposited parts governs solidification, and consequently, the resultant microstructure, porosity, and residual stress formation (Saboori et al. (2020a)).

The Chapters from 2.2.5.1 to 2.2.5.8 present an explanation of the most important DED parameters among those presented in Figure 2.4. It is also explained their significance and influence on the DED process, regarding the majority of the materials processes in DED. Therefore, in these chapters, it is addressed the common trends for varying DED parameters, not taking into account materials whose properties after DED processing deviate from the normal pattern. However, later on this document, Chapters 2.3.1.3 and 2.3.1.1 present some conclusions about the impact of DED

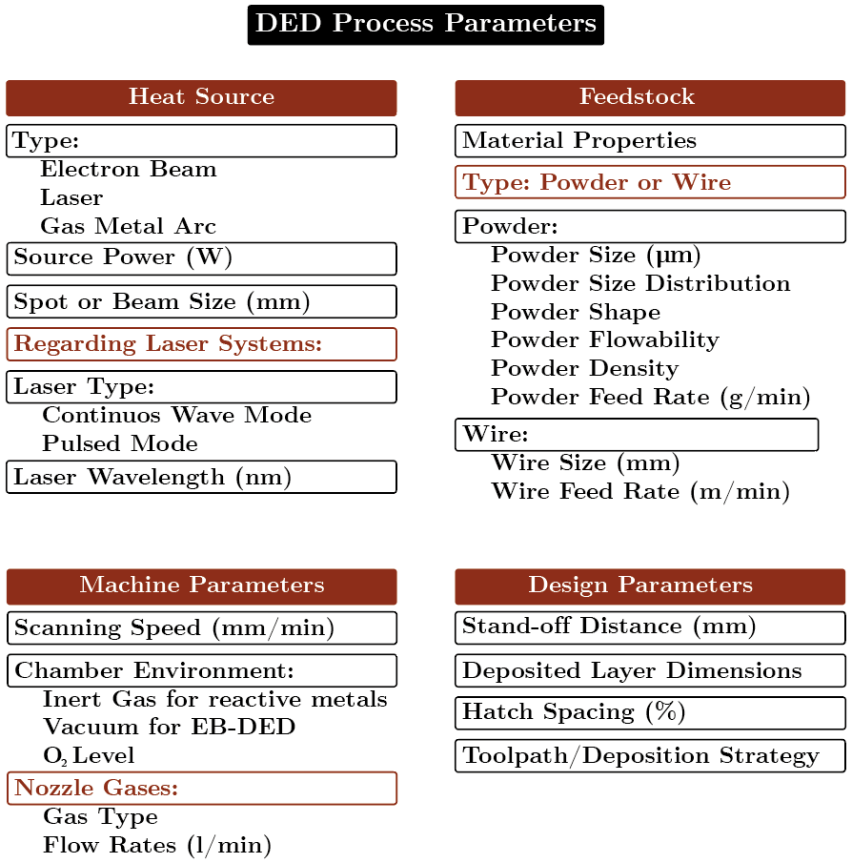

Figure 2.4: DED process parameters (Adapted from Dutta (2020) and Castanheira (2022)).

parameters regarding the processing of AISI 316L powder specifically. This information, from the review of recent studies about AISI 316L DED processing, corroborates the information stated from Chapters 2.2.5.1 to 2.2.5.8.

2.2.5.1 Laser Power

The laser power indicates the amount of heat energy delivered by the laser during the DED process to melt the feedstock material to the substrate. This parameter is considered pivotal since, for many mechanical and microstructural properties, is the parameter with greatest influence. It is also the parameter that impacts the most the process efficiency (Ghasempour-Mouziraji et al. (2024)).

In case of a very high laser power, the dilution proportion (Equation 2.7) between the printed material and the substrate will consequently be very high, which can lead to the reduction of the building rate and degradation of the corrosion and mechanical properties of the printings. High laser power can also lead to possible plasma formation and vaporization of the printed material (Goodarzi et al. (2015)).

However, very low laser power values must also be prevented since it can lead to an inefficient melting of the material and consequently lack of dilution, lack of fusion, and porosities (Ghasempour-Mouziraji et al. (2024)).

Therefore it is pivotal to achieve an optimum value for the laser power according to the feedstock and the substrate materials, as well as the combination of the other process parameters.

2.2.5.2 Laser spot size

The laser spot size (commonly measured in mm) is the diameter of the laser beam that is focused onto the workpiece during the DED process. The Figure 2.5 illustrates this parameter. This parameter has an inverse relationship to the energy density, as shown later in Chapter 2.2.5.9. A very large spot size can lead to a greater productivity in case of proper energy density. However, the dimensional tolerances of the final part may be poor (Mahamood (2018)). On the other hand, a small spot size must be used if the aim is to produce a final part very detailed and with restricted dimensional tolerances, since the decrease in spot size leads to a decrease of the width of the be printings. However, a smaller size leads to lower deposition rates (Wolf (2016)).

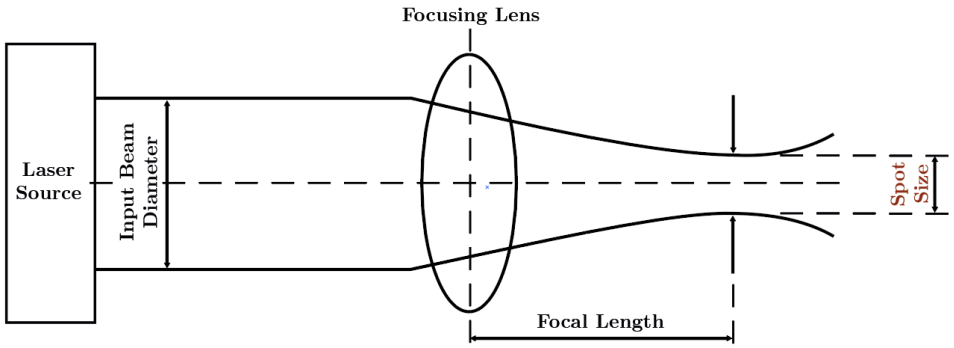

Figure 2.5: Schematic of Laser Spot Size.

2.2.5.3 Powder Feed Rate

The powder feed rate represents the amount of feedstock (in this case powder) that is injected into the melt pool in a certain period of time, and it is usually measured in g/min. This parameter directly influences the layer thickness of the deposited track and the properties of the final part, namely, metallurgical, physical, chemical, mechanical and tribological properties. The density and the material distribution of the final part are the most important properties and are both influenced by the powder feed rate. A very high value of powder feed rate can lead to lack of fusion or inappropriate powder melting and consequently poor properties, high roughness and a greater waste of feedstock. On the other hand, a very low value of powder feed rate leads to a reduced building efficiency, lower material density, decrease in layer height and can cause keyholes due to substrate material vaporization (Mahamood (2018)).

2.2.5.4 Scanning Speed

Scanning speed is the rate at which the printing head moves relative to the substrate. This parameter has a direct impact on the building rate. Higher scanning speeds lead to smaller local absorbed

energy concentrations and consequently reduced pool melting time. This also impacts the solidification behavior which affects the final mechanical properties. Higher scanning speeds also lead to a smaller powder feed rate and its respective consequences which are stated in Chapter 2.2.5.3. Besides that, lack of fusion, porosity and unmelted powder are other problems associated with high scanning speeds. On the other hand, a lower scanning speed may lead to a greater dilution and evaporation of material (Mahamood (2018)). For the industry, scanning speed is the parameter with greater impact on the cadence and therefore cycle times, since higher scanning speeds lead to lower cycle times. However there must be a balance to match a high cadence with a good quality of the part. Dutta (2020) stated that usually scanning speeds between 300 mm/min and 2000 mm/min.

2.2.5.5 Carrying Gas

As explained before in the Chapter 2.2.2, the powder to be deposited and melted is carried from the hoppers to the nozzle with the assistance of a carrying gas (Ruiz et al. (2018)). Besides that, this gas also protects the powder from reacting with the environment especially when the metal is reactive at high temperatures. However, the environmental protection function is mostly ensured by the shielding gas (Goodarzi et al. (2015)). Therefore, the Carrying Gas Flow Rate, commonly measured in l/min, has an impact on the quality of the DED process. A very high flow rate leads to excessive pressure in the nozzle and high velocity of the powder and consequently blowing away the powder from the melt pool. On the other hand, a too low flow rate may lead to a poor transportation of the powder and to contamination of the powder due to the lack of protection (Mahamood (2018)). The most common carrying gas is Argon followed by Nitrogen (Ruiz et al. (2018)).

2.2.5.6 Shielding Gas

As stated above in Chapter 2.2.5.5, a shielding gas is normally used to protect the melt pool from atmospheric contamination (specially oxidation in the case of reactive metals) by creating an inert protective atmosphere. Other option for melt pool protection is the deposition inside an inert chamber. The shielding gas has a large influence on the quality of the printings. For example, it can lead to porosity formation which can be avoided with a proper gas selection (Ruiz et al. (2018)). The interaction between the carrying and shielding gas flows impacts the spatial distribution of the powder in the nozzle's focal point which has effect on the process efficiency.

2.2.5.7 Tool path strategy

The selection of the printing path in DED process is key to mitigate defects. It influences the residual stress distribution, the porosity occurrence, the microstructure and the mechanical, metallurgical and geometric properties of the fabricated part (Ahn (2021), Shamsaei et al. (2015)).

In the case of a printing with discontinuous tracks, the laser needs to be turned on and off multiple times. Therefore, the printing strategy can be chosen to minimize the number of times

the laser is switched on and off. It is important to mention that the path should be as continuous as possible, since gaps in a printed track can lead to parts with low quality (Shamsaei et al. (2015)).

It is important to take into account residual stresses and thermal distortions, which can be significantly decreased by selecting the appropriate printing path. For instance, uneven surface heating may result from asymmetrical printing tracks, which may lead to the development of thermal tensions (Shamsaei et al. (2015)).

The most commonly used paths are illustrated in Figure 2.6, being from left to right, Raster, Zig-zag, Chessboard, Offset-Out, Offset-in and Fractal. It is important to mention that those paths may have different nomenclature in some literature.

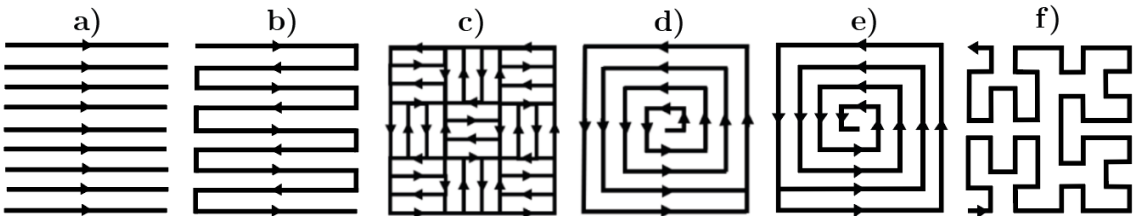

Figure 2.6: Common tool paths in DED systems: a) Raster, b) Zig-zag, c) Chessboard, d) Offset-Out, e) Offset-in, f) Fractal (Adapted from Ribeiro et al. (2020) and Hu and Cong (2018)).

In cases where the powder has a high thermal conductivity, an offset path is preferred since it results in a more uniform temperature distribution. In those cases, the Chessboard is also a viable option. The raster path is the most commonly used mainly due to its ease implementation and non-dependency on shape of the cross section allowing for printing of thin or thick shapes. The fractal and offset patterns are a challenge when it comes to parts with a complex geometry, however, they can lead to good geometric accuracies (Ribeiro et al. (2020)).

2.2.5.8 Hatch spacing and Overlapping

The hatch spacing is the distance between the centers of two following printed tracks/lines. If this distance is smaller than the sum of the two halves of adjacent track widths, then it can be said that there is overlapping. The overlap percentage corresponds to the percentage of a previous deposition track that is covered by an adjacent deposition track, and it is an important parameter in DED processes (Pei et al. (2017)). Figure 2.7 presents a scheme of the hatch spacing and overlapping concepts.

Due to the dome shape of the deposited tracks, it is necessary to have an overlap to prevent inter-tracks porosity, being the common overlap ratio 25% of the width of the deposited track (Gibson et al. (2015)). However some researchers defend the benefits of applying a greater Overlapping. For example, Yu et al. (2011) stated that an overlap of 50% lead to a better quality of DED produced parts by avoiding defects, specially when printing following the offset-out and fractal tool paths (Figure 2.6). Besides that, the elongation, tensile strength, and reduction of area were higher for an overlap of 50% than for an overlap of 45%, considering the same paths.

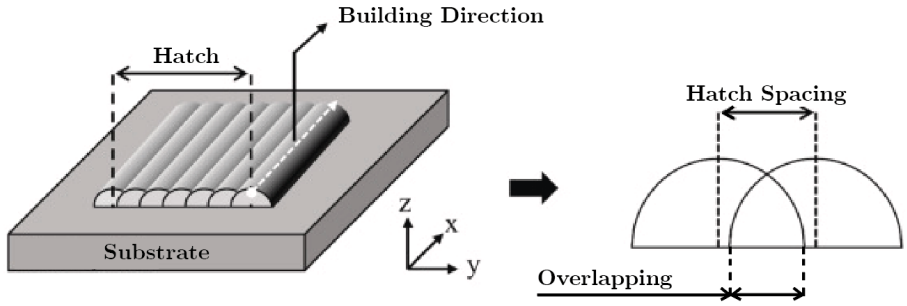

Figure 2.7: Schematics of hatch spacing ad overlapping (Adapted from Kim et al. (2024)).

2.2.5.9 Key Formulae

The quality and efficiency of the DED process results from the combination of multiple variables, as stated and explained above. Therefore, several researchers have been developing formulae that relate various DED parameters, in order to better understand which is the best set of parameters to select.

The parameters which affect the most the bead formation in DED processes are the laser power, scanning speed and powder feed rate. Therefore, several researchers suggested a laser energy per unit length (LEL, Π) and a powder feed per unit length (PFL, Γ) to quantify the correlation between those 3 parameters (Ahn (2021)). Those unit lengths are presented in Equations 2.1 and 2.2, being P the Laser Power, v the scanning speed and m_p the powder feed rate.

$$LEL = \Pi \ [J/mm] = \frac{P \ [W]}{v \ [mm/min]} \tag{2.1}$$

$$PFL = \Gamma \ [J/mm] = \frac{m_p \ [g/min]}{v \ [mm/min]} \tag{2.2}$$

In order to establish a relationship between interlayer (lack of fusion) and intralayer (keyholing) porosity, Dass and Moridi (2019) introduced the parameter GED, ω. Those two types of porosities are explained below in Chapter . The GED parameter is presented in Equation 2.3 and d_i is the beam diameter of the laser.

$$GED = \omega \ [J/mm^2] = \frac{P \ [W]}{v \cdot d_i \ [mm/min \cdot mm]} \tag{2.3}$$

The Volumetric energy density, VED (Equation 2.4) is similar to GED but includes the width (w) and height (h) of the deposited track (Kim et al. (2021)).

$$VED \ [J/mm^3] = \frac{P \ [W]}{v \cdot h \cdot w \ [mm/min \cdot mm \cdot mm]} \tag{2.4}$$

The speed per feed, SPF (Equation 2.5) links the Scanning Speed (v) to the Powder Feed Rate (m_p) by determining the traveled distance by the printing head for the deposition of 1g of feedstock

(Ferreira et al. (2021)).

$$SPF \ [mm/g] = \frac{v \ [mm/min]}{m_p \ [g/min]} \tag{2.5}$$

Finally, the Powder Deposition Density, PDD (Equation 2.6) indicates the amount of powder that is spread per each mm^2 during the printing process and therefore relates the Powder Feed Rate (m_p) with the scanning speed (v) and the laser spot size (φ) (Ferreira et al. (2021)).

$$PDD \ [g/mm^2] = \frac{m_p \ [g/min]}{v \cdot \varphi \ [mm/min \cdot mm]} \tag{2.6}$$

2.2.6 Typical Defects in DED produced parts

The main defects observed in DED produced parts are: porosity, residual stress, cracking and delamination. Those defects and its origins, causes and mitigation methods are explained below.

2.2.6.1 Porosity

Other common defect is the presence of porosity. This defect may come from different origins such as: unmelted particles; gas porosity from shielding and carrying gases; porosity from melt pool instability, porosity from shrinkage in fast solidification, porosity from lack of fusion and keyhole porosity (Dutta (2020)).

Regarding gas porosity, it is characterized by its spherical shape and relatively small size (10 μm - 200 μm). It can be also caused by an excessive heating of the melt pool which leads to gas entrapment. Besides that, the atomization process applied to produce the powder feedstock, may also lead to entrapped gases (Dutta (2020)).

Moreover, regarding shrinkage porosity, metals with larger solidification range and higher viscosity are more susceptible (Dutta (2020)).

Keyhole porosity manifests as tiny voids or bubbles within the material, similar to miniature keyholes. It is formed due to excessive energy input or inadequate shielding gas coverage during the printing. When energy levels soar too high, material vaporization occurs, trapping gas bubbles as the molten material solidifies. These trapped bubbles weaken the structure, forming spherical or elongated voids (Dass and Moridi (2019)).

On the other hand, lack of fusion porosity results from from incomplete bonding between deposited material and the base or adjacent layers. This defect arises when energy input falls short or depositing parameters are not finely tuned. It results in unfused patches or gaps between the clad and the base material, appearing as cracks, voids, or incomplete penetration (Dutta (2020)).

Dass and Moridi (2019) proposed a new type of porosity according to the origin: the mixed-mode porosity. This porosity emerges due to the combination of both keyholing and a lack of fusion in cases when a high linear heat input is excessive for the upper layers of the powder while the high feed rate do not allows the bottom layers to melt efficiently (since they are shielded by the upper powder). Therefore, the top powder volume suffers keyholing while the bottom powder volume experiences a lack of fusion. Figure 2.8 presents a graph of the linear heat input versus the

powder feed rate, which shows the processing regions associated with the 3 types of porosities. In this graph, it is possible to observe that mixed-mode porosity occurs by combining high Powder Feed Rate and high Heat Input, which is according to the explanation of this phenomenon.

The same researchers also linked the parameter GED (previously presented above in Chapter 2.2.5.9) to establish a relationship between lack of fusion and keyholing porosity. The academics found that the chance of a lack of fusion defect caused by low dilution increases with decreasing GED in the low GED region, whereas the possibility of keyhole porosity caused by high dilution decreases with rising GED in the high GED region. These trends are illustrated in Figure 2.8.

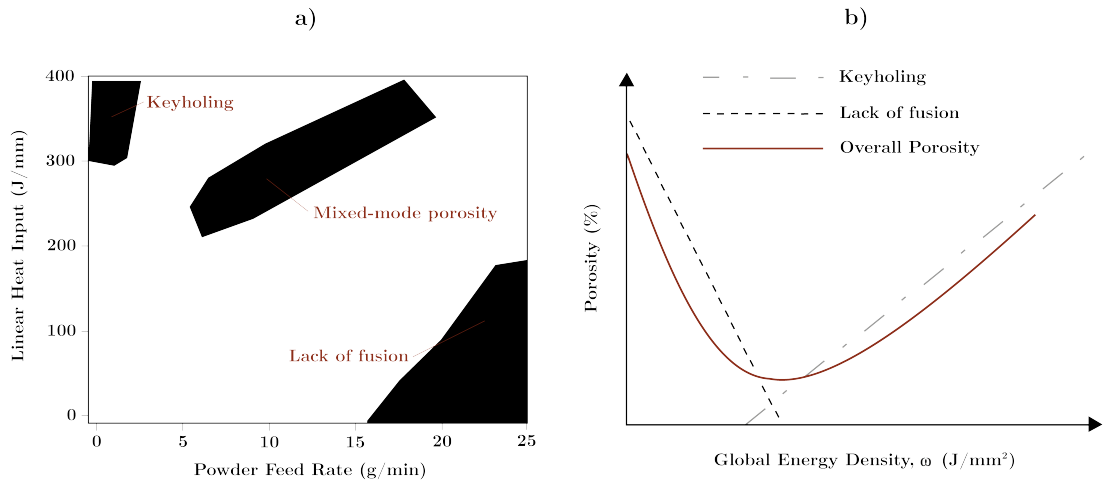

Figure 2.8: a) Linear Heat Input vs. Powder Feed Rate graph with the 3 processing zones which lead to porosity (Adapted from Dass and Moridi (2019)); b) Porosity occurence regarding global energy density (ω) (Adapted from Dass and Moridi (2019)).

According to Zheng et al. (2019), increasing scanning speed and reducing laser power leads to increased pore density as pores coalesce faster. Additionally, high scanning speed or low laser power could result in lack-of-fusion porosity. However, the effectiveness of increasing laser power to reduce porosity is limited by splatter ejection in keyhole formation. Thus, the laser power must be correctly selected because either low power values or high power values lead to porosities in the final DED part.

Besides the classification according to the origin of the porosities, it is also possible to classify the porosities according to their location. For example, Dass and Moridi (2019) classify porosity in DED parts into 2 categories: interlayer porosity and intralayer porosity.

Interlayer porosity occurs due insufficient energy input which leads to high solidification cooling rates and to un-melted regions. This porosity occurs near the substrate or between un-melted tracks, when the heat input is lower and/or the powder flow rate is greater. Interlayer pores are commonly large and irregular shaped (Dass and Moridi (2019)).

On the other hand, intralayer porosity is linked to the use of inert shielding gas which leads to gas entrapment. Another reason for this porosity is the vaporization in the melt pool, that also leads to gas entrapments. Intralayer pores occur in regions having lower solidification cooling rates and are usually spherical shaped (Dass and Moridi (2019)).

2.2.6.2 Residual Stresses

The primary causes of residual stress during AM processing are the dynamic temperature distribution and the fast cooling/heating cycles. During deposition, the same material is melted, reheated and remelted which leads to an intricate thermal history which makes DED produced parts prone to residual stresses. Residual stresses may lead to distortion, cracking and delamination while compromising the dimensional tolerances of the part to be produced. Residual stresses near the surface are tensile whereas those in the center are compressive stresses. Also, those stresses tend to be higher when dealing with dissimilar materials (due to different thermal expansion coefficients) therefore maximum residual stress values are observed at the substrate–deposit interface (Dass and Moridi (2019)). Residual stresses may also come from phase transformations. The liquid to solid transformation and solid-state transformations (e.g. martensitic transformation or precipitations) ersult in volumetric changes therefore result in residual stresses in the printings and in the substrate. Materials characterized by higherprintsolidification shrinkage, higher coefficient of thermal expansion, high Young's modulus and yield stress usually tend to have more residual stresses in the final part (Dutta (2020)). Those defects may be mitigated by preheating the substrate or the initial feedstock or by post-processing stress relieving techniques, namely heat treatments or Hot Isostatic Pressure (Dass and Moridi (2019)).

2.2.6.3 Delamination

Other common defect is delamination and it can be caused by insufficient heat input and consequently lack of bonding between consecutively deposited layers. Delamination corresponds to the separation between the substrate and the printed material, or the separation between successive printed layers. This defect distinguishes from porosities due to its larger size (200 μm - 1 mm or larger) and non-spherical shape. Delamination be result of insufficient melting and fusion (due to low energy densities), non-uniform and quick cooling, uneven thermal distribution and the presence of interlayer residual stresses (Liu et al. (2021)).

2.2.6.4 Cracking

Lastly, other defect that may occur in DED produced parts is cracking, which have various reasons. It can occur due to shrinkage in cooling since layers have higher contraction comparing with the underlying layers or substrate, which leads to the formation of residual tensile stresses. This type of cracking is commonly know as solidification or hot cracking (Svetlizky et al. (2021)).

Besides that, cracking can also occur due to the melting of precipitations at the grain boundaries during heating. The melting of the precipitations happen because they have a lower melting temperature than that of the original alloy. Alloys that have large thermal contraction, solidification shrinkage and a large gap between the liquidus and solidus temperature, such as Ni-based alloys, are the most prone to suffer this type of cracking. This cracking type is usually named liquation cracking and occur in the partially melted zone of the printing (Svetlizky et al. (2021)).

Lower scanning speeds or a higher preheat temperature can help to mitigate cracking (Dutta (2020)).

It is important to mention that delamination and cracking are defects that can not be mitigated through post-processing. Therefore, their occurrence must be avoided through deposition parameters optimization and/or preheating of substrate and/or feedstock (Svetlizky et al. (2021)).

2.2.7 Printings Assessment

The analysis of a final DED produced part is pivotal to understand and access the efficiency of the process. This chapter illustrates how this assessment is usually conducted and its relevant aspects.

2.2.7.1 Bead analysis: shape and geometry

The analysis of the melt pool geometry is pivotal since it is an indicator of the efficiency of the AM parameters. The Figure 2.9 shows a scheme of a single printed track cross section and its geometric parameters: width (w), height (h), depth (d) and wetting angle (θ).

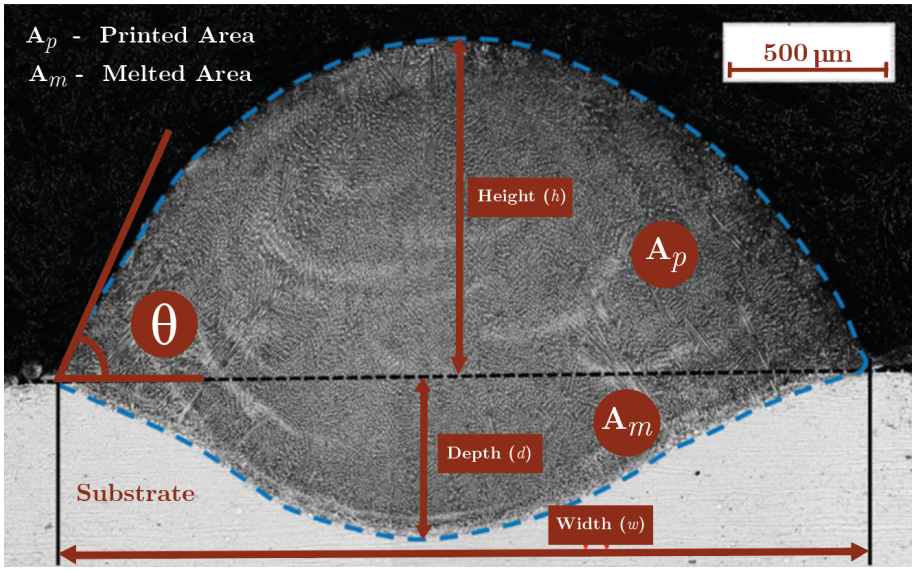

Figure 2.9: Cross section view of a single line deposition and its geometrical parameters (Adapted from Sreekanth et al. (2020)).

Wetting angle The wetting angle θ, can be indicative of the printing quality since its value is directly related to the interfacial energies, namely the liquid-vapor γ_{LV}, solid-vapor γ_{SV} and solid-liquid γ_{SL} interfaces energies. Normally, a low wetting angle is due to a high laser energy while a high wetting angle (greater than 90º) is due to oxidation since an oxide substrate is less wettable by a melted metal (Toyserkani et al. (2004)).

Dilution Dilution is the zone of the substrate (or below the addition material) melted during the DED process. The presence of dilution in the substrate provides a metallurgical bonding between

the printed material and the substrate since they mix together during melting. The proportion of dilution quantifies the degree to which the substrate material and the deposited material mix during the process and therefore serves to quantify the metallurgical bonding level. The dilution proportion is calculated through Equation 2.7. Dass and Moridi (2019) stated that this value should be between 10% and 30%. The authors concluded that keyhole defects occurs when the dilution ratio surpasses 30%, while the lack of fusion defects emerge when the dilution ratio is below 10%. However, in some cases, a higher dilution might be acceptable or even desired, particularly if the goal is to achieve a gradual transition in properties between the substrate and the deposited material. This can be important for applications where a strong metallurgical bond is required.

$$D = \frac{d}{h+d} = \frac{A_m}{A_m + A_p} \tag{2.7}$$

A low dilution value is usually related to a high powder flow rate and/or low energy input. On the other hand, a high dilution value results from low powder feed rate and high energy input (Dass and Moridi (2019)). The dilution tends to increase with an increase in the laser power and a decrease in the travel speed (Toyserkani et al. (2004)).

Melted Area Shape The melted area, A_m corresponds to the substrate material that has been melted. It ensures the metallurgical bonding between the substrate and the printed track. The melted area is preferred to be as thin as possible, with the minimum depth to guarantee a proper bonding. Regarding the A_m geometry, it should be uniform and shallow. However, since the laser beams usually have a Gaussian distribution, the energy tends to concentrate in the central part of the printing track which leads to an increase of the melted area in the center, as shown in Figure 2.9(Goodarzi et al. (2015)).

Another common melted area shape occurs when it is formed 2 smaller united melted area shapes within the bead width. One possible cause for this shape is a ring shape distribution of the laser energy which leads to the formation of two burn-in peaks. Excessively high scanning speed may also lead to this ring shape distribution (de Lange et al. (2005)).

An asymmetrical melt pool shape is also common and one possible reason to this is a lateral powder feeding, which leads to concentrations of convective heat (Goodarzi et al. (2015)).

Marangoni force Besides that, the melt pool shape may also be influenced by the Marangoni convection force (de Lange et al. (2005)). This force is originated from the Marangoni effect, which is a convective heat transfer mechanism that influences melt pool flow dynamics. The Marangoni forces are formed as a result of variations in surface tension and temperature along the melt pool, causing movement in the liquid melt pool. This motion is mainly from high surface tension regions to low surface tension regions and influences the melt pool depth (Dass and Moridi (2019)).

The Marangoni number (M_a) is a dimensionless number that characterizes the Marangoni flow for any DED process and is provided in Equation 2.8:

$$M_a = \frac{d\gamma}{dT} \cdot \frac{dT}{dx} \cdot \frac{L^2}{\eta \cdot \alpha} \tag{2.8}$$

where γ is the surface tension, dT/dx is the temperature gradient, L is the characteristic length, α is the thermal diffusivity and η is the viscosity of the melt pool.

Therefore, the surface tension and temperature influence the melt pool motion due to the Marangoni effect, as illustrated in Figure 2.10. When the surface tension gradient (i.e. the curve slope) is negative (Figure 2.10a)), the melt pool depth is small while when the surface tension gradient is positive (Figure 2.10b)) this depth increases. In the first case there is bulk turbulence flow while on the second case occurs surface turbulence in the melt pool, which may also retain unwanted oxides. Figure 2.10c) demonstrates the shift from a positive to negative surface tension gradient at a specific temperature, T_O. This transition represents a melt pool flow change from surface to bulk turbulence. (Mills and Shirali (1998)).

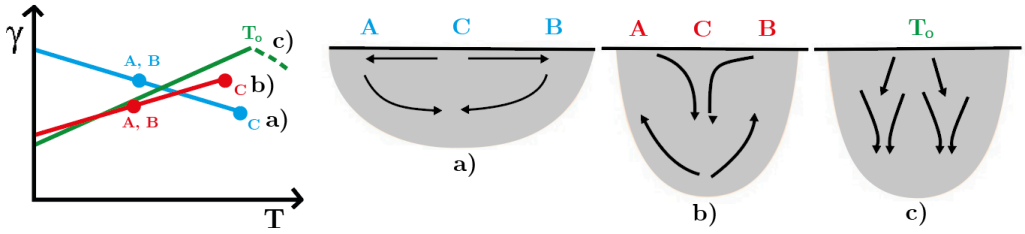

Figure 2.10: Schematic of Marangoni effect of bead pool shape with variation of surface tension and temperature of the melt pool, with reference to DED systems. a) Melt pool shape for negative tension gradient, b) melt pool shape for positive tension gradient, and c) Melt pool shape in the case of a surface tension gradient change from positive to negative (Adapted from Dass and Moridi (2019)).

Besides that, the Marangoni convection forces increase with the increase in Laser Power and depend on the chemical composition of the material (Goodarzi et al. (2015)).

There are other forces involved in the DED process such as: aerodynamic drag (outward drag forces caused by the plume formed above the melt pool); buoyancy (upward movements of the melt pool due to density changes caused by thermal gradients in the melt pool); Lorentz forces (due to electric and magnetic fields) and forces from the powder jet flow (Dass and Moridi (2019)). That last one may also influence the shape of the melt pool because the powder particles and gas flow have a high kinetic energy, therefore, when injected into the melt pool, induce frictional and pressure forces and consequently influence the melt pool shape (Goodarzi et al. (2015)).

2.2.7.2 Porosity Assessment

The amount of porosity in a DED produced part is an important measurement to assess the efficiency of DED processes in order to achieve the optimal deposition parameters. This defect is directly linked with the mechanical and physical properties of the final parts, such as corrosion, oxidation and fatigue resistance of the built components (Svetlizky et al. (2021)). Porosity can be evaluated both qualitatively and quantitatively and some commonly used techniques include the

Archimedes principle, X-ray computed tomography, and optical microscopy. As explained in the Chapter 2.2.6, porosities can be classified either by its location (Intralayer or interlayer porosities) or by its origin (lack of fusion or keyhole, as explained below).

2.2.7.3 Microstructure Assessment

The microstructure analysis of final DED parts is pivotal to observe several defects. Firstly, it is important to understand the common microstructure of DED produced parts and the parameters which influences it. Later on this document, in Chapter 2.3.1.2, it is presented the typical microstructure of DED parts from 316L powder specifically.

Typical Microstructure of DED produced parts The morphology and grain size of DED parts is mainly affected by the thermal history of DED components, such as high cooling and heating rates, pronounced temperature gradients, and bulk temperature increases. The final solidified microstructure is determined by the following variables: local solidification rates, the temperature gradient at the liquid/solid interface (G), and the cooling rate/thermal gradient (R). The key solidification parameters are G/R and G×R, which significantly affect the geometry of the liquid/solid interface and grain size, respectively. (Saboori et al. (2020a)). According to Selcuk (2011), low G/R values result in equiaxed structures while high G/R values lead to columnar structures. Several scholars have studied optimized G and R values to obtain the desired microstructure and mechanical properties. It is well understood that the optimal values are determined by the component's geometry, environmental conditions, and the properties of the material. Bontha et al. (2006) showed that higher solidification rates favor a transition from columnar gain to an equiaxed morphology. Besides, a rise in the cooling rate leads to microstructure refinement. Others researchers have been studying the heat transfer modes in the melt pool, in order to understand the thermal history of DED parts and consequently the microstructural results (Saboori et al. (2020a)). The conclusions are that the central zone of the melt pool is dominated by convective heat transfer mode while on the heat affected zone and melt pool borders the prevailing mode is solid conduction. In addition, a complicated mix of convective-conductive-radiating heat transfer is observed at the borders of the laser track, when the lateral sides of the melt pool are exposed to the environment.(Saboori et al. (2020a)).

Microstructure Analysis As stated above, through microstructure analysis it is possible to observe defects such as the presence of inclusions, i.e. impurities or particles formed during the DED process. Their origins may be the feedstock materials or contaminations such as oxides. Inclusions lead to worst mechanical properties since they act as stress concentrations spots and can induce cracking.

Likewise, through microstructure analysis it is possible to observe the HAZ (Heat Affected Zone), i.e. the areas that that did not melt, but still suffered alterations of the microstructure because of the exposure to high temperatures. The HAZ may be seen at naked eye and can weaken the mechanical properties. The analysis of new phases formation in this zone is also important. For

instance, during the DED process, phases like martensite can be developed. To prevent undesirable phases from appearing, the substrate can be preheated. On the other hand, a post processing heat treatment may recover the original desired mechanical properties (Liu et al. (2021)).

2.2.7.4 Residual Stresses, Cracking and Delamination

Residual Stresses may be accessed by techniques such as Hole drilling, ring-core ringing, serial sectioning or X-ray diffraction (Svetlizky et al. (2021)).

Cracking and delamination can be detected via radiography and cross sectioning being the opening and characterization of cracks by Scanning Electron Microscopy the most common technique.

2.3 Directed Energy Deposition of austenitic stainless steel powder

To serve as theoretical foundations for the practical part of this work, it was important to investigate about the state-of-the-art of DED processing of austenitic stainless steels. Due to the reasons that will be presented alter in Chapter 3.1, firstly the bibliographical research only covered the DED processing of AISI 316L powders. However, in the final stage of the work, the need arose to research about the processing of AISI 301 or similar alloys such as AISI 304. Nevertheless, it was found that DED processing of those 2 steel grades has not yet been much researched by academics. The few studies that were found either draw conclusions that were already presented in the AISI 316L bibliographic research or focused on topics not relevant to this work or studied the deposition of 301/304 powders mixed with other materials powders. The first aspect is related to the the extensive research that DED processing of 316L that has been done in the last years. The strong mechanical and corrosion properties of the 316L steel made this material by far the most processed and investigated, regarding DED studies (Saboori et al. (2020a)).

Therefore, this chapter presents the conducted literature review on DED processing of AISI 316L powder. It is shown, firstly, the influence of DED parameters in the the final 316L DED parts, with special emphasis for the impact on mechanical properties. Then, it is presented some feasible applications of DED processing of 316L powders, such as cladding and building of thin wall structures, also mentioning the applications of this steel in the aerospace industry.

2.3.1 DED processing of AISI 316L powder

Several articles were reviewed in order to study the current state-of-the-art of Directed Energy Deposition of AISI 316L powder. Therefore, this chapter analyses several aspects such as: the impact of DED parameters on the bead geometry of AISI 316L depositions, the common microstructure found in AISI 316L DED produced parts and the typical values of mechanical properties achieved by DED printing AISI 316L powder as well as its relation with the DED parameters.

presents the properties that come from the DED processing of AISI 316L powder as well as its possible applications. Besides that, the commonly found microstructure is studied as well as the influence of DED parameters in the mechanical properties and bead geometry, specifically regarding AISI 316L.

2.3.1.1 Bead geometry

Since, in the pratical part of this work, the first printings are single line depositions, it is important to understand the impact of the different DED parameters in the bead geometry of AISI 316L depositions.

Influence of DED parameters in bead geometry Ding et al. (2023) produced 316L SS clads on a U71Mn rail. Besides studying the influence of processing parameters on the wear behavior, the scholars also studying its influence on the bead geometry. The authors accessed the influence of

Laser power and scanning speed while maintaining powder feeding rate at 15g/min and the results are shown in Figure 2.11.

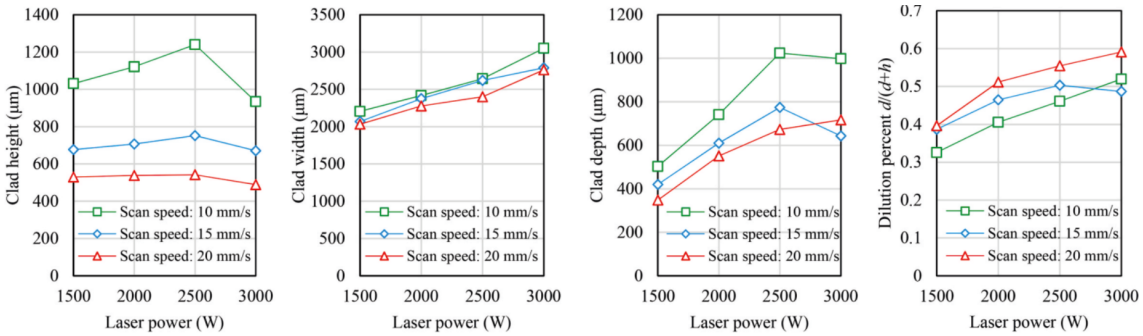

Figure 2.11: Influence of laser power and scanning speed on the bead geometry (Adapted from Ding et al. (2023)).

Goodarzi et al. (2015) studied the influence of process parameters on the shape of the melt pool and on the melted areas of the clad bead substrate. They used a design of experiment (DOE) method considering different laser power, scanning speed and powder feed rate values. The authors concluded that with an increase of the linear energy input (increase of the laser lower or decrease of the scanning speed), the volume of the melted substrate tended to increase. In addition, it was found that the burn-in shape changed (became asymmetrical and the melted substrate depth decreased) with the increase in powder feeding rate. Regarding the melted areas of the clad bead substrate, the melted volume of the substrate is an important parameter which measures the quality of the laser cladding process. The best cladding quality is achieved when the base material surface just melts enough to obtain a good metallurgical bonding between the clad layer and the substrate material. The authors concluded that laser power is the most significant factor for the substrate melted volume, explaining 62% of the values variation, followed by Powder feeding (13%) and Cladding speed (10%). An increase in laser power leads to an increase in the melted substrate volume, while the feeding power and cladding speed have an opposite effect. The substrate material used was the S355 structural steel.

2.3.1.2 Microstructure

After solidification, AISI 316L DED components typically have three structure morphologies: columnar grains, which represent an elongated morphology that develops in the direction of a high thermal gradient; columnar-equiaxed grains; and equiaxed grains. (Saboori et al. (2020a)) Those morphologies are shown in Figure 2.12 b) and can be caused as a result of different G and R values (as previously explained in Chapter 2.2.7.3). In Figures 2.12 a) and 2.12 b) it is possible to observe the common curved border of the melt pool which is consequence of the Gaussian distribution of laser energy (Saboori et al. (2020a)).

In Figure 2.12, it is also evident that the temperature gradients in the direction perpendicular to the curved melt pool boundaries are intense and clearly oriented. This results in the formation of a marked directional formation of dendrites from the melt pool borders and converging towards

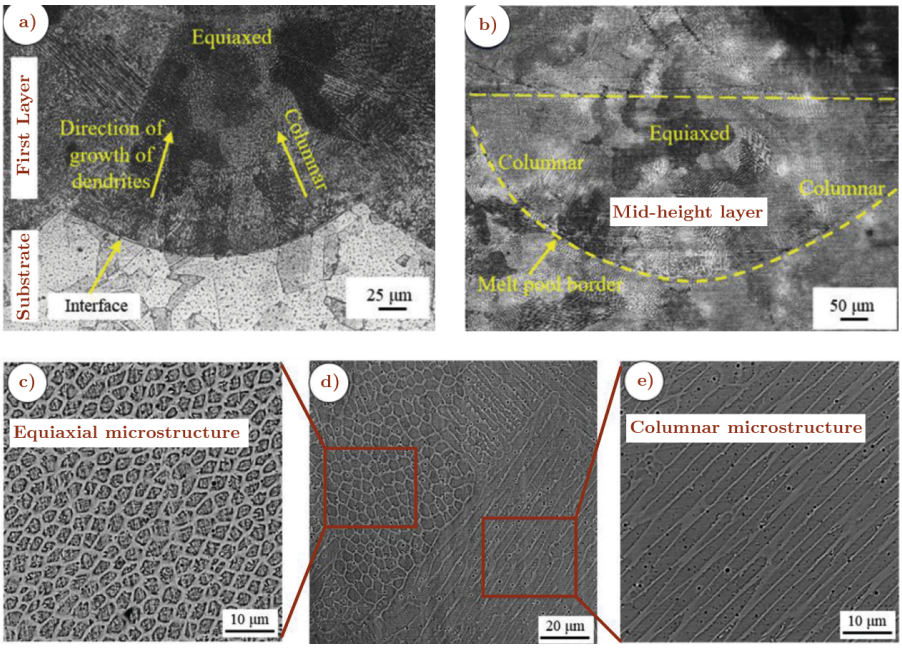

Figure 2.12: Observed microstructure from micrographs of the DED AISI 316L SS samples (Adapted from Saboori et al. (2019)).

the middle of the melt pool. On the other hand, Equiaxed dendrites are more probable to form in the central region of the melt pool, where the heat transfer mode has changed and is no longer preferentially oriented.

The Figure 2.12 a) shows a cross section of the first deposited layer, which was directly printed on the substrate while the Figure 4.29 b) presents the cross section of a mid-height layer of a printed vertical structure. The columnar structure in the mid-height layer grows in the direction of the highest thermal gradient. The variation in the microstructure of components along the building direction causes an oscillation in the microhardness values along that direction. Therefore, the microhardness decreases from the first to the second layer, progressively increasing towards the last layers (Kadiri et al. (2008)). This variation in microhardness is due to the varying solidification rate. Furthermore, during deposition, due to the reheating of previously deposited layers, the center area is subjected to cycle reheating, resulting in the development of a heat affected zone area that stays at higher temperatures for an extended period of time. Consequently, finer microstructure and greater microhardness are expected for the bottom and top of DED parts, which experience higher cooling rates than other regions (Saboori et al. (2020a)).

According to Aversa et al. (2020), the microstructure of DED 316L components is generally composed of large columnar grains with thin austenitic cells surrounded by retained δ-ferrite. This distinct microstructure is responsible for the remarkable mechanical properties of DED parts, which are typically greater (higher strength and lower ductility values) compared to components of the same alloy produced using conventional methods.

The Schäffler diagram is often used to predict the final microstructure of the material. This diagram predicts the presence of ferrite, martensite, and austenite phases as a function of Cr and

Ni equivalents. However, it is reported that this diagram is not a precise tool, therefore the result is an approximation of the final microstructure. This diagram is frequently employed to predict the microstructure of corrosion-resistant steels with carbon content up to 0.25% resulting from welding. In the DED process, the cooling rate is always greater than the welding rate, hence solidification is not under equilibrium conditions. Therefore, it is strongly advised that, in addition to the Schäffler diagram, the pseudo-binary predictive phase diagram is utilized (Saboori et al. (2020a)).

In regard to inclusion formation, the presence of Si and Mn oxides is a prevalent unwanted feature in 316L DED-produced parts. Even with adequate gas shielding, the development of these oxides is difficult to prevent due to the steel's strong reactivity with oxygen. Nevertheless, it should be emphasized that their effect on DED generated parts in comparison to conventional steelmaking methods is more moderate, mainly due to the final reduced size and spherical shape of the oxides (Saboori et al. (2020a)). However, the presence of these oxides reduces the corrosion resistance of 316L parts (Ganesh et al. (2012)).

2.3.1.3 Mechanical properties

The Hardness and the tensile properties are important indications of the quality of an AM process. The Hardness assesses a material's resistance to local plastic deformation and it is an important parameter in DED because it quantifies the wear resistance and durability. For example, if the DED process creates components with variable or inadequate hardness, they may fail early, causing safety risks and increasing maintenance costs. Moreover, the tensile properties include tensile strength (US), yield strength (YS), and elongation (ε) and evaluate the ability of a material to withstand tensile stresses. These properties are critical in determining how a material will function under mechanical load.

Therefore, the mechanical properties of DED materials have been extensively studied, and multiple tensile and hardness measurements of DED produced AISI 316L samples are available in the literature.

The Annex A reports the mechanical properties of DED AISI 316L stainless steel samples produced in different conditions. Those respective processing conditions are also presented in Annex B. The Table 2.1 gathers all the data from Annex A and summarizes it by presenting the minimum, maximum and average values of mechanical properties of AISI 316L parts produced through DED powder processing.

Table 2.1: Minimum, maximum and average values of mechanical properties obtained through DED processing of AISI 316L powder (Data gathered in the bibliographic review and presented in detail in Annex B).

Mechanical Properties	Yield Strength [MPa]	Tensile Strength [MPa]	Elongation [%]	Hardness [HV]
Minimum	229	571	10	92
Maximum	639	776	61	427
Average	**443 ± 119**	**609 ± 100**	**37 ± 13**	**230 ± 82**

These values can be compared with the tensile properties and hardness of AISI 316L samples obtained by conventional technologies, which are presented in the Table 2.2.

Table 2.2: Mechanical properties of AISI 316L parts obtained through conventional manufacturing methods.

Reference	Manufacturing Process	Yield Strength [MPa]	Tensile Strength [MPa]	Elongation [%]	Hardness [HRB]
Saboori et al. (2020b)	SLM	495 - 500	610 - 620	38 - 48	-
	Wrought	255 - 310	450	30	-
	As Cast	262	552	55	-
Ren-bo et al. (2011)	Solution treated	245	585	61,2	75,8
	Hot rolled	220	565	64,5	73,2
Tolosa et al. (2010)	Wrought	220 - 270	520 - 680	40 - 45	-

From the available data, it is possible to observe that the tensile strength of DED AISI 316L samples is generally higher than that of conventionally manufactured steels. The reason for this is the unique microstructure of DED parts (reduced grains and dendrite size and presence of residual δ ferrite). Those microstructural features are related to the high cooling rate in the DED process and also explained the commonly low ductility found in DED produced parts (Saboori et al. (2020a)).

By analyzing the Table 2.1 it is possible to note that there is a wide variation in the mechanical properties. These discrepancies are generally due to differences in the DED parameters. This impact of the DED parameters on the mechanical properties is explained below.

Influence of DED parameters in mechanical properties

Laser Power and Scanning Speed Saboori et al. (2020a) gathered data from a series of studies that analyzed the mechanical properties of DED produced 316L samples. In adittion, the authors specified the processing conditions of those studies, namely the power, scanning speed, building direction and shielding environment (local shielding or chamber). From this data, it was possible to access that the lowest YS, US, and ε values were obtained with the highest laser power and the lowest scan speed. Zhang et al. (2014) demonstrated that the higher the laser power, the lower the YS and US, while the opposite is true for the scanning speed increase. This is explained by the different cooling rates since high power and low scan speed lead to the formation of larger melt pools which leads to a lower cooling rate, while, on the other hand, low power and high scan speed lead to the formation of smaller melt pools that solidify with an extremely high cooling rate. However, the authors were not able to found a correlation between energy input and elongation.

The same authors also concluded that, with the decrease of laser power, the hardness tends to decrease due to the faster cooling rate. The high cooling rate has an influence similar to quenching on microstructure and properties of deposited material, thus forming a microstructure with high strength and hardness. The same effect was detected for the decrease in scanning speed due to the faster solidification rate of the melt pool (Zhang et al. (2014)). Those results were later corroborated by Ding et al. (2023) who produced 316L SS clads on a U71Mn rail and studied the

influence of processing parameters on the mechanical properties, specially on the wear behavior. The authors assessed the influence of Laser power and scanning speed in hardness while maintaining powder feeding rate at constant values. In adittion, the researchers also observed an increase in hardness on the HAZ, which rose from 200HV to 900HV, approximately.

Fan et al. (2023) studied the cladding of 316L powder on a G20Mn5QT Steel substrate. They concluded that the microhardness, wear resistance, and micro-shear strength of the cladding layers increase as laser power increases, whereas the tensile strength and yield strength increase initially and subsequently decrease. Besides that, the scholars concluded that low laser power values lead to a weak metallurgical bond between the 316L stainless steel cladding layer and G20Mn5QT steel and consequently a low shear strength.

Building Direction Guo et al. (2017) studied the impact of the building direction on the mechanical by printing 316L powder on both the perpendicular and parallel direction with respect to the building platform, as observed in Figure 2.13. The authors showed that the highest mechanical properties (YS, US, and ε) were noticed in the samples printed in the parallel direction and this was justified to the greater metallurgical bonding of these samples along the tensile direction. On the horizontal samples the loading direction was parallel to the sliced layers and there was at least one layer in which the scanning direction was parallel to the direction of the tensile loading.

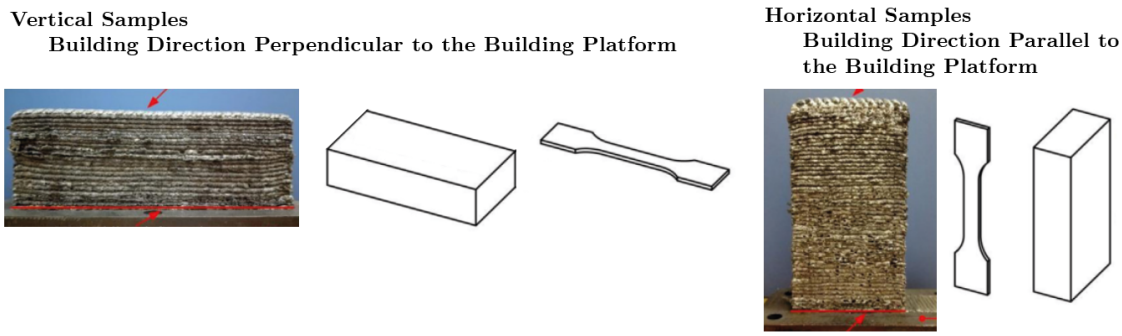

Figure 2.13: AISI 316L printed in perpendicular and parallel direction and schematic for obtaining specimens for tensile tests (Adapted from Guo et al. (2017)).

Ziętala et al. (2016) and Zhang et al. (2014) achieved different results regarding the elongation which was superior in the vertical samples. This was attributed to the improved ductility due to the dentrites along the growth direction.

Overall, horizontally built samples often achieve the highest YS and US, although the impact of building direction on elongation value remains uncertain. This mismatch may be due to various building variables such as porosity and inclusion content, as well as the impact of other strengthening phenomena (Saboori et al. (2020a)).

2.3.1.4 Applications of DED processing with AISI 316L powder

This chapter presents the possible applications that may arise from this work. Firstly, the applications of AISI 316L austenitic steel in the aerospace industry are presented, followed by the two more specific applications of DED AISI 316L powder processing: construction of thin-walled structures and cladding.

Applications of AISI 316L in the aerospace industry The "New Space Portugal" program aims to change the Portuguese space sector's specialization profile by pushing the development of new innovative, exportable, and technologically complex products and services across the value chain. Since this work is developed under this program, it is important to present the applications of this dissertation in the aerospace sector, including the applications of this steel in various components, highlighting its unique properties.

Stainless steel is widely utilized in aircraft and space components given its high strength-to-weight ratio, durability, hardness, and mechanical properties at high temperatures. Among the various stainless steel classes, the most used are the austenitic, precipitation hardened (PH), and maraging (martensitic and aged). Although other alternative emerging materials are increasingly being studied and processed, stainless steels are still very used mainly to its great mechanical properties at high temperatures, cost effectiveness and ease of fabrication. (Blakey-Milner et al. (2021)).

The AISI 316L stainless steel stands out from the other stainless steel grades, mainly from its corrosion resistance, while exhibiting other desired characteristics for the aerospace industry (excellent mechanical properties high strength-to-weight ratio). The AISI 316L owns its corrosion resistance mainly to the presence of molybdenum in its chemical composition which improve the alloy's resistance to pitting and crevice corrosion in chloride environments, which is critical for aerospace parts that undergo exposure to harsh and changing atmospheric conditions (Marlin Steel, 2024).

Firstly, the 316L stainless steel can be used in aircraft structural components such as fuselage frames, landing gear, and engine mounts since this steel can can withstand the substantial stresses and other extreme conditions related to the aerospace industry (for example the temperature conditions (-30 to 370ºC)) (Metal Exponents, 2024).

Furthermore, the AISI 316L's resistance to oxidation and scaling at extreme temperatures makes it ideal for use in high-temperature applications like as jet engine components, exhaust manifolds, and heat exchangers. The alloy preserves its its mechanical properties at temperatures greater than 800°C, ensuring reliable performance in critical high-heat zones in aerospace systems (Ant Weld, 2024).

Besides that, this steel is also used for manufacturing fluid systems such as fuel and hydraulic lines. The capacity of AISI 316L steel tolerate both cryogenic and high temperatures guarantees that these systems perform successfully across the wide range of temperatures found in aerospace operations. Furthermore, the AISI 316L corrosion resistance is critical for preventing leaks and ensuring the fuel system's safe operation (Marlin Steel, 2024).

Finally, the non-magnetic characteristic of AISI 316L is critical for avionics and other sensitive electronic systems, since it minimizes magnetic interference, ensuring reliable and precise functioning of navigational and communication equipment (Metal Exponents, 2024).

Deposition of AISI 316L of Thin-Walled Structures through DED A thin-walled structure (or just thin wall) is a structure with a small thickness in comparison to their other dimensions (such as height, length, or diameter). Thin walls are widely employed in the aerospace, automotive, and medical industries, where lightweight and precise components are needed. For instance, turbine blades, cooling ducts, and structural supports are examples of thin-walled structures. The building of thin wall through AM technologies allows the construction of complex and intricate shapes that would be more difficult to achieve using conventional manufacturing processes while being more efficient in terms of material usage, cost and time (Liu and Li (2006)). Conventional metal forming and machining processes, such as rolling and extrusion, are laborious and inefficient, particularly for thin-wall constructions, leading to high buy-to-fly ratios (Davim (2014)). Powder-bed techniques, such as Selective Laser Melting (SLM) or Electron Beam Melting (EBM), can easily manufacture small-scale aerospace components (<300 mm). However, large-scale major airplane components pose challenges due to build chamber size limitations. Therefore, other processes, like Direct Energy Deposition (DED) and wire-fed Wire-Arc Additive Manufacturing (WAAM), are used in this scenario. These technologies use multiple-pass deposition to create thin wall structures following a layer-by-layer strategy, resulting in a 'near net shape' part (Luzin and Hoye (2017)).

Due to the practical part of this work, it is necessary to investigate recent articles regarding the production of AISI316L thin-walled structures through DED.

Yu et al. (2018) studied the building of hollow thin-walled cylinders through LENS. The authors concluded that deformation and defects can be caused by an incorrect z-axis increment, variations in the working distance between the lens and the table, such as an uneven substrate surface and differing inclination angles, thermal beam focusing, and a lack of preheating. Furthermore, these defects can be adjusted to provide a suitable thin-walled part. For example, reducing the deviation of the working distance, improving and modifying the inclination angles, and using an adequate preheating temperature (PT = 600 °C) are all helpful strategies for avoiding defects.

Wang et al. (2016) and Wang et al. (2017) studied the effect of different depositions strategies, pulse laser parameters, building and loading angles on the microstructure and mechanical properties of AISI 316L oblique thin-walled parts. From those 2 articles, the tensile properties regarding horizontal samples produced with a continuous laser were observed and are presented in the Table 2.3.

Table 2.3: Mechanical properties of AISI 316L Thin-walled structures.

Reference	Tensile Strength (MPa)			Elongation (%)		
Wang et al. (2016)	596,2	626,4	650,8	7	9,5	9
Wang et al. (2017)	642	645	704	15	16,5	17

As it is possible to observe, those properties do not deviate much from the values presented above in the Chapter 2.3.1.3 but it is anyway important to highlight those studies since they are the ones carried out in a situation closest to that of the practical part of this work.

In the literature, it is also possible to find other studies regarding the deposition of AISI 3116L thin-walled structures although most of the researches focuses on themes such as open loop control, numerical modeling and in-situ monitoring, which are not the focus of this work.

DED cladding using AISI 316L powder Cladding is a metal deposition technique applied in coating deposition processes in which a layer of material is applied onto the surface of a substrate (Torres et al. (2019)). Cladding aims to enhance the substrate material properties or provide additional functionalities. This can include improving corrosion resistance, wear resistance, thermal protection, or even aesthetic appeal. Cladding using DED is a method that offers unique advantages in achieving these coating goals. Among those advantages it could be highlighted the ease to customize the deposition parameters (which leads to coatings with tailored properties), the energy and material usage efficiency and the versatility to use a wide range of materials.

AISI 316L Corrosion resistance The application of 316L powder for DED cladding comes, in a great part, from the corrosion resistance of this stainless steel. Therefore, many researchers have aimed to study the corrosion performance of 316L DED produced parts.

Ziętala et al. (2016) studied the corrosion resistance of AISI 316L SS fabricated using DED, by comparing DED samples with samples produced with conventional methods. The authors concluded that the corrosion potential of SS316L DED-manufactured steel and classically manufactured steel is equivalent. The 316 L SS fabricated using DED showed low values of corrosion current density which represents a lower corrosion rate. The authors justified this with the formation of the passive oxide layer due to the presence of chromium in the bulk of the material. However, they stated that pitting corrosion occurs much easier on the DED samples due the chromium segregation and the dual phase structure which lead to to lower values of breakdown potential and repassivation potential.

Rzeszotarska et al. (2023) studied the corrosion performance of LENS produced 316L samples and concluded that the LENS samples had better corrosion resistance than the reference sample. However, the authors were not able to found a clear relationship between the printing parameters and the corrosion resistance. However, regarding pitting corrosion resistance, the scholars were able to conclude that this resistance decreases with increasing feed rate.

Sarma et al. (2021) studied LENS produced 316L samples in order to compare its performance regarding wear and corrosion resistance, in comparison with wrought samples of the same material. They concluded that the increase in powder flow rate and laser power leads to an increase in the corrosion rate while the scanning speed has the opposite effect. The powder flow rate was the parameter with greater significance on corrosion resistance. The authors concluded that the corrosion rate was higher for wrought SS316L in comparison with the LENS produced samples.

Revilla and Graeve (2022) investigated the corrosion behavior of 316L stainless steel clads built via laser metal deposition on wrought material. The HAZ was the main factor contributing to the system's corrosion activity due to the extensive depletion of alloying elements (such as Cr and Mo) in this region, which severely reduced its pitting resistance. The HAZ also has a high oxygen concentration due to heat oxidation. Furthermore, tiny (<30 μm in diameter) partially unmelted powder particles dispersed across the surface of the clad were extremely prone to corrosion initiation, probably due to their comparatively high surface energy and thus high reactivity. The researchers also discovered that samples produced with a higher laser energy density showed more severe corrosion attack along the HAZ.

2.4 Powder Production for DED Processing

2.4.1 Powder Production Processes

The powder production methods can be divided into 5 groups: Atomization Processes, Melt Spinning, Rotating Electrode Process (REP), Mechanical Processes and Chemical Processes (Kassym and Perveen (2020)). The atomization methods include gas, water, centrifugal and plasma atomization (David L. Bourell and Seifi (2020b)). The chemical methods include oxide reduction, thermal decomposition, or precipitation from solutions. The selection of the production process depends on the availability of the equipment, the chemical and physical properties of the material, and also on the required production rates and powder properties such as flowability, density, size, shape, structure, and size distribution. The mechanical methods, since are the ones studied in this work, are detailed in the Chapter 2.4.2.

Briefly, the atomization processes involves melting the feedstock metal and then disintegrating it into fine droplets using a high-velocity gas or water stream. These droplets quickly cool and solidify into powder particles as they fall through a cooling chamber. The particles are then collected and classified by size and shape.

Gas atomization (GA) is the most commonly used technique to produce powder since it leads to spherical particles and a controlled particle size distribution. However, it has as drawbacks the high energy (to melt solid metal) and gas consumption (to generate the gas streams) and limitation in alloys composition. Besides that, the equipment used for atomization, such as high-pressure gas systems and specialized nozzles, can be expensive to purchase and maintain. (Fullenwider et al. (2019)).

Water atomization is also applied to achieve faster powder solidification rates while reducing production costs. In comparison with GA, this approach yields powder with smaller particle sizes, a wider particle size distribution, and a more irregular shape. Using water atomized powder as feedstock in AM showed comparable mechanical properties, indicating that irregular (i.e., not sphere-like) morphology can be employed in metal AM (Tan et al. (2017)).

However, the production of gas or water atomized powder demands the melting of the metal prior to ejection from the atomization nozzles. This requires considerable energy to account for the enthalpy variation between the liquid and solid phases (Jacobson and McKittrick (1994)). This limitation of atomization methods is one of the primary reasons why mechanical milling methods are being investigated to generate powder.

2.4.2 Mechanical Milling Processes

The Mechanical Milling techniques for Powder production, also known only as Milling processes, can be divided into four main categories: attritor ball milling; roll milling; planetary milling and disc milling. Each technique presents a different capacity, velocity, ability to minimize the contamination of the powder and ability to control the process by changing the temperature and/or

additives. The milling processes are based on plastic deformation and consequent fracture of previously dried and cleaned swarf or chips. The fragmentation of the particles occurs due to the impact or compaction. In some cases, friction may also have a role in the fragmentation. Therefore the fragmentation is highly dependent on the milling technique which influences the powder characteristics (Batista et al. (2021)).

The mechanical milling processes stand out due to its economic advantage since, comparatively to the gas atomization process, milling methods have lower costs, namely the production, maintenance and raw material costs (Wei et al. (2023)).

However, there are several disadvantages of mechanical milling processes such as the possibility of contamination, noise generation and long milling and cleaning times (Piras et al. (2019)). The last one may be the more critical since the generation of very fine powder with a narrow size distribution is a very time-consuming process. In addition, the friction and collisions involved in milling may lead to overheat of the materials which impacts the stability and properties of the final powder. Therefore, the selection of milling parameters is pivotal to determine the properties of the final powder. The parameters should be optimized in order to avoid the overheat and consequent cold welding (as detailed below) and in order to minimize the work time.

2.4.2.1 Milling parameters

After the selection of the milling technique, there are several variables intrinsic to the milling techniques that greatly influence the evolution of the powder characteristics, namely, the milling time, velocity, grinding bodies properties (size and material), Ball-to-Powder Ratio (BPR) (in the case of techniques that work with grinding balls), temperature, atmosphere and process control agents (PCAs) (Batista et al. (2021)).

Milling time The milling time affects the milling energy and, consequently, influence the powder characteristics. The milling time impacts the degree of powder particle size reduction and the level of homogeneity obtained, as longer milling times typically result in smaller particles. However, it should be noticed that for longer times than required, the formation of undesirable phases can occur, and the process is more prone to contamination. The milling time is considered the most important parameter and it is usually selected so that a balance between cold welding and fragmentation of the power particles can be achieved (Suryanarayana (2001)). Cold welding is the phenomenon where two metal surfaces, under certain conditions, adhere or weld together without the application of heat. This process typically occurs in a vacuum or inert gas environment, where the absence of air prevents oxidation and contamination of the metal surfaces. The lack of an oxide layer and the intimate contact between the metal surfaces induce this phenomenon.

Milling velocity and temperature The milling velocity or milling speed (rotations per minute, rpm) also affects the milling energy. Higher speeds lead to higher impact energies and consequently smaller particles sizes. However, too high velocities will lead to high temperatures which may be critical and induce cold welding. Wei et al. (2023) stated that ball milling should not be

performed at velocities greater than 600rpm to avoid excessive heating and consequently potential thermally induced reactions between the specimens and the milling media (jar and ball). However, high velocities may be desired in situations where diffusion must be promoted, for example, when the alloying and/or homogenization of the powder is required (Suryanarayana (2001)). Also regarding the milling temperature, it is important to mention that, in some cases, milling is performed under cryogenic conditions. The proper milling temperature is determined by various factors, including the material being processed, the milling time, the milling environment, and the milling equipment. To reduce milling-induced defects, it is recommended to mill at temperatures lower than the material's melting point or decomposition temperature (Wei et al. (2023)). In the majority of the cases, the increase in temperature is adverse since it will promote the contamination of the powder, unless a controlled atmosphere is applied (Suryanarayana (2001)).

Grinding Bodies Regarding the container properties, the size and material of grinding bodies (balls and jar) is crucial. The material must be chosen in order to withstand the high impact of the grinding bodies therefore the balls and jar must present similar hardness. In the contrary case, some particles of the grinding bodies can be dislodged and further incorporate the powder, which is considered contamination. Also, if the powder particles are considerably harder than the grinding bodies, it can lead to the imprisonment of the powder particles into the grinding bodies and to their damage. Some common materials used for the grinding bodies are hard steel, stainless steel, tungsten carbide (WC), or ceramics such as alumina or zirconia. The jar material must not be ductile since it would absorb most of the impact energy and thus the residual impacts would not be sufficient to change the particles morphology.

Ball-to-Powder Ratio and Balls Size The BPR is a parameter that has been highly studied by researchers since it highly influences the energy of the process, i.e. the energy that is transferred from the milling balls to the particles. The most common values vary from 10:1 to 100:1, depending on the capacity of the mill. For instance, a BPR of 20:1 means that the balls weight is 20 times greater than the weight of the material to be grinded. In general, the milling time required decreases with the increase in the ball-to-powder ratio since the increase in the balls quantity leads to increased collisions frequency and therefore increased fragmentation and increased reduction in particle size culminating in a more efficient milling process (Suryanarayana (2001)). However, a higher BPR leads to greater wear on the grinding bodies (Wei et al. (2023)).

The ball diameter is also a crucial factor because it affects the force per impact, stress per impact, and collision frequency. Larger balls are related with a lower milling energy and are employed to break down coarser feed materials. On the other hand smaller balls result in a faster particle size decrease and produce fine powder by reducing free space between the balls (Fullenwider et al. (2019)).

Additives and PCAs The presence of additives can improve the efficiency of the milling process. The milling atmosphere (temperature and possible presence of gases) and the use or not of

Process Control Agents (PCAs) are very important conditions (Batista et al. (2021)). Gaseous aids are often common in the milling processes and they may be either inert gases such as helium or argon (nitrogen is not used as it can react with some metal powder such as titanium and titanium alloys) or cooled air. Argon is the most commonly used and helps to avoid oxidation of the metal particles and contaminations during milling. Solid additives are usually in the form of powder, granulate or pellets, and are used to bind fat or moisture. They are sometimes added to the material when grinding in planetary ball mills or vibratory disc mills, since, if mixed in the correct ratio, they prevent the material from harden and help in the size reduction (Retsch GmbH Haan - The Art of Milling (2017)).

PCAs are important in order to prevent cold welding between particles or adhesion between particles and balls and further agglomeration. They can be solid, liquid, or gaseous. The most common PCAs used are stearic acid (SA), methanol, hexane, and ethanol. The selection of the PCA concentration is based on the grinding medium used, the amount of powder, the thermal and chemical properties of the selected PCA as well as the material properties. The concentration and nature of the PCA influences the final shape, size, and purity of a powder particle (Batista et al. (2021), Suryanarayana (2001)).

2.4.2.2 Disc Milling

Disc Milling is a mechanical milling process that may be employed for the production of metal powder from industrial chips. Figure 2.14 shows a scheme of the grinding bodies and the disposal of the material to be grinded, in a disc milling apparatus. The particles are fragmented and disintegrated as a result of the disc and/or ring's impact and friction with the particles positioned between the ring and the jar. The jar is tightly attached to the plate of the vibratory machine, and the entire

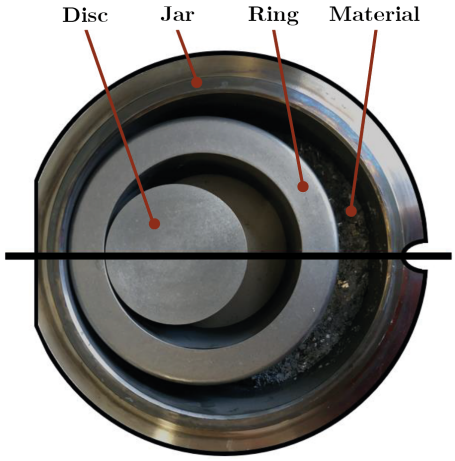

Figure 2.14: Grinding bodies of disc mill (Adapted from Retsch GmbH Haan (2024)).

grinding set is closed with a cover. The machine's plate undergoes circular horizontal vibrations, causing a centrifugal force to act on the grinding bodies, resulting in high frictional, impact, and pressure forces that immediately fracture the material (Retsch GmbH Haan (2016)). The higher the friction, the more effective the process, with improved fineness and reproducibility in a shorter

amount of time. The friction intensity is affected by both the weight of the grinding bodies and the differential velocity (Retsch GmbH Haan (2024)).

For the best results in terms of powder production, there are some rules that must be followed, regarding the displacement of the grinding bodies and the material. First, the material should be placed between the ring and the jar (as presented in Figure 2.14), occupying a maximum of one third of the total jar volume. Secondly, the area between the disc and the ring should remain empty. Lastly, the grinding bodies should be placed eccentric and touching in one point, as it can be seen in Figure 2.14, represented by the horizontal black line (Retsch GmbH Haan (2024)).

2.4.2.3 Planetary Ball Milling

Planetary ball milling is the most widely used milling technology for producing powder from chips. In this operation, the milling media has immense energy due to the movement of the milling stocks and balls against the inner wall of the jar (Wei et al. (2023)). As a result, centrifugal forces may exceed up to 20 times the acceleration of gravity (El-Eskandarany et al. (2021)). This mill usually consists of one or multiple cylindrical jar/s (similar to the jars on disc milling) mounted on a a rotating sun, as presented in the Figure 2.15 a). In this work, the mill used was design for only one jar.

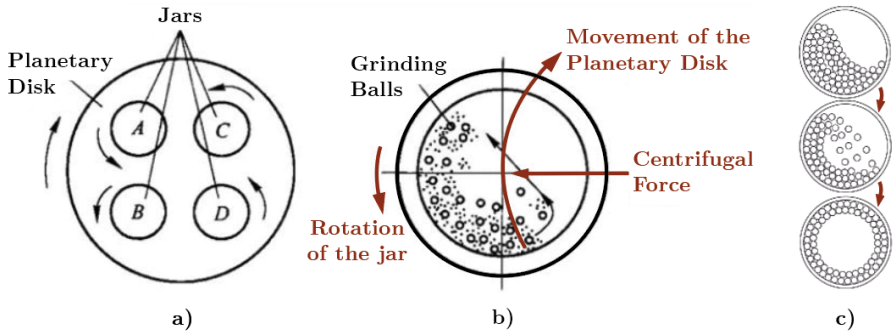

Figure 2.15: a) Overall layout of planetary disk (with multiple jars); b) Horizontal section of grinding jar; c) Ball Motion pattern in a jar during milling (Adapted from MTI Corp and Burmeister and Kwade (2013)).

This assembly (jar and rotating sun wheel) is mounted on a planetary disk that rotates around its own axis while also orbiting around the central axis of the sun wheel. Therefore, the terminology "planetary" comes from this motion of the grinding jar, which combines rotation and orbital movement, as seen in Figure 2.15 b). This motion leads to a high energy impact and attrition forces. The grinding balls are placed inside the jars along with the material to be processed and, as the sun wheel and planetary disk rotate, the grinding balls inside the jars move along a circular path due to the centrifugal forces generated by the rotation, as seen in Figure 2.15 b) (Suryanarayana (2001)).

These milling tools are made of durable materials like hardened and corrosion-resistant steel, zirconium dioxide, or tungsten carbide, which can tolerate harsh environments. Employing such

materials reduces tool deterioration and potential contamination of the resultant powder (Wilkening et al. (2017)).

2.4.2.4 Mechanical Properties of powder produced through milling processes

The plastic deformation induced during the milling process, along with the accumulation of internal strain lead to the grain reinforcement of stainless steel powder structures. This effects may induce strengthening and, for example, Enayati et al. (2007) reported an increase in hardness for stainless steel recycled powder due to the formation of a nanosized martensite phase. Other authors reported the same effect for powder from different materials (aluminum alloys, titanium alloys, Tin Bronze, among others) (Batista et al. (2021)). However, it is also noted in the literature, some cases in which a decrease in mechanical properties was noted.

2.4.3 Quality and Requirements for DED powder feedstock

The feedstock plays a pivotal role in the DED process and, therefore, it must follow some necessary requirements. Usually it analyzed 4 powder characteristics commonly known as the "4S's": Shape, Size, Size Distribution and Structure. This combination of those characteristics influence the powder properties, namely the density and flowability. As a consequence, those 2 powder properties affect the effectiveness of the DED process and the properties of the final part. The 4 characteristics and properties above mentioned are explained in detail below. The influence of milling parameters and conditions is also related with those characteristics.

Besides the "4S's" there are other factors which affect the powder properties. For example, the environmental conditions such as moisture on the powder particles can lead to porosity and can reduce the powder flowabiliy due to capillary actions. Therefore, powder drying processes must be applied before use and the storage in proper dry places is preferential. Besides that, reactive powder (e.g. titanium and aluminum alloys) must be stored in inert gas environments.

2.4.3.1 Particle Shape

The particle shape is essentially its forms, which may be spherical, granular, dentritic, acicular, rounded, angular (sharp edged or roughly polyhedral), flaky (plate-like shape), and irregular. Those morphologies are illustrated in Figure 2.16a). It is preferred to have spherical shaped powder and without any satellite since it leads to greater density and flowability. A satellite (Figure 2.16b)) is a smaller and secondary particle that loosely attached to a larger primary particle. These satellites are formed during the milling process due to the mechanical forces applied to the powder and due to the cold welding phenomenon.

In order to study the particles shape it is common to measure their aspect ratio, i.e. the (ratio between the longest dimension of a particle and its shortest dimension. Therefore it is possible to access the particle shape in a quantitative and qualitative ways (Batista et al. (2021)).

Regarding the production of powder via milling, Batista et al. (2021) stated that the particle shape depends on the on the material, milling technique, milling time, and variables of the process

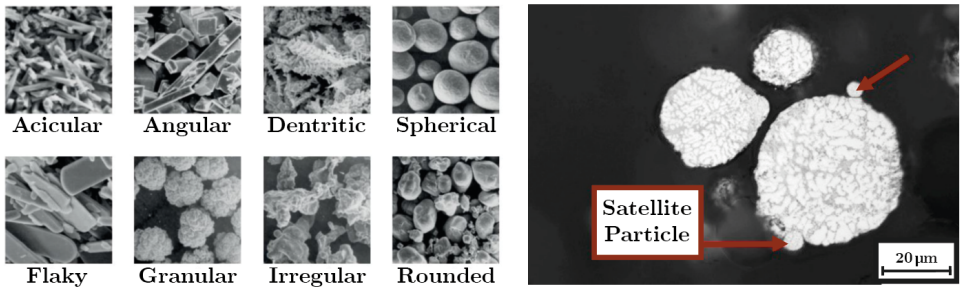

Figure 2.16: a) Typical powder particle shapes (Adapted from ISO 3252:2023); b) Example of satellite particle (Adapted from Chu et al. (2021)).

such as the BPR or the presence of PCAs (Process Control Agents). During the first hours of milling, the particles tend to have a flake-like shape, however, with increasing milling time, the shape tends to become rounded or spherical. Soufiani et al. (2010) justified this shape change to the repeated cold welding, fracture and plastic deformation of the powder. Regarding the milling technique, from planetary ball milling is expected to have spherical shape with smooth surfaces. In ball milling,it is established that the diameter of the balls influences the morphology of the powder particles. Fullenwider et al. (2019) found that using a comparable BPR, large balls (diameter = 20mm) readily break up chips to coarse powder particles, while small balls (diameter = 6mm) successfully alter the powder morphology to near spherical.

2.4.3.2 Particle Size and Size Distribution

The particle size is defined by the ISO 3252:2023 as the "linear dimension of an individual particle" and allows the analysis of the fragmentation evolution in the course of a mechanical milling process. The powder particle size defines the geometric precision and the minimum buildable feature sizes. Typical powder size used in DED processes is in the range of 45–150 μm which is much larger than the range used in PBF processes (15–45 μm). The particle size depends on the fragmentation, which is directly associated with the characteristics of the material, the milling process and conditions and the presence of additives. Some techniques that are often used to analyze the particle size are sieving, image analysis acquired by transmitting optical microscope (OM) or stereoscopic macroscope (SM) or scanning electron microscope (SEM). Other techniques include static light scattering (SLS), laser particle size analyzer (LPSA) or laser diffraction (LD) particle size analyzer (PSA) (Batista et al. (2021)).

ISO 3252:2023 defines particle size distribution as "the percentage (by numbers, volume or mass) of each portion, into which a powder sample is categorized according to size". It is considered one of the most important characteristics of a powder sample, since it defines the behavior of the powder in packing and, consequently, its density. It determines the degree of fragmentation and influences the feedstock feeding and the density of the final part (David L. Bourell and Seifi (2020b)). A non-uniform distribution commonly leads to an increase in porosity due to a non

consistent powder flow rate (Dutta (2020)). A common way to show the particle size distribution is to present it with the D10, D50 and D90. As an example, if D10 = 30 μm, it means that 10% of the powder particles of a sample have dimensions of 30 μm or less.

Regarding the production of powder through milling processes, usually the particle size depends on the materials characteristics and processing conditions. Regarding the size distribution, it depends on the presence of additives or reinforcements, milling time or milling technique (Batista et al. (2021)).

2.4.3.3 Particle Structure

The particle structure is an important characteristic to consider when analyzing metal powder. It can be analyzed by several methods such as SEM, Electron Backscatter Diffraction (EBSD), Transmission Electron Microscopy (TEM), Selected Area Diffraction (SAD) mode, or X-ray Diffraction (XRD). The study of the grain size and the presence of martensitic structures are some examples of usually important verifications since they have an impact on the mechanical and physical properties of the final parts. In the case of AM processes such as DED, the powder particles are melted and solidified, which means that their structure changes, thus, it is not relevant studying the structure of powder which will be melted.

2.4.3.4 Flowability

Flowability corresponds to the tendency that the powder particles have to resist differential movement between them when subjected to an external stress or gravity. The main restraining forces involved are friction, adhesion (attraction between particles and walls) and cohesion (attraction between particles) (López-Córdoba and Goyanes (2017)). DED is one of several metal AM processes in which powder flowability greatly influences the efficiency of the process. This property is essential for obtaining an uniform and consistent feedstock transmission (powder flow) which is high necessary. Flowability can be affected by powder shape, powder size distribution, powder density and by external variables such as humidity, or triboelectric charge buildup (David L. Bourell and Seifi (2020c)).

It is known that spherical powder without satellites have better flowability than irregular powder (Dutta (2020)). This is due to the lack of friction and mechanical interlocking of the particles, in the case of spherical ones. However, for very fine particles, this is not the case since highly fine powder, independently of their shape, present a very low or even null flowability. The powder density also influences the flowability since an increase in density leads to an increase in flowability. It must also be taken into account the effect of humidity which induces surface tensions, forcing the particles to stay attached to each other therefore decreasing the flowability (David L. Bourell and Seifi (2020c)).

The most common method used to measure the flow rate of metal powder is the Hall Flow Test, which consists of measuring the required time for the metal powder to flow through the orifice of a flowmeter funnel, according to the American Society for Testing and Materials (ASTM) Standard

Test Method B 213 (ASTM B213-9). When the metal powder cannot pass through the orifice of the Hall Flow funnel, then the Carney flow test method has to be performed, since its orifice is larger (David L. Bourell and Seifi (2020c)). This last method can be performed considering the ASTM Standard Test Method B 964 (ASTM B964-09).

2.4.3.5 Density

As stated above, the density of the powder affects the flowability properties and consequently, the efficiency of the printing process. There are two types of powder sample density: loose/apparent density and tap density. Besides that, the bulk density of a powder particle can also be measured.

Bulk Density Firstly, the bulk density, also known as pycnometer density, corresponds to the density of a powder particle and it allows the identification of internal voids within a powder particle. Besides, it enables the comparison between powder particles (German (2012)). In the case of powder particles produced through a milling process, it is common to have internal voids. When cold welding happens, the powder particles get attached to each other to form larger ones. The bonding between particles can be poor and voids can form in their interfaces. The gas pycnometer is the most common equipment used to measure the density of a powder particle. It uses a gas, usually He, since it is able to reach the smallest pores (with diameter dimensions lower than one nanometer) (Castanheira (2022)).

Loose/Apparent Density Secondly, the loose/apparent density (g/cm^3) corresponds to the weight per unit of volume of loose powder. This property depends on the particle size, particle size distribution, particle shape and particle surface roughness (Neikov et al. (2019)). Usually, with a decrease in particle size, the loose density increases, because, with smaller particles, the interspace between them is also smaller. Therefore, the filling of empty spaces between particles with other smaller particles can increase considerably the loose density, thus, increasing the wide range of particle sizes, increases the loose density. Regarding the particle shape, the loose density increases with the increase of the sphericity since there is less friction in the packing of the particles. Finally, a reduction in the surface roughness decreases the frictional forces and consequently increases the loose density (Neikov et al. (2019)). The loose/apparent density can be calculated with the ASTM Standard Test Method B 212 using the Hall flowmeter funnel, as for the flowability measurements (ASTM B212-99). For powder that are non-free-flowing, then the ASTM Standard Test Method B 417 is more recommended (ASTM B417-00). For powder that cannot flow through a Carnet funnel, the Scott Volumeter is used (Neikov et al. (2019)).

Tap Density Finally, the tap density (g/cm^3) corresponds to the density of a powder when its container is tapped, promoting the packing of the particles. The tap density is always greater than the loose density, but it also depends on the particle size, particle shape, particle size distribution, and particle surface roughness. The increase from the loose density to the tap density depends

mostly on the particle size and shape. To measure this type of density, the ASTM Standard Test Method B 527 (ASTM B527-93) is used (Neikov et al. (2019)).

2.4.4 Upcycling machining chips into powder for DED Processing

2.4.4.1 Chips formation and morphology

Metal chips are produced from several machining operations such as turning, end-milling, drilling, stamping, grinding, laser cutting etc. Because of their small size, chips created during grinding and laser cutting can be recycled without any pre-processing. However, the contamination of chips with wheel contaminants, as well as high temperature oxidation, limited their usage for recycling. The majority of recyclable chips come from machining operations such as turning, drilling, end-milling, and shaping. Those processes typically result in relatively large chips that can be cleaned readily using washing and chemical treatments. As a result, larger chips must be broken down into smaller chips in order to be efficiently recycled.(Dhiman et al. (2021)).

The size and shape of the chips are decided by the machining parameters. The chips geometry is defined by the chip's height (h_{chip}), width (w_{chip}) and thickness (t_{chip}). These dimensions are governed by the machining conditions and cutting tool geometry. The type of workpiece material and the machining environment or cutting fluid also influence the chips morphology and dimensions. It is possible to state that the smaller the chips, the easier and more sustainable they are to recycle.

2.4.4.2 State-of-the-art of austenitic stainless steel chips upcycling into powder for DED Processing

Jackson et al. (2020) studied the option of mechanically produce 316L powder for DED in contrary to the common gas atomization process for producing feedstock powder. The authors produced chips on a vertical milling center and then reduced the particles size in an oscillation ball mill. The resultant powder between 45μm and 150μm was then used for DED feedstock. The researchers also used atomized powder (of the same alloy and size range) as DED feedstock, to work as benchmark. The scholars noticed that both final parts had identical surface texture, microstructure, and mechanical properties. The only notable changes were in hardness and ultimate tensile strength, which are due to interstitial elements in the milled powder. The mechanically produced powder was bigger and less spherical than gas-atomized powder. The gas-atomized powder also had higher Hall flow rates and flowability. There was a greater concentration of titanium and oxygen on the mechanically produced powder. This is due to the wear of the milling media and to exposure to air during milling, respectively. However, this unwanted composition (although still considered by the authors as within the specifications) may be improved through a more controlled procedure. In general, this study showed optimistic results which suggested that Mechanically-generated feedstock is a viable alternative to gas atomized feedstock for DED.

From the study mentioned above (Jackson et al. (2020)), Jackson et al. (2023) went further and accessed the energy consumption of the mechanically-generated 316L powder production process

and compared it to the energy consumption of the gas atomization process. The authors concluded that the two feedstock production methods had similar specific energy consumptions. However it is important to state that the energy required in the machining process was taken into account.

Fullenwider et al. (2019) studied a two-stage strategy to produce powder from AISI 304L machining chips. The as-received chips had serrations along the length and their size ranged from 5 to 20mm. It is important to note that the AISI 304L chemical composition is very similar to the composition of the SS studied in this work. The authors used a planetary ball mill under Ar atmosphere, at 500 rpm and BPR 15:1 with 6 and 20mm SS balls. They optimized the milling conditions (milling time and balls size) in order to achieve final particles in the range of 38-150μm. Their morphology was rounded and had an average aspect ratio of 1.37. It was found that intense plastic deformation caused austenite to transform into martensite. This austenite to martensite phase transformation, together with other strengthening processes (grain size refinement and higher dislocation density), contributed to a 44% improvement in the hardness of ball milled powder particles in comparison to machining chips. Comparing with the gas atomized powder, the hardness was 50% higher. The two-stage was crucial since, in the first stage (24hrs), it was used large balls (20mm) to provide the necessary plastic deformation to break up the machining chips to coarse particles while on the second stage (36hrs), it was used small balls (6mm) to modify the powder morphology to near-spherical. Therefore, for the same milling time, it was more efficient to reduce the particles size below 150μm (as desired for DED processing) using the two-stage strategy in comparison with a single stage. The increased milling time resulted in a reduction in particle aspect ratio and proportion of flattened particles. The results revealed that a high frequency of low-force impacts on individual particles is preferred for producing a spherical or near-spherical powder morphology, because a particle tends to produce a spherical morphology when impacted from several random directions with low-force impacts. This was demonstrated numerically by a drop in aspect ratio and qualitatively by an increase in particles with rounded features and smooth surfaces. In contrast, particle size refinement is performed through high-force impacts. Later the scholars deposited the powder in a single track via LENS and concluded that the hardness was 21% higher than the measured hardness of a single track deposited using gas atomized powder. Besides that, the single tracks exhibited proper adhesion and an uniform melt pool geometry, which allow the authors to conclude that it is potentially feasible to use ball milled powder created from machining swarf as an alternative feedstock material in metal AM.

Enayati et al. (2007) produced nanocrystalline steel powder through ball milling. Although the material used was an austenitic stainless steel, its chemical composition differed slightly from the AISI 316L composition. The as-recevied chip had an average length of 2-4mm and a C-shape and non-stringy morphology. The authors used a planetary ball mill under Ar atmosphere with 5 20mm hardened chromium steel milling balls. The BPR was 10:1 and the velocity 100rpm. After 50h of milling the particles size was 300μm and after 100h it was 60μm. The authors reported an increase in hardness for stainless steel recycled powder due to the formation of a nanosized martensite phase.

Mendonça et al. (2018) produced duplex stainless steel (UNS S31803) powder from 2mm

spiral shaped machining chips by using a planetary ball mill for 20hrs at a milling speed of 350rpm and BPR 15:1. Duplex stainless steels (DSS) are two-phase austenite (γ-CFC) and ferrite alloys which are capable of combining the good properties of both ferritic and austenitic stainless steels. The authors investigated the addition of niobium carbide (NbC) and concluded that it reduced the transformation of austenite into martensite and reduced the particles size. After 5h of milling the particles size was 600μm and after 20h it was 220μm without NbC and 150-500μm and 175μm with 3% NbC. Other study (Mendonça et al. (2019)) aimed to produce powder from chips of the same duplex stainless steel (UNS S31803). The chips average size was 8mm and the objective of the work was to study the influence of the addition of vanadium carbide (VC). The authors used a high-energy planetary ball mill under Ar atmosphere at 250 and 350rpm, for 10 and 50h with 0.3% of VC. They concluded that carbide addition had the highest influence on all milling parameters, followed by grinding time, rotation speed, and powder-to-ball weight ratio. Milling at 350rpm for 50 hours with a PBR of 20:1 and 3% VC resulted in particles ranging from 20 to 135 μm. The addition of VC increased the efficiency of the milling process with a decrease of almost 50% of the particle size. The authors reported an increase in hardness for stainless steel recycled powder due to the formation of a nanosized martensite phase.

Castanheira et al. (2024) investigated the possibility of transforming AISI 303 stainless steel chips into powder feedstock for DED printing. Using a disc milling method, all chips were transformed into particles ranging in size from 38 to 212 μm, with irregular and flake-like shapes. The powder was then printed on a AISI 1045 substrate. The general results were positive although the final analysis revealed some fracture defects, porosities or oxides occurrence.

Chapter 3

Materials and Methods

3.1 Materials

This section provides a brief overview of the handled materials, as well as its properties.

In this work, the intended DED feedstock material was AISI 316L. The AISI 316L is a chromium-nickel-molybdenum austenitic stainless steel developed as a low-carbon variation of the AISI 316 stainless steel. It is renowned for its exceptional corrosion resistance, durability, and good mechanical properties. Both the corrosion resistance and the mechanical properties can be preserved at temperatures as high as 500ºC (Davies (2009)). The AISI 316L low carbon content (<0.03%) makes this steel especially valuable for welding or additive manufacturing, as the precipitation of carbides becomes significantly restricted. The low carbon content prevents the depletion of chromium near the grain boundaries and the consequent formation of chromium carbides at the boundaries. Besides that, the presence of Molybdenum as an alloying element has a pivotal role on the characteristic corrosion resistance (by creating a passive oxide layer) of this austenitic stainless steel while contributing to a improvement in mechanical properties (Trelewicz et al. (2016)). In addition, the Ni presence enhances the stability of the passive film, while Mo increases the steel's resistance to pitting and crevice corrosion in chloride-containing environments (Davis and Committee. (1994)).

The initial idea was to obtain AISI 316L machining chips supplied by a metalworking industry. However, there was no availability so the solution was to machine a 316L cylinder block at INEGI. In the final stages of thesis development (more specifically in June), a chemical analysis was performed on this cylinder block, through an OES (Optical Emission spectroscopy) equipment. The obtained results (which are the average of 4 measurements) are presented in the Table 3.1.

Table 3.1: Chemical composition (wt%) of the handled material obtained through OES analysis.

Chemical composition (wt%) of the handled material														
C	**Si**	**Mn**	**P**	**S**	**Cr**	**Mo**	**Ni**	**Sb**	**Co**	**Cu**	**V**	**W**	**Sn**	**Fe**
0.04	0.29	1.27	0.03	0.03	17.56	0.38	7.80	0.01	0.15	0.42	0.07	0.02	0.01	71.83

From the analysis of those results and comparison with the AISI 316L composition (presented in Table 3.2), it was clear that the handled material was not AISI 316L. There was a mistake when the material was taken from its storage location at INEGI, so the wrong block was unequivocally picked up for machining. The major difference in the composition was the low content of Molybdenum, which, as stated above, has a pivotal role in the AISI 316L steel, regarding the corrosion resistance and mechanical properties. Besides that, the carbon and sulfur content were slightly superior while the Nickel content was considerably inferior.

Table 3.2: Chemical composition (wt%) of AISI 316L stainless steel (European Steel and Alloy Database).

Chemical Composition (wt%) of the AISI 316L								
C	**Si**	**Mn**	**P**	**S**	**Cr**	**N**	**Ni**	**Mo**
max 0,03	max 1	max 2	max 0,045	max 0,015	16,5 - 18,5	max 0,11	10 - 13	2 - 2,5

Therefore, the need arose to understand which steel was studied and processed in this work. It was clear that the handled material was a chromium-nickel austenitic stainless steel thus the steel grades that matched the obtained chemical composition were investigated. Consequently, two different grades were identified and their chemical compositions are presented in the Table 3.3.

Table 3.3: Chemical composition (wt%) of possible stainless steels (European Steel and Alloy Database).

Chemical Composition (wt%) of possible stainless steels									
Stainless Steel number (EN and AISI Standard)	**C**	**Si**	**Mn**	**P**	**S**	**Cr**	**N**	**Ni**	**Cu**
1.4301 / AISI 304	max 0,07	max 1	max 2	max 0,045	max 0,03	16 - 18	max 0,11	6 - 8	-
1.4319 AISI 301	max 0,07	max 1	max 2	max 0,045	max 0,03	16 - 18	max 0,11	6 -8	0,5

By analyzing those compositions, the 1.4319 grade stood out for the presence of Copper, which was not reported for the other steel. Therefore, it was considered that the steel that was machined, milled and then DED processed, in this work, was the 1.4319 grade (AISI 301).

3.1.1 AISI 301

AISI 301 is a popular austenitic stainless steel known for its versatile properties and wide-ranging applications. Its chemical composition (namely the high content of Manganese and Nickel) gives AISI 301 excellent corrosion resistance in various environments, making it suitable for use in both mildly corrosive and high-temperature conditions. Additionally, AISI 301 offers good formability, ductility, and weldability, allowing it to be easily shaped and fabricated into different components and structures. One of the key advantages of AISI 301 is its high strength-to-weight ratio, which is achieved through cold working processes such as rolling, bending, or drawing. This results in increased tensile strength and hardness, making AISI 301 suitable for applications requiring strength and durability. Furthermore, AISI 301 exhibits good fatigue resistance, making it suitable for cyclic loading applications. AISI 301 is a cost effective steel and finds a widespread use across

various industries, including automotive, aerospace, electronics, and medical. Despite its many advantages, AISI 301 also has some limitations. One of the main disadvantages is its susceptibility to corrosion in chloride-containing environments, which can lead to pitting and crevice corrosion if not properly protected (Jr. and Rethwisch (2020)).

The Table 3.4 presents the common mechanical, physical and thermal properties of the AISI 301 stainless steel.

Table 3.4: AISI 301 stainless steel properties (European Steel and Alloy Database).

Mechanical Properties		
Tensile Strength	**Yield Strength**	**Elongation**
500 -850 MPa	>250 MPa	>40%
Physical Properties		
Density	**Melting point**	**Electrical Resistivity**
7.9 g/cm^3	1400 - 1450 ℃	0.75-0.85 $\mu\Omega$·m
Thermal Porperties		
Thermal conductivity	**Specific Heat Capacity**	**Coefficient of Thermal Expansion:**
15-20 W/(m·K)	500 J/(kg·K)	16-18 µm/m·K

3.1.2 Substrate Material

In this work, the substrate material is different from the feedstock material. The feedstock material used is AISI 301 stainless steel, while the substrate material is AISI 1045 steel. The choice of the substrate material was done according to the materials availability at INEGI. The substrate material is not a target of study in this work since this project focuses more on the construction of thin-walled structures through DED and not on the production of clads. Hence, the substrate material is negligible thus it is not important to do an overview of the AISI 1045.

3.2 Methods

3.2.1 Powder Production

This section describes the performed steps during transformation of machining chips into powder, which represented first practical part of this study. This first stage covers the conducted milling procedures by detailing the employed parameters and used equipment.

3.2.1.1 Collection of chips

As stated earlier, the initial idea was to collect machining chips from a metalworking industry. However, due to lack of availability, the chips were collected after the machining of a AISI 301 cylinder block on a DMU 60 eVo linear 5-axis machining center at INEGI. The machining parameters were: Feed rate of 85 mm/min, Feed per Tooth of 0.0143 mm, Plunge rate of 600.00 and a Spindle Speed of 990 rpm. The block was machined without any lubricant and the CNC station was previously cleaned in order to avoid any contamination on the chips.

Figure 3.1 presents the collected chips. According to the standard chip forms classification from the ISO 3685:1993, it was possible to observe in the collected chips many types of swarf namely short ribbon chips, short tubular and conical spiral types. These chips ranged in size from 2 to 10 mm.



Figure 3.1: Collected Chips.

3.2.1.2 Milling Procedure

In this work, it was used two different milling techniques: disc milling and ball milling. This section describes the used equipment as well as the followed procedures. The process of selection of milling parameters is also presented and explained. Briefly, the sets of parameters were selected in order to achieve the greatest amount of powder (in weight percentage) in the size range intended for DED processing (50-150μm) while keeping the processing time as short as possible. This last

criteria was taken into account since this work tries to present this process as a viable alternative to industrial powder production through atomization.

Disc Milling Firstly, it was conducted the disc milling procedure, using the Vibratory Disc Mill RS1, presented in Figure 3.2. According to the datasheet of the machine, the grinding bodies are made of AISI 420 martensitic stainless steel, and the jar volume is 250 ml.



Figure 3.2: Vibratory Disc Mill RS 1 and positioning of the grinding bodies.

As stated previously in Chapter 2.4.2.2, a proper procedure regarding the material placing was followed. Firstly, before any material being placed, all grinding bodies (jar, disc, and rings) were cleaned with acetone and dried so that the metal would not be contaminated with other materials from previous milling works. Then, before any milling work, the ring and disc were positioned, as illustrated in Figure 3.2. Afterwards, the chips were placed between the disc and the jar wall, occupying a maximum of one third of the total volume jar.

Regarding the milling parameters involved (i.e. the milling time and milling speed), the milling conditions developed by Castanheira (2022) were studied. In that work, the authors used the same equipment to mill machining chips of a similar stainless steel (AISI 303). The 5th condition of that work was the most efficient, i.e lead to the greatest amount of final powder in the size range intended for DED processing, thus this condition was followed. This procedure was conducted and the resultant powder was sieved and weighed according to the size ranges, as it is explained below in the Chapter 3.2.2.1.

The above mentioned 5th condition, has been renamed PN5 (Procedure Number 5) in the current study and its parameters are presented in Table 3.5.

The PN5 procedure has four stages and, in all its four stages, the mill operates at maximum rotation, which is 1407 ± 3 rpm. On the other hand, the milling time and material quantity varies in those stages. In the first one, the as received chips are placed occupying one third of the jar volume and are milled for 5 min. The second and third stages are equal: 60 grams of particles previously milled in the first stage are placed in the jar and the machine mills for 30 min. In the fourth and last stage, those two 60g batches are placed together on the jar and the equipment

Table 3.5: Disc Milling procedure.

Procedure	Material Quantity	Milling Speed [rpm]	Milling cycle [min] (mill time/break time)	Mill time [h:min]	Total time [h:min]
PN5	1/3 of the jar volume	1407 ± 3	5/0	00:05	00:05
	60g		5/10	00:30	01:20
	60g		5/10	00:30	01:20
	120g		5/10	00:10	00:25
Total	-	-	-	01:15	04:10

operates for 10 min. In order to prevent the machinery from overheating and the material from oxidizing (even though oxidation does not appear to occur for stainless steel), the milling process has to be intermittent. As a result, the milling process was limited to operating continuously for 5 minutes before pausing for 10 min. Furthermore, after every 30 minutes of milling, the equipment was paused for 30 minutes. Therefore, for the PN5 procedure, the util time, i.e. the time the mill worked, was 01:15 while the total time (mill time and break time) was 04:10.

The main focus of this work was not the use of disc milling to produce powder for DED processing since it was already known that disc milling does not produced rounded particles. Hence, the study proceeded using planetary ball milling. Therefore, only the PN5 condition was tested and no other disc milling conditions were developed and evaluated. With the PN5 results it was already possible to compare this milling process to planetary ball milling.

Moreover, in the current study, it was aimed at comparing 3 milling conditions and 3 materials as well, by comparing the results of the current study with those presented in Castanheira (2022) and da Cunha (2023). Those authors used the same equipment that was employed in this work to mill AISI 303 chips (Castanheira (2022)) and AISI P20+Ni swarf (da Cunha (2023)).

Planetary Ball Milling Secondly, it was conducted the planetary ball milling procedures, using the Retsch PM 100 equipment, presented in Figure 3.3. This equipment reaches a top speed of 650 rpm and its hardened stainless steel jar has a volume of 500 mL. The balls used in this work were also made from hardened stainless steel and have as diameter sizes 5 and 30 mm.

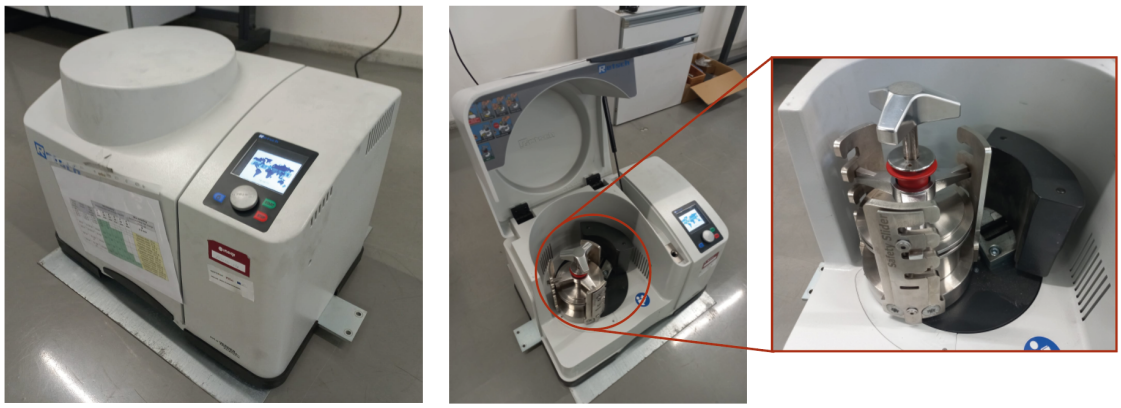

Figure 3.3: Planetary Ball Mill Retsch PM 100 and detail of the jar positioning and counterweight.

Due to the fact that some chips were curled, the swarf was firstly submitted to a 5 min milling in the above mentioned disc mill in order to flatten the chips. Then, the planetary ball milling bodies were cleaned with acetone and dried to avoid contaminations from other materials used in previous milling procedures. Afterwards, for each milling run, the material was placed and the set of jar, lid, balls and material was weighed in order to properly adjust the counterweight.

Regarding planetary ball milling, the parameters involved are: material weight, ball weight, milling speed and mill and break times.

As a starting point, the PN3 (Procedure Number 3) conditions, developed by da Cunha (2023) (who used the same equipment) were selected and performed. This procedure was chosen since it was the one which resulted in the greatest amount of final powder in the size range for DED processing.

Subsequently, three new conditions (NP1, NP2 and NP3) were developed for the process optimization, as presented in 3.6.

Table 3.6: Planetary Ball Milling Procedures.

Procedure	Material Weigth [g]	Ball Weigth [g]	Ball Diameter [mm]	Ball to Powder Ratio (BPR)	Milling Speed [rpm]	Milling cycle [min] (mill time/ break time)	Stage Time [h:min]	Total Time [h:min]	Util Time [h:min]
PN3	120	878	30 5	7,32	600 450	1/9 1/3 2/3	01:05 04:20 03:15	08:40	03:48
NP1	120	889	20	7,41	600	2/5	13:20	13:20	03:48
NP2	120	889	30 5	7,41	450	1/3 2/3	04:45 03:15	08:00	03:48
NP3	120	889	5	7,41	450	2/3	03:15	03:15	01:18

NP1 (New Procedure 1) was conducted in order to eliminate the need to change the balls mid-process by operating always with 20mm balls.

The NP2 condition (New Procedure 2) is very similar to PN3 with the only difference that the 2 first PN3 stages were merged in a single NP2 stage. The util mill time was conserved but the new stage did not performed at 600 rpm as the PN3 1st stage did. The elimination of one step simplifies the process, making it more suitable for implementation in industry. Moreover, this new procedure reduced the total time in 40min while maintaining the util time, which is also favorable to industry implementation.

Finally, NP3 (New Procedure 3) was developed with the aim of reprocessing powders of dimensions >212 μm left over from previous milling operations. Therefore, in the NP3 condition, the initial material was particles that had already been milled by planetary ball milling. Once again, in order to facilitate the industrialization of the process, the NP3 conditions are the same as the NP2 2nd stage parameters.

It is important to recollect that the majority of the above mentioned procedures start with a 30mm balls stage followed by one or more 5mm balls stage/s. As explained in the bibliographic review, larger balls efficiently break up machining chips into coarse powder particles, while smaller balls effectively modify the powder morphology toward a near-spherical configuration (Fullenwider et al. (2019)). This conclusion is already very well established since other researchers (such

as da Cunha (2023)) have been employing this strategy. However, the NP3 condition arises with the goal of assess the relevance of the first stage with 30mm balls when milling already milled particles. The importance of a 1st stage with larger balls is known when the input material is as received chips or flattened chips although when the input material is already milled particles, the relevance of this 1st stage with larger balls may be reduced.

It is also important to note that the purpose of the current work was studying the mechanical characterization of a printed stainless steel using upcycled powder and not specifically the powder production process. Therefore, a larger number of different milling procedures was not developed to enhance the milling productivity and the final characteristics and properties of the powder. Nevertheless the available time and equipment constraints were also a factor that made the optimization of the milling process not a priority.

3.2.2 Powder Characterization

After the milling process, the resultant powder was characterized in order to assess the milling process efficiency as well as the powder characteristics and properties. This chapter presents the used equipment and the performed procedures for the analysis of the powder characteristics.

3.2.2.1 Particle Size Distribution and Particle Shape

Sieving After each milling operation, the resultant powder particles were sieved, separated and weighted according to their size ranges. The amount of powder in the size range intended for DED processing determined the efficiency of the milling condition. The recommended particle dimensions for the DED process are between 45 μm and 150 μm (Ghasempour-Mouziraji et al. (2024)). However, due to the material availability, the size range considered in this work is from 38 μm to 212 μm, considering previous studies (Castanheira (2022) and da Cunha (2023)).

Therefore, the sieving was performed following the standard International (2016) and using two standard sieves (with apertures of 38 μm and 212 μm, as seen in Figure 3.4). The 212 μm sieve was placed on the top of 38 μm sieve and this set was placed on top a of a receiver. Then the resultant particles were deposited on the 212 μm sieve and a proper lid fixed this set to the vibratory machine, as presented in Figure 3.4. The machine worked for 10 min at maximum amplitude. This process was conducted inside a glove box for safety and health reasons. All the sieving apparatus is presented in the Figure 3.4.

This sieving technique typically comes with certain inaccuracies since some particles have varied size depending on direction (length or width). Therefore, elongated particles with a length greater than the sieve aperture but a width smaller than the aperture can flow into the sieve. This means that in the micrographic examination, particles with an average size greater or smaller than the apertures may be identified. Electrostatic forces or particle entrapment can both cause the presence of smaller particles.

After the 10min sieving, the separated particles were weighted and stored according to their sizes.

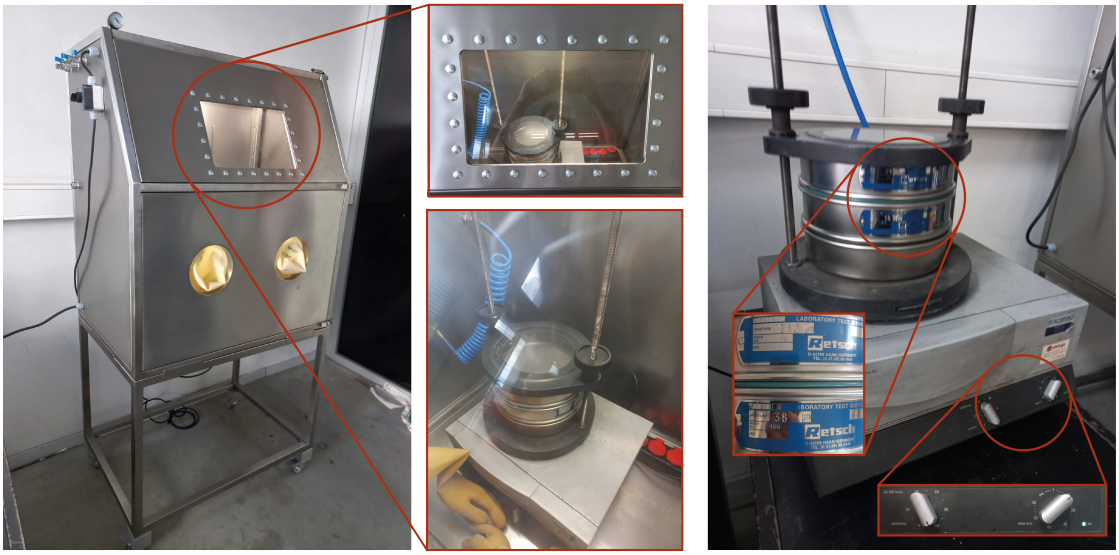

Figure 3.4: Sieving apparatus: globe box, vibratory machine and standard sieves (38 and 212 μm).

Powder Analysis through SEM analysis With the SEM results, it was possible to visualize the powder particles and consequently finding the particles size distribution and the particles shape. The software ImageJ was employed for image analysis to measure the dimensions of the particles, as presented in Figure 3.5.

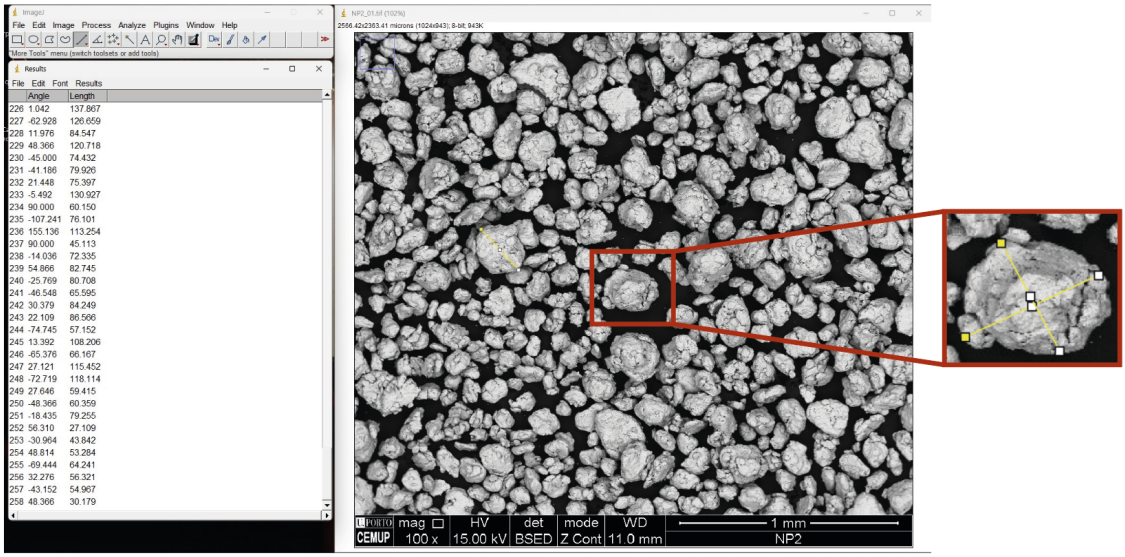

Figure 3.5: Particle size measurements on SEM results using the ImageJ software.

The particles dimensions were measured both in the shortest and longest directions, i.e. both the width and length of the particle. Therefore, with those measurements, both the size distribution (with the mean values between width and length) and the particles aspect ratio were calculated. Those measurements were only carried out on previously sieved powder in the 38-212 μm size range as this is powder that would be suitable for DED processing.

It is important to note that, very flattened shaped particles commonly appeared in the images inclined and therefore its dimensions were inaccurate. Consequently, in those cases, a smaller number of particles (around 80) were eligible to be measured using the ImageJ software. On the other hand, the more spherical particles were more easily eligible to be measured. In those cases, an average of 800 particles for each powder were measured.

The PN5, PN3 and NP2 samples were observed at CEMUP (Materials Center of the University of Porto) and, for each powder, using a 100x magnification, 5 different images were captured.

However, as it will be explained later in Chapter 4.1.1.2, there was a need to analyze a second sample of the powder produced under NP2 conditions as well as the powder produced under NP3 conditions. By this time, the equipment at CEMUP was not available, so the SEM equipment at the FEUP's Department of Metallurgical and Materials Engineering (DEMM) was used. It is important to note that this equipment only permitted to observe samples with a minimum magnification of 520x while the pictures captured at CEMUP were taken with a magnification of 100x. Therefore, a direct comparison between the images captured at CEMUP and the images captured at DEMM could not be done, which also affected the particles size and shape analysis.

Observation by optical microscopy Besides the SEM analysis, the powder was also polished and observed by an optical microscope (Leica DM6 M) in order to asses the microporosities and internal voids inside the particles.

3.2.2.2 Density and Flowability Measurements

Loose Density The loose density was measured according to the standard ASTM B212-99 using a Copley Scott Volumeter, as presented in Figure 3.6.

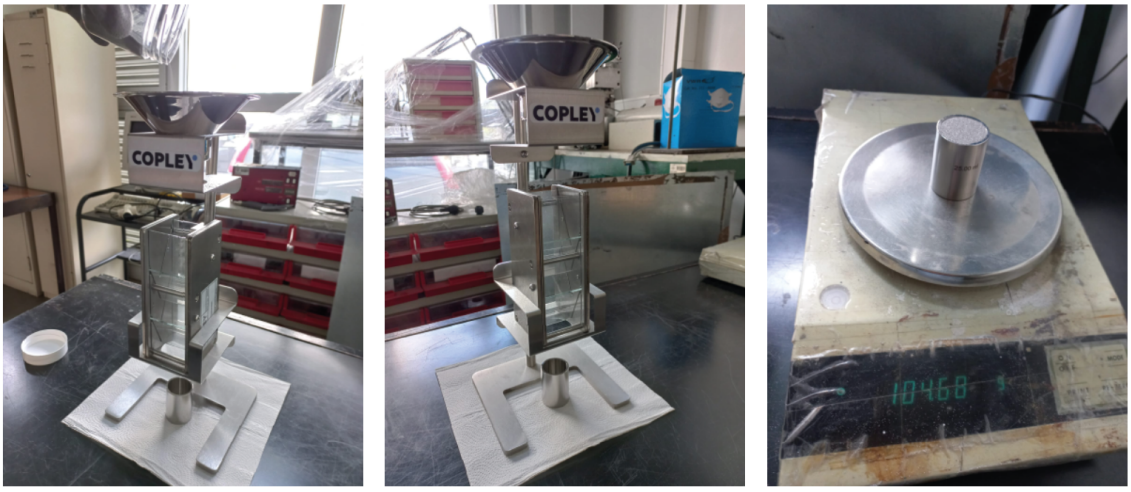

Figure 3.6: Equipment used to measure the loose density of the powder.

The powder was loaded into the Scott Volumeter, in order to fill the metallic container placed below. When the container was full, a spatula was used to level off the powder with the top of the cup. Then, since the container volume (25 mL) were known, the weight of powder was measured,

in order to calculate the loose density. The process was repeated two more times in order to improve the results accuracy and/or precision.

Tap Density The tap density was determined considering the standard ASTM B527-93, using a Copley JV 100i Tapped Density Tester, as presented in Figure 3.7.

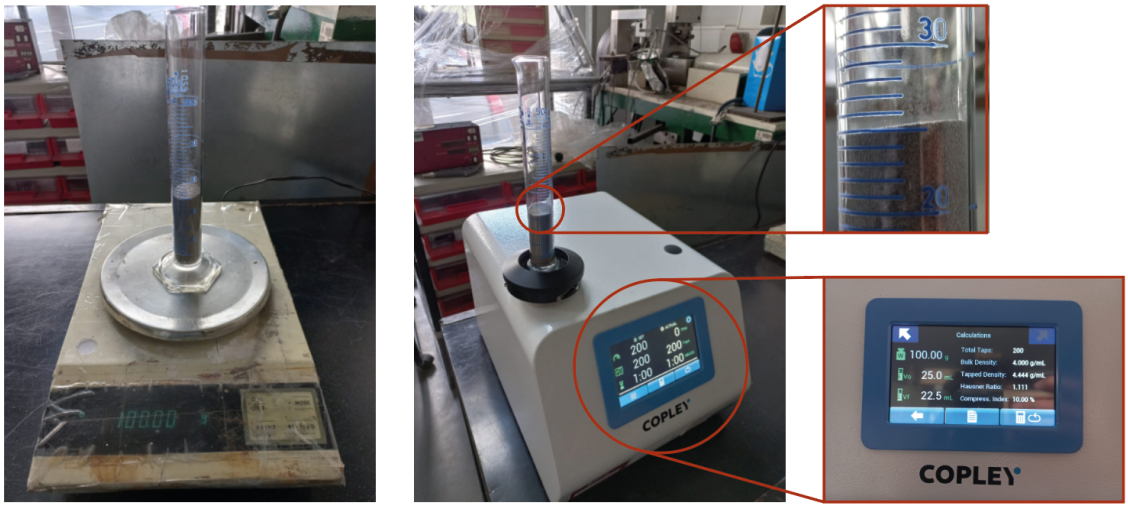

Figure 3.7: Equipment used to measure the tap density of the powder.

Firstly a powder mass of 100 ± 0.5 g was poured into a graduated cylinder. Then, the cylinder was placed and locked on the tester which was programmed for 200 taps in one minute. Afterwards, the final volume was visually observed in order to calculate the tap density. The process was repeated two more times in order to improve the results accuracy and/or precision.

Flowability For the measurement of the flowability of the powder, the standard ASTM B213-9 was considered. This standard implies the use of a Hall Flowmeter funnel which was not available. Therefore it was used a regular glass funnel with similar dimensions (orifice of 2.5 mm in diameter and a cone slope of 30º) and a simple glass cylinder to collect the powder, as shown in Figure 3.8.

Regarding the procedure, firstly, it was weighted 50g of powder which was then placed at the funnel with the discharge orifice blocked with a dry finger. Then, at the same time, the orifice was unblocked and a timer was started. The timer was stopped when all the 50g of powder left the funnel. The process was repeated another time using fresh 50g quantity of powder. It was only done two repetitions because of this rule sincee, at time of testing, there was not enough powder to do more than two tests using fresh powder.



Figure 3.8: Equipment used to measure the flowability of the powder.

3.2.3 DED Printings

This Chapter presents the followed procedure and the used equipment in the DED processing and consequent assessment of the printings.

3.2.3.1 DED Setup and Procedure

DED Equipment The Figure 3.9 shows the DED equipment used in this work. The equipment is composed by a KUKA 6-axis industrial robot equipped with a COAX12V6 set nozzle head. This nozzle head has a cooling capacity in continuous operation up to 6000W. In the nozzle, there is an E-MAqS system, mounted with a powder splitter, a Fraunhoffer IWS powder splitter, that diverts the powder flow into four different channels. The table used to perform the depositions is a DEMMELER 3D welding table. The energy source is a coherent highlight FL3000 fiber laser presenting a Gaussian distribution with a wavelength of 1070 ± 10 nm. Its maximum power is 3000 W in continuous wave (CW) mode.

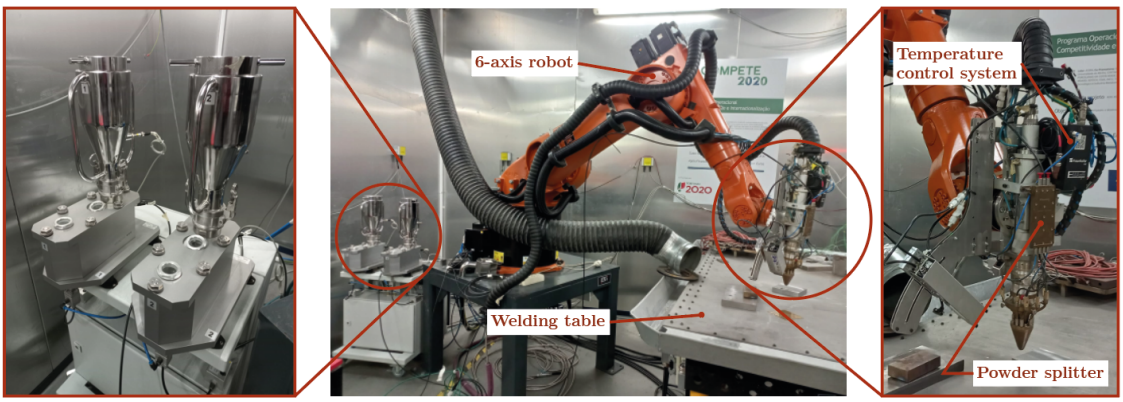

Figure 3.9: DED equipment used for the printings with details of the powder feeders (on the left) and the nozzle head (on the right).

The equipment has two independent Medicoat AG Disk powder feeders that operate between 0.5 g/min and 100 g/min without pulsation. All this setup is placed inside a chamber which is locked during the depositions. Once any printing is done, the chamber can be opened and the user, equipped with a proper mask and thermal gloves can grab the final part.

Material Linearization Firstly, both the commercial and upcycled powders were transferred to the two available powder feeders. Then, before depositing any feedstock, a material linearization was performed. This is necessary because there is no linear correlation between the powder flow rate and the valve aperture. In this process, the valve is opened 10 times starting from 100% and decreasing 10% at a time until it reaches 10% aperture. The valve stays open each time for 2min and the deposited powder is collected and weighted. Before starting the timer, it was necessary to verify if the powder flow was stable in order to ensure precise results. Lastly, the flow values were obtained (by dividing the weight results by the two minutes) and inputed into the software Medicoat software, as seen in Figure 3.10.

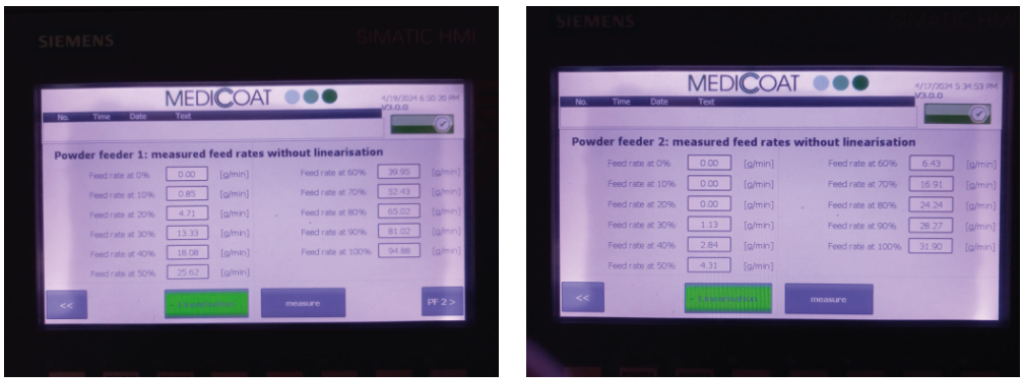

a) b)

Figure 3.10: Linearization process in the Medicoat software: a) upcycled powder; b) commercial powder).

The software auto compensates the non-linearization of the powder feed rate considering those values and according to Equation 3.1:

$$Valve\,Aperture\,(\%) = \frac{100}{PFR_{aperture=100\%}} \cdot PFR_{real} \tag{3.1}$$

where $PFR_{aperture=100\%}$ represents the amount of powder that leaves the valve when it is 100% opened, PFR_{real} is the powder flow rate that is intended to be deposited and $Valve\,Aperture$ the value of the valve percentage aperture considered by the software.

Software To perform any printing, the depositions parameters need to be introduced into a .CSV file. Both this .CSV file and a GCODE are coupled into a python application created at INEGI, merging as a .SRC file. This file can be ran in the RoboDK software interface, which is the software used for the programing and simulation of the DED robot. The .SRC is then transfered

to the DED system by a USB port. Before any printing, the code is run with the laser and powder feeder off, in order to verify if the toolpath is correct and to place properly the substrate. Then, the DED chamber is closed and the depositions are performed.

Substrate The substrate plates were made of medium carbon steel AISI 1045. As stated in the Chapter 3.1.2, the choice of this material was purely due to the material's availability at INEGI. The plates were rectified before the deposition to assure a flat top surface since an inclined deposition surface would lead to the construction of non-vertical structures. The substrate was non-preheated thus the depositions were performed at room temperature.

3.2.3.2 Single line and Thin Wall depositions

In this section, the printings parameters used in all the depositions are presented. The depositions can be divided into 2 groups: single line depositions and thin wall depositions. The single lines are one-layer printings of short tracks while the thin walls are vertical structures resulting from the successive deposition of layers on top of each other.

Work Plan: intended and performed depositions In this work, regarding the DED printings, the work plan consisted of: (1) depositing single lines with different sets of parameters and (2) depositing thin-walled structures that would be machined into tensile testing specimens.

The goal of the single line depositions was to achieve an optimized set of parameters taking into account the clad dimensions and the dilution as well as the presence of defects such as lack of fusion or oxidation. From those printings, it would also be possible to access the influence of parameters on the melt pool geometry and productivity of the process. This process is also commonly known as parametrization.

Having chosen the optimized set of parameters, a group of thin-walled structures would be build using the previously selected settings. However, when printing multi-layer depositions, it is necessary to study other parameters such as toolpath strategy, overlap ratio and pause time between layers. Then, the thin walls would be printed in order to obtain the tensile specimens for mechanical characterization.

The initial idea was to follow this procedure for both commercial and upcycled powders. Therefore, AISI 316L gas atomized powder (supplied by Sandvik Materials Technology (2024)) was deposited. A series of single line and thin wall depositions were performed with this powder, until it was discovered, as stated earlier in Chapter 3.1, that the upcycled powder material was not AISI 316L but AISI 301. The purpose of the printings with AISI 316L commercial powder was to serve as benchmark for upcycled powder, by comparing the characteristics and properties of the powder and by assessing the structures build by DED (regarding the mechanical properties, microstructure, occurrence of defects and chemical analysis). Therefore, since the upcycled powder was made of AISI 301 and not AISI 316L, the printings using commercial powder became pointless because the comparison could not be drawn.

Therefore, in this work, it is only presented the depositions performed with AISI 301 upcycled powder.

Fixed Parameters Parameters such as spot size, carrying gas flow rate, shielding gas flow rate, stand-off distance and nozzle head inclination angle were already defined according to the equipment and technician suggestions based on previous works. The values of those parameters, which remained fixed throughout all printings, are presented in the Table 3.7.

Table 3.7: Fixed parameters for the AISI 316L depositions.

Shielding gas flow rate	Carrying gas flow rate	Stand-off distance	Inclination angle	Laser spot size
10 l/min	4 l/min	13 mm	5º	2.1 mm

Single Line Depositions (Parametrization) As stated above, the goal of the single line depositions was to choose an optimal set of parameters. Since the parameters presented in Table 3.7 are constant, the parameters that had to be selected were: laser power, scanning speed and powder feed rate. To chose those parameters, the criteria used came from the calculation of the Global Energy Density (GED or ω $[J/mm^2]$), which Equation was presented earlier in Chapter 2.2.5.9.

Then, since the material to be deposited was thought to be AISI 316L, the selected sets of parameters were chosen according to a bibliographic review of 316L DED processing. The Annex A presents all the sets of parameters taken from the literature regarding DED processing of AISI 316L powder. Besides that, the GED value is also presented and is possible to observe that this value ranges from 13 to 100 J/mm^2. Since the spot size value in this work is fixed, the GED value for a spot size of 2.1 mm is also presented and it ranges from 9 to 237 J/mm^2.

In the majority of studies presented in Annex A, the authors also performed a parametrization in order to obtained the optimal parameters for the specific equipment used. However, in the majoritiy of the cases presented in Annex A, it is only presented the final optimal set of parameters. Nevertheles it was relevant to look at all the tested parameters in the study developed by Castanheira (2022). In that work, the authors used the same DED equipment and also deposited powder produced through the transformation of chips into DED feedstock through milling. However, it is important to note that the practical experiment in that work had 3 major differences: the material was a different stainless steel grade (AISI 303), the powder was generated through disc milling and not ball milling and the shielding gas flow rate (35 l/min) and laser spot size (1.5 mm) values were different. However, due to the major similarities between this work and Castanheira (2022), the DED parameters used by Castanheira (2022) were still a solid starting point for the deposition of the AISI 301 upcycled powder. The authors tested 21 different sets of parameters, with the GED varying between 31 and 267 J/mm^2.

Having in consideration those GED values as well as the common values for the 3 parameters, 9 sets of parameters were selected. Those sets were considered according to the Design of Experiments method Taguchi L9 and are presented in Table 3.8. Having those parameters selected, a line of 20 mm was printed for each of the 9 sets.

Table 3.8: Printing parameters selected according to the literature review, combined considering the Taguchi L9 method - Upcycled Powder.

Line	Laser Power [W]	Scanning Speed [mm/s]	Powder Feed Rate [g/min]	Spot Size [mm]	GED [J/mm^2]	Number of layers	Vertical Overlap [%]
1	1600	5	3	2,1	152	1	-
2	1600	10	6	2,1	76	1	-
3	1600	15	10	2,1	51	1	-
4	2000	5	6	2,1	190	1	-
5	2000	10	10	2,1	95	1	-
6	2000	15	3	2,1	63	1	-
7	2400	5	10	2,1	229	1	-
8	2400	10	3	2,1	114	1	-
9	2400	15	6	2,1	76	1	-

In this work all the printings are numbered according to the chronological order in which they were deposited, as it is possible to observe in the Tables present in this section.

After the top analysis of those tracks, it was decided to deposit 3 extra tracks combining 3 sets of parameters that were not tested in the Taguchi L9. Those parameters are presented in Table 3.9

Table 3.9: Printing parameters selected according to previous depositons - Upcycled Powder.

Line	Laser Power [W]	Scanning Speed [mm/s]	Powder Feed Rate [g/min]	Spot Size [mm]	GED [J/mm^2]	Number of layers	Vertical Overlap [%]
10	2000	15	10	2,1	67	1	-
11	2400	15	10	2,1	76	1	-
12	2400	8	10	2,1	143	1	-

Those 12 lines were sufficient to select a proper set of parameters, as it will be explained later in Chapter 4.2.1. However, it is still acknowledge that parametrization could have been pursued further but the available time and equipment constraints also limited this process.

Thin Wall Depositions Having chosen the optimized set of parameters from the single line depositions, a group of thin-walled structures were build using the previously selected settings. However, when printing multi-layer depositions, it is necessary to study other parameters such as toolpath, overlap ratio and pause time between layers.

Having said that, 3 walls were printed with upcycled powder. The parameters of those depositions (presented in Table 3.10) are explained later in the Chapter 4.2. The deposition of a 4th wall was not possible due to insufficient powder available.

Table 3.10: Printing parameters selected according to previous depositons - Upcycled Powder.

Wall	Laser Power [W]	Scanning Speed [mm/s]	Powder Feed Rate [g/min]	Spot Size [mm]	GED [J/mm^2]	Number of layers	Vertical Overlap [%]
1	2400	5	10	2,1	229	21	0
2	2400	5	10	2,1	229	15	0
3	2400	5	10	2,1	229	15	0

3.2.4 Printings Assessment

This section presents all the practical procedures conducted and equipment used in order to analyze the DED printings.

3.2.4.1 Top view analysis

During the single line depositions, after the printings, the deposited tracks were visually observed from the top. This analysis (conducted with the help of a Olympus SZH Stereo Microscope equipped with a Leica MC170 HD camera) allowed to assess the oxidation (through the track surface color), the track's width and height and their evolution along the track's length (i.e. if the track had an uniform and continuous aspect). From the visual analysis, it is also possible to detect some defects such as the presence of unmelted powders, high surface roughness and burning of the substrate. This analysis allows to assess the efficiency of the deposition parameters up to certain point. It was possible to eliminate some parameters values from this analysis but it was also pivotal to observe the printings cross sections. However, for a productivity purpose, a great number of depositions were carried out and only then the cross section analysis was conducted. This is due to the fact that the cross sectioning follows a procedure that was not practical to perform everytime a deposition was done.

3.2.4.2 Cross section Analysis

As stated above, after a significant amount of deposited tracks, the depositions and the substrate were cut either with a wire-cut electrical discharge machining (EDM) equipment (3.11b) or with an abrasive cut-off machine (Metkon METACUT 302) (Figure 3.11b). The printings with commercial powder were easily cut with the EDM but the printings with upcycled powder could not be cut with the same equipment since the electrode wire would constantly break due to the presence of oxides. After the cutting, the face to be analyzed was rectified in order to eliminate the burned layer from the EDM operation. Following that, the samples were grinded with SiC grinding papers of, successively, meshes of 120, 320, 600, 1000, 1200 and 2400 at 150rpm, using a Struers Pedemax-2 semi-automatic machine (3.11c). Then the samples were polished on a water-based microcrystalline diamond suspension of 3 μm and 1 μm respectively, using a cloth disc on the Struers Pedemax-2. Having performed this preparation, the track's cross sections were observed at a Leica DM6 M Microscope. Sometimes to better distinguish the printed material from the substrate, the sample was etched using a 10% Nital solution for 10 seconds.

The cross section analysis is pivotal when studying powder DED processing, since it allows the assessment of the the adhesion, the dilution and occurrence of defects. Moreover, this analysis allowed to obtain micrographs from which it was later measured the geometric parameters of the melt pool, using the ImageJ software. Those parameters (width (w), height (h), depth (d), melted area (A_m), printed area (A_p) and wetting angle (θ)) were presented earlier in Figure 2.9 and explained in the Chapter 2.2.7.1. The most important aspects to analyze in this step is the track height (since it is the main indicator of the printing productivity) and the dilution (calculated



a) b) c)

Figure 3.11: Equipment used for sample preparation (a) and b) for cutting substrate and printings and c) for polish and grind the face to analyse) :a) Wire-cut EDM equipment; b) abrasive cut off machine; c) Grinding and polishing machines.

with the melted and printed areas) which is a indicator of the metallurgical bonding between the substrate and deposited material.

3.2.4.3 Microstructural analysis

In order to assess the microstructure of the printed thin walls, a proper sample preparation procedure was followed. Firstly, an abrasive cut-off machine (Metkon METACUT 302) was used to cut a cross section of the printed part. This sample was then hot mounted on resin using a Struers CitoPress-5 mounting press (Figure 3.12a)). The sample was subsequently grinded and polished using the procedure stated above in Chapter 3.2.4.2. The samples were then observed by a Leica DM6 M Microscope (Figure 3.12c)) and by a Thermo Scientific Phenom XL G2 Desktop Scanning Electron Microscope (SEM) (Figure 3.12b)).

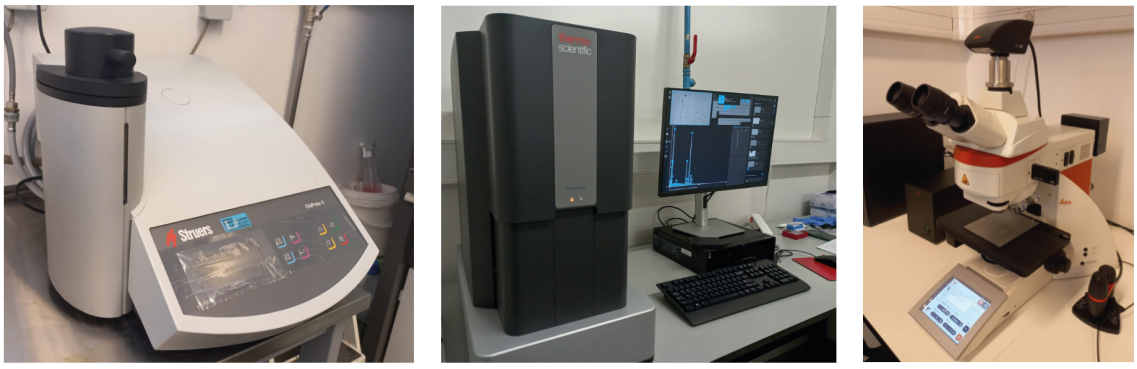

a) b) c)

Figure 3.12: Equipment used for sample preparation and microstruture analysis: a) Hot mounting press for resin samples preparation; b) SEM Equipment (Thermo Scientific Phenom XL G2 Desktop); c) Optical Microscope (Leica DM6 M).

In order to quantify the amount of inclusions present in the printings, the ImageJ was again used, specially the tools "Threshold" and "Analyze Particles" which gave as output the number of inclusions in the wall, the average size, aspect ratio and the inclusions area. This procedure is shown in Figure 3.13.

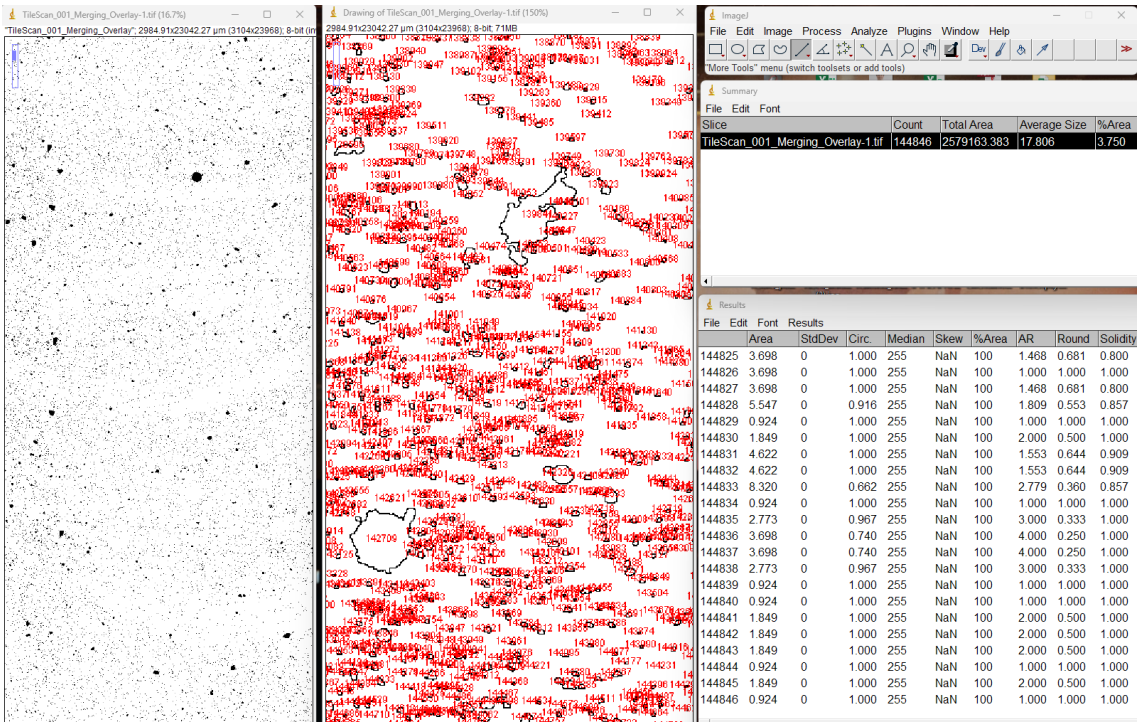

Figure 3.13: Inclusions measurements on printed wall micrograph using the ImageJ software.

3.2.4.4 Chemical analysis

The chemical composition assessment had different goals. Firstly, the chemical compositions of both the AISI 301 original block (as supplied) and the DED printed thin wall were measured in order to understand the chemical changes from the milling and deposition processes. Secondly, the chemical composition of a DED printed thin wall was assessed along its height, to evaluate if the chemical composition is uniform throughout its building direction. Finally, the chemical composition of the inclusions observed by SEM was assessed in order to understand the type and origin of those inclusions.

The chemical composition measurements were performed by two different techniques. The chemical composition of the original block was assessed through Optical Emission Spectrometry (OES). Briefly, this technique involves exciting the atoms in a sample so that they emit light (photons) at characteristic wavelengths, which are then measured to identify and quantify the elements present. It is a quantitative method and the equipment used was a SPECTROMAXx with iCAL 2.0 (Figure 3.14a)).

On the other hand, the analysis of the chemical composition along the thin wall height as well as the inclusions analysis could not be performed through OES since it was necessary to perform a very localized analysis. Therefore, it was employed the SEM/EDS (Energy Dispersive X-ray Spectroscopy) technique, using the Thermo Scientific Phenom XL G2 Desktop SEM equipment (Figure 3.14b),c)).

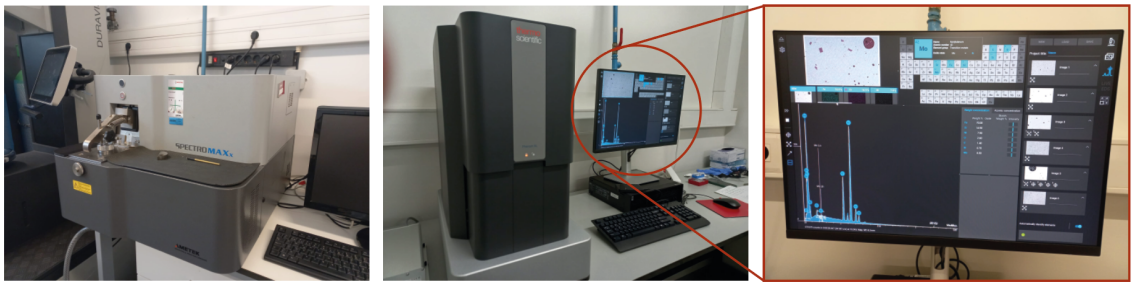

a) b) c)

Figure 3.14: Equipment used for the chemical composition assessment: a) SPECTROMAXx with iCAL 2.0 (Quantitative analysis); b) and c) Thermo Scientific Phenom XL G2 Desktop SEM equipment (Semi-quantitative analysis).

Briefly, the SEM/EDS method works by directing a focused electron beam onto a sample, causing it to emit various signals, including characteristic X-rays. The EDS detector analyzes these X-rays to identify and quantify the elements present. This technique is a semi-quantitative method, i.e. an analytical technique that provides approximate, rather than exact, measurements of the quantity or concentration of a substance within a sample. These methods yield results that are more precise than qualitative (which merely identify the presence or absence of a substance) but less precise than fully quantitative methods (which provide exact numerical values). SEM/EDS is considered a semi-quantitative method for chemical analysis due to several inherent limitations. For instance, in the SEM/EDS method, low-energy x-rays (associated with light elements such as C or O) are usually absorbed or scattered and therefore its detection is perturbed. Additionally, high background noise in the low-energy region and overlaps with other elemental peaks complicate accurate identification and quantification. These factors lead to significant deviations from the actual composition, making the results for light elements unreliable.

3.2.4.5 Microhardness measurements

The microhardness measurements were performed on a DED printed thin wall using a ZwickRoell microhardness tester (Figure 3.15). The test was carried out on a resin mounted sample, considering a Vickers indenter at 0.1 kgf for 15 seconds. The indentations were performed on a transversal cross section in a direction parallel with the building direction, to provide a microhardness profile. The indentations had a 1 mm distance between them and the measurements were carried out 6 times for better precision. The measurements were performed in the top 25mm of the wall thus the microhardness was not measured on the lower part of the wall. This choice comes from the fact that this work focuses on the building of thin walled structures and not on the construction of clads. Therefore the study of the substrate and consequently of the first printed layers is negligible.



Figure 3.15: ZwickRoell microhardness tester.

3.2.4.6 Tensile Tests

In this work, the tensile tests served to compare the tensile properties of the thin-walled structures build by DED processing of the AISI 301 upcycled powder to the tensile properties of the AISI 301 as supplied.

The tensile specimens of the original AISI 301 cylinder block were obtained through wire-cut EDM. The same was tried to obtain specimens of the upcycled powder printings but, as stated above, the electrode wire would constantly break due to the presence of oxides. Therefore the upcycled powder specimens were machined in a CNC machining center (DMU 60 eVo linear 5-axis) at INEGI. The Figure 3.16a) shows a schematic that shows how the specimens were obtained from the thin-walled structure. Figure 3.16b) presents the dimensions of those specimens (taken from a technical drawing authored by INEGI and presented in the Annex C).

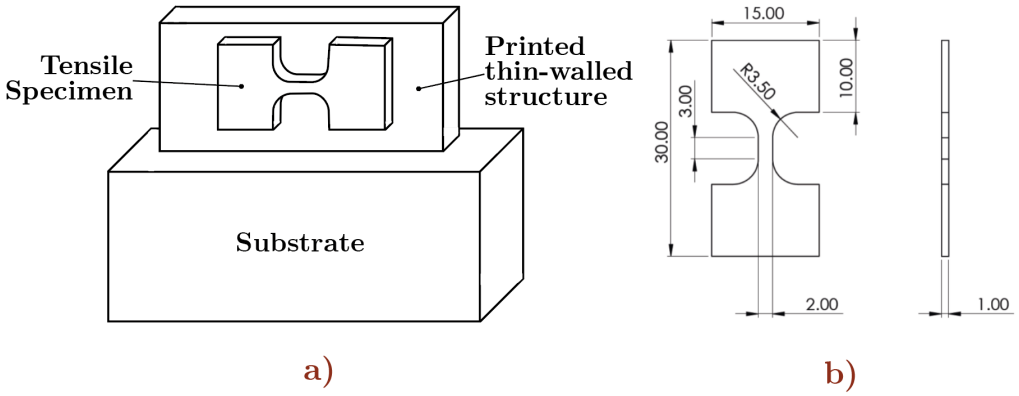

Figure 3.16: a) Schematic of the specimen obtained from the thin-walled structure; b) Tensile specimen dimensions

After the machining (conventional or EDM) of the samples, they were painted by spraying

a thin layer of white paint in order to uniformize the surface's diffuse reflectivity. Then, dark paint was spread using an airbrush (with a nozzle set of 0.2 mm), in order to create a speckle pattern (with an average speckle size of less than 15 μm). This pattern is necessary for the digital image correlation (DIC) processing, which is explained below. The Figure 3.17a) shows the tensile specimens after machining while the 3.17b) shows the specimens after painting.

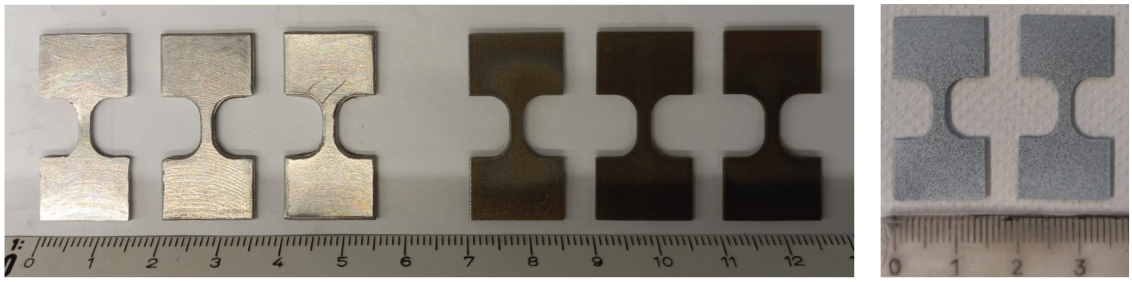

a) b)

Figure 3.17: Tensile specimens: a) taken from the DED printed thin wall (the 3 on the left); taken from the as supplied AISI 301 cylinder block (the 3 on the right); b) tensile specimens after painting for DIC processing.

Before carrying out the tensile tests, the thickness and width of all the specimens was measured and those measurements are presented in Annex O. Then, the specimens were tested in an equipment developed by Cruz et al. (2022) in INEGI, the Miniaturized Specimen Tester Device (MSTD) which is shown in Figure 3.18.

This device was developed with the goal of testing miniaturized specimens on a reduced scale, as is the case here. The samples were tested at room temperature, in a constant crosshead speed of 0.5 mm/min, until fracture. A 5 Megapixel Baslerac A2440-75 μm, 2448 × 2048 px camera with a telecentric InfaimonOPE-TC-23-9.45 mm lens was used to conduct an image acquisition (using a 5Hz aquisition rate) of the gauge-length area (L_0=2.5mm). Then, the digital image correlation technique (DIC) was used for the record of the deformation field evolution over time. Digital Image Correlation (DIC) measures deformation, displacement, and strain on the surface of a sample by capturing a series of images of a specimen's surface during the test, and then analyzing these images to track and measure changes in the surface pattern (in this case the speckle pattern created with dark paint). The used software for the data post-processing was the VIC-2D.v6.

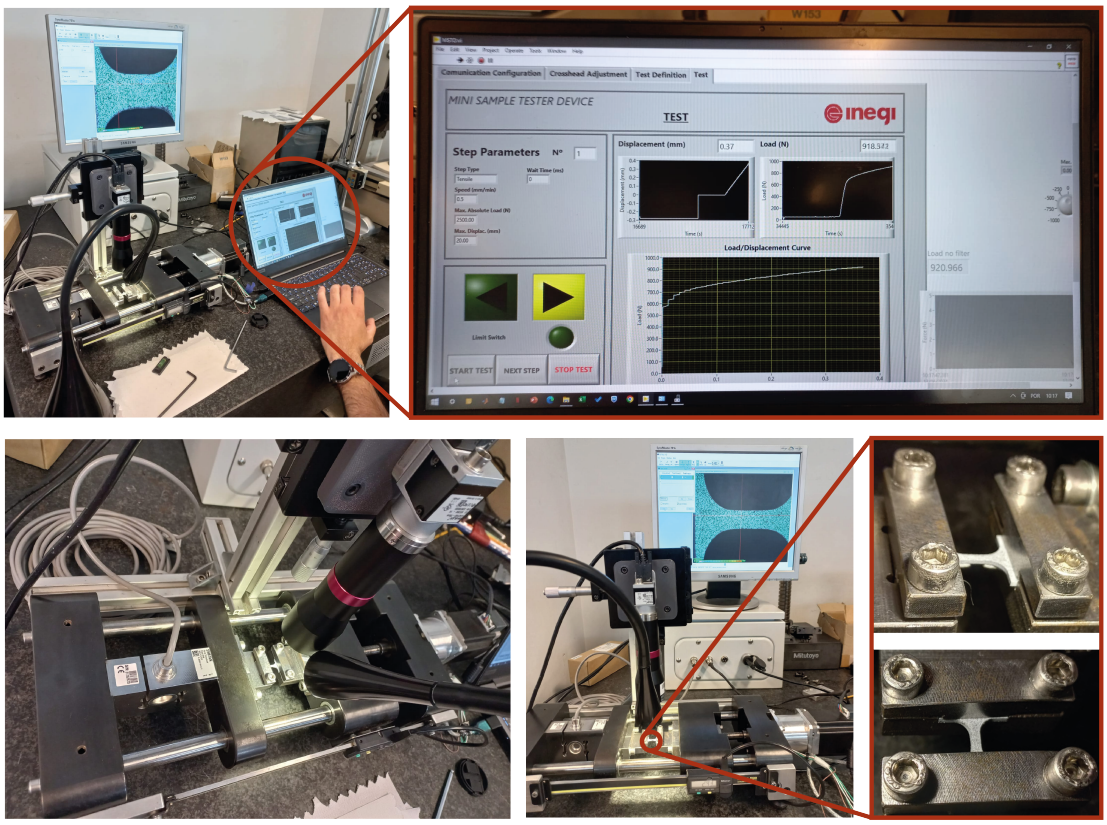

Figure 3.18: Tensile testing apparatus.

Observation of the fracture surfaces After the tensile testing, the specimen's fracture surfaces were observed using the Thermo Scientific Phenom XL G2 Desktop SEM equipment (shown earlier in Figure 3.12b), in order to understand the mode of failure of each specimen (namely the extent of suffered plastic deformation) and assess the presence of possible stress concentrators.

Chapter 4

Results and Discussion

This chapter presents all the results obtained in this work, as well as the critical discussion regarding those. Firstly, the results obtained from the production and characterization of the upcycled powder are presented and discussed. Secondly, the results from the DED printings are displayed and discussed.

4.1 Powder Production and Characterization

This section presents the results regarding the transformation of machining chips into feedstock powder for DED processing.

It is important to note that, in this section, the results from this work are presented and discussed but also compared to the results from the previous works of Castanheira (2022) and da Cunha (2023), since in those studies, the authors used the same milling equipment and some of the same milling conditions. Therefore, those works can serve as a direct comparison between 3 different materials (2 austenitic stainless steels and one medium carbon low alloy tool steel).

4.1.1 Milling Productivity

As stated in the previous chapter, the productivity of a certain milling procedure, regarding powder production for DED processing, is defined by the amount of resultant powder in the desired size range, which was considered 38 to 212 μm in this work.

Figure 4.1 presents the amount of resultant powder in weight percentage (wt %) regarding each milling procedure (both disc and ball milling). For each procedure, 2 different batches (for better precision) were sieved and weighted according to their size range. Those groups of 2 batches are identified in Figure 4.1 by a proper color scheme (each group of 2 batches is represented by 2 shades of the same color). The bars illustrated with striped pattern represent the results of milling procedures that were not originally developed in this work: the reddish bars with vertical stripes are related to the disc milling procedure, which was developed by Castanheira (2022) while the orange bars with horizontal stripes are related to the ball milling procedure developed by da Cunha (2023). The solid color bars (green, blue, and yellow) represent results from milling procedures

originally elaborated in this dissertation. This color code is also present throughout the document, in the presentation of the results of the characteristics and properties of the different powders.

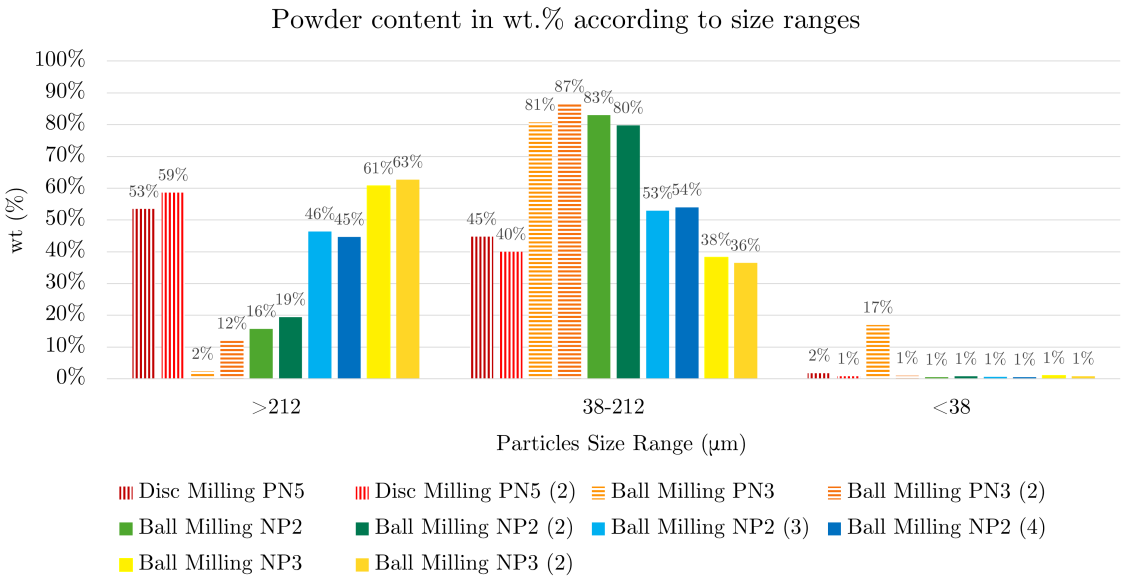

Figure 4.1: Resultant powder content in wt. % for each milling procedure

It is important to note that the previously presented NP1 procedure (originally developed in this work and whose parameters are shown in Table **??**) does not have representation on the Figure 4.1 results nor on any of the results presented throughout this section because this procedure only produced 16% (in wt %) of powder in the 38-212 μm range. In addition, the most serious aspect was the fact that this procedure, in only one run, severely damaged the milling media in only one NP1 run, by inducing the adhesion of the material to be milled to the jar and balls. This incident also occurred for other procedure, but to a significantly lesser extent, as will be explained later in this section.

4.1.1.1 Comparison of the same milling conditions for different materials

As stated above, the results from this work are compared to those from the previous works of Castanheira (2022) and da Cunha (2023), since in those studies, the authors used the same milling equipment and some of the same milling conditions. Therefore, those works can serve as a direct comparison between 3 different materials (2 austenitic stainless steels and one medium carbon low alloy tool steel).

To understand the milling performance of a certain material, it is important to analyze two mechanical properties: Elongation (quantifies the ductility) and Fracture toughness. Ductile materials (characterized by high ductility) tend to deform plastically under high-energy impacts instead of fracturing which makes particle size reduction difficult. Moreover, ductile materials are more prone to cold welding. On the other hand, brittle materials (low elongation) will fracture more readily under the same conditions, leading to more efficient size reduction. Regarding the fracture toughness, it quantifies the ease of brittle fracture. Materials with high fracture toughness resist crack initiation and propagation, making them harder to break down. Usually, those materials require longer milling times or higher energy inputs to achieve the desired particle size reduction.

Therefore, the common elongation an fracture toughness values of the 3 materials compared here were investigated using the Granta EduPack software and are presented in Figure 4.2.

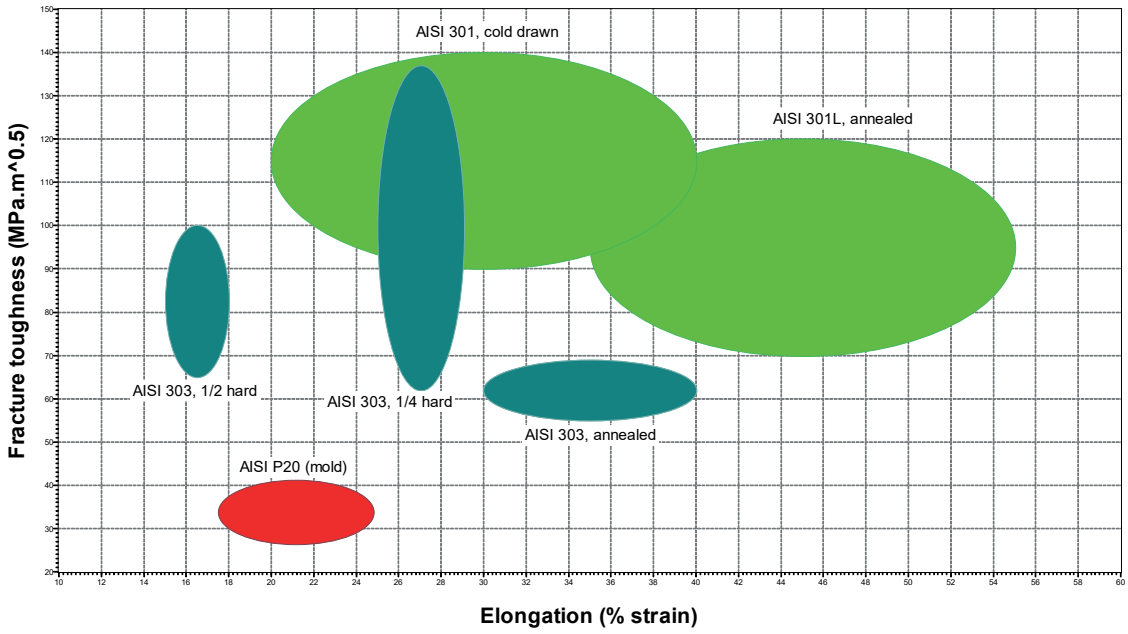

Figure 4.2: Elongation and Fracture Toughness of AISI 301, AISI 303 and AISI P20+Ni (Granta Design (2021)).

The 3 different materials are the austenitic stainless steels AISI 301 and AISI 303 and the medium carbon low alloy tool steel AISI P20+Ni. AISI 303 stainless steel specifically designed to exhibit improved machinability (through the addition of sulfur) while maintaining good corrosion resistance in mild environments. Thus 303 stainless steel is commonly used in applications

requiring extensive machining, such as fasteners, fittings, and gears (Castanheira (2022)).

On the other hand, AISI P20+Ni is a low-alloy tool steel designed for plastic mold applications. This steel is characterized by its high wear resistance (achieved through the addition of Nickel), and its good machinability and polishability. Thus P20+Ni has a balanced combination of durability and ease of machining, which makes it ideal to the manufacture of large plastic molds or casting dies (da Cunha (2023)).

Firstly, as it is possible to observe, the ductility and fracture toughness of AISI P20+Ni are the lowest by a significant difference, which is very common when comparing tool steels to austenitic stainless steels. However, it is important to to note that the Granta Edupack software did not had available about the AISI P20+Ni specifically but only about the P20. It is known that the addition of Ni to this steel improves its ductility and fracture toughness compared to standard P20, but those properties do not usually come close to those of austenitic stainless steels (da Cunha (2023)).

Moreover, from the Figure 4.2, it is also possible to observe that the elongation and fracture toughness values of the two stainless steels (301 and 303) varies a lot according to the different processing conditions of the supplied material. However, from the research on stainless steel suppliers databases, it was noted that usually AISI 301 presents a greater ductility and fracture toughness, in comparison with AISI 303. The lower toughness and ductility of the AISI 303 is, in great part, due to the sulfur addition.

On the other hand, it it known that chips mechanical properties are affected by the milling conditions. Higher milling speeds lead to higher milling energies causing a grain refinement and consequently a decrease in ductility. Therefore the mechanical properties of the chips not only depend on the production process and heat treatment of the original material but also on the steel's thermomechanical history developed during machining. In this work, the machining conditions are known but the machining conditions related to Castanheira (2022) work are unaware. Both in this work and in Castanheira (2022) the production process and heat treatment of the original material is also unknown.

Having this in mind, the most probable hypothesis is that the AISI 301 chips processed in the present study have a greater ductility and fracture toughness, in comparison with the AISI 303 chips milled by Castanheira (2022). However, due to the above mentioned reasons, it is not possible to confirm this point.

Disc milling Firstly, as stated previously, the disc milling PN5 conditions are the same as those adopted by Castanheira (2022). In that work, the authors milled AISI 303 chips and the milling productivity results are presented in Table 4.1.

Castanheira (2022) results come very close with the results presented in the red bars of Figure 4.1, which is expected since AISI 303 and AISI 301 are both austenitic stainless steels with close chemical compositions. However, it is noted a slightly superior content of AISI 303 powder in the 38-212μm size range. This difference may be explained by the lower ductility and fracture toughness of the AISI 303 steel, which led to an easier fracturing of this steel and consequently a

Table 4.1: Powder content in wt (%) according to the size range - Comparison of the PN5 milling conditions for 3 different materials.

Powder content in wt (%) - Disc Milling PN5			
Size range [μm]	**>212**	**38 - 212**	**<38**
AISI 301	56	42	2
AISI 303 (Castanheira (2022))	54	36	10
AISI P20+Ni (da Cunha (2023))	27	63	5 (5g lost)

more efficient particle size reduction. The greater amount of AISI 303 powder in the <38 μm size range for the AISI 303 powder is also in line with this explanation.

da Cunha (2023) also used the same disc milling conditions to transform AISI P20+Ni tool steel chips into powder for DED feedstock and the results are presented in the above mentioned Table 4.1. In comparison with the stainless steels results, the milling of the tool steel produced a greater amount of powder in the 38-212 μm size range and a smaller amount of powder in the >212 μm size range. This is expected and it is due to the tool steel's greater brittleness and lower ductility (Figure 4.2), which leads to a easier fracturing of the particles and consequently more effective size reduction.

Ball Milling Regarding the ball milling conditions, the ball milling PN3 conditions are the same as those adopted by da Cunha (2023). As stated above, in that work, the authors milled AISI P20+Ni tool steel chips. However, the productivity results can not be compared since da Cunha (2023) sieved the resultant powder using sieves with different apertures (20, 53, 150 and 212 μm).

4.1.1.2 Milling conditions developed in this work

As stated above, the first ball milling conditions tested were the PN3 conditions, which were developed by da Cunha (2023). In that work, the authors tried 5 different ball milling conditions and the PN3 conditions stood out for producing the greatest amount of powder in the 38-212 μm size range, as seen in Annex Q. Although the employment of this condition for the milling of AISI 301 chips led to great results (around 85% of the final powder in the desired size range), it was decided to develop a new condition, NP2, in order to reduce the number of stages from 3 to 2, while maintaining the same util milling time and decreasing the total time. This decision was made in order to simplify the milling process, making it more suitable for implementation in industry. The productivity of NP2 (illustrated in the green bars of Figure 4.1) dropped very slightly so that about 80% of the resulting powder was in the desired size range, which represented a very positive outcome and classified those conditions as very productive. This showed that the merge of the 2 first PN3 stages into the 1st NP2 stage (and a consequent elimination of a 30mm balls stage at 600rpm) did not have a significant effect on the milling productivity.

With those results, the milling parameters could have been optimized in order to maintain or increase productivity while decreasing the total milling time. However, since the results were already very positive, and taking into account the time frame for the thesis, it was decided to

continue producing powder using the NP2 conditions until there was enough powder for the DED printings.

As the chips were continuously milled, for practical purposes, the resultant powder was no longer weighted according to the size range. However, after a couple NP2 runs, it was observed that the amount of resultant powder in the 38-212 μm size range had dropped. Therefore, the powder from 2 NP2 runs was sieved and weighted and the results are presented in the blue bars of Figure 4.1. As noted, the amount of powder in the 38-212 μm size range has dropped to approximately 50% while the amount of powder with its size greater than 212 μm had risen to roughly 45%. The reasons for this change in the process productivity comes from the overuse of the grinding media (lid, jar but especially balls) that suffered adhesion of the AISI 301 powder being milled, as shown in Figure 4.3.

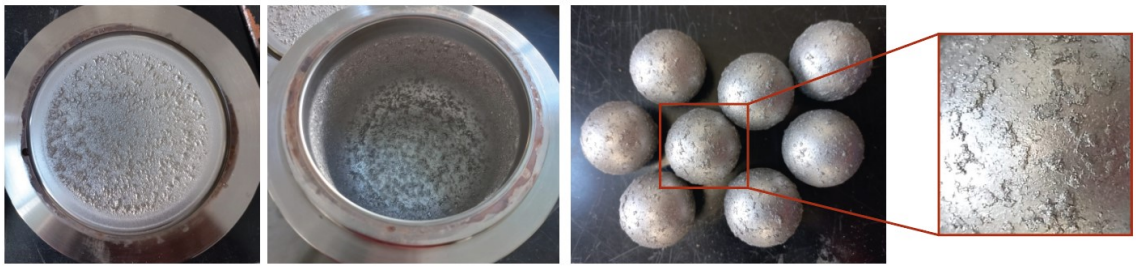

Figure 4.3: Overused lid, jar and 30mm grinding balls.

It is important to note that only the 30 mm balls (shown in Figure 4.3) suffered overuse while the 5mm spheres remained intact. This adhesion of the material to grind lowered the ease of mill since it reduced the hardness of the balls either by changing its surface material or by changing the geometry creating peaks and valleys on the balls surface.

Finally, the NP3 condition was developed with the aim of reprocessing powders of dimensions >212 μm left over from previous milling operations. Once again, in order to facilitate the industrialization of the process, the NP3 conditions are the same as the NP2 2nd stage parameters. Therefore, it was possible to obtain an average of 37% in wt.% of the resultant powder in the desired size range while an average of 62% remained with its size greater than 212 μm. Those results are presented on the yellow bars of Figure 4.1. This proves that 5 mm balls do not have the same ability to break down particles in comparison with the 30 mm balls. Therefore, to improve the amount of resultant powder in the desired size range, it should be necessary to run a 1st stage using 30mm balls. However, the NP3 results could be considered fairly satisfactory since, using a single stage and relatively fast procedure (3h15min), it was possible to obtain almost 40% (in wt %) of the resultant powder in the desired size range.

4.1.1.3 Overall productivity of the milling process

Giving the above presented results, only the NP2 powder was used as DED feedstock. The NP3 procedure was employed only to assess the strategy of reprocessing powders left over from pre-

vious milling operations and to investigate if a single 5mm balls stage would break down coarse particles. Therefore, the powder produced in NP3 conditions was not used as DED feedstock. The same applies to PN5 and PN3 powders since the production of those powders served to compare the efficiency and results of 2 different milling processes (disc and ball milling) and 3 different materials (AISI 301, AISI 303 and AISI P20+Ni)

In total, it was produced around 800g of NP2 powder in 10 runs, which represented an overall productivity of 67% regarding the wt % of resultant powder in the desired size range (38-212 μm). The total milling time was 86h40 (including break time).

4.1.2 Particle Size Distribution

Figures 4.4 to 4.8 present the Particle Size Distribution (PSD) of the powder produced in this work, according to the different milling conditions.

In those graphs it is possible to observe both the absolute frequency of particles for a determined size range as well as the cumulative frequency. To corroborate this data, the particles size values equivalent to 10%, 50% and 90% of cumulative frequency (commonly known as D10, D50 and D90) are presented in Table 4.2. This analysis was only carried out on previously sieved powder in the 38-212 μm size range.

Table 4.2: D10, D50 and D90 for powder produced according to different milling conditions.

Procedure	PSD [μm]		
	D10	D50	D90
Disc Milling PN5	120,7	190,0	299,0
Ball Milling PN3	64,5	90,6	146,3
Ball Milling NP2	55,6	94,3	152,3
Ball Milling NP2 with overused balls	65,2	139,5	214,7
Ball Milling NP3	68,4	130,0	202,3

As stated previously, the histograms presented below result from particles measurements on SEM micrographs, using the ImageJ software. It is important to note that, this procedure is not the most accurate for assessing PSD. For example. the laser diffraction method would be significantly more accurate since this technique analyzes the sample in volume, thus, it presents data from all the particles of the sample, in all the directions. However, there was no availability to assess the PSD through laser diffraction.

4.1.2.1 Disc Milling results

Firstly, it is important to recollect that only 80 particles produced in the PN5 disc milling conditions were measured since the majority of the particles in the SEM micrographs were inclined and due to the flaky shape of the particles, its dimensions were inaccurate. Moreover, in Figure 4.4, it is possible to observe particles larger than 212 μm that were able to flow vertically or diagonally

through the sieves apertures, due to their elongated shape. The PN5 powder was not the only sample in which these larger particles were observed although it was the sample that had the largest number of these particles, due to its very elongated shape.

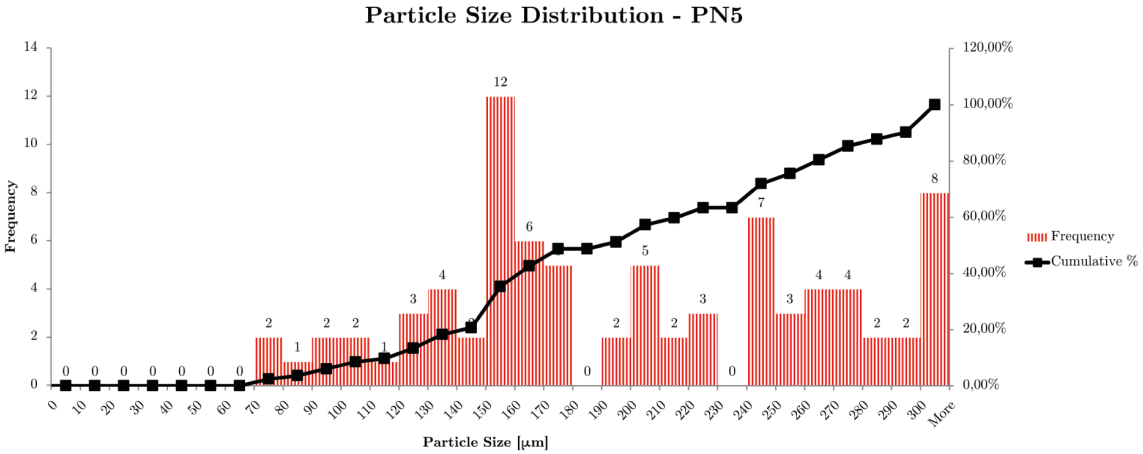

Figure 4.4: PSD of the powder produced through the PN5 disc milling conditions.

Moreover, from the obtained data, it is possible to observe that the disc milling PN5 condition hardly produced any powder smaller than 120 μm since the D10 value is 120 μm. This observation, together with the sieving results presented in the previous chapter, show that disc milling hinders the production of AISI 301 powder with dimensions below 100 μm, and is not a very effective process for producing powder for DED processing.

Regarding the results from Castanheira et al. (2024), who milled AISI 303 chips using the same procedure and the D10, D50 and D90 values (obtained by laser diffraction) are presented in Table 4.3. Those values were lower which corroborates the conclusion taken with the powder wt % results (Chapter 4.1.1.1), i.e. AISI 301 offers greater resistance to size reduction due to its greater toughness and ductility. The comparison with size distributions of AISI P20+Ni produced in PN5 conditions cannot be done since da Cunha (2023) did not perform this analysis for the powder produced via this procedure.

Table 4.3: D10, D50 and D90 for powder produced in the PN5 disc milling conditions - Comparison for 2 different materials.

PSD [μm] - Disc Milling PN5			
	D10	**D50**	**D90**
AISI 301	120	190	299
AISI 303 (Castanheira (2022))	35	110	268

4.1.2.2 Ball Milling results

Regarding the ball milling results, it is clear that this method is much more able to produce powder with dimensions below 100 μm, which is observed in the D10 values (around 60 μm), as seen in Table 4.2.

PN3 and NP2 results Both PN3 (Figure 4.5) and NP2 (Figure 4.6) produced powder very suitable for DED processing since the majority of the produced powder is in the 50-150 μm size range, which is considered the optimal particle size for DED. This is justified by the D10 and D90 values, which are respectively around 60 and 150 μm for both powders, as seen in Table 4.2.

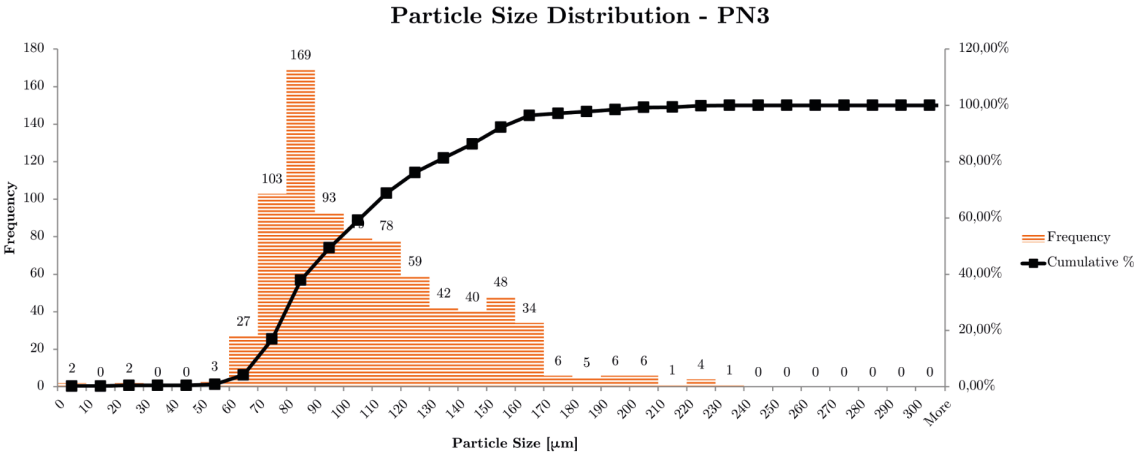

Figure 4.5: PSD of the powder produced through the PN3 ball milling conditions.

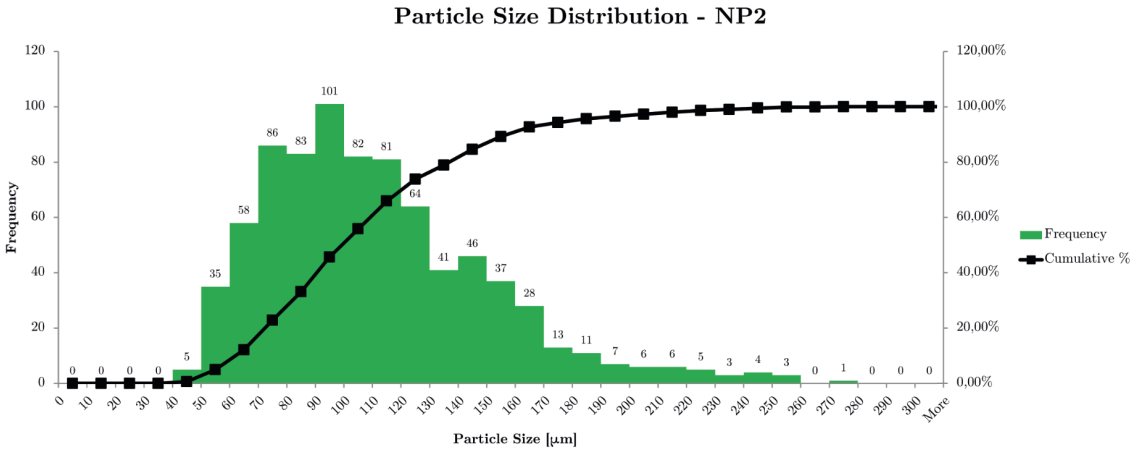

Figure 4.6: PSD of the powder produced through the NP2 ball milling conditions.

As stated above, the NP2 powder was produced in conditions originally developed in this work. Regarding its size distribution, the results were very positive since the majority of the produced powder is in the 50-150 μm size range, as seen in Figure 4.6 and Table 4.2. The only drawback in comparison with the PN3 condition is the less narrow size distribution (NP2 conditions lead to a greater number of particles with its sizes lower than 60 μm or greater than 170 μm). Besides that, the D10, D50 and D90 values for both PN3 and NP2 powders were very close, as seen in Table 4.2. Once again, this showed that the merge of the first two PN3 stages into the 1st NP2 stage (and a consequent elimination of a 30mm balls stage at 600rpm) did not have a significant effect on the final PSD.

Comparison of the same milling conditions for different materials The comparison of size distributions for powders produced in PN3 conditions for AISI P20+Ni cannot be done since da Cunha (2023) did not perform this analysis for the powder produced via this procedure.

Effect of the balls overuse on the PSD The balls overuse had a clear effect on the size distribution of the resultant particles. In comparison with the results from fresh balls (Figure 4.6), the distribution obtained using overused balls (Figure 4.7) became wider but only due to the greater number of larger particles because the number of particles smaller than 60 μm remained close to zero. This was also reflected in an increase in the values of D10, D50 and D90, as seen in the Table 4.2. Those results show that the adhesion of material to the 30mm balls negatively affects their ability to break down coarse particles. Besides that, the balls overused also lead to a more elongated shape of the particles since a considerable number of particles larger than 212 μm were measured (as stated above, those particles can only flow through the sieve apertures due to their elongated shape).

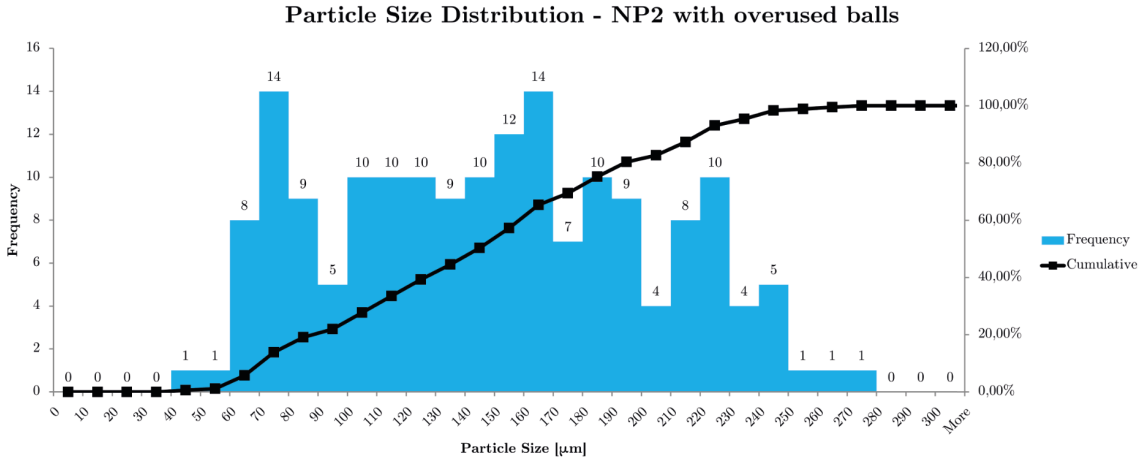

Figure 4.7: PSD of the powder produced through the NP2 ball milling conditions with overused balls.

NP3 results Lastly, the size distribution of powder produced in NP3 conditions (Figure 4.8) was very close to that of powder produced in NP2 conditions with overused balls (Figure 4.7). The distribution is wider due to the greater number of larger particles and, as consequence, the D10, D50 and D90, are also greater, as seen in Table 4.2. These results are in line with the milling productivity results since it is corroborated that 5mm balls hinder the break down of coarse particles. However, around 60% (in wt %) of the resultant powder has its size lower than 150 μm, which is a fairly satisfactory result since the NP3 procedure has a single stage and is relatively quick.

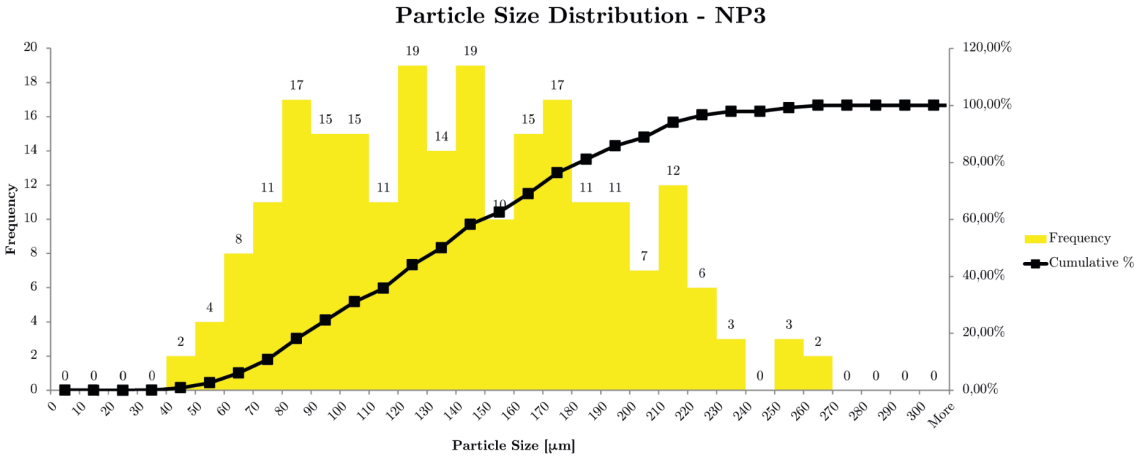

Figure 4.8: PSD of the powder produced through the NP3 ball milling conditions.

In general, the results show that 50 and 150 μm aperture sieves could have been employed and the productivity wouldn't have dropped substantially. This would have prevented the deposition of particles larger than 200 μm, which, a priori, would have improved the characteristics and properties of the powder but also the quality (mechanical properties and occurrence of defects) of the DED printings.

4.1.3 Particles Aspect Ratio, Size and Shape

The average aspect ratios and average particle sizes of the different powders produced in this work are presented in Table 4.4. Those results come from the the measurements on SEM micrographs using the ImageJ software and, as was the case with the size distribution analysis, this assessment was only carried out on previously sieved powder in the 38-212 μm. Along the discussion, the SEM micrographs of produced powder are also presented, in order to assess the particles shape and to support the drawn conclusions. For simplicity, only one micrograph of each powder (the one considered most representative) is presented although, for all powder samples, at least 5 different micrographs were obtained. All those micrographs can be found in Annex D.

Table 4.4: Aspect Ratio and Average Particle Size results according to different milling conditions.

Procedure	Aspect Ratio (Average ± Standard Deviation)	Powder Particle Size (Average ± Standard Deviation)
Disc Milling PN5	1,85 ± 0,61	204,3 ± 74,6
Ball Milling PN3	1,46 ± 0,57	98,7 ± 32,9
Ball Milling NP2	1,52 ± 0,62	101,1 ± 39,3
Ball Milling NP2 with overused balls	1,46 ± 0,34	138,6 ± 53,7
Ball Milling NP3	1,53 ± 0,55	132,1 ± 49,8

4.1.3.1 Disc Milling results

Regarding the disc milling results, it is clear that the aspect ratio and average particle size values of the PN5 produced powder are significantly higher than those relative to the ball milled powder. The high aspect ratio (1,85) is expected since disc milling produces powder with an elongated, irregular and flaky-like shape, which is possible to observe in Figure 4.9. The high average particle size (204 μm) is also expected due to the previously shown results of PSD (Figure 4.4). Once again, this data corroborates the conclusions that disc milling hinders the production of AISI 301 powder with dimensions below 100 μm, and is not a very effective process for producing powder for DED processing.

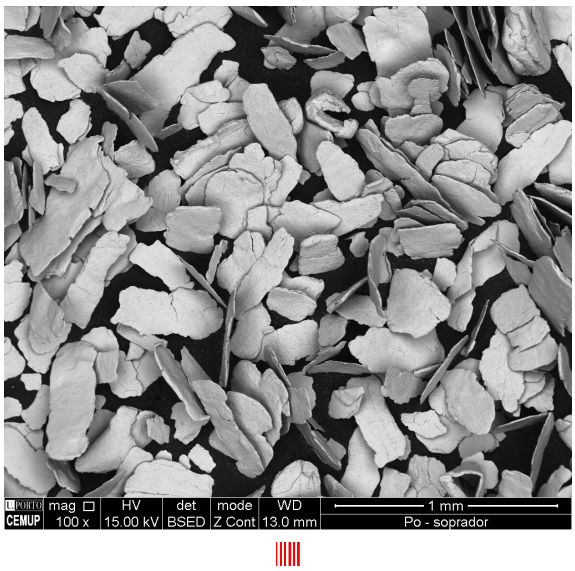

Figure 4.9: SEM micrograph of particles in the 38-212 μm size range produced in disc milling PN5 conditions.

In the PN5 powder micrographs, it was also possible to observe some cases of cold welding, i.e. fragmentation and later bonding of smaller particles, helped by the significant pressure applied between powder particles during the milling process.

Comparison of the same milling conditions for different materials Both Castanheira (2022) and da Cunha (2023) also obtained elongated, irregular and flaky-like particles by milling AISI 303 and AISI P20+Ni chips, respectively. The AISI 303 powder showed a greater thickness, which is due to the higher occurrence of the cold welding phenomenon. As stated earlier, more ductile materials are more prone to cold welding. In Chapter 4.1.1.1, although the data from the Granta EduPack software showed that AISI 303 may be, in some cases, more ductile than AISI 301, the analysis of various datasheets from stainless steels suppliers showed that usually AISI 301 is more ductile (in the majority of the cases AISI 301 datasheets presents higher elongation values). Therefore, this result (greater occurrence of cold welding) may lead to the hypothesis that the AISI 303 steel processed by Castanheira (2022) may be more ductile than the AISI 301 steel studied in the present work.

The comparison of aspect ratio and average particle size for powders produced in PN5 conditions for AISI 303 AISI P20+Ni cannot be done since da Cunha (2023) and Castanheira (2022) did not perform this analysis for the powder produced via this procedure.

4.1.3.2 Ball milling results

After the powder observation by SEM, it was clear that ball milling produces powders with a more spherical shape, thus coming closer to powders produced by conventional technologies such as atomization. For instance, Figure 4.10 presents a micrograph of particles in the 38-212 μm size range produced by the ball milling PN3 conditions, in which is possible to observe the particle shape (mainly approaching rounded with some flaky-like particles).

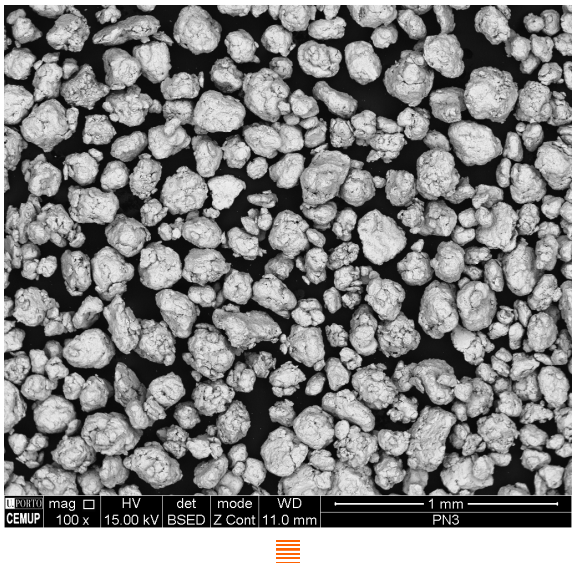

Figure 4.10: SEM micrograph of particles in the 38-212 μm size range produced in the ball milling PN3 conditions

This shape is reflected in the aspect ratios, which revolve around 1.5 for powders produced under any ball milling conditions, as seen in Table 4.4. Therefore, this data shows the ball milling

process is a stable process, capable of producing particles with similar shape and aspect ratio regularly, even when changing milling parameters.

The average particle sizes of both PN3 and NP2 were also very close (around 100μm). This showed that the merge of the 2 first PN3 stages into the 1st NP2 stage (and a consequent elimination of a 30mm balls stage at 600 rpm) did not have a significant effect on aspect ratio or average particles size.

Regarding the powder produced in the other ball milling conditions (NP2 with overused balls and NP3), although the aspect ratios were similar (around 1,5), the average particle size rose to around 130 μm. This information is in line with the size distributions (Figures 4.7 and 4.8) which show a greater number of particles with larger dimensions.

Comparison of the same milling conditions for different materials The comparison of aspect ratio and average particle size for powders produced in PN3 conditions for AISI P20+Ni cannot be done since da Cunha (2023) did not perform this analysis for the powder produced via this procedure. However, the authors presented SEM micrographs of this powder and the particles shape was similar. In both cases, the majority of the particles had shapes approaching rounded but some flaky-like particles were still observed.

Microporosities Besides the SEM observation, the powder samples produced in conditions originally developed in this work, were also observed in an optical microscope after being polished. The goal of this analysis was to assess the presence of possible microporosities. Those features were identified in the AISI P20+Ni powder produced by da Cunha (2023) through ball milling as well as in the AISI 301 powder produced in this work (in both NP2 and NP3 conditions). Castanheira (2022) also observed those microporosities on the AISI 303 disc milled powder but in a significantly lower frequency, which is expected due to the different mechanisms involved in this milling method. The microporosities are expected in the ball milled powders since, in this milling method, the particles suffer repetitive and high-energy impacts with the milling balls, resulting in the particles fracturing. Therefore, it is conceivable for minute voids or microporosities to emerge within the particles. Those pores may also appear at the interfaces between particles united through the cold welding phenomenon, due to insufficient milling energy which led to poor bonding of the 2 particles. In addition, the signs of the cold welding phenomenon are very present in the powder samples produced by ball milling, which indicates that this method induces this phenomenon to a greater extent. It is expected that those microporosities voids remain in the final printings, forming porosities and promoting the formation of oxides in those voids, which is undesirable. This aspect arises as a disadvantage of the employment of planetary ball milling for the production of DED feedstock powder, in comparison with disc milling.

The Figures 4.11 to 4.13 present micrographs of the AISI 301 powder produced through ball milling in the NP2, NP2 with overused balls and NP3 conditions, respectively. In those 3 Figures, the micrographs labeled a) present SEM images of the resultant powder in the 38-212 μm size

range, while the micrographs labeled b) present images of the same powder but polished and observed in an optical microscope, in order to assess the presence of voids or microporosities.

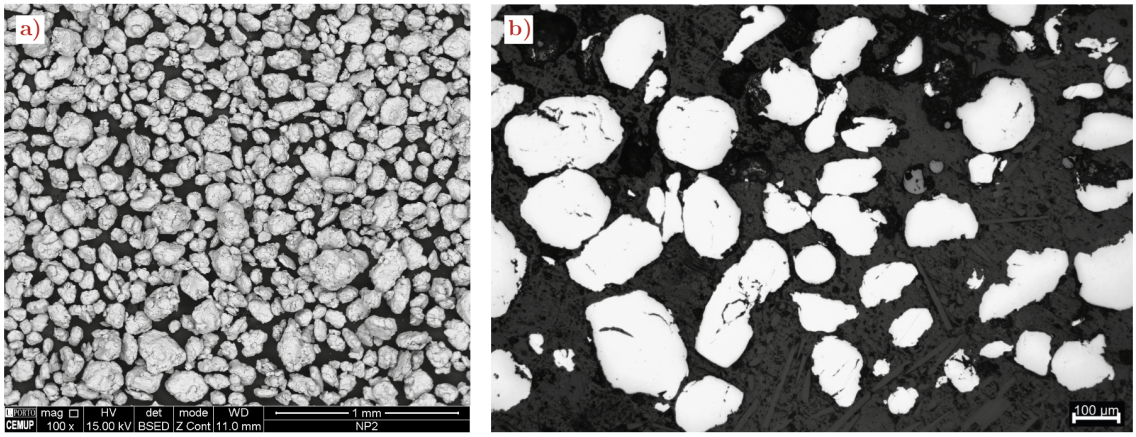

Figure 4.11: Micrographs of: a) particles in the 38-212 μm size range produced in the ball milling NP2 conditions (SEM image); b) polished particles in the 38-212 μm size range produced in the ball milling NP conditions (observed in an optical microscope).

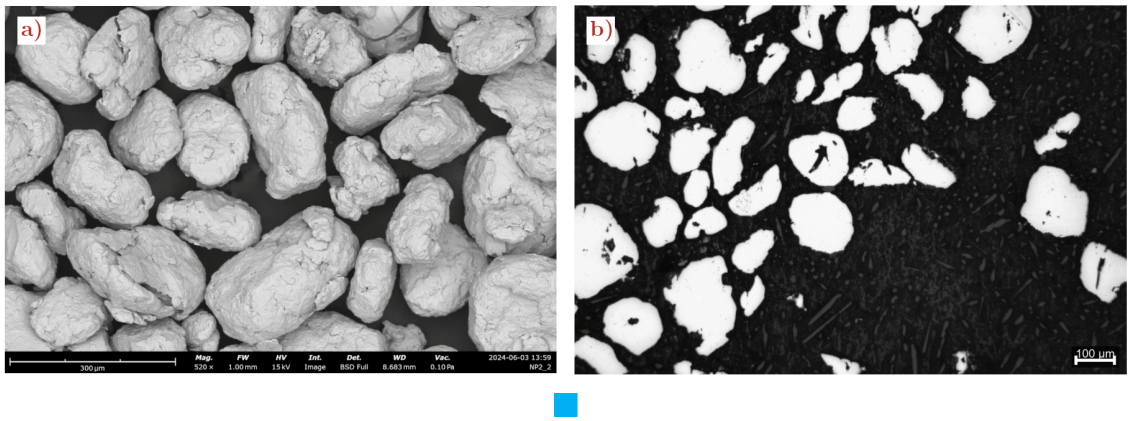

Figure 4.12: Micrographs of: a) particles in the 38-212 μm size range produced in the ball milling NP2 wigh overused balls conditions (SEM image); b) polished particles in the 38-212 μm size range produced in the ball milling NP2 with overused balls conditions (observed in an optical microscope).

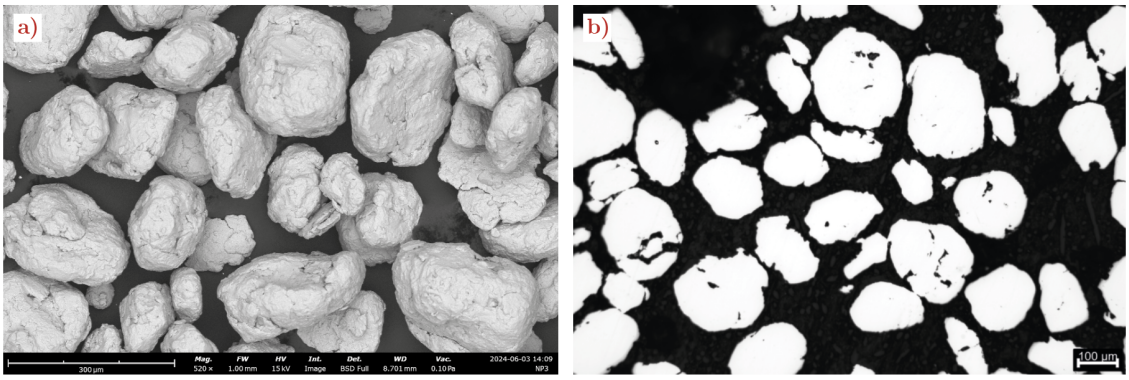

Figure 4.13: Micrographs of: a) particles in the 38-212 μm size range produced in the ball milling NP3 conditions (SEM image); b) polished particles in the 38-212 μm size range produced in the ball milling NP3 conditions (observed in an optical microscope).

From those micrographs, it possible to draw some conclusions. Firstly, the narrower PSD of PN3 powder (Figure 4.5) is visible in the micrographs, since the majority of the particles have similar sizes. Contrarily, in the NP2 micrographs, it is possible to observe a greater number of smaller particles (which is according to the NP2 PSD (Figure 4.6) and its lower D10 value (55 μm) (Table 4.2)).

Finally, it seems that the particles produced in the NP2 with overused balls and NP3 conditions had lower surface roughness. However, this conclusion cannot be certain since the powders produced in those 2 conditions were observed in different SEM equipment, using a different magnification, in comparison with the powders produced in PN3 and NP2 conditions.

Anyway, the lower surface roughness in the NP3 particles may be explained by the fact that only 5mm balls were used since the major role of those smaller balls is the particles rounding and not their fragmentation (which would lead to cold welding and consequently a more rough surface). Nevertheless, in the NP3 samples, it is possible to observe some cold welding marks which were probably already in the initial particles, since the feedstock in this procedure is powder which has already been milled but whose dimensions are larger than 212 μm. In the case of the NP2 with overused balls sample, the lower surface roughness may be explained by most successful cold welding.

4.1.4 Density and Flowability Measurements

Figure 4.14 presents the average values of the tap density, loose density and flowability measurements. Those results are also presented below in Table 4.5 alongside the standard deviation values.

As stated above, the initial idea of this work was to study the AISI 316L stainless steel and not the AISI 301. For that reason, AISI 316L commercial powder (produced by gas atomization and supplied by Sandvik Materials Technology (2024)) was also assessed to serve as benchmark for the upcycled powder.

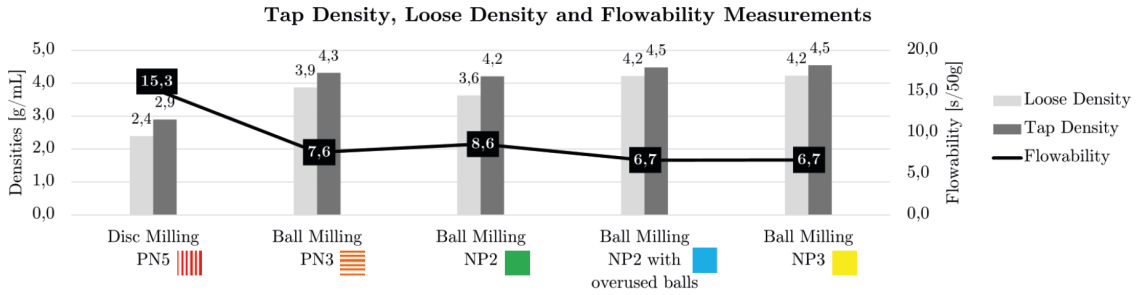

Figure 4.14: Tap Density, Loose Density and Flowability results in mean values.

From a general point of view, it possible to observe that the multiple ball milling procedures led to similar values of tap density, loose density and flowability. This observation corroborates the statement presented above in Chapter 4.1.3.2 that ball milling is a stable process, capable of producing particles with uniform properties even when changing milling parameters.

4.1.4.1 Tap and Loose Densities

Firstly, it is possible to observe that the higher values of density are directly associated with the better flowability values. This is expected since higher densities leads to a better particle packaging (Neikov et al. (2019)). Besides that, all the tap density values are greater than loose density values, as anticipated since, in the loose state, the particles are less compacted and have more void spaces between them. Those voids allow more air or empty space within the material, leading to a lower density measurement. When the material is tapped or vibrated, these void spaces are reduced, resulting in a higher density measurement.

The PN5 powder produced by disc milling showed the worst tap and loose density values, which is expectable due to the flattened shape of the particles and their larger dimensions. The AISI 303 powders produced by Castanheira (2022) through the same PN5 disc milling condition presented better loose and tap densities values (2,9 and 3,6 for loose and tap densities, respectively). This is attributed to the wider PSD of the AISI 303 powder, as seen earlier in Table 4.3. The AISI P20+Ni powders produced by da Cunha (2023) in the same PN5 disc milling condition also presented better loose and tap densities values (3,0 and 4,0), which is also justified by a wider PSD. The comparison with the tap and loose density of AISI P20+Ni powders produced in the PN3 conditions cannot be done since da Cunha (2023) did not perform this test.

Table 4.5: Average and standard deviation values from the tap density, loose density and flowability measurements.

Milling Procedures		Disc Milling PN5	Ball Milling PN3	Ball Milling NP2	Ball Milling NP2 (with overused balls)	Ball Milling NP3	AISI 316L atomized powder
Loose Density	Average and Standard Deviation	2.39 ± 0.13	3.87 ± 0.04	3.63 ± 0.04	4.22 ± 0.04	4.23 ± 0.03	4.35 ± 0.03
Tap Density	Average and Standard Deviation	2.90 ± 0.03	4.31 ± 0.03	4.21 ± 0.04	4.48 ± 0.03	4.55 ± 0.03	4.85 ± 0.02
Flowability	Average and Standard Deviation	15.32 ± 0.07	7.61 ± 0.00	8.61 ± 0.10	6.66 ± 0.17	6.6 ± 0.07	5.7 ±7 0.08

The tap and loose densities values of the ball milled powder are substantially superior. All four powder samples had roughly comparable density values, which was expected given the same particle shapes (close to spherical). The PSD also effects loose and tap densities, by the adjustment of particles in void interspaces. The relationship between PSD and powder density is illustrated in the Figure 4.15. The schematic shows that, until a certain point, a wider PSD leads to greater density values since the powder packaging ability increases. This may explain why the powder produced in the NP2 with overused balls and NP3 conditions presented greater density values. Those 2 powder samples, although presented a greater number of larger particles (represented by higher values of both average particle size and D90), had a wider PSD which may led to better powder packaging due to the adjustment of particles in void interspaces.

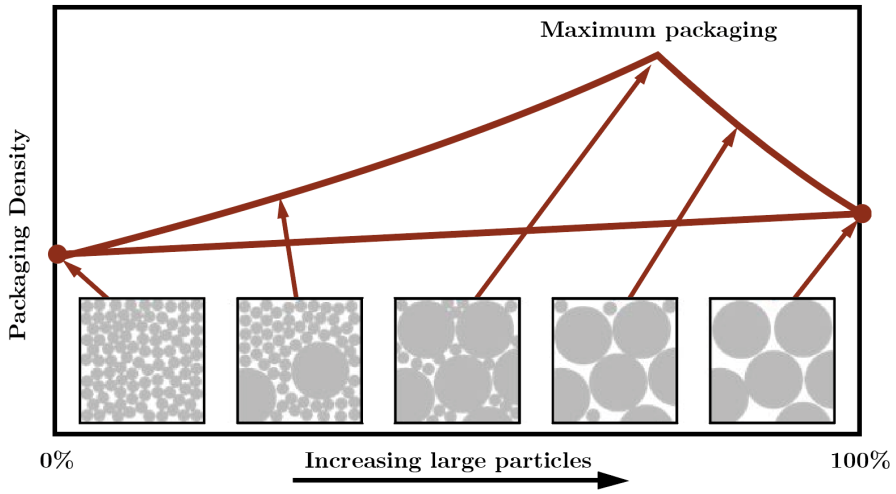

Figure 4.15: Evolution of the packaging density according to proportion between smaller and larger particles (adapted from Ddungu (2020)).

4.1.4.2 Flowability

Regarding the flowability results, it is possible to observe that the PN5 disc milled powder had the greatest value of all the results, as expected due to the greater particles size and flattened particle shape which leads to more interlocking and friction between particles. The AISI 303 and AISI P20+Ni powders produced by Castanheira (2022) and da Cunha (2023), respectively, in the same PN5 disc milling condition presented worst flowability (18,2 and 19,40 respectively). This is not expected since those powders showed better densities values. However, both Castanheira (2022) and da Cunha (2023) did not use the exact same apparatus for the flowability measurements, which may explain these results.

On the other hand, as was the case with the densities results, the flowability of the ball milled powder is significantly superior. Once again, all four powder samples presented relatively similar flowability values, which is expected since all the samples presented similar particle shapes (approaching spherical).

The PSDs also influence flowability since narrower distributions ususally lead to better flowability results (David L. Bourell and Seifi (2020c)). This was the case for the PN3 and NP2 samples since the PN3 powder presented a narrower distribution and a better flowability. However, the powder produced in NP2 with overused balls and NP3 conditions, should had a worst flowability (due to the wider PSD) which is not the case. Nevertheless, the possible lower surface roughness of these particles (this hypothesis was presented above in Chapter 4.1.3.2) could justify these values.

The comparison of the flowability values of powders produced in PN3 conditions for both AISI 301 and AISI P20+Ni cannot be done since da Cunha (2023) did not perform this test on this powder.

It is important to note that the flowability results are crucial since they can represent a constraint when depositing the powder, by imposing a maximum limit on the powder feed rate. As stated in Chapter 3.2.3.1, before any deposition, it is necessary to perform a material linearization in order to achieve a linear correlation between the powder flow rate and the nozzle valve aperture. In this work, the DED equipment was able to deliver a maximum of 31,9g/min of upcycled AISI 301 powder (as seen in Figure 3.10). However, Castanheira (2022), using the same equipment, only achieved a maximum powder feed rate of 7,42 which limited the DED parametrization process in that work.

4.1.4.3 Comparison with gas atomized powder

Although AISI 301 and AISI 316L differ in chemical composition, a comparison can be made between upcycled AISI 301 powder and commercial AISI 316L powder in terms of density and flowability measurements, since those characteristics only depend on the particle shape and size, surface roughness and size distribution.

As stated above, Table 4.5 presents the obtained results for the densities and flowability measurements of the AISI 316L commercial powder. Those results show that the powder produced

in this work through ball milling came very close to the commercial one, in terms of density and flowability, which represents a very positive outcome.

4.2 Printings Assessment

This section presents and discusses all the obtained results regarding the DED processing of upcycled AISI 301 powder and the subsequent assessment of the printings, namely top view and cross section analysis, microstructure and chemical analysis and microhardness and tensile testing.

4.2.1 Top view and cross section analysis

4.2.1.1 Parametrization

Top view Figure 4.16 presents the top view of the lines 1 to 12 which were all result of depositions of upcycled powder.

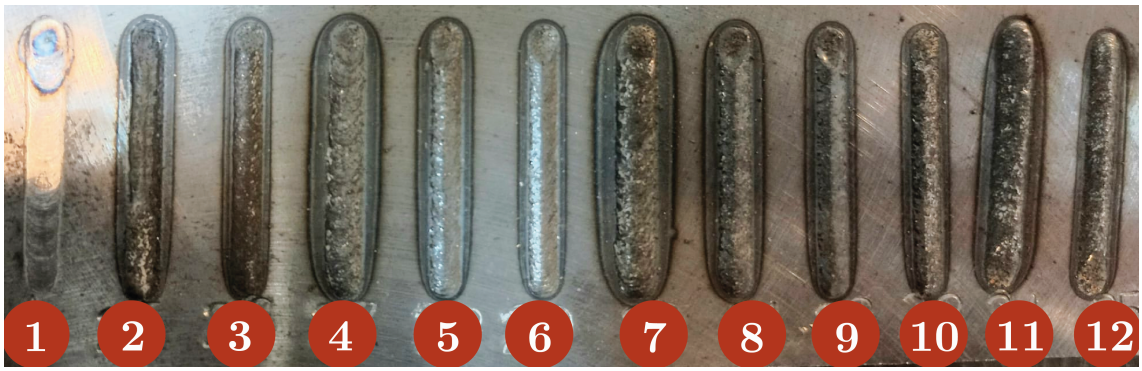

Figure 4.16: Top views of printed lines 24 to 35.

Firstly, lines 1 and 2 are invalid since the system failed to release powder. This malfunction happened because, at time of printing, the powder was already circulating in the system, flowing from the hoppers to the nozzle head. Thus, the control system considered that the feeding process was operational, i.e powder was being released though the nozzle. However, since those were the first printings, there was not enough time for the powder to reach the nozzle. Therefore, in line 1 the deposition was nonexistent and, in line 2, the track was very thin and irregular. From lines 3 to 12, no malfunction of any kind was detected. Since the results from lines 3 to 12 were very satisfactory, it was decided that there was no need to deposit again the lines 1 and 2, mainly because the 2 tracks were deposited with 1600W such as the line 3 that was not very successful while the other tracks printed with higher laser power values looked preferential.

From the top view analysis, it is possible to state that lines 3 to 12 are relatively uniform, linear and homogeneous. Lines 6, 9 and 5 stood-out for being the most uniform. On the other hand, all the lines have unmelted particles on the surface which leads to a high surface roughness typical of DED prints.

The lines 4 and 7 are the most irregular, as can be seen by their wavy pattern on the top surface. The same 4 and 7 lines also stood out for their greater width and larger HAZ. The greater width can be advantageous depending on the thickness of the structure to be built but the larger HAZ is not desired, since it can be a sign of excessive heat input. The results of those 2 lines were

expected since those are the ones with higher GED, as seen in Table **??**. However, those high GED lines presented a rougher surface bead. On the other hand, lines associated to lower GED values (3, 6 and 9 to 11) were thinner and more linear.

Lines 5 and 6 stood out for their non-oxidated and metallic aspect, represented by their greyish color. The other lines are darker due to the presence of slag and indicate an oxidized surface and consequently, a higher presence of oxides. The slag is composed of oxides and other compounds that result from the reaction between the metal material being deposited and atmospheric gases or impurities in the substrate. The metallic aspect of lines 5 and 6 is desired since a non-metallic top surface is inconvenient when depositing multi-layered printings because since it can affect the wetability and dilution of the following layers.

Cross Section After the top view analysis, the cross sections of those lines were analyzed and the respective micrographs are presented in Figure 4.17.

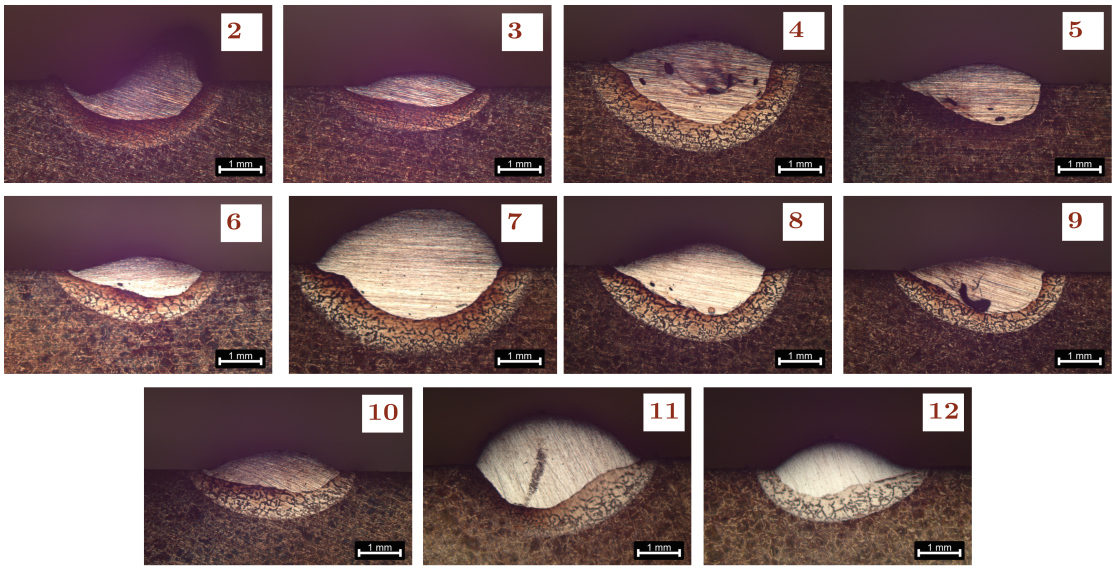

Figure 4.17: Cross section views of lines 2 to 12.

The geometric parameters of those lines were measured using the software ImageJ, and are presented in the Table 4.6.

Table 4.6: Geometrical measurement results of the lines 3 to 12.

Line	w [m]	d [m]	h [m]	Am [m^2]	Ap [m^2]	Dilution [%]	Right Wetting angle [θ] [º]	Left Wetting angle [θ] [º]	Average Wetting angle [θ] [º]
3	2996	485	**365**	885193	525814	**63%**	34	32	**33**
4	3685	1398	**515**	3426227	1077190	**76%**	22	27	**25**
5	3208	946	**485**	1958162	953473	**67%**	49	19	**34**
6	3004	625	**353**	1170900	569201	**67%**	33	15	**24**
7	4170	1249	**1264**	3433339	3654506	**48%**	69	47	**58**
8	3461	1058	**594**	2356929	1111714	**68%**	15	37	**26**
9	3125	948	**388**	1955356	615298	**76%**	29	15	**22**
10	3103	480	**503**	924548	945310	**49%**	40	27	**33**
11	3683	1032	**1001**	2150246	2556701	**46%**	48	65	**57**
12	3141	649	**647**	1144198	1105368	**51%**	38	40	**39**

With those results, it was necessary to choose one of those sets of parameters to continue the depositions. The lines 3 to 6 and 8 to 10 were excluded due to their low bead height. This lack of height may be caused by high scanning speeds (lines 3, 6, 9 and 10), low powder feed rates (lines 6 and 8) or low laser power (line 3).

Moreover, it was possible to observe some defects such as porosities (lines 4, 5 and 8) and lack of fusion at the interface (line 9). Those internal defects highlight the importance of analyzing the cross sections since top view analysis do not allow their detection.

Therefore the lines 7, 11 and 12 remained and the line 7 stood out by having larger bead and no defects. However, the line 7 presented a melt pool a little asymmetrical, which is not desired. This asymmetry was also observed in other lines (for example 8 or 11) and it may come from misalignment of the laser optics. However, since this malfunction was not severe and the DED equipment availability was short, the depositions continued. Besides that, the dilution of line 7 was 48% which represents a value well above that which would be sufficient to guarantee a proper metallurgical bonding to the substrate or printed layer underneath (30%). Nevertheless, the dilution is not an impactful factor here for 2 reasons: (1) all tracks presented a high dilution value, ranging from 45% to 76% and (2) a dilution of 48% is more than enough to induce a deep remelting of the printed layer underneath, in the case of the depositions of successive stacked layers in thin wall structures.

Having those aspects in mind, the line 30 was chosen as optimized set of parameters for the depositions of upcycled powder. This choice comes mainly from the high productivity of this line, as seen by its width and height, which were the greatest from these 11 tracks. The optimization of parameters could have been refined in order to try to achieve a set of parameters that would lead to a lower dilution while maintaining the clad height and producing a track with a more metallic aspect (without an oxidated surface). However, this parametrization process was not continued since the amount of upcycled powder available was limited and the use of the DED equipment was constrained by other works at INEGI and by the deadline of this work.

4.2.1.2 Thin walls printings

Having the printing parameters selected (2400W, 5mm/s and 10g/min), the next stage was the printing of the thin-walled structures in order to obtain specimens for tensile testing. However, as stated in Chapter 3.2.3.2, when printing multi-layer depositions, it is necessary to study other parameters such as toolpath strategy, idle time between layers and overlap ratio.

Regarding the toolpath, it was known from the bibliographic review and from past experience that a wall should be printed with printing directions alternating between layers, as represented in Figure 4.18a). Otherwise, it is very probable to have overmelted zones and to occur warping on the top surface, due to the formation of deep melt pools and consequent excessive thermal energy buildup. In extreme cases, this warping may even led to a separation of the printing from substrate, as seen in Figure 4.18b). Moreover, it is known from previous works, that if if the printing directions do not alternate between layers, the wall would have irregular height with one side of the wall being considerably higher.

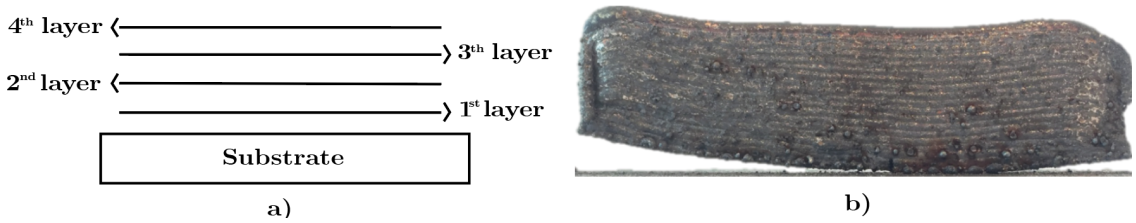

Figure 4.18: a) Tool path employed; b) Warping and separation from substrate (adapted from Miedzinski).

The alternation of building directions in this toolpath strategy would led to the creation of better heat dissipation paths, which is desired. However, the employment of this tool path strategy may not alone ensure a proper heat dissipation of the printing. Therefore, sometimes it is necessary to implement an idle time between consecutive printings. Previous experience with AISI 316L commercial powder also showed that, the absence of idle time did not allow for construction at height. Figure 4.19 compares the height of 2 single layer depositions with a 5 layer and a 10 layer depositions and shows that, due to the non-existent idle time, the height of the multi-layered structures was well above expected, due to the deep melt pools created. Besides that, the height of those multi-layer printings was not uniform since, on both walls, a valley was observed in the middle of the wall's top surfaces.

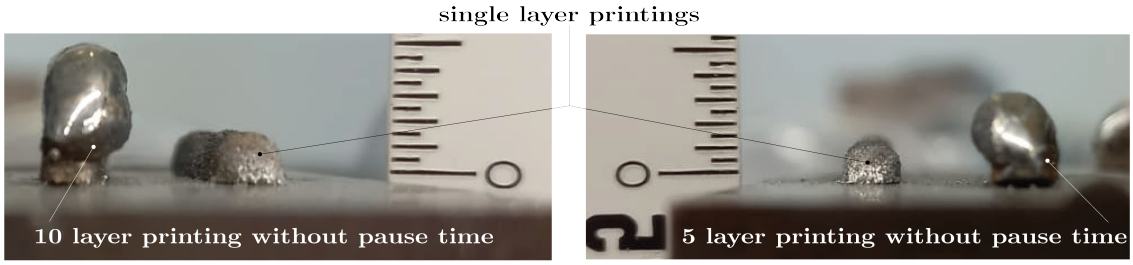

Figure 4.19: Single and multi layer printings performed with AISI 316L commercial powder.

It is important to note that those defects occur because the performed printings are small (tracks of 35mm). When printing large parts (which is totally suitable for DED), by the time a deposition occurs on a previously deposited structure, the temperature of the printed material has already dropped significantly thus the idle time would not be necessary. Other method to eliminate the need of idle time is to have variable DED parameters (especially laser power) throughout the deposition. This can be achieved by either by trial and error experiments or by the implementation of closed-loop control systems (to monitor the melt pool size, shape and temperature) that automatically adjust the DED parameters in real time (Akbari and Kovacevic (2019)). However, since these monitoring technologies are not available at INEGI, this solution was not possible.

Having this in mind, it was decided that, since the amount of upcycled powder was limited, the printing strategy should be conservative, in order to not waste powder on walls that would not have enough height for the extraction of tensile specimens. Therefore, it was decided to implement a 5 minute break between consecutive layers. The choice of this idle time came from previous experience of DED performance at INEGI.

The only parameter that was left to decided was the overlap ratio. As seen above in Figure 4.17 and Table 4.6, the employed parameters (corresponding to those of line 30) led to a significantly high dilution (48%). Therefore, it was admitted that a 0% vertical overlap would be enough to ensure proper bonding between adjacent layers. Therefore, the 1st thin wall was printed with an increment of the nozzle head in the z-axis of 1,2mm, which was the height of the line 30 (as seen above in Table 4.6). In order to ensure this height was correct, the deposition of line 30 was repeated. The height of these 2 lines was then measured in multiple points and the height was uniform and equal to 1,2mm.

Having the parameters selected and the layer height confirmed, it was necessary to calculate the number of layers required to achieve the desired wall dimensions, i.e the dimensions that would allow the extraction of tensile specimens from the thin wall (according to the schematic showed earlier in Figure 3.16). It is know from the bibliographic review (Chapter 2.3.1.3) that DED produced samples build in the parallel direction to the substrate led to highest mechanical properties due to the greater metallurgical bonding of these samples along the tensile direction. Therefore it was decided to print thin wall structures that would allow the extraction of horizontal specimens from the walls.

Since the specimens are 30mm high and 15mm wide, the idea was to build a wall with 35mm of length and 25mm of height. The extra 5mm on the length represent a safety margin which do not need to be very high since, usually, the length of DED printings is uniform and do not present any major deviations from the expected. On the other hand, the height of DED printings is affected by the overlapping in the z-axis and heat accumulation. Moreover, the efficiency of powder melting and the presence of spatters also affect the building efficiency. The height of DED depends on the distances between the top surface of the previously deposited layer, the spot size plane and the nozzle head height. Those distances may vary during the multi-layered deposition process so the expected height of a final DED printing is usually not equal to the resulting height. Therefore, the thin wall was projected to have a height of 25mm, in order to have a 10mm safety

margin, which would be more reliable. Having that in mind, the wall was printed in a 21 layer deposition since, theoretically, that would lead to a height of 25,2mm, considering a layer height of 1,2mm ($21 \cdot 1.2 = 25,2$mm).

In order to confirm that the 0% vertical overlap was enough to ensure proper bonding between adjacent layers, the 1st printed wall was cut and its cross section was inspected in order to assess any lack of fusion defects. As will be shown later, the bonding between adjacent layers was satisfactory using an overlap ratio of 0% thus the DED parameters were fully selected and the depositions of other walls could be pursued.

Figure 4.20 presents the 1st printed wall. From these images it is possible to see that the side surfaces of the wall look burned out and oxidized. This aspect is attributed to the high tendency of upcycled powder to react with Oxygen. Moreover, the surfaces were also very rough, although after observing the transversal cross section, is was observed that this aspect was only superficial. The high surface roughness is attributed to the characteristics of upcycled powder, namely the particles shape and the wider PSD. This is not commonly observed in commercial (gas atomized) powder depositions since those particles are spherical and have a thinner PSD (50-150 μm).



Figure 4.20: 1st printed wall.

The measured height of the 1st wall was 4mm higher than the expected one, as presented in Table 4.7 and Figure 4.21. Therefore, the number of layers for the 2nd and 3rd walls needed to be altered. The new layer height was recalculated (as seen in Table 4.7) and a new number of layers was estimated. Then, the 2nd and 3rd walls were printed and their height were measured. The height of the 2nd and 3rd walls was considerably different from the expected and from each other. The understanding of those discrepancies needed further study of this subject, which was not the focus of this work. However, it was noted that, predicting the final height of a DED produced structure with upcycled powder was more challenging than with commercial powder.

Table 4.7: Calculation of the number of layers for each wall and measurements of the wall dimensions.

Wall nº	Z-axis increment [mm]	Number of layers	Expected height [mm]	Measured Height [mm]	Measured Length [mm]
1	1,2	25 ÷ 1,2 = 20,8 ≈ **21**	21 · 1,2 = **25,2**	29	36
2	29 ÷ 21 = **1,38**	20 ÷ 1,38 = 14,49 ≈ **15**	20,7	19	35
3				24	34

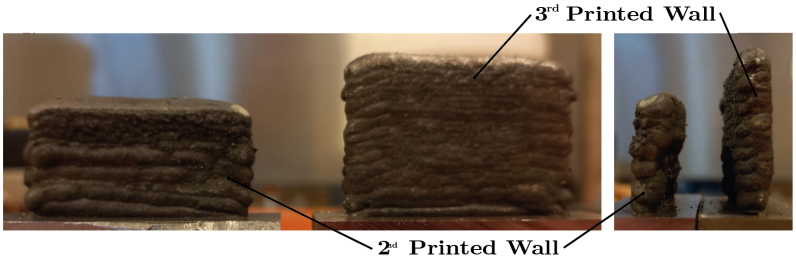

Figure 4.21: 2nd and 3rd printed walls.

The Figures 4.22 and 4.23 show the 2nd and 3rd printed thin walls. Those walls also presented very rough side surfaces and some burnt-out marks. Moreover, the aspect of the 2 side surfaces of the 3rd wall was considerably different which may come from the laser misalignment which leads to a greater heat input in one side of the wall.

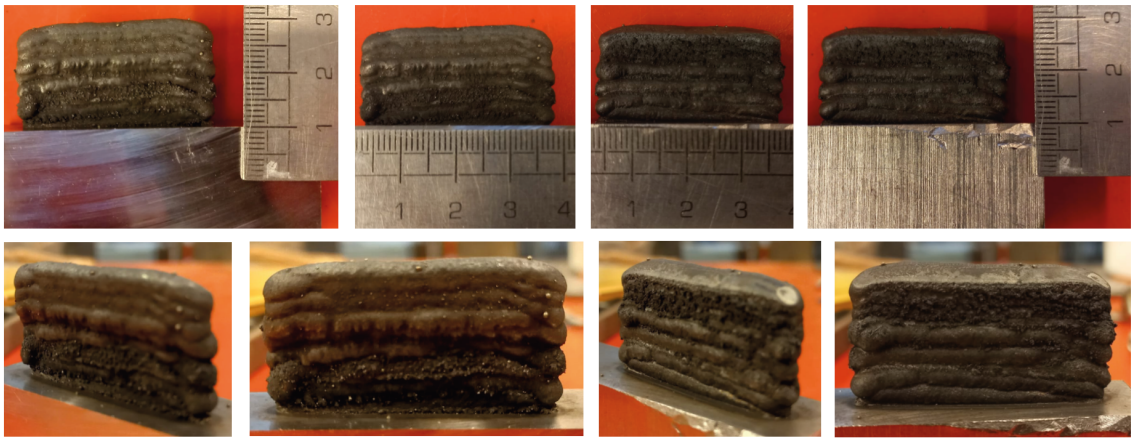

Figure 4.22: 2nd printed wall.

As stated earlier, after the deposition of the 1st thin wall, the printed structure was cut and its cross section was inspected in order to assess any lack of fusion defects. The micrograph of that wall is presented in Figure 4.24 and it is possible to see a clear and considerable dilution between consecutive printed layers, as desired. However, the dilutions areas are not uniform for all the layers.

Moreover it is possible to observe 2 discontinuities (most probably lack of fusion defects) at the interfaces of subsequent layers, as highlighted in the Figure 4.24. However, since those discontinuities occurred at interfaces of subsequent layers, they can also be inclusions formed due to the oxidation in the underneath layer which lead to a worst wetability and adhesion of the deposited layer.

In Figure 4.24, it is also possible to observe asymmetrical dilution areas, which, as stated above, came from a misalignment in the laser optics. Additionally, it is seen that the wall is not fully vertical, which may come from the same reason. The wall is also thinner at the bottom which may be explained by the fact that the first layers were printed on a non-preheated substrate and

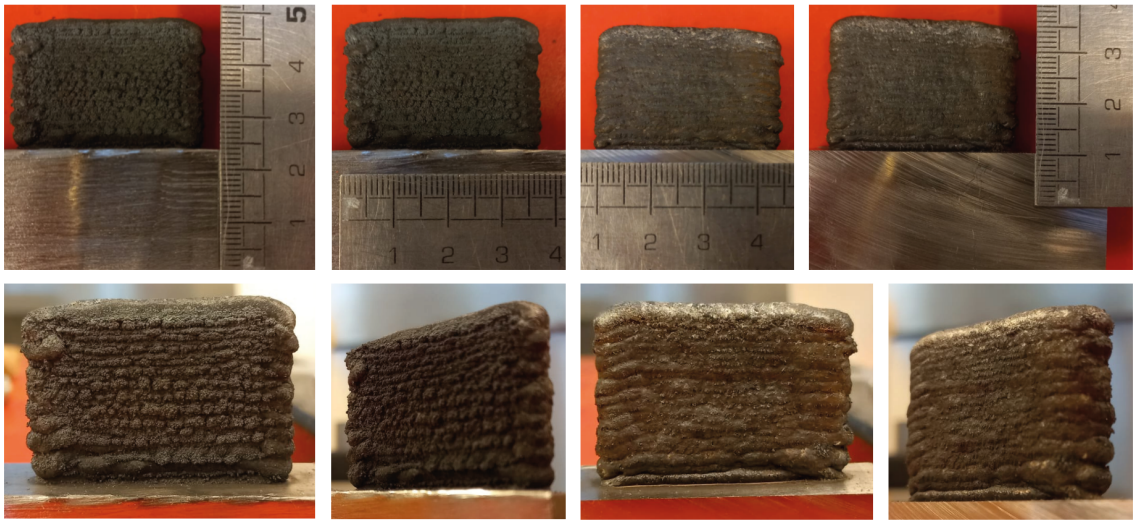

Figure 4.23: 3rd printed wall.



Figure 4.24: Macrograph of the 1st printed wall (observed under an optical microscope).

thus the thermal energy supplied by the laser probably was not sufficient to melt as much powder as the powder was melted in the following layers.

The macrograph of the 1st thin wall observed in Figure 4.25 was also obtained. This Figure is shown in greater detail in Annex E. In this Figure, besides the previously mentioned aspects, it is also possible to see the high amount of inclusions in the wall.

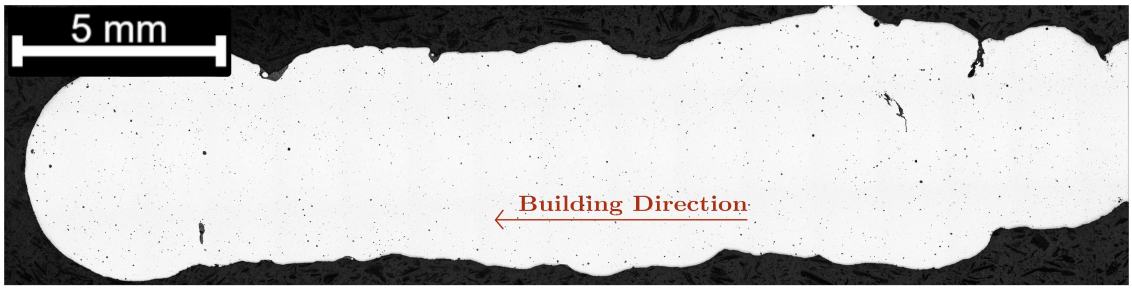

Figure 4.25: Macrograph of the 1st printed wall (observed under an optical microscope).

4.2.2 Microstructure Analysis

In order to quantify the amount of inclusions, the micrograph presented above (Figure 4.25) was analyzed in the ImageJ software, which revealed around 14000 inclusions, with an average size of 17.8 μm and average aspect ratio of 1.39. The sum of the inclusions covered around 3.8% of the total wall area.

Then, the thin wall was observed at higher magnifications both by optical microscopy and by SEM. All the obtained micrographs are presented in the Annex E. In order to understand if the wall was uniform along its building direction, 3 different zones were assessed, as illustrated in Figure 4.26. The bottom part of the wall was not assessed Therefore, the substrate and by consequence the first printed layers were not studied.

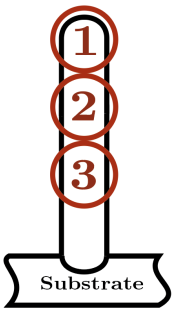

Figure 4.26: Schematic of the 3 zones of the DED printed thin wall where the microstructure was assessed.

Firstly, this analysis did not reveal any major microstructural difference between the 3 different observation zones, which proved that, regarding this aspect, the thin wall is uniform throughout its height. Additionally, this evaluation showed again the high content of inclusions (with a variety of sizes) on the wall, being the majority of them angular and irregular shaped. However rounded and

spherical inclusions were also observed. Due to its shape, those spherical spots could be porosities originated by gas entrapment during DED processing. However, when observing those spots with a higher magnification it was possible to conclude that these were oxides since there was no void space. Some of the inclusions observed are presented in Figure 4.27.

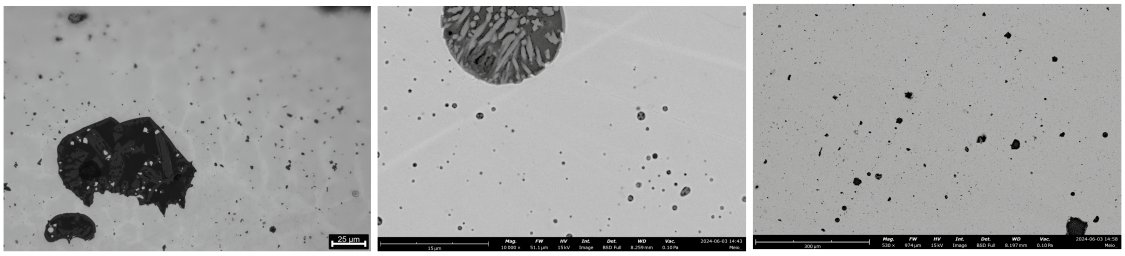

Figure 4.27: Inclusions observed in the DED printed thin wall.

However the chemical composition of those rounded inclusions was assessed in order to confirm that these are oxides, as will be shown in Chapter 4.2.3.

In Zone 3, it was observed a defect with a particularly different shape, as seen in Figure 4.28. This defect is relatively large so it was also visible in both Figures 4.24 and 4.25.

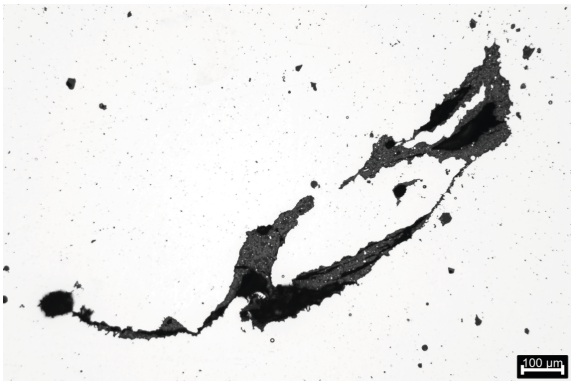

Figure 4.28: Defect observed in Zone 3.

It is difficult to conclude about the origin of this defect but it could be a larger inclusion caused by a lack of fusion defect. The fact that this defect occurs at the interface of of subsequent layers (specifically between 2 of the first layers deposited) may indicate that this defect is due to a lack of bonding caused by the accumulation of oxides on the bead surface.

Regarding the microstructure, it was possible to observe that the prevalent structure was columnar dendrite, as seen in Figure 4.29. These structures grow predominantly in a vertical or column-like orientation relative to the solidification front and are formed with high gradients at the liquid/solid interface (G) and low cooling rates (R), which is the case in DED.

However, the presence of brighter regions as seen above in Figure 4.29, can be attributed to the formation of δ-ferrite. To prove this hypothesis, it was required further analysis, for example by EBSD (Electron Backscatter diffraction) and XRD (X-ray Diffraction).

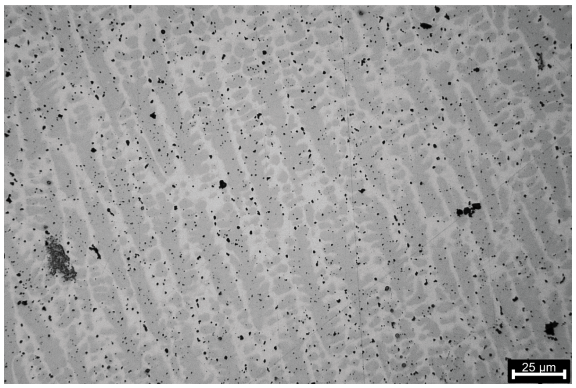

Figure 4.29: Columnar dentritic structures observed.

Besides that, tools such as the Schaeffler and DeLong Diagrams could have been used in order to predict the δ-ferrite phase formation. Schaeffler and DeLong Diagrams based on the composition of the alloy (namely on the Nickel and Chromium Equiavalents parameters). The DeLong diagram is an adaptation of the Schaeffler diagram, with an added focus on predicting the amount of ferrite in austenitic stainless steel. This diagram also uses chromium and nickel equivalents but includes a correction for nitrogen content, which affects the austenite stability. However, it is important to note that these diagrams are based on simplified empirical relationships and may not capture all the complexities of the alloying elements and their interactions during the DED process. The actual solidification process can be influenced by factors not considered in the diagrams, such as cooling rates and thermal gradients. Besides that, the DED process involves rapid heating and cooling, which can lead to non-equilibrium solidification conditions. The diagrams are based on equilibrium or near-equilibrium conditions, so they may not fully account for the rapid thermal cycles experienced during DED printing.

4.2.3 Chemical analysis

The chemical analysis of the DED printed thin walls aimed at 3 different objectives. Firstly, the chemical composition of the original AISI 301 block (as supplied) was compared to the chemical compositions of the printings. This analysis aims to assess the chemical composition changes induced by the milling and deposition processes. Secondly, the chemical compositions of different height zones of the DED printed thin wall were assessed in order to evaluate if the chemical composition of the wall is uniform along the building direction. Finally, the chemical composition of the observed inclusions was measured to comprehend their type and origin.

4.2.3.1 Comparison between the original and the DED printed materials

Table 4.8 presents the chemical compositions of both the original AISI 301 block (which has been machined and whose scraps have been processed into powder) and the DED printed thin wall. Those results were obtained trough OES measurements, which represent a quantitative method.

Table 4.8: Quantitative chemical composition (wt%) of the original AISI 301 block (as supplied) and DED printed thin wall.

Quantitative Chemical Composition (wt%) of the original AISI 301 block (as supplied) and DED printed thin wall								
	Fe	**Cr**	**Ni**	**Mn**	**Mo**	**Si**	**C**	**Cu**
Original block (as supplied)	71,825	17,560	7,795	1,268	0,381	0,290	0,040	0,418
DED printed thin wall	72,733	17,057	7,800	0,857	0,393	0,142	0,081	0,408

From these results, it is possible to observe that the milling and deposition of AISI 301 led to some changes, to a small degree, in the chemical composition. The Fe and C content increased while the Cr, Mn and Si decreased. The C content increased probably due to the manual handling preparation of the chips and the particle powders. On the other hand, the decrease of Mn, Cr and Si comes from oxides formation and migration of those elements to the slag. The depletion of Mn, Cr and Si may affect the printings corrosion resistance and to some extent its mechanical properties.

In order to corroborate these results, the chemical composition of both the original block and the DED printed thin wall was assessed again but now using the SEM/EDS method, which represents a semi-quantitative analysis. Therefore, since Carbon and Oxygen are light elements, the results of those elements cannot be considered valid and thus are highlighted at red. It is important to note that those measurements were obtained in observation zones where no major inclusions were detected, named matrix zones. This was done since one of the goals of this analysis was to understand which elements have been lost from the matrix to form inclusions. Therefore, having measuring the chemical composition on these matrix zones, the chemical composition of the inclusions would not influence the results. The EDS measurements results are presented in Table 4.9 and the respective spectra and images of the analysis zones are presented in Annexes F and G.

Table 4.9: Semi-quantitative chemical composition (wt%) of the DED printed thin wall and original block matrices

Semi-quantitative chemical composition (wt%) of the DED printed thin wall and original block matrices						
		Fe	**Cr**	**Ni**	**Mn**	**C**
Original block (as supplied) matrix	**Average and Standard Deviaton**	71.926 ± 0.213	16.901 ± 0.635	8.490 ± 0.342	1.282 ± 0.076	1.402 ± 0.227
DED printed thin wall matrix	**Average and Standard Deviaton**	73.076 ± 0.188	16.773 ± 0.111	8.908 ± 0.118	1.244 ± 0.052	0.844 ± 0.598

The SEM-EDS results reveal a slight decrease in Mn and Cr and increase in Ni. Therefore, it seems that chemical composition is stable in microscale. However, it is important to note that, due to the nature of the EDS measurements, those results may had been influenced by volume interaction.

Once again, it is shown an increase in Fe content and decrease of Mn and Cr. However it is possible to observe that, against the spectrometry results, Ni content increased and the Mn and Cr content drop was slighter. During the experimental procedure, it was observed that, sometimes the SEM equipment detected the spectra Mn peak as a Cr peak. These malfunction, allied to the semi-quantitative nature of this method may explain these results.

4.2.3.2 Measurements along the thin wall heights

In order to assess if the chemical composition of the wall varies along its height, multiple semi-quantitative chemical composition measurements on the DED printed thin wall were performed. Those measurements were conducted in 3 different zones of the thin wall, according the the same schematic presented above in Figure 4.26.The results are presented in Table 4.10 and the respective spectra and images of the analysis zones are presented in Annex H.

Table 4.10: Semi-quantitative chemical composition (wt%) of the DED printed thin wall (with upcycled powder).

Semi-quantitative chemical composition (wt%) of the DED printed thin wall								
	Fe	**Cr**	**Ni**	**Mn**	**Mo**	**Si**	**C**	**O**
Measured at Zone 1								
Average	70,591	16,233	8,367	0,551	0,501	-	1,904	1,854
Standard Deviation	0,451	0,301	0,151	0,551	0,000	-	0,301	0,050
Measured at Zone 2								
Average	70,567	16,267	8,100	1,333	0,567	-	1,300	1,866
Standard Deviation	0,663	0,131	0,147	0,205	0,095	-	0,215	0,523
Measured at Zone 3								
Average	70,421	16,166	8,309	1,101	0,551	0,100	1,702	1,652
Standard Deviation	0,091	0,018	0,083	0,002	0,049	0,100	0,104	0,054
Entire Wall (Average values of the 3 zones measurements)								
Average	**70,532**	**16,228**	**8,236**	**1,043**	**0,543**	**0,100**	**1,587**	**1,801**
Standard Deviation	0,504	0,187	0,179	0,459	0,073	0,100	0,341	0,357

From these results, it is possible to observe that there was no major deviation in the chemical composition of the thin wall along its height.

da Cunha (2023) reported a decrease in the Cr and Mn along the height of a AISI P20+Ni printed volume. This decrease is undesired since it can affect the stability of certain steel phases. For instance, Mn and Ni have a crucial role in the stabilization of the austenitic phase and therefore, its content decrease may lead to the partial transformation of austenite to ferrite, affecting

toughness and ductility. Moreover, the Cr content decrease heavily affects the steel corrosion resistance. However, this phenomena was not observed here, which represent a positive result.

4.2.3.3 Analysis of inclusions

Besides the chemical composition analysis of the overall thin wall, it also interesting to analyze some inclusions that were observed on the SEM and were suspected to be oxides. Those inclusions are identified in Figure 4.30 and the respective obtained chemical compositions are presented in Annex I. The respective spectra and images of the analysis zones are also presented in the same Annex. In total, the chemical composition of 15 inclusions was assessed through SEM/EDS.

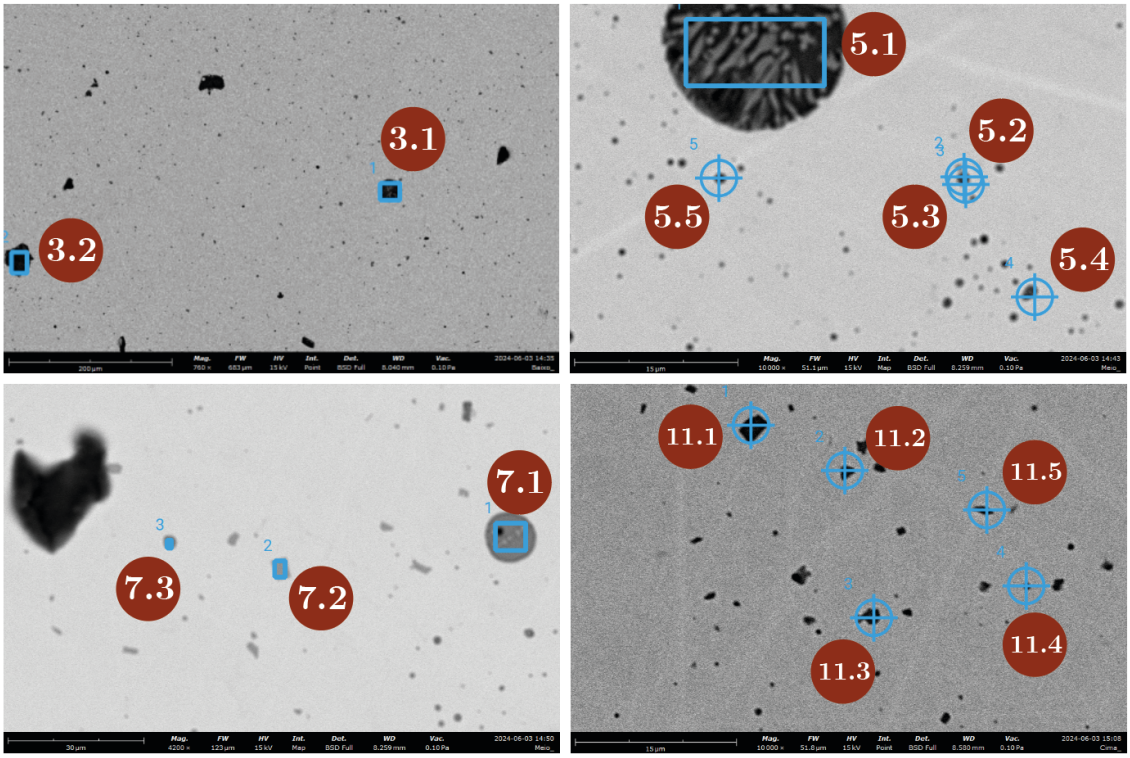

Figure 4.30: Inclusions observed on the DED printed thin wall.

The results show a significant concentration of oxygen content in those spots which explains that, as suspected, they represent oxides formed during the printing process. The spectra manifest high concentrations of Cr, Fe and Mn, clearly indicating the presence of corresponding oxides. The presence of Al and Ni was also detected in their compositions. The oxides shape was observed to understand whether there is any relationship between the shape (rounded and angular) of the inclusions and their composition. However, all oxides with both shapes presented similar compositions.

Oxides origin In order to assess the origin of those oxides, the original AISI 301 block (as supplied) was observed by SEM and it was revealed the presence of a considerable amount of

inclusions on the original block. Figure 4.31 presents the inclusions observed in the original block in comparison with those observed in the DED printed thin wall.

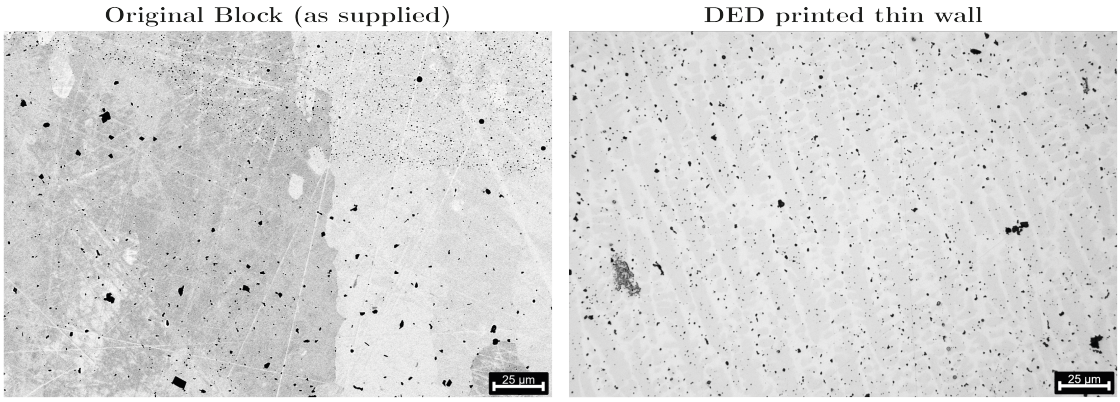

Figure 4.31: Inclusions observed on the original block (as supplied) in comparison with those observed in the DED printed thin wall.

Micrographs (obtained with equal magnifications) of both the original block and the thin wall were analyzed using the ImageJ software in order to evaluate the size, aspect ratio and extent of occurrence of the oxides. It was observed that the oxides present in the original block have an average size of 0.5 μm and an average aspect ratio of 1.40. Besides that, the oxides covered around 2.19% of the total analysis zones. On the other hand, the oxides observed in the thin wall micrographs have an average size of 1.80 μm and an average aspect ratio of 1.49. Those oxides covered around 3.25% of the total analysis zones. With this results, it is possible to conclude that there is a greater occurrence of oxides in the printings, as expected, and those oxides are larger in comparison with the ones observed in the original block.

The other micrographs of the inclusions observed on the original block are presented in Annex J. It is possible to observe that those inclusions are both spherical and irregular shaped and their sizes vary widely. These inclusions probably remained in the chips and consequently in the powder and finally in the DED printed wall thus being one of the reasons for the high content of inclusions in the DED printed thin wall. In order to support this hypothesis, the chemical compositions of those inclusions was assessed through EDS. The measured chemical composition and respective spectra and analysis zones of those oxides is presented in Annex K. In those measurements, a high content of Cr and Mn was detected, clearly indicating the presence of corresponding oxides. As stated above, the same oxides were also detected on the DED printed thin wall.

However, it is still known that a great portion of the inclusions observed in the DED printed thin wall are result of both milling and printing processes. The milling procedures were not performed under controlled atmosphere which may have led to contamination of the powder with oxygen and other elements. Since Planetary Ball Milling is a high energy process, the resultant powder from milling becomes more reactive with oxygen, which makes the printings with those powders more prone to the formation of oxides. On the other hand, the AISI 303 disc milled powders printed by Castanheira (2022) resulted in a smaller oxides content since the powders reactivity

was lower.

Besides that, during the milling, the powder suffers work hardening and grain refinement which makes the particles more reactive to oxygen, due to the increase in their internal energy. Regarding the DED processing, the oxides formation is commonly linked with insufficient shielding which may expose the melt pool to atmospheric oxygen and resulting in oxide formation.

4.2.4 Microhardness test

Figure 4.32 shows the evolution of the microhardness along the height of a DED printed thin wall with upcycled powder. These results are the average of 6 different measurements, whose results are shown in detail in Annex L. Those results were obtained in the upper 25mm of the 1st DED printed wall (i.e. the zone from where the tensile specimens were taken) thus, in the 4mm of the wall closest to the substrate, the microhardness was not assessed, since, the focus of this work is not on the relationship between the printed wall and substrate.

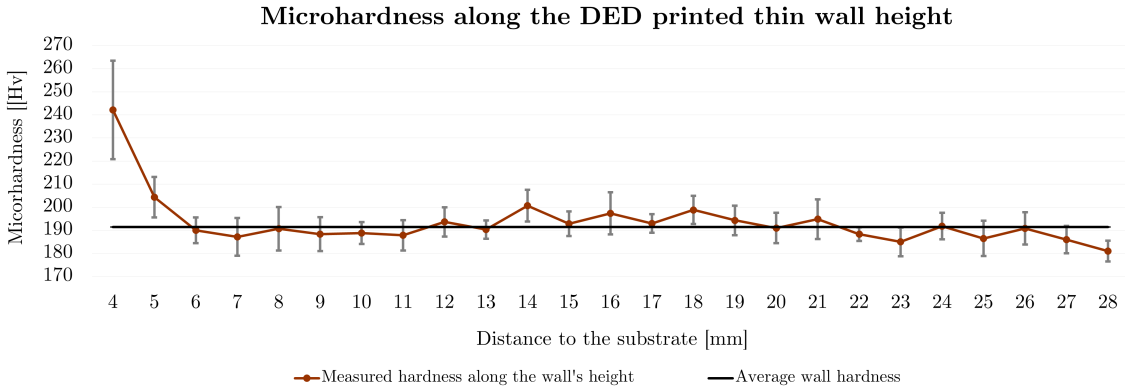

Figure 4.32: Microhardness along the height of a DED printed thin wall with upcycled powder.

Those results show that the microhardness evolution was uniform in almost the entire wall with an average hardness (black line of Figure 4.32) of 191 HV0.1 $\pm$ 11. The major deviation was on the lower zone of the wall, which presented a microhardness around 240 HV0.1 $\pm$ 21. This comes from the fact that the depositions were performed on a non-preheated substrate, which lead to a rapid cooling of the first printed layers and probable a grain refinement. It is curious to note that, although the first measurement was 4mm above the substrate interface, the effect of the non-preheated substrate is still observed. This means that the absence of substrate preheating affected the deposition, at least, until the 4th deposited layer.

4.2.5 Tensile Tests

Figure 4.33 present the engineering curves obtained from the tensile tests. The 3 orange lines represent the curves of the specimens DED printed with upcyled powder (identified by the letter U from "Upcycled") while the 3 blue lines represent the curves of the specimens taken from the original block (identified by the letters AS from "As Supplied"). The real curves and the isolated

curves for each specimen can also be seen in Annex M. Moreover, Annex N presents some images of the deformation field during the tensile tests obtained though DIC.

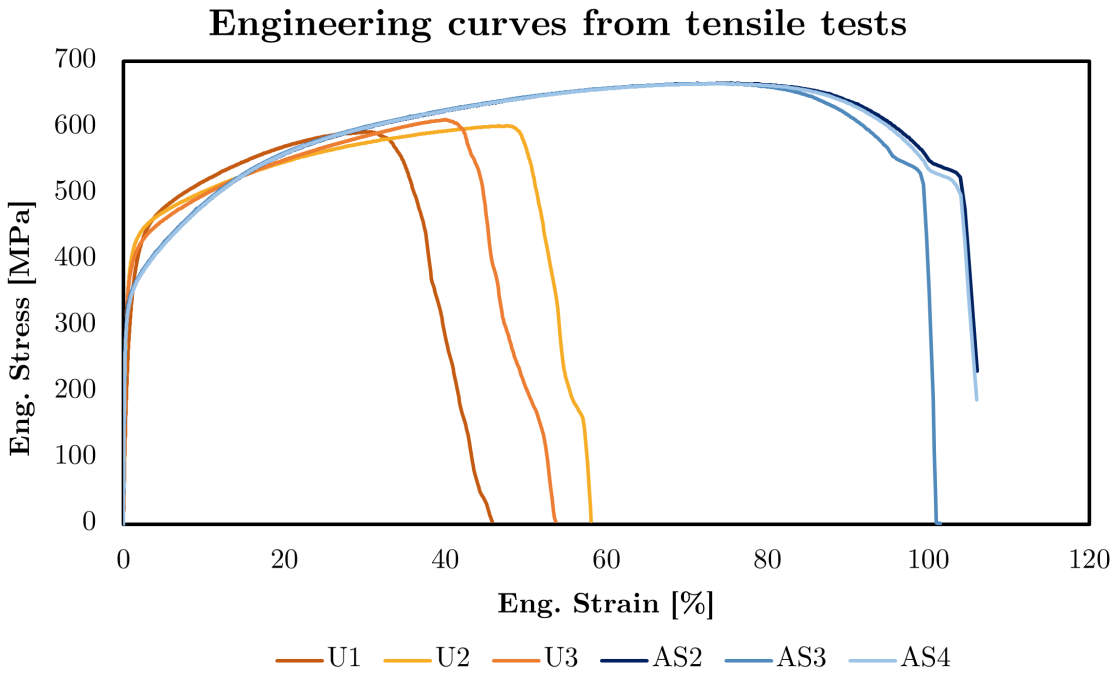

Figure 4.33: Engineering curves of specimens DED printed with upcycled powder (U1, U2 and U3) and specimens taken from the original block (as supplied) (AS1, AS2 and AS3)

Table 4.11 shows the Yield Strength (YS), Ultimate Tensile Strength (UTS) and total elongation values obtained from the tensile testing of the 6 different specimens.

Table 4.11: Yield strength, ultimate tensile strength and total elongation results from the tensile tests.

Sample			Yield strength	Ultimate tensile strength	Total elongation
Type	**Number**	**ID**	**[MPa]**	**[MPa]**	**[%]**
DED	**1**	**U1**	260,64	593,52	45,8
printed with	**2**	**U2**	343,66	602,35	58,11
upcycled	**3**	**U3**	337,82	611,7	53,92
powder	**Average**		**314,04**	**602,52**	**52,61**
From the	**2**	**AS2**	311,32	667,39	106,07
original	**3**	**AS3**	302,74	666,46	101,45
block	**4**	**AS4**	297,76	667,26	106,02
(as supplied)	**Average**		**303,94**	**667,04**	**104,51**

It is important to note that, the results from the AS1 specimen are not presented since the sample did not fracture and therefore the test was considered invalid.

From those results, it is possible to observe that the AISI 301 as supplied specimens had performed significantly better in the plastic regime, since the total elongation of the AS specimens was roughly the double of the total elongation for the U specimens. This is expected since DED

produced parts usually have lower ductility due to presence of defects and the high cooling rates involved which lead to a the formation of a unique microstructure (reduced grains and dendrite size and presence of residual δ ferrite) (Saboori et al. (2020a)).

The UTS of the AS specimens was also superior but only around 10%. This is expected since, on the one hand, it is common for parts produced by DED to have higher yield strength values, due to the same above mentioned reasons that make parts produced by DED have lower ductility. On the other hand, the high content of porosities and oxides, due to the alternative powder production process applied here, leads to a decrease on the tensile strength since those defects work as stress concentrators and crack initiation sites.

However, it possible to note that the yield strength was greater for the tensile specimens printed with upcycled powder which means that those specimens performed better in the elastic regime. This can be attributed to the grain size refinement that may have occured during printing. EBSD analysis is needed to further confirm this hypothesis.

Finally, from the results it is possible to observe that the as supplied specimens presented greater precision while the upcycled powder specimens presented a wider range of YS, UTS and elongation values. If the machining process of the specimens of the same for the 2 sample types, it would be possible to argue that parts produced through the DED processing of upcycled powder would have less uniform mechanical behavior. However, the upcycled powder specimens had to be machined in a CNC center and therefore the dimensional precision of the specimen's gauge length zone was compromised. For instance, it was noted that the specimen's side faces were not completely vertical. On the other hand, the as supplied specimens were obtained by wire-cut EDM which provides a significantly greater dimensional uniformity. Thus, since the U1 specimen presented worse tensile properties in comparison with the U2 and U3, it could be suggested that this worst mechanical behavior was induced by a defect originated during the specimen machining. On the other side, one could hypothesize that the CNC machining led to severe plastic conformation and consequently martensite formation in the specimen. However, even if this phenomenon had occurred, it would have been on a micro scale, affecting only the surfaces of the specimen.

4.2.5.1 Observation of the fracture surfaces

After the tensile testing, 3 different fracture surfaces were observed: 1 of an AS specimen and 2 of U specimens. The Figure 4.34 shows a micrograph of a fracture surface for each type of specimens. The other fracture surface micrographs are presented in Annex P.

From the SEM observations, it is possible to observe that both specimens suffered ductile fracture, due to the formation of dimple structures, result of a significant plastic deformation. Moreover, AS specimens revealed larger cup-like depressions that form as a result of the material undergoing significant plastic deformation before failure. Besides that, it was observed that AS specimens presented larger dimples thus absorbed more energy in the plastic regime before fracturing. This observation is according to the elongation values. In both specimens, it is possible to observe inclusions, although the U samples have those defects in larger concentrations, which may be one reason for the decrease in ductility.

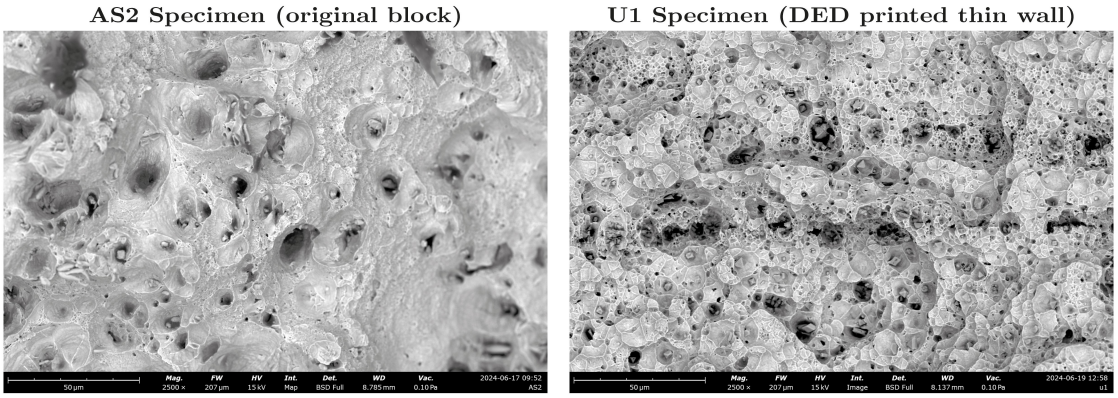

Figure 4.34: Observed fracture surfaces of AS2 and U1 specimens.

Chapter 5

Conclusions and Future Works

5.1 Conclusions

The main goal of this study was to produce, characterize and deposit AISI 301 stainless steel powder produced through the milling of machining chips. Therefore, this work studied the feasibility of this sustainable powder production process for additive manufacturing being able to replace conventional processes, namely atomization. The work's objectives were met and the results were evaluated.

AISI 301 stainless steel chips were transformed into powder through 2 distinct milling processes: ball milling (BM) and planetary ball milling (PBM). Regarding DM, only one procedure was tested although, for PBM, 3 different procedures were tested. The procedures differ from each other due to the different milling parameters: milling and pause times, milling speed and, in the case of PBM, balls diameter. The PBM developed procedures were designed to minimize not only the milling time but also the number of milling stages, which require changing the balls and reprogramming the equipment.

Only one DM procedure was conducted since it was already known from previous studies that the DM method would led to powder with weak characteristics and properties. Therefore, the performance of the DM procedure only served to draw comparisons between the DM and PBM processes and its resulting powder.

The PBM parametrization was not further pursued since one of the developed procedures (named NP2) produced very positive results regarding the milling productivity. The productivity is quantified by the amount (in mass percent) of final powder that is within the particle size range intended for DED processing (in this work was considered to be 38 to 212 μm). Around 80% (in wt. %) of the powder produced in the NP2 procedure was in the desired size range.

However, it was noted that repeating the NP2 procedure led to overuse of the milling media since the material being milled adhered to the jar and balls. This overuse lowered the productivity to 50%. Even so, the productivity of this PBM procedure was higher than that of DM (around 45%).

Moreover, other PBM procedure (named NP3) was developed in order to reprocess powders of dimensions >212 μm left over from previous milling operations. This process only used 5mm balls, while all the other PBM processes used, first, 30mm balls to break down chips and, then, 5mm balls to provide a spherical shape to the powder particles. The NP3 productivity was around 35%. This result reinforced the need to employ a 30mm balls milling stage in order to ensure a proper particle size reduction, not only when milling as received chips but when milling larger previously milled particles.

In this work, it was also performed the same milling conditions as those performed by Castanheira (2022) and da Cunha (2023). Those authors also milled machining chips into powder and used the same equipment. Castanheira (2022) milled AISI 303 stainless steel chips using DM while da Cunha (2023) milled AISI P20+Ni tool steel chips using DM and PBM. The milling productivity of those works was compared and it was possible to draw some conclusions about the ease of mill according to different steels. It was noted that more brittle materials are more easily fractured, while the opposite is found for more ductile materials. On the other hand, more ductile materials are more prone to cold welding.

The powders produced through different procedures were characterized regarding its particle size distribution (PSD), aspect ratio and shape. The powder properties such as tap density, loose density and flowability were also measured.

The DM results were significantly less effective compared with those of PBM, considering the particles shape, size distribution, flowability and densities. The employment of the DM method hardly produced powder smaller than 100μm and the resulting powder was elongated and flaky-like shaped (with an average aspect ratio of 1,85). Those 2 results led to considerably lower density and flowability results, in comparison with the PBM powders. However, by comparing the obtained results with those of Castanheira (2022), it was concluded that more ductile steels have the potential to provide better results when milled by BM, due to its greater propensity to cold welding which leads to more rounded powder particles.

On the other hand, from the results of Castanheira (2022), it was possible to conclude that DM powders have a significantly lower content of microporosities and voids within the particles. Besides that, DM produces powder less reactive with oxygen, in comparison with PBM which promotes the steel reactivity due to the high milling energy involved.

Regarding the PBM powders reuslts, the size distributions of PBM powders were narrower and the aspect ratios and average particle sizes were smaller. The PBM process showed a great uniformity since all the tested procedures presented similar results regarding particles aspect ratio ($\approx$ 1.5) and shape (rounded and approaching spherical).

The NP2 procedure resulted in a very good PSD, characterized by a D10 = 55μm and a D90 = 152μm, which suggests that the majority of the produced powder was in the ideal size range for DED processing (50-150μm).

The overuse of the milling media proved to have an impact on the PSD which became wider but only due to the greater number of larger particles. This showed that the adhesion of material

to the balls and jar negatively affected the ability to break down coarse particles. However, the aspect ratio and particles shaped remained very similar.

The PN3 procedure also led to a wider PSD due to the greater number of larger particles. This corroborated the need of a 30mm balls stage to effectively break down larger particles. Nevertheless, the particles exhibited similar shape and aspect ratio.

The tap density, loose density and flowability results of PBM powder were substantially superior to those of DM powder and came very close to those of commercial gas atomized powder. The differences in the densities and flowability results in the PBM powders was very slight and was justified by the differences in the PSD's which led to better or worse particles packaging.

Due to its better results, the NP2 procedure was followed in order to produce the powder that would be later processed by DED. This procedure has 2 stages (one with 5mm balls and other with 30mm balls, in that order) and a total time of 8h00 (including break time). In total, it was produced approximately 800g of NP2 powder in 10 runs.

The depositions were then performed on a non-preheated dissimilar substrate. The parametrization process was relatively simple since the initial 9 chosen sets of parameters immediately obtained almost positive results. The chosen parameters were a laser power of 2400 W, a scanning speed of 5 mm/s and a powder feed rate of 10 g/min. This set of parameters led to printed tracks with a height of 1.2mm (indicating great productivity), a dilution of 48% and no major defects identified. However, those parameters are not optimal since the the single line printing performed under those conditions presented a dark (indicating the presence of oxides) and irregular aspect. The parametrization process could have been extended in order to find a set of parameters that would lead to a metallic aspect of the printings and a lower dilution, since a dilution value of 30% is already considered sufficient to guarantee a good metallurgical bond. However, the parametrization was not further carried on due to time and equipment availability constraints.

Then, 3 thin walls were built using the above mentioned selected parameters. Besides those parameters, the multi-layer printings were deposited using a 0% vertical overlap ratio, a 5min idle time between layers and printing directions alternating between layers. The choice of the overlap ratio came from the high dilution verified in the parametrization depositions while the toolpath strategy and the implementation of idle time came from the literature review as well as prior experience in the DED performance at INEGI. The choice of those parameters aimed to avoid overmelting by ensuring a proper heat dissipation of the printing.

From those 3 printed walls, one of them was assessed regarding its microstructure, chemical composition and microhardness. All three walls were machined into tensile specimens. Those specimens were taken from the upper regions of the wall so that the first printed layers, which are heavily influenced by the non-preheated substrate, would not impact the results.

The observed wall presented proper dilution between layers although it was also observed 2 lack of fusion defects at layers interfaces.

Moreover, it was noted that the inclusions occurrence was substantial since they covered a considerable area % of the wall. Through the chemical composition analysis, it was proven that those inclusions (with variable size and shapes) were oxides (mainly Cr and Mn). Besides that,

in comparison with the as supplied steel, the printed wall presented a slightly reduced Cr, Mn and Si content, which comes from this heavy oxides formation. The printings performed in this study presented a significantly superior amount of oxides in comparison with the results of Castanheira (2022). This observation highlights the disadvantages of DM in comparison with PBM for DED feedstock powder production. As stated above, PBM produces powder with a greater content of microporosities, which remain in the final printings and became ideal for the oxide formation in those voids. Moreover, the main PBM disadvantage is the greater reactivity to oxygen of the PBM powders (when not milled in a controlled atmosphere), which promotes oxide formation in the printings, as observed in this study.

Additionally, it was observed that the as supplied material (the AISI 301 block that was machined) presented a great amount of inclusions as well. Therefore, although the majority of the inclusions observed in the printings result from the milling and deposition (due to insufficient shielding) processes, the original material also presented inclusions that probably remained in the printed structures.

The analyzed thin wall is homogeneous along its height since the chemical composition and microstructure was similar in 3 different height zones of the wall. The prevalent microstructure was composed by columnar dentrites, as expected in DED printings. The microstructure observation suggested the formation of δ-ferrite although this hypothesis needeed further study and testing to be confirmed.

The microhardness evolution was almost uniform throughout the wall height with the exception of the lowest 4mm of the wall, where the hardness was superior. This was attributed to the non-preheated substrate (a medium-carbon steel) which led to a rapid cooling of the first printed layers and probably to grain refinement. Those results showed that, the employment of a non-preheated dissimilar substrate can have an impact until the 4th printed layer.

The tensile testing compared the tensile properties of specimens printed with upcycled powder (obtained from the thin wall depositions) with specimens of the original material (as supplied). The upcycled powder (U) specimens resulted in a bit superior Yield Strength (YS), a slightly inferior Ultimate tensile Strength (UTS) and a considerably lower (almost half) elongation, when compared with the as supplied (AS) specimens. DED produced parts usually have higher YS and UTS but lower elongation. Therefore the results were expected with exception of the inferior UTS of the U specimens, which may be attributed to the high content of oxides in the printings, since those defects act as stress concentrators and crack initiation sites.

The specimens fractured surfaces were observed by SEM and it was possible to conclude that both U and AS specimens suffered ductile fractures, although AS specimens absorbed more energy in the plastic regime before fracturing, which is consistent with the elongation results.

5.2 Future Works

Following the finish line of this study, there are still opportunities for additional investigation and testing to improve and complete the scope of this research. These possible options for additional

research help to expand the comprehensiveness and depth of this work, while they can work as starting points for future investigations. The following suggestions are brought up for consideration:

- Pursue the milling parameters optimization by varying the other parameters such as the Ball to Powder ratio;
- Characterize and measure the powder properties not only after the entire milling procedure but also after each stage, in order to better understand the impact of the milling parameters on the ease of particle size reduction, ease of cold welding and particles morphology;
- Perform X-ray diffraction analysis of the block, powder particles and chips to study the presence of oxides;
- Complete the literature review with a review of oxide formation (occurrence level, chemical composition, etc.) and δ-ferrite formation in DED prints of austenitic stainless steels;
- Perform the milling process in a controlled atmosphere, to prevent oxides formation during the depositions;
- Investigate the cost and production time of atomized powder as well as the currently available large scale milling technologies for powder production in order to make an economical and industrial comparison between those two powder production processes;
- Sieve the resultant powder into a narrower and more suitable size range for DED (50-150 μ) in order to repeat the powder characterization, DED printings and respective printings assessment and observe the possible different results;
- Assess the oxygen content in the original material, milled powder and final depositions, using a proper equipment for oxygen content (for example LECO's ONH836);
- Pursue DED parameters optimization in order to reduce oxidation and lower dilution;
- Perform and assess thin wall printings with AISI 301 commercial powder in order to serve as a direct benchmark for mechanical properties and occurrence of defects;
- Perform the thin wall printing on a preheated substrate to evaluate if the higher hardness of the first layers remained;
- Perform corrosion resistance tests on both the printed material and the original material (as supplied);
- Predict the δ-ferrite phase formation through the employment of Schaeffler and DeLong diagrams;
- Perform EBSD analysis on the printings to evaluate the possible grain refinement and δ-ferrite formation during printing.

References

Dong Gyu Ahn. Directed energy deposition (ded) process: State of the art, 3 2021. ISSN 21980810.

Meysam Akbari and Radovan Kovacevic. Closed loop control of melt pool width in robotized laser powder–directed energy deposition process. *International Journal of Advanced Manufacturing Technology*, 104:2887–2898, 10 2019. ISSN 14333015. doi: 10.1007/s00170-019-04195-y.

Ant Weld, 2024. Stainless steel: The future of aerospace manufacturing. URL https://www.antweldcleaner.com/innovations-technology/stainless-steel-the-future-of-aerospace-manufacturing/. Acessed: 19th May, 2024.

ASTM B212-99. Astm b212-99: Standard test method for apparent density of free-flowing metal powders using the hall flowmeter funnel, 1999. URL https://www.astm.org/Standards/B212.htm.

ASTM B213-9. Astm b213-97: Standard test methods for flow rate of metal powders using the hall flowmeter funnel, 1997. URL https://www.astm.org/Standards/B213.htm. Reapproved 2003.

ASTM B417-00. Astm b417-00: Standard test method for apparent density of non-free-flowing metal powders using the hall flowmeter funnel, 2000. URL https://www.astm.org/Standards/B417.htm.

ASTM B527-93. Astm b527-93: Standard test method for tap density of metal powders and compounds, 1993. URL https://www.astm.org/Standards/B527.htm.

ASTM B964-09. Astm b964-09: Standard test methods for flow rate of metal powders using a carney funnel, 2009. URL https://www.astm.org/Standards/B964.htm.

ASTM F2792-12a. Astm f2792-12a: Standard terminology for additive manufacturing technologies, December 2012. DOI: 10.1520/F2792-12A, available at https://www.astm.org/Standards/F2792.htm.

Alberta Aversa, Abdollah Saboori, Erica Librera, Michele de Chirico, Sara Biamino, Mariangela Lombardi, and Paolo Fino. The role of directed energy deposition atmosphere mode on the microstructure and mechanical properties of 316l samples. *Additive Manufacturing*, 34, 8 2020. ISSN 22148604. doi: 10.1016/j.addma.2020.101274.

Bassem Barkia, Pascal Aubry, Paul Haghi-Ashtiani, Thierry Auger, Lionel Gosmain, Frédéric Schuster, and Hicham Maskrot. On the origin of the high tensile strength and ductility of additively manufactured 316l stainless steel: Multiscale investigation. *Journal of Materials*

Science and Technology, 41:209–218, 3 2020. ISSN 10050302. doi: 10.1016/j.jmst.2019.09.017.

Catarina Duarte Batista, Adriana André Martins das Neves de Pinho Fernandes, Maria Teresa Freire Vieira, and Omid Emadinia. From machining chips to raw material for powder metallurgy—a review, 9 2021. ISSN 19961944.

Regita Bendikiene, Antanas Ciuplys, and Lina Kavaliauskiene. Circular economy practice: From industrial metal waste to production of high wear resistant coatings. *Journal of Cleaner Production*, 229:1225–1232, 8 2019. ISSN 0959-6526. doi: 10.1016/J.JCLEPRO.2019.05.068.

Byron Blakey-Milner, Paul Gradl, Glen Snedden, Michael Brooks, Jean Pitot, Elena Lopez, Martin Leary, Filippo Berto, and Anton du Plessis. Metal additive manufacturing in aerospace: A review. *Materials and Design*, 209, 11 2021. ISSN 18734197. doi: 10.1016/j.matdes.2021.110008.

Srikanth Bontha, Nathan W. Klingbeil, Pamela A. Kobryn, and Hamish L. Fraser. Thermal process maps for predicting solidification microstructure in laser fabrication of thin-wall structures. *Journal of Materials Processing Technology*, 178:135–142, 9 2006. ISSN 0924-0136. doi: 10.1016/J.JMATPROTEC.2006.03.155.

Christine Friederike Burmeister and Arno Kwade. Process engineering with planetary ball mills. *Chem. Soc. Rev.*, 42:7660–7667, 2013. doi: 10.1039/C3CS35455E. URL http://dx.doi.org/10.1039/C3CS35455E.

Lara Castanheira. Production of sustainable powders for direct energy deposition (ded), 2022.

Lara Castanheira, Jorge Gil, Rui Amaral, Teresa Vieira, Ana Reis, and Omid Emadinia. Parametrization and characterization of ded printings using recycled aisi 303 powder particles. *Powder Technology*, 435, 2 2024. ISSN 1873328X. doi: 10.1016/j.powtec.2024.119453.

Kyu Taek Cho, Luis Nunez, John Shelton, and Federico Sciammarella. Investigation of effect of processing parameters for direct energy deposition additive manufacturing technologies. *Journal of Manufacturing and Materials Processing*, 7, 6 2023. ISSN 25044494. doi: 10.3390/jmmp7030105.

Fuzhong Chu, Kai Zhang, Haopeng Shen, Meijuan Liu, Wenjing Huang, Xi Zhang, Enquan Liang, Zongyan Zhou, Liming Lei, Juan Hou, and Aijun Huang. Influence of satellite and agglomeration of powder on the processability of alsi10mg powder in laser powder bed fusion. *Journal of Materials Research and Technology*, 11:2059–2073, 3 2021. ISSN 2238-7854. doi: 10.1016/J.JMRT.2021.02.015.

JOhn Coykendall, Mark Cotteler, Louis Librandi, and Jeff Carbeck anc Jim Joyce. 3d opportunity in aerospace defense. https://www2.deloitte.com/content/dam/insights/us/articles/additive-manufacturing-3d-opportunity-in-aerospace/DUP_706-3D-Opportunity-Aerospace-Defense_MASTER2.pdf, 2014.

Daniel J. Cruz, Jose Xavier, Rui L. Amaral, and Abel D. Santos. A miniaturized device coupled with digital image correlation for mechanical testing. *Micromachines*, 13, 11 2022. ISSN 2072666X. doi: 10.3390/mi13112027.

Jonathan M. Cullen and Julian M. Allwood. Mapping the global flow of aluminum: From liquid aluminum to end-use goods. *Environmental Science & Technology*, 47(7):3057–3064, 2013. URL https://doi.org/10.1021/es304256s. PMID: 23438734.

D. d. A. Maciel. Fatigue behaviour of inconel 625 produced by directed energy deposition, 2021.

Mariana Sofia Teixeira da Cunha. Development of new sustainable tool powders for additive manufacturing processes´mariana. Master's thesis, Faculty of Engineering of the University of Porto, September 2023.

Adrita Dass and Atieh Moridi. State of the art in directed energy deposition: From additive manufacturing to materials design, 2019. ISSN 20796412.

Howard Kuhn David L. Bourell, William Frazier and Mohsen Seifi. Components of directed energy deposition systems. In *SM Handbook®, Volume 24 - Additive Manufacturing Processes*, volume 24, chapter 20.3, pages 20.3.1–20.3.12. ASM International, 2020a. ISBN 978-1627081864.

Howard Kuhn David L. Bourell, William Frazier and Mohsen Seifi. Metal powder production and powder size and shape distributions. In *SM Handbook®, Volume 24 - Additive Manufacturing Processes*, volume 24, chapter 15, pages 15.1–15.13. ASM International, 2020b. ISBN 978-1627081864.

Howard Kuhn David L. Bourell, William Frazier and Mohsen Seifi. Powder characterization for metal additive manufacturing. In *SM Handbook®, Volume 24 - Additive Manufacturing Processes*, volume 24, chapter 16, pages 16.1–16.12. ASM International, Materials Park, OH, 2020c. ISBN 978-1627081864.

Catrin M. Davies. Predicting creep crack initiation in austenitic and ferritic steels using the creep toughness parameter and time-dependent failure assessment diagram, 2009. ISSN 8756758X.

J. Paulo Davim, editor. *Machining of Titanium Alloys*. Springer International Publishing, Cham, Switzerland, 2014. ISBN 978-3-319-12116-4. doi: 10.1007/978-3-319-12117-1.

J. R. (Joseph R.) Davis and ASM International. Handbook Committee. *Stainless steels*. ASM International, 1994. ISBN 0871705036.

John Ddungu. Determining the particle size distribution of metal powders, Sep 2020. URL https://www.malvernpanalytical.com/en/learn/knowledge-center/insights/determining-the-particle-size-distribution-of-metal-powders. Acessed: 8th June, 2024.

D.F. de Lange, J.T. Hofman, and J. Meijer. Influence of intensity distribution on the meltpool and clad shape for laser cladding. In E. Beyer, F Dausinger, A Ostendorf, and A. Otto, editors, *Proceedings of the third International WLT-conference on Lasers in Manufacturing, 14-17 June 2005, Munich, Germany*, pages 323–327. AT-Fachverlag GmbH Stuttgart, June 2005. ISBN 3-00-016402-2. 3rd International WLT-Conference on Laser in Manufacturing, LIM 2005 ; Conference date: 13-06-2005 Through 16-06-2005.

Sahil Dhiman, Ravinder Singh Joshi, Sachin Singh, Simranpreet Singh Gill, Harpreet Singh, Rakesh Kumar, and Vinod Kumar. A framework for effective and clean conversion of machining waste into metal powder feedstock for additive manufacturing, 10 2021. ISSN 26667908.

Haohao Ding, Tao Yang, Wenjian Wang, Yi Zhu, Qiang Lin, Jun Guo, Qian Xiao, Lu Gan, and Qiyue Liu. Optimization and wear behaviors of 316l stainless steel laser cladding on rail material. *Wear*, 523:204830, 6 2023. ISSN 0043-1648. doi: 10.1016/J.WEAR.2023.204830.

Bhaskar Dutta. *Directed Energy Deposition (DED) Technology*. 01 2020. ISBN 9780128035818. doi: 10.1016/B978-0-12-819726-4.00035-1.

M. Sherif El-Eskandarany, Abdulsalam Al-Hazza, Latifa A. Al-Hajji, Naser Ali, Ahmed A. Al-Duweesh, Mohammad Banyan, and Fahad Al-Ajmi. Mechanical milling: A superior nanotechnological tool for fabrication of nanocrystalline and nanocomposite materials. *Nanomaterials*, 11(10), 2021. ISSN 2079-4991. doi: 10.3390/nano11102484. URL https://www.mdpi.com/2079-4991/11/10/2484.

M. H. Enayati, M. R. Bafandeh, and S. Nosohian. Ball milling of stainless steel scrap chips to produce nanocrystalline powder. *Journal of Materials Science*, 42:2844–2848, 4 2007. ISSN 00222461. doi: 10.1007/s10853-006-1371-2.

EuRIC aisbl (2020). *Metal Recycling Factsheet*. EuRIC aisbl, 2 2020. URL https://circulareconomy.europa.eu/platform/en/knowledge/metal-recycling-factsheet-euric.

European Steel and Alloy Database. Steel number: searchable database of steels and alloys. URL https://www.steelnumber.com/index.php. Acessed: 8th June, 2024.

Yunjie Fan, Yongsheng Zhao, Yan Liu, Shao Xie, Chao Ge, Xiaohui Han, and Hui Chen. Parameter optimization and mechanical properties of laser cladding of 316l stainless steel powder on g20mn5qt steel. *Coatings*, 13(3), 2023. ISSN 2079-6412. doi: 10.3390/coatings13030481. URL https://www.mdpi.com/2079-6412/13/3/481.

André Alves Ferreira, Rui Loureiro Amaral, Pedro Correia Romio, João Manuel Cruz, Ana Rosanete Reis, and Manuel Fernando Vieira. Deposition of nickel-based superalloy claddings on low alloy structural steel by direct laser deposition. *Metals*, 11, 8 2021. ISSN 20754701. doi: 10.3390/met11081326.

Blake Fullenwider, Parnian Kiani, Julie M. Schoenung, and Kaka Ma. Two-stage ball milling of recycled machining chips to create an alternative feedstock powder for metal additive manufacturing. *Powder Technology*, 342:562–571, 1 2019. ISSN 1873328X. doi: 10.1016/j.powtec.2018.10.023.

P. Ganesh, Raju Giri, R. Kaul, P. Ram Sankar, Pragya Tiwari, Ashok Atulkar, R. K. Porwal, R. K. Dayal, and L. M. Kukreja. Studies on pitting corrosion and sensitization in laser rapid manufactured specimens of type 316l stainless steel. *Materials Design*, 39:509–521, 8 2012. ISSN 0261-3069. doi: 10.1016/J.MATDES.2012.03.011.

Randall M. German. Powders for metal injection molding (mim). In Donald F. Heaney, editor, *Handbook of Metal Injection Molding*, chapter 3, pages 50–83. Woodhead Publishing, Cambridge, UK, 2012. ISBN 978-1845699604. URL https://www.elsevier.com/books/handbook-of-metal-injection-molding/heaney/978-1-84569-960-4.

Mehran Ghasempour-Mouziraji, Joana Lagarinhos, Daniel Afonso, and Ricardo Alves de Sousa. A review study on metal powder materials and processing parameters in laser metal deposition. *Optics Laser Technology*, 170:110226, 2024. ISSN 0030-3992. doi: https://doi.org/10.1016/j.optlastec.2023.110226. URL https://www.sciencedirect.com/science/article/pii/S0030399223011192.

Ian Gibson, David Rosen, and Brent Stucker. *Additive Manufacturing Technologies: 3D Printing, Rapid Prototyping, and Direct Digital Manufacturing*. Springer, 2nd edition, 2015. ISBN 978-1493921126. doi: 10.1007/978-1-4939-2113-3. URL https://link.springer.com/book/10.1007/978-1-4939-2113-3. A comprehensive reference on additive manufacturing technologies, including 3D printing, rapid prototyping, and direct digital manufacturing.

Damir Godec, Joamin Gonzalez-Gutierrez, Axel Nordin, Eujin Pei, and Julia Ureña Alcázar. *A Guide to Additive Manufacturing*. Springer International Publishing, 2022. ISBN 978-3-031-05862-2. doi: 10.1007/978-3-031-05863-9. URL https://link.springer.com/10.1007/978-3-031-05863-9.

Prashanth Konda Gokuldoss, Sri Kolla, and Jürgen Eckert. Additive manufacturing processes: Selective laser melting, electron beam melting and binder jetting-selection guidelines, 2017. ISSN 19961944.

Dara Moazami Goodarzi, Joonas Pekkarinen, and Antti Salminen. Effect of process parameters in laser cladding on substrate melted areas and the substrate melted shape. *Journal of Laser Applications*, 27, 2 2015. ISSN 1042-346X. doi: 10.2351/1.4906376.

Granta Design. Granta EduPack 2021 R1, 2021. Acessed: 8th June, 2024.

Peng Guo, Bin Zou, Chuanzhen Huang, and Huabing Gao. Study on microstructure, mechanical properties and machinability of efficiently additive manufactured aisi 316l stainless steel by high-power direct laser deposition. *Journal of Materials Processing Technology*, 240:12–22, 2 2017. ISSN 0924-0136. doi: 10.1016/J.JMATPROTEC.2016.09.005.

Yingbin Hu and Weilong Cong. A review on laser deposition-additive manufacturing of ceramics and ceramic reinforced metal matrix composites. *Ceramics International*, 44:20599–20612, 12 2018. ISSN 0272-8842. doi: 10.1016/J.CERAMINT.2018.08.083.

ASTM International. ASTM B214-16: Standard Test Method for Sieve Analysis of Metal Powders, 2016. Available at: https://www.astm.org/b0214-16.html.

ISO 3252:2023. ISO 3252:2023: Powder metallurgy - Vocabulary, 2023. URL https://www.iso.org/standard/74838.html.

ISO 3685:1993. Tool-life testing with single-point turning tools, 1993. Standard for machining chip forms classification.

Joanna Izdebska-Podsiadły. *Polymers for 3D Printing*. Elsevier, 1st edition, 6 2022. ISBN 9780128183113. URL https://www.elsevier.com/books/polymers-for-3d-printing/izdebska-podsiadly/978-0128237223.

Marcus A. Jackson, Justin D. Morrow, Dan J. Thoma, and Frank E. Pfefferkorn. A comparison of 316 l stainless steel parts manufactured by directed energy deposition using gas-atomized and mechanically-generated feedstock. *CIRP Annals*, 69:165–168, 1 2020. ISSN 17260604. doi: 10.1016/j.cirp.2020.04.042.

Marcus A. Jackson, Dan J. Thoma, and Frank E. Pfefferkorn. Investigation of remanufacturing methods utilizing mechanically-generated and gas-atomized feedstock production for directed energy deposition processing through specific energy consumption modeling. *International Journal of Precision Engineering and Manufacturing - Green Technology*, 10:675–691, 5 2023. ISSN 21980810. doi: 10.1007/s40684-022-00443-x.

Loren A. Jacobson and Joanna McKittrick. Rapid solidification processing. *Materials Science and Engineering: R: Reports*, 11:355–408, 3 1994. ISSN 0927-796X. doi: 10.1016/0927-796X(94)90022-1.

William D. Callister Jr. and David G. Rethwisch. *Materials Science and Engineering: An Introduction*. Wiley, Hoboken, NJ, 10th edition, 2020. ISBN 978-1119405498. URL https://www.wiley.com/en-us/Materials+Science+and+Engineering%3A+An+Introduction%2C+10th+Edition-p-9781119405498.

Haitham El Kadiri, Liang Wang, Mark F. Horstemeyer, Reza S. Yassar, John T. Berry, Sergio Felicelli, and Paul T. Wang. Phase transformations in low-alloy steel laser deposits. *Materials Science and Engineering: A*, 494:10–20, 10 2008. ISSN 0921-5093. doi: 10.1016/J.MSEA.2007.12.011.

Kazybek Kassym and Asma Perveen. Atomization processes of metal powders for 3d printing. *Materials Today: Proceedings*, 26:1727–1733, 1 2020. ISSN 2214-7853. doi: 10.1016/J.MATPR.2020.02.364.

Kyoung Wook Kim, Gi Su Ham, Sun Hong Park, Jung Wook Cho, and Kee Ahn Lee. Direct energy deposition of ultrastrong wc-12co cemented carbide: Fabrication, microstructure and compressive properties. *International Journal of Refractory Metals and Hard Materials*, 99:105591, 9 2021. ISSN 0263-4368. doi: 10.1016/J.IJRMHM.2021.105591.

Tae Wook Kim, Dong Hyeon Kim, Young Tae Cho, and Choon Man Lee. Manufacturing high strength ti alloy with in-situ cu alloying via directed energy deposition and evaluation of material properties. *Journal of Materials Research and Technology*, 28:1810–1823, 1 2024. ISSN 22387854. doi: 10.1016/j.jmrt.2023.12.115.

M. Kucukvar and S. Kucukvar. *Handbook of Research on Waste Management Techniques for Sustainability*, chapter Upcycling of Metal Wastes: An Innovative Approach to Sustainable Development. IGI Global, 2018.

Hyoung Keun Lee. Effects of the cladding parameters on the deposition efficiency in pulsed nd:yag laser cladding. *Journal of Materials Processing Technology*, 202:321–327, 6 2008. ISSN 0924-0136. doi: 10.1016/J.JMATPROTEC.2007.09.024.

Wei Li, Sreekar Karnati, Caitlin Kriewall, Frank Liou, J. Newkirk, Karen M. Brown Taminger, and William J. Seufzer. Fabrication and characterization of a functionally graded material from ti-6al-4v to ss316 by laser metal deposition. *Additive Manufacturing*, 14:95–104, 3 2017. ISSN 2214-8604. doi: 10.1016/J.ADDMA.2016.12.006.

Milton Sergio Fernandes De Lima and Simon Sankaré. Microstructure and mechanical behavior of laser additive manufactured aisi 316 stainless steel stringers. *Materials and Design*, 55:526–532, 2014. ISSN 18734197. doi: 10.1016/j.matdes.2013.10.016.

Jichang Liu and Lijun Li. Direct fabrication of thin-wall parts by laser cladding. *Journal of Manufacturing Processes*, 8:1–7, 1 2006. ISSN 1526-6125. doi: 10.1016/S1526-6125(06)70096-2.

Michael Liu, Abhishek Kumar, Satish Bukkapatnam, and Mathew Kuttolamadom. A review of the anomalies in directed energy deposition (ded) processes potential solutions - part quality defects. *Procedia Manufacturing*, 53:507–518, 1 2021. ISSN 2351-9789. doi: 10.1016/J.PROMFG.2021.06.093.

Vladimir Luzin and Nicholas Hoye. Stress in thin wall structures made by layer additive manufacturing. volume 2, pages 497–502. Materials Research Forum LLC, 1 2017. doi: 10.21741/9781945291173-84.

Alex López-Córdoba and Silvia Goyanes. *Food Powder Properties*. 01 2017. ISBN 9780081005965. doi: 10.1016/B978-0-08-100596-5.21198-0.

Rasheedat Modupe Mahamood. *Laser Metal Deposition Process of Metals, Alloys, and Composite Materials*. Springer, 1st edition, 2018. ISBN 978-3-319-64984-9. doi: https://doi.org/10.1007/978-3-319-64985-6. URL https://link.springer.com/book/10.1007/978-3-319-64985-6.

Marlin Steel, 2024. Why stainless steel is essential for the aerospace industry. URL https://www.marlinwire.com/blog/why-you-should-use-stainless-steel-for-aerospace-applications. Acessed: 19th May, 2024.

Federico Mazzucato, Alberta Aversa, Roberto Doglione, Sara Biamino, Anna Valente, and Mariangela Lombardi. Influence of process parameters and deposition strategy on laser metal deposition of 316l powder. *Metals*, 9, 11 2019. ISSN 20754701. doi: 10.3390/met9111160.

Claudiney Mendonça, Adhimar Flávio Oliveira, Leonardo Albergaria Oliveira, Manoel Ribeiro da Silva, Mirian de Lourdes Noronha Motta Melo, and Gilbert Silva. Structural and magnetic properties of duplex stainless steel (uns s31803) powders obtained by high energy milling of chips with additions of nbc. *Materials Research*, 21, 2018. ISSN 15161439. doi: 10.1590/1980-5373-MR-2017-0717.

Claudiney Mendonça, Patricia Capellato, Emin Bayraktar, Fábio Gatamorta, José Gomes, Adhimar Oliveira, Daniela Sachs, Mirian Melo, and Gilbert Silva. Recycling chips of stainless steel using a full factorial design. *Metals*, 9, 2019. ISSN 20754701. doi: 10.3390/met9080842.

Metal Exponents, 2024. 5 different applications for stainless steel in the aerospace industry, 2020. URL https://metalexponents.com/blog/applications-stainless-steel-aerospace/. Acessed: 19th May, 2024.

Mattias Miedzinski. Materials for additive manufacturing by direct energy deposition: Identification of material properties that can have an influence on the building process or the resulting component properties.

K C Mills and A Shirali. Marangoni effects in welding, 1998. URL https://royalsocietypublishing.org/.

MTI Corp. Mti corp - leading provider of lab equipments and advanced crystal substrates. URL https://www.mtixtl.com/MSK-SFM-15.aspx.

Mohammad Taghi Nasiri and Mohammad R. Movahhedy. A new design of continuous coaxial nozzle for direct metal deposition process to overcome the gravity effect. *Progress in Additive Manufacturing*, 7:173–186, 4 2022. ISSN 23639520. doi: 10.1007/s40964-021-00223-0.

Oleg D. Neikov, Stanislav Naboychenko, and Irina M. Safonov. *Handbook of Non-Ferrous Metal Powders*. Elsevier, Amsterdam, Netherlands, 2nd edition, 2019. ISBN 978-0128163553. URL https://www.elsevier.com/books/handbook-of-non-ferrous-metal-powders/neikov/978-0-12-816355-3.

P. V. Nidheesh and M. Suresh Kumar. An overview of environmental sustainability in cement and steel production. *Journal of Cleaner Production*, 231:856–871, 9 2019. ISSN 0959-6526. doi: 10.1016/J.JCLEPRO.2019.05.251.

Erik Oberg, Franklin D. Jones, Holbrook L. Horton, Henry H. Ryffel, Christopher J. McCauley, Ricardo Heald, and Muhammed Iqbal Hussain. Directed energy deposition (ded). In *Machinery's Handbook*, chapter 7.4.9.4, pages 1552–1557. Industrial Press, Inc., 31st edition, 2020. ISBN 978-0831137311. Comprehensive reference work for mechanical and manufacturing engineers, designers, draftsmen, toolmakers, and machinists.

Ester M. Palmero and Alberto Bollero. *3D and 4D Printing of Functional and Smart Composite Materials*, pages 402–419. 07 2021. ISBN 9780128035818. doi: 10.1016/B978-0-12-819724-0.00008-2.

Wei Pei, Wei Zhengying, Chen Zhen, Li Junfeng, Zhang Shuzhe, and Du Jun. Numerical simulation and parametric analysis of selective laser melting process of alsi10mg powder. *Applied Physics A: Materials Science and Processing*, 123, 8 2017. ISSN 14320630. doi: 10.1007/s00339-017-1143-7.

Carmen C. Piras, Susana Fernández-Prieto, and Wim M. De Borggraeve. Ball milling: a green technology for the preparation and functionalisation of nanocellulose derivatives. *Nanoscale Adv.*, 1:937–947, 2019. doi: 10.1039/C8NA00238J. URL http://dx.doi.org/10.1039/C8NA00238J.

Song Ren-bo, Xiang Jian-ying, and Hou Dong-po. Characteristics of mechanical properties and microstructure for 316l austenitic stainless steel, 2011.

Retsch GmbH Haan - The Art of Milling (2017). *The Art of Milling - An expert Guide to Neutral-to-Analysis Size Reduction and Homegenization in the Laboratory*, 2017.

Retsch GmbH Haan (2016). *Product Information - Vibratory Disc Mill RS 200*. Retsch GmbH Haan, Germany, 2016.

Retsch GmbH Haan (2024). *How to Obtain the Best Results with the Vibratory Disc Mill RS 200*, 2024.

Reynier I. Revilla and Iris De Graeve. Microstructural features, defects, and corrosion behaviour of 316l stainless steel clads deposited on wrought material by powder- and laser-based direct energy deposition with relevance to repair applications. *Materials*, 15, 10 2022. ISSN 19961944. doi: 10.3390/ma15207181.

Kandice S.B. Ribeiro, Fábio E. Mariani, and Reginaldo T. Coelho. A study of different deposition strategies in direct energy deposition (ded) processes. *Procedia Manufacturing*, 48:663–670, 2020. ISSN 23519789. doi: 10.1016/j.promfg.2020.05.158.

Jose Exequiel Ruiz, Magdalena Cortina, Jon Iñaki Arrizubieta, and Aitzol Lamikiz. Study of the influence of shielding gases on laser metal deposition of inconel 718 superalloy. *Materials*, 11, 8 2018. ISSN 19961944. doi: 10.3390/ma11081388.

Magdalena Rzeszotarska, Dariusz Zasada, Tomasz Płociński, Wojciech J. Stępniowski, and Marek Polański. On the influence of manufacturing parameters on the microstructure, mechanical properties and corrosion resistance of aisi 316l steel deposited by laser engineered net shaping (lens®). *Materials*, 16, 3 2023. ISSN 19961944. doi: 10.3390/ma16051965.

Abdollah Saboori, Alberta Aversa, Federico Bosio, Emilio Bassini, Erica Librera, Michele De Chirico, Sara Biamino, Daniele Ugues, Paolo Fino, and Mariangela Lombardi. An investigation on the effect of powder recycling on the microstructure and mechanical properties of aisi 316l produced by directed energy deposition. 766:138360, 10 2019. ISSN 0921-5093. doi: 10.1016/J.MSEA.2019.138360.

Abdollah Saboori, Alberta Aversa, Giulio Marchese, Sara Biamino, Mariangela Lombardi, and Paolo Fino. Microstructure and mechanical properties of aisi 316l produced by directed energy deposition-based additive manufacturing: A review, 5 2020a. ISSN 20763417.

Abdollah Saboori, Gabriele Piscopo, Manuel Lai, Alessandro Salmi, and Sara Biamino. An investigation on the effect of deposition pattern on the microstructure, mechanical properties and residual stress of 316l produced by directed energy deposition. *Materials Science and Engineering: A*, 780, 4 2020b. ISSN 09215093. doi: 10.1016/j.msea.2020.139179.

Sandvik Materials Technology. Osprey® 316l. https://www.metalpowder.sandvik/en/webshop/metal-powders/austenitic-stainless-steel/osprey-316l/, 2024. Accessed: 2024-06-09.

I. Kartikeya Sarma, V. Srinivas, and S. Kanmani Subbu. Comparison of wear and corrosion resistance behaviour of lens tm deposited ss 316l alloy and wrought alloy. *Materials Today: Proceedings*, 38:3279–3282, 1 2021. ISSN 2214-7853. doi: 10.1016/J.MATPR.2020.10.019.

C. Selcuk. Laser metal deposition for powder metallurgy parts. *Powder Metallurgy*, 54:94–99, 4 2011. ISSN 00325899. doi: 10.1179/174329011X12977874589924.

Nima Shamsaei, Aref Yadollahi, Linkan Bian, and Scott M. Thompson. An overview of direct laser deposition for additive manufacturing; part ii: Mechanical behavior, process parameter optimization and control. *Additive Manufacturing*, 8:12–35, 10 2015. ISSN 2214-8604. doi: 10.1016/J.ADDMA.2015.07.002.

A. Mahboubi Soufiani, M. H. Enayati, and F. Karimzadeh. Fabrication and characterization of nanostructured ti6al4v powder from machining scraps. *Advanced Powder Technology*, 21:336–340, 5 2010. ISSN 09218831. doi: 10.1016/j.apt.2009.12.018.

Suhas Sreekanth, Ehsan Ghassemali, Kjell Hurtig, Shrikant Joshi, and Joel Andersson. Effect of direct energy deposition process parameters on single-track deposits of alloy 718. *Metals*, 10, 1 2020. ISSN 20754701. doi: 10.3390/met10010096.

C. Suryanarayana. Mechanical alloying and milling. *Progress in Materials Science*, 46:1–184, 1 2001. ISSN 0079-6425. doi: 10.1016/S0079-6425(99)00010-9.

David Svetlizky, Mitun Das, Baolong Zheng, Alexandra L. Vyatskikh, Susmita Bose, Amit Bandyopadhyay, Julie M. Schoenung, Enrique J. Lavernia, and Noam Eliaz. Directed energy deposition (ded) additive manufacturing: Physical characteristics, defects, challenges and applications. *Materials Today*, 49:271–295, 10 2021. ISSN 1369-7021. doi: 10.1016/J.MATTOD.2021.03.020.

Jun Hao Tan, Wai Leong Eugene Wong, and Kenneth William Dalgarno. An overview of powder granulometry on feedstock and part performance in the selective laser melting process. *Additive Manufacturing*, 18:228–255, 12 2017. ISSN 2214-8604. doi: 10.1016/J.ADDMA.2017.10.011.

Itziar Tolosa, Fermín Garciandía, Fidel Zubiri, Fidel Zapirain, and Aritz Esnaola. Study of mechanical properties of aisi 316 stainless steel processed by "selective laser melting", following different manufacturing strategies. *International Journal of Advanced Manufacturing Technology*, 51:639–647, 11 2010. ISSN 02683768. doi: 10.1007/s00170-010-2631-5.

Edwar A Torres, Luis H R Apolinario, Helen R Araujo, Ivan B M Picchi, Tiago, and F A Santos. Banding and microstructural features in laser cladding of a 304 substrate using 316 powder. *Optics Laser Technology: Volume 109*, 2019. doi: 10.1007/s00170-020-06418-z/Published. URL https://doi.org/10.1007/s00170-020-06418-z.

Ehsan Toyserkani, Amir Khajepour, and Stephen F. Corbin. *Laser Cladding*. CRC Press, Boca Raton, FL, 1st edition, 2004. ISBN 978-0849330346. doi: https://doi.org/10.1201/9781420039177. URL https://www.crcpress.com/Laser-Cladding/Toyserkani-Khajepour-Corbin/p/book/9780849330346.

Jason R. Trelewicz, Gary P. Halada, Olivia K. Donaldson, and Guha Manogharan. Microstructure and corrosion resistance of laser additively manufactured 316l stainless steel. *JOM*, 68:850–859, 3 2016. ISSN 15431851. doi: 10.1007/s11837-016-1822-4.

Xinlin Wang, Dewei Deng, Meng Qi, and Hongchao Zhang. Influences of deposition strategies and oblique angle on properties of aisi316l stainless steel oblique thin-walled part by direct laser fabrication. *Optics and Laser Technology*, 80:138–144, 6 2016. ISSN 00303992. doi: 10.1016/j.optlastec.2016.01.002.

Xinlin Wang, Dewei Deng, Hongli Yi, Haiyan Xu, Shuhua Yang, and Hongchao Zhang. Influences of pulse laser parameters on properties of aisi316l stainless steel thin-walled part by laser material deposition. *Optics and Laser Technology*, 92:5–14, 7 2017. ISSN 00303992. doi: 10.1016/j.optlastec.2016.12.021.

Leong Kean Wei, Shayfull Zamree Abd Rahim, Mohd Mustafa Al Bakri Abdullah, Allice Tan Mun Yin, Mohd Fathullah Ghazali, Mohd Firdaus Omar, Ovidiu Nemeș, Andrei Victor Sandu, Petrica Vizureanu, and Abdellah El-hadj Abdellah. Producing metal powder from machining chips using ball milling process: A review. *Materials*, 16(13), 2023. ISSN 1996-1944. doi: 10.3390/ma16134635. URL https://www.mdpi.com/1996-1944/16/13/4635.

Martin Wilkening, Andre Düvel, Florian Preishuber-Pflügl, Klebson da Silva, Stefan Breuer, Vladimir Šepelák, and Paul Heitjans. Structure and ion dynamics of mechanosynthesized oxides and fluorides. *Zeitschrift für Kristallographie - Crystalline Materials*, 232(1-3):107–127, 2017. doi: doi:10.1515/zkri-2016-1963. URL https://doi.org/10.1515/zkri-2016-1963.

Markus Wolf. Improving the efficiency of the dmld process. *Laser Technik Journal*, 13:32–34, 9 2016. ISSN 1613-7728. doi: 10.1002/latj.201600028.

Jun Yu, Xin Lin, Liang Ma, Junjie Wang, Xingling Fu, Jing Chen, and Weidong Huang. Influence of laser deposition patterns on part distortion, interior quality and mechanical properties by laser solid forming (lsf). *Materials Science and Engineering: A*, 528:1094–1104, 1 2011. ISSN 09215093. doi: 10.1016/j.msea.2010.09.078.

Tianbiao Yu, Jiayu Sun, Wanrui Qu, Yu Zhao, and Lin Yang. Influences of z-axis increment and analyses of defects of aisi 316l stainless steel hollow thin-walled cylinder. *International Journal of Advanced Manufacturing Technology*, 97:2203–2220, 7 2018. ISSN 14333015. doi: 10.1007/s00170-018-2083-x.

Kai Zhang, Shijie Wang, Weijun Liu, and Xiaofeng Shang. Characterization of stainless steel parts by laser metal deposition shaping. *Materials and Design*, 55:104–119, 2014. ISSN 18734197. doi: 10.1016/j.matdes.2013.09.006.

B. Zheng, J. C. Haley, N. Yang, J. Yee, K. W. Terrassa, Y. Zhou, E. J. Lavernia, and J. M. Schoenung. On the evolution of microstructure and defect control in 316l ss components fabricated via directed energy deposition. *Materials Science and Engineering: A*, 764, 9 2019. ISSN 09215093. doi: 10.1016/j.msea.2019.138243.

H. R. Zhi, H. T. Zhao, Y. F. Zhang, and B. Dampilon. Microstructure and crystallographic texture of direct energy deposition printed 316l stainless steel. *Digest Journal of Nanomaterials and Biostructures*, 18:1293–1303, 10 2023. ISSN 18423582. doi: 10.15251/DJNB.2023.184.1293.

Michał Ziętala, Tomasz Durejko, Marek Polański, Izabela Kunce, Tomasz Płociński, Witold Zieliński, Magdalena Łazińska, Wojciech Stępniowski, Tomasz Czujko, Krzysztof J. Kurzydłowski, and Zbigniew Bojar. The microstructure, mechanical properties and corrosion resistance of 316 l stainless steel fabricated using laser engineered net shaping. *Materials Science and Engineering: A*, 677:1–10, 11 2016. ISSN 09215093. doi: 10.1016/j.msea.2016.09.028.

Annex A - Summary of the state-of-the-art of AISI 316L Powder DED Processing - Analysis, conclusions and obtained mechanical properties from recent studies

Table 5.1: Mechanical properties and other conclusions drawn in works regarding AISI 316L powder DED

Reference	Bead Width (mm)	Bead Heigth (mm)	Bead Depth (mm)	Hardness (HV)	Tensile Strength (Mpa)	Yield Strength (Mpa)	Elongation (%)	Notes	Conclusions
Fan et al. (2023)	-	-		-	626 - 742	363 - 574	10,4 - 35,3	Besides the tensile properties, the microstructure, microhardness, impact properties and frictional wear properties were investigated.	The microhardness, wear resistance, and micro-shear strength increase with the increase in laser power, while the tensile strength and yield strength first increase and then decrease with the increase in laser power. When the laser power is low, due to insufficient energy, the metallurgical bond between the 316L SS cladding layer and G20Mn5QT steel is weak, resulting in a lower shear strength. When the laser power is higher, althoug the shear strength is higher, the dilution rate does not meet the repair requirements. It was detected some pores and crack defects.
Rzeszotarska et al. (2023)	-	-	-	183 - 236	642 - 686	-	40 - 53	After deposition the samples were stress relieved through annealing at 400ºC for 5h. Besides the mechanical properties, the corrosion resistance (eletrochemical and in salt chamber) were also accessed, as well as the final microstructure.	The deposiiton parameters had a minor impact on the mechanical properties and microstructure. The hardness slightly increases with increasing scanning speed and powder feed rate. The corrosion resistance of LENS produced samples is greater, comparatively with conventionally produced samples. It was not possible to draw conclusions regarding the influence of the parameters. However, it was noted that the pitting resistance decreases with increasing feed rate.
Ribeiro et al. (2020)	0,8	0,3	-	209 - 228	-	-	-	-	The goal of this study was to access the influence of the toolpath strategy and overlap. The contour path presented less distortions, the lowest roughness and the highest density. Raster strategy lead to a thermal non uniform distribution. The linear or chessboards strategies lead to higher hardness. A greater overlap leads to denser final parts.
Mazzucato et al. (2019)	-	-	-	212 - 250	-	-	-	-	The increase in laser power leads to the increase in melt pool depth and decrease in hardness. The increase in overlap % also decreases the hardness. The melt pool shape is affected by the scanning strategy and the overlap. For high overlap values, the final shape of the metal bead strongly depends on the deposition strategy involved.
Zhi et al. (2023)	-	-	-	261,74	-	-	-	-	This work aims to study the microstructural features and crystallographic texture of 316L DED printed parts. The sample contained equiaxed cellular and elongated morphology. The grain size varies from about 12.48 to 156.08 μm with average value of 29.79 μm measured.
Barkia et al. (2020)	-	-	-	-	-	440 378	51,5 54,5	Measured in the parallel direction to the deposited layers Measured in the perpendicular direction to the deposited layers	This study contributes to the understanding of the relationships between the LENS pro-cessing, microstructures, and resulting mechanical performances of 316 L stainless steel, key to satisfy the demands for new applications. It is stated that the builidng orientation had little to no effect on the mechanical properties of the DED produced samples.

Mechanical properties and other conclusions drawn in works regarding AISI 316L powder DED - continuation

Reference	Bead Width (mm)	Bead Heigth (mm)	Bead Depth (mm)	Hardness (HV)	Tensile Strength (Mpa)	Yield Strength (Mpa)	Elongation (%)	Notes	Conclusions
Cho et al. (2023)	1,31 1,13 1,10	0,38 0,33 0,25	0,33 0,28 0,22	163 - 208	-	-	-		This study investigated 316L DED through experimental and physics-based modeling. The DED process was access through the parameters Global Energy Density and Linear Mass Deposition. It was found that the desirable values for the parameters in order to achieve a properdilution and a suitable powder efficiency.
Saboori et al. (2020b)	-	-	-	-	620 - 649	405 - 469	17 - 23	-	In this study, the effect of 2 different deposition patterns, 67° and 90° rotation per layer, on the microstructure, inclusion content, cooling rate, PCAS value, mechanical properties and residual stress of 316L SS fabricated via DED process was investigated. The cooling rate in 67° samples was lower and the mechanical porperties were worst. It was detected oxides (Si, Mn) in the samples. It also also studied the role of oxygen content and it was concluded that the increase in oxygen content leads to a 50% decrease in ductility.
Ziętala et al. (2016)	-	0,3	-	289 272	703 776	479 576	46 33	Measured in the perpendicular direction to the deposited layers Measured in the parallel direction to the deposited layers	The hardness of the LENS produced samples is comparable to the hardness of annealed 316L steel. The YS and TS are higher than those of conventionally fabricated material. The tensile properties measured parallel to the layers were higher than those measured perpendicular to the layers while an inverse relationship for total elongation was observed. The corrosion resitance was also accessed. The samples presented low values of corrosion current density, which leads to a smaller corrosion rate. The corrosion resistance is caused by the formation of a passive oxide layer. However, it was stated that LENS samples are more prone to pitting corrosion.
Lima and Sankaré (2014)	-	-	-	-	414 530 539	229 261 207	37,8 43,4 45,0	It was conducted 3 different measurements for different processing conditions.	This article studied high aspect ratio 316L structures made by superposiiton of consecutive layers. The samples presented defects such as pores and craks. The mechanical properties were comparable to those reported in the literature. The Cr and Ni contents of the clads felt inside a 5–10% delta ferrite range, according to the Scheaffler diagram.
Zhang et al. (2014)	2	0,46		331 - 427	558 352	639 536	21 46	Measured in the parallel direction to the deposited layers Measured in the perpendicular direction to the deposited layers	An increase in laser power leads to increase in clad height and width while the opposite trend occurs regarding scanning speed and powder flow rate. The mechanical properties (except elongation) were superior when measured in the parallel direction regarding the printing direction. The increase in laser power lead to decrease in hardness, YS and TS, while the elongation evolution was irregular. The increase in scanning speed lead to the increase in the 4 mechanical properties. The effect of scanning speed is mrore significant than laser power. Besides that, the solidification velocity and temperature gradient are more sensitive to thescanning speed. There was a strong metallurgical bonding between clad and substrate.

Mechanical properties and other conclusions drawn in works regarding AISI 316L powder DED - continuation

Reference	Bead Width (mm)	Bead Heigth (mm)	Bead Depth (mm)	Hardness (HV)	Tensile Strength (Mpa)	Yield Strength (Mpa)	Elongation (%)	Notes	Conclusions
Jackson et al. (2020)	-	-	-	95 92	603 571	427 411	46 61	Deposition of mechanically-generated powder. Deposition of gas atomized powder.	This study compares the microstructure and mechanical properties of DED produced samples both using mechanically generated powder and gas atomized powder. Identical process conditions resulted in parts with similar surface texture, microstructure and mechanical properties.
Aversa et al. (2020)	-	-	-	-	628 670	469 628	31 34	N_2 Shielding gas N_2-filled build chamber	This article studied the effect of the protective atmosphere on the microstucture and mechanical performance of 316L deposirted parts by depositing either under simple local shielding or in a build chamber. The use of a build chamber allowed the achievement of slightly higher TS and elongation due to the reduced size of the oxide inclusions. However, the atmosphere do not have a relevant effect on the microstructure.
Saboori et al. (2019)	-	-	-	-	628 651	469 458	31,2 16,2	Deposition of fresh powder Deposition of reused powder	This work studied the effect of recycling powder from previous depositions on the microstructure and mechanical properties of AISI 316L samples. The reused powder leads to lower elongation, which is justified by the presence of large inclusions. The higher mechanical strength of DED samples in comparison with conventionally produced samples is attributed to the final composition and finer microstructure due to the faster cooling rates.

Annex B - Summary of the state-of-the-art of AISI 316L Powder DED Processing - DED Processing Parameters used in recent studies

Table 5.2: DED parameters applied in other studies regarding AISI 316L powder deposition.

Reference	Substrate	Laser Power (W)	Laser Spot Size (mm)	Stand-off distance (mm)	Scanning speed (mm/s)	Global Energy Density (GED) (J/mm^2)	GED for spot size of 2.1mm	Powder feeding rate (g/min)	Carrier gas flow (Gas, rate (L/min))	Shielding gas flow (Gas, rate (L/min))	Powder diameter (m)	Hatch (mm)	Overlap (%)	Toolpath Strategy	Notes
\cite{fanZhao}	G20Mn5QT	2300	4	-	8,33	-	-	14	Ar,7	Ar, 40	97,21% in the 50-150 range	-	40%	-	Those parameters were optimized in this work.
\cite{RzeszotarskaZasada}	-	435 450 450	0,8	-	6 10 20	**90,63** **56,25** **28,13**	**237,89** **147,66** **73,83**	7,85	Ar, 4	Ar, 20	97% in the 44-106 range	-	-	-	The samples were produced via LENS.
\cite{ribeiroMariani}	-	600	0,8	-	33,33	**22,50**	**59,06**	5	Ar, 5	Ar, 6	44 - 88	0.44 , 0.55	45% , 31.25%	Linear, Zigzag, Chessboard and Contour	-
\cite{mazzucatoAversa}	316L	300 600	1	10	7,5	**40,00** **80,0**	**84,00** **168,00**	2,52	Ar, 4	Ar, 15	-	-	50%, 70%	Circular (with and without overlap)	-
\cite{ZhiZhao}	AISI 304	400	-	-	10	-	-	-	-	-	d10 =39.41 d50 = 63.28 d90 = 90.69	0,5	-	-	-
\cite{Saboori2020}	316L	900	-	7,5	15	-	-	3,5	Ar, 5	Ar	d10 =51.4 d50 = 71.2 d90 = 91.3	0,45	50%	Interleave layers 67º and 90°apart	-
\cite{zhengHaley}	316L	328	-	7,5	16,9	-	-	28	Ar	Ar	44 - 105	0,25	34%	-	The samples were produced via LENS.
\cite{zietalaDurejko}	316L	400	-	-	15	-	-	5	-	-	44 - 105	0,45	-	-	The samples were produced via LENS.
\cite{zhangWang}	A3	1000	2	10 - 20	8	**62,50**	**65,63**	4		Ar, 5-15	-	-	-	-	Those parameters were optimized in this work.
\cite{BarkiaAubry}	-	600	-	-	6,35	-	-	6			45 - 106	0,4	-	-	-
\cite{Azinpour2020}	-	417	0,8	-	14,67	**36,79**	**96,58**	3	-	-	-	0,5	-	-	-
\cite{Lin2020}	316L	1400	3		6	**77,78**	**54,44**	15	Ar	Ar	d10 =61.38 d50 = 91.64 d90 = 132.6	-	-	-	-
\cite{Kim2019}	316L	400	3		10	**13,33**	**9,33**	10	Ar	N_2	44 - 106	-	31%	-	Those parameters were optmized in this work.
\cite{Yang2017]	316L	360	-	9,5	16,3	-	-	10	-	-	-	0,39	-	Interleave layers 90° apart	-

Table 5.3: DED parameters applied in other studies regarding AISI 316L powder deposition - continuation.

Reference	Substrate	Laser Power (W)	Laser Spot Size (mm)	Stand-off distance (mm)	Scanning speed (mm/min)	Global Energy Density (GED) (J/mm^2)	GED for spot size of 2.1mm	Powder feeding rate (g/min)	Carrier gas flow (Gas, rate (L/min))	Shielding gas flow (Gas, rate (L/min))	Powder diameter (m)	Hatch (mm)	Overlap (%)	Toolpath Strategy	Notes
\cite{Tan2019}	S235JR	1400	3	-	16,6	**28,00**	**19,60**	14	Ar	Ar	45 -105	-	-	-	-
\cite{goodarzipekkarinen}	S355	2000, 2500, 3000, 3500, 4000, 4500	-	15	6.67, 8.33, 10, 13.33 16.67	-	-	20, 30, 40	Ar	Ar	53 - 150	-	-	-	-
\cite{teselara}	AISI 1045	750	1,5	12	5	**100,00**	**140,00**	5,2	Ar, 4	Ar, 35	38 - 212	-	40%	Raster Path	It was deposited AISI 303 powder produced by disc millling of machining chips.
\cite{Jackson2020}	316L	275	-	-	8.47	-	-	8,2	-	-	45 - 150	0,38	-	-	Powder produced through oscillation ball milling of machining chips.

Annex C - Technical Drawing of the specimen for tensile testing

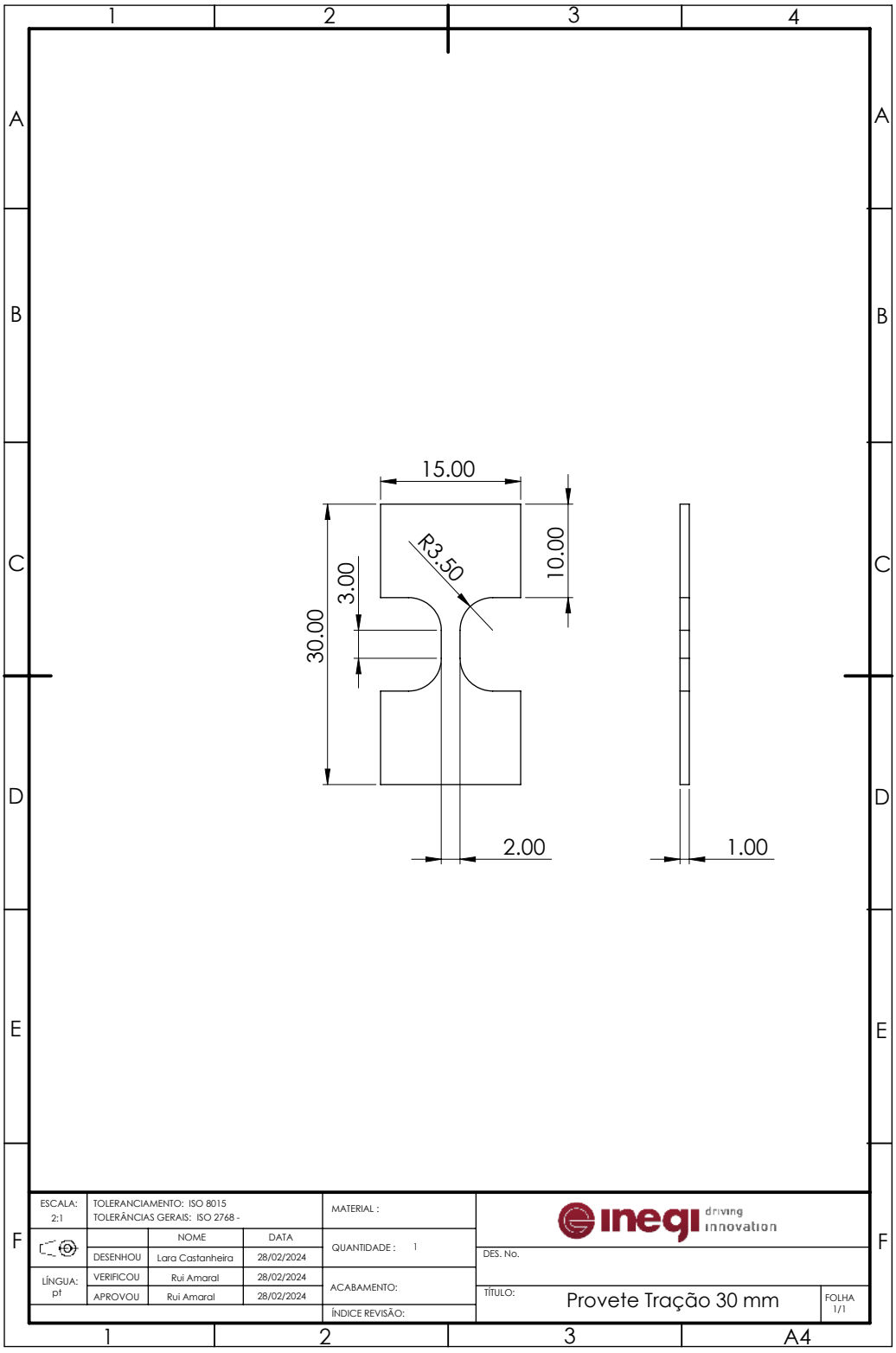

Figure 5.1: Technical Drawing of the specimen for tensile testing.

Annex D - Micrographs of the powder produced through disc and ball milling

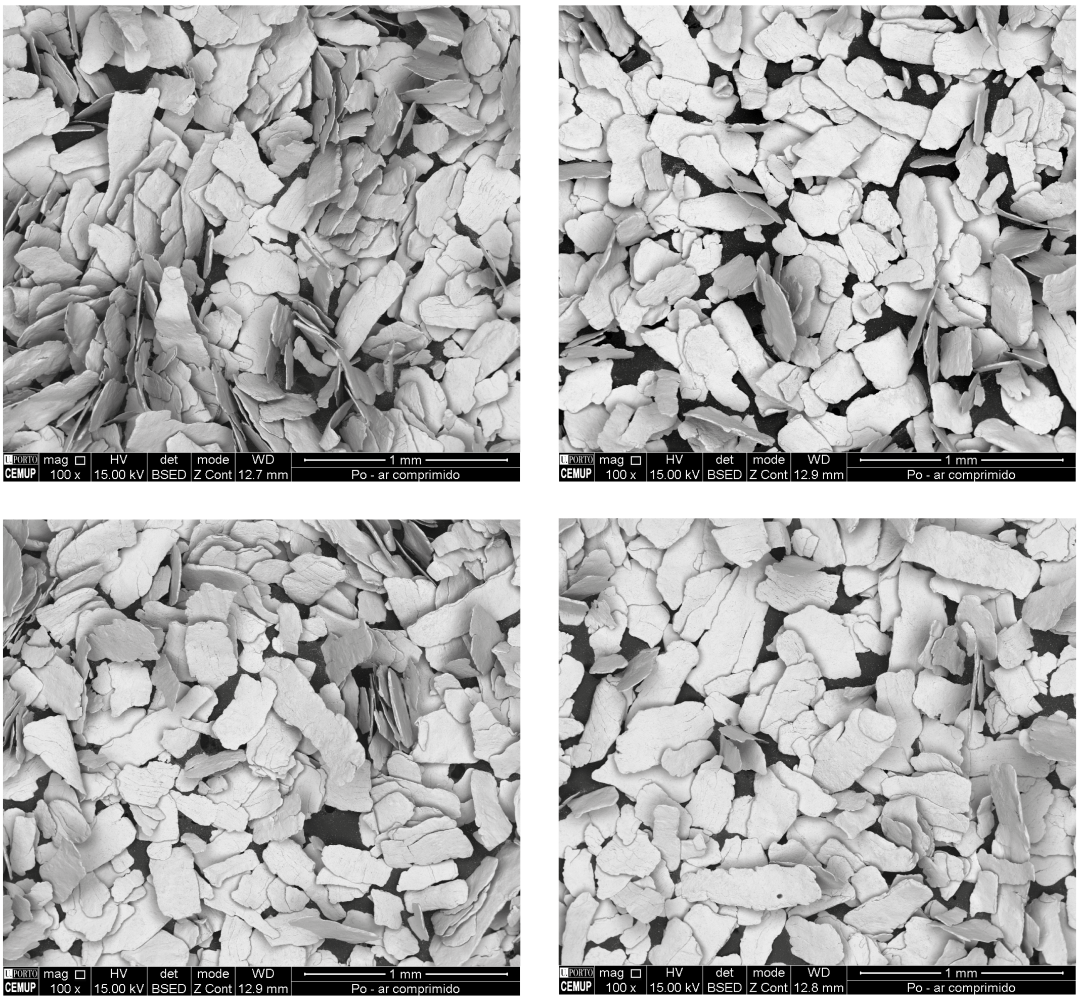

Figure 5.2: SEM micrographs of powder produced in the PN5 disc milling conditions.

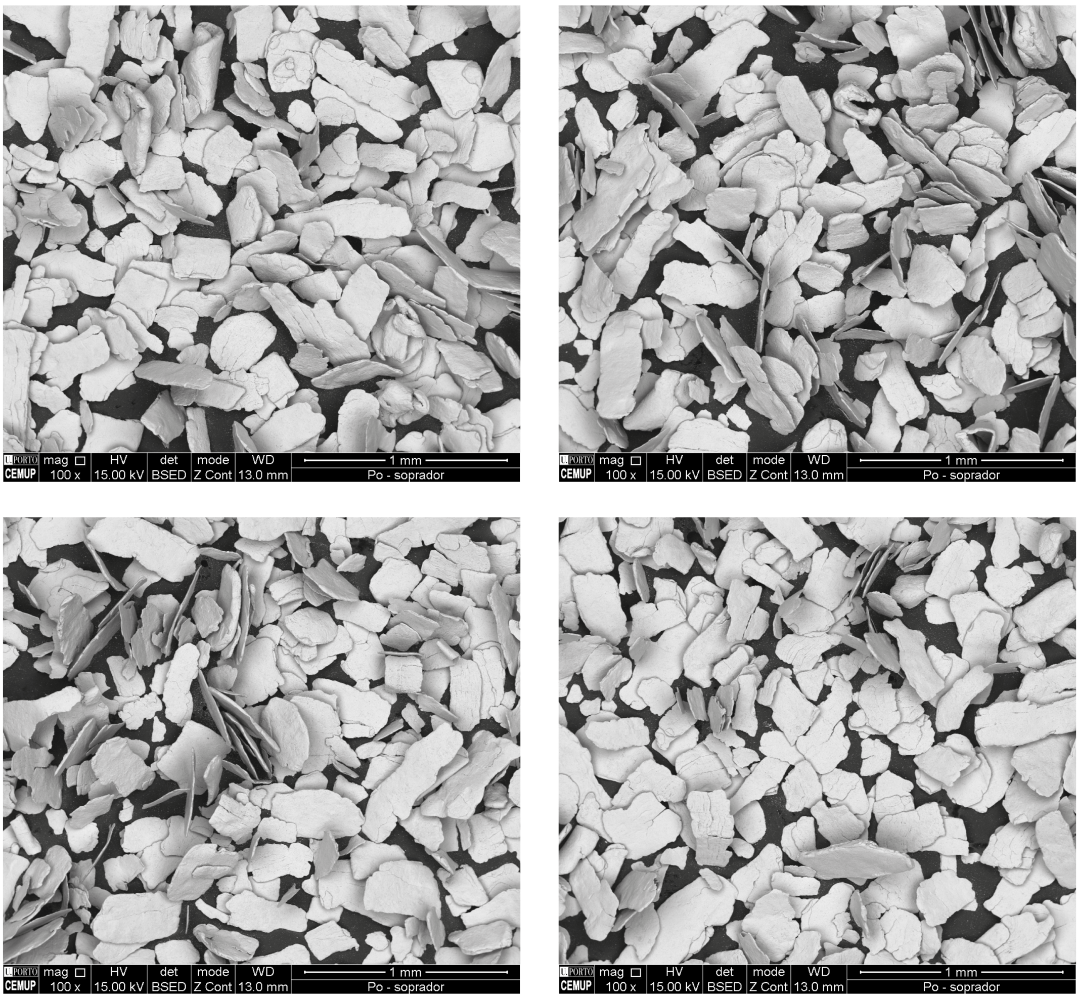

Figure 5.3: SEM micrographs of powder produced in the PN5 disc milling conditions.

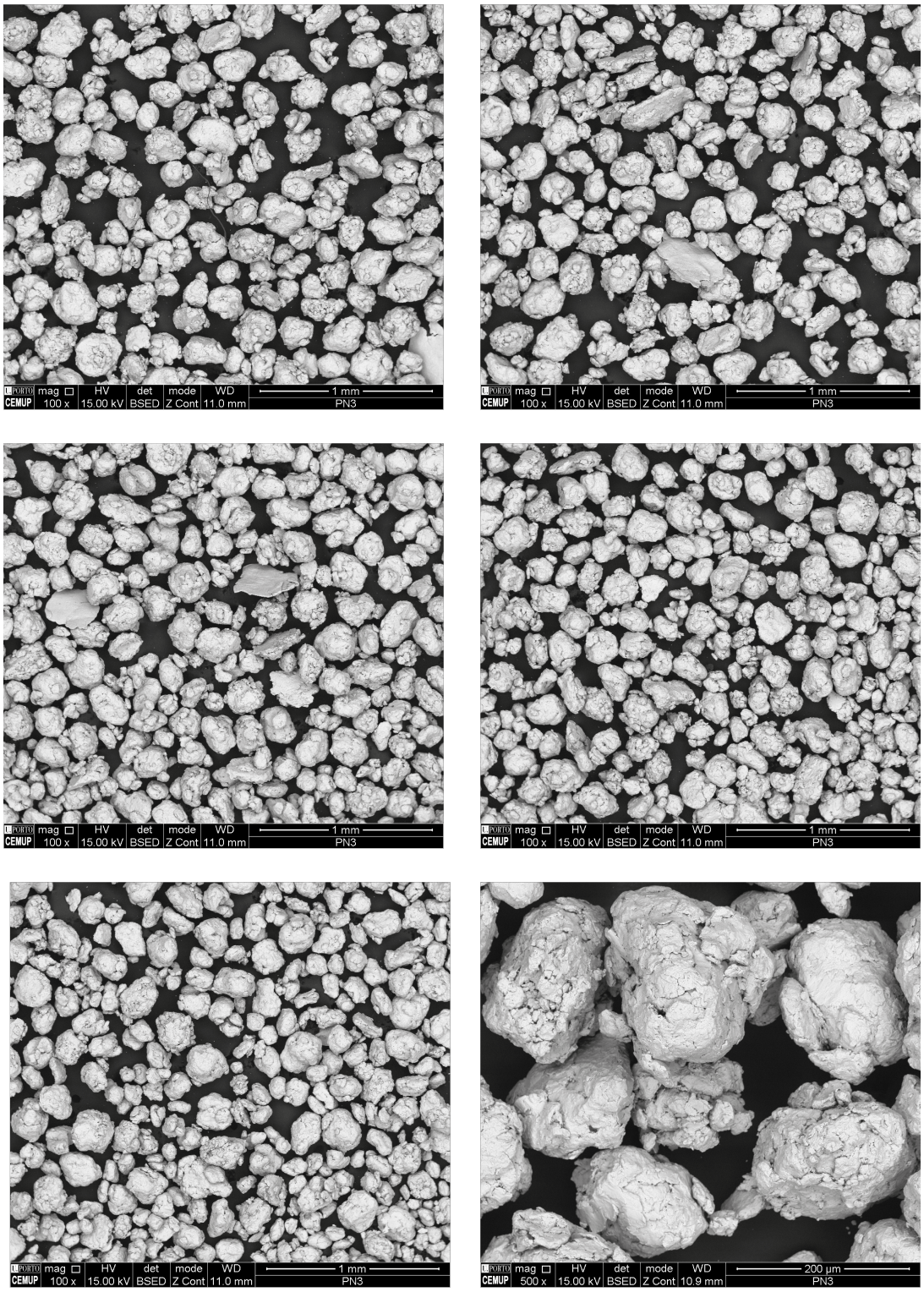

Figure 5.4: SEM micrographs of powder produced in the PN3 ball milling conditions.

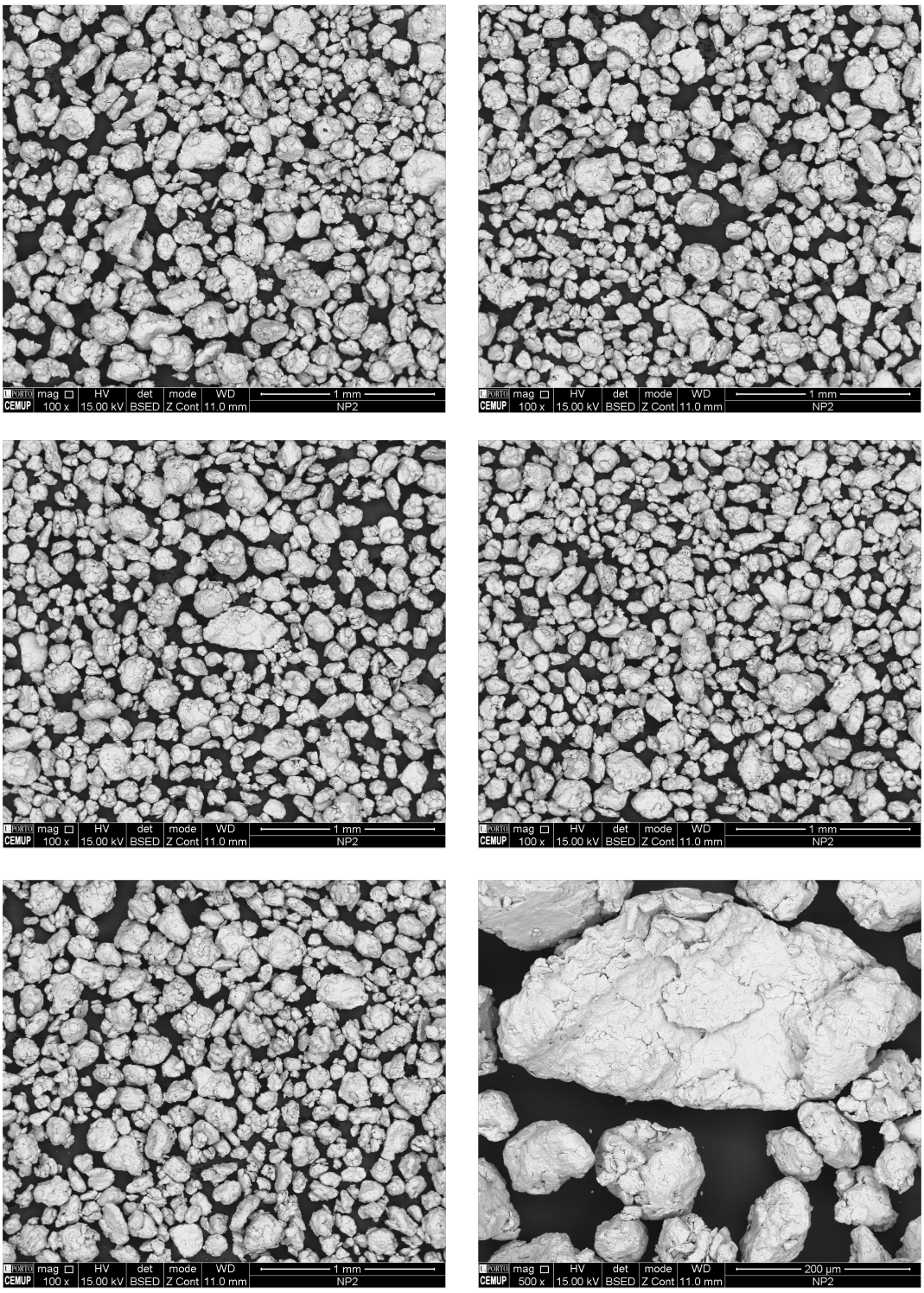

Figure 5.5: SEM micrographs of powder produced in the NP2 ball milling conditions.

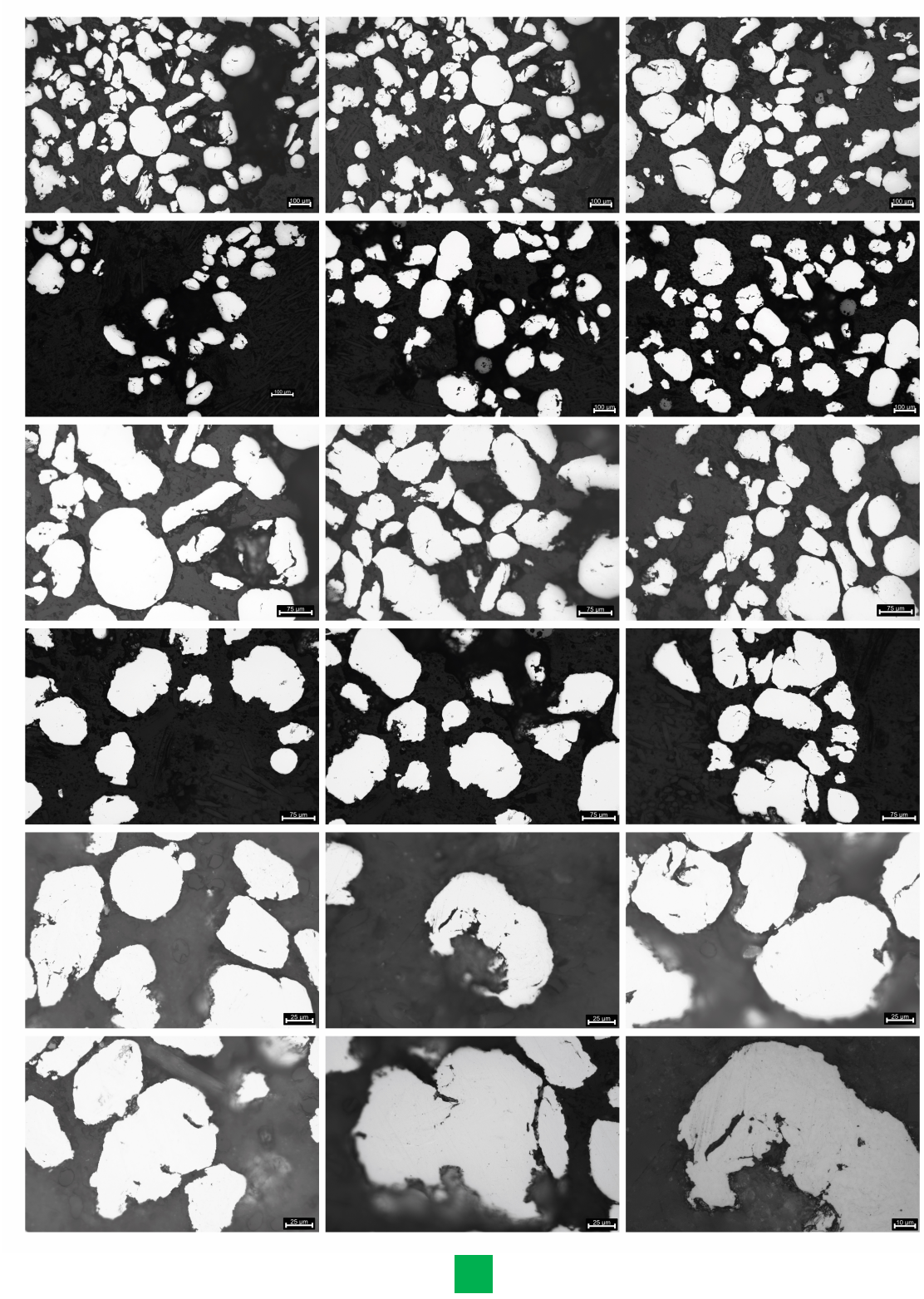

Figure 5.6: Micrographs of powder produced in the NP2 ball milling conditions (polished sample observed under optical microscopy).

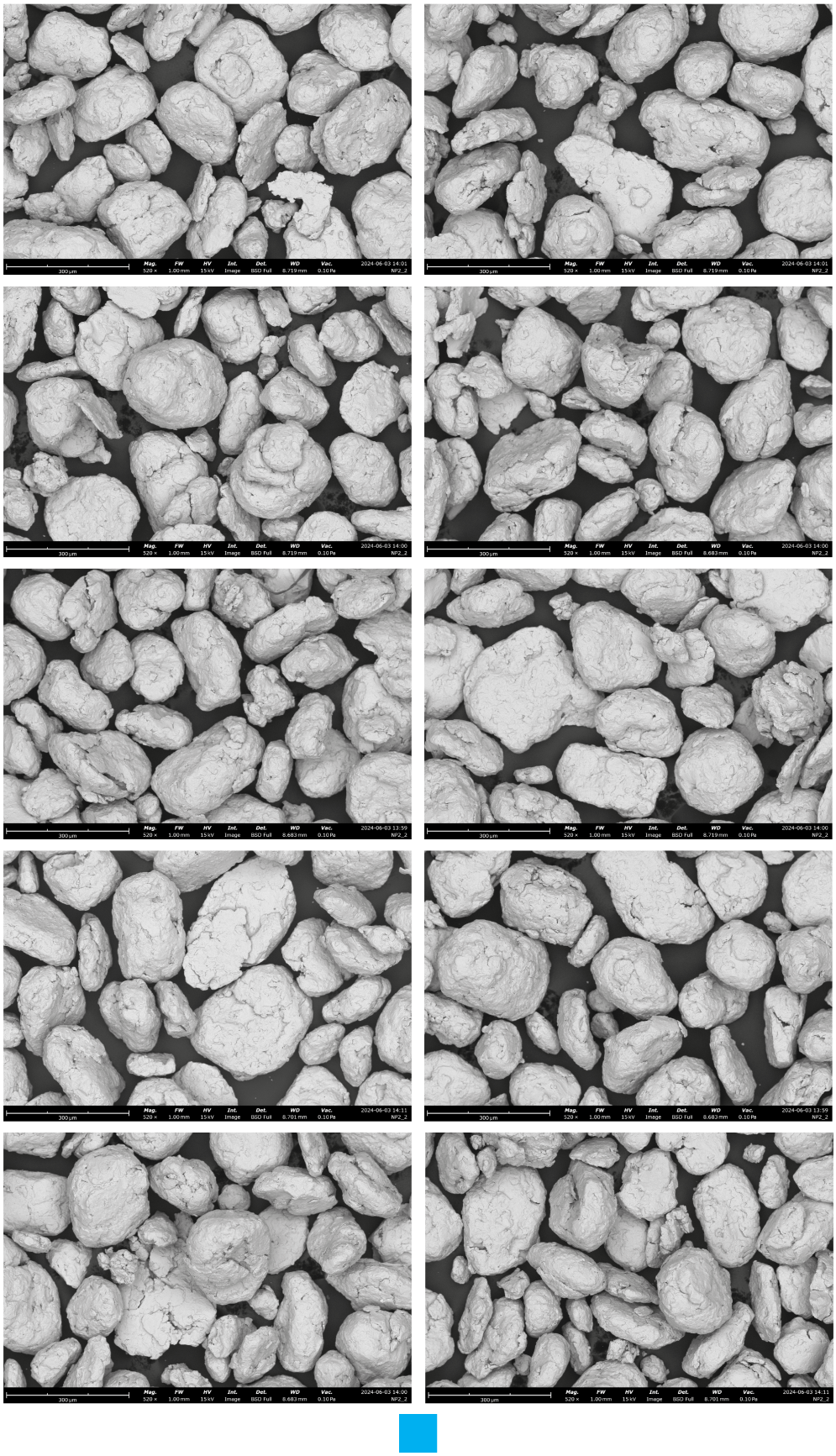

Figure 5.7: SEM micrographs of powder produced in the NP2 (with overused balls) ball milling conditions.

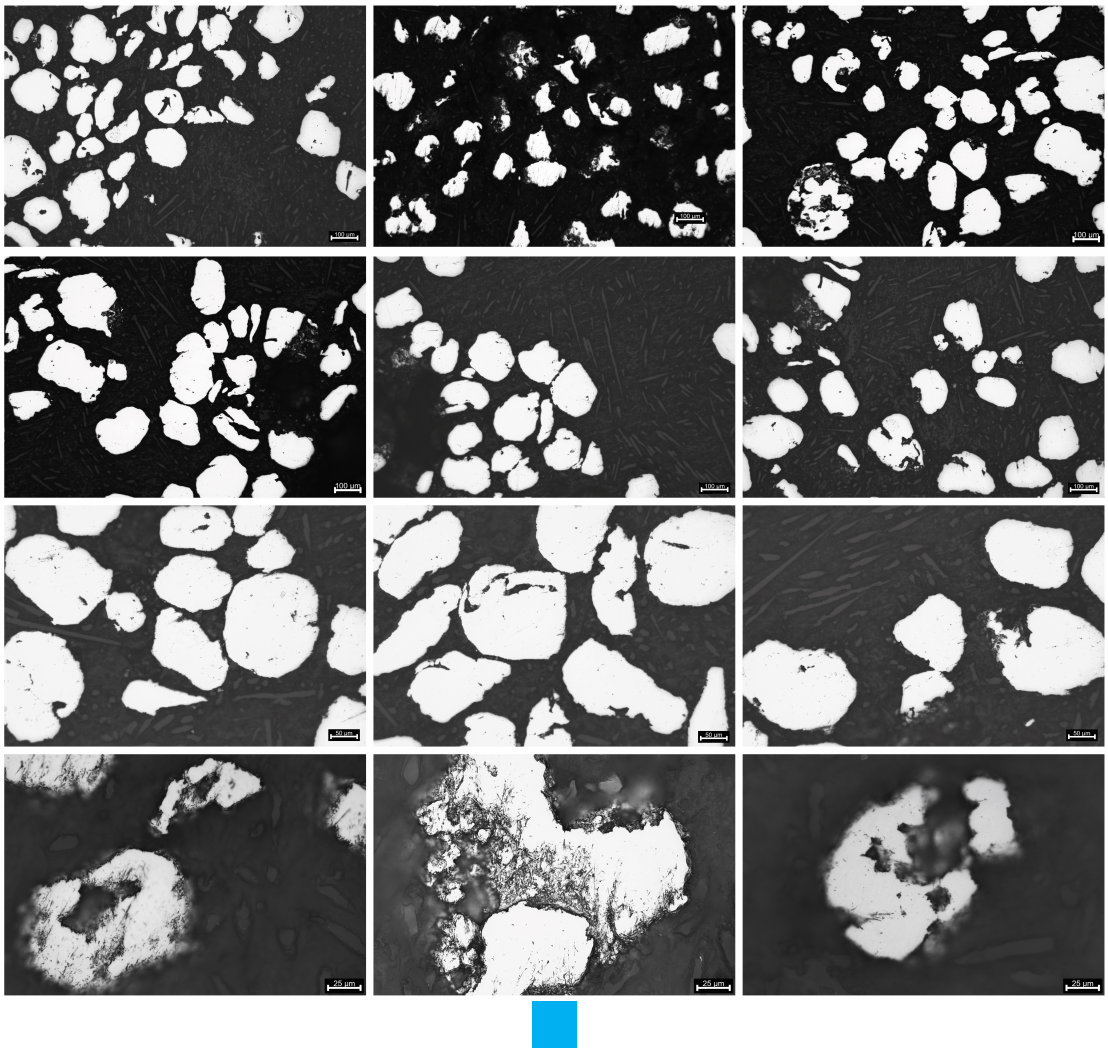

Figure 5.8: Micrographs of powder produced in the NP2 (with overused balls) ball milling conditions (polished sample observed under optical microscopy).

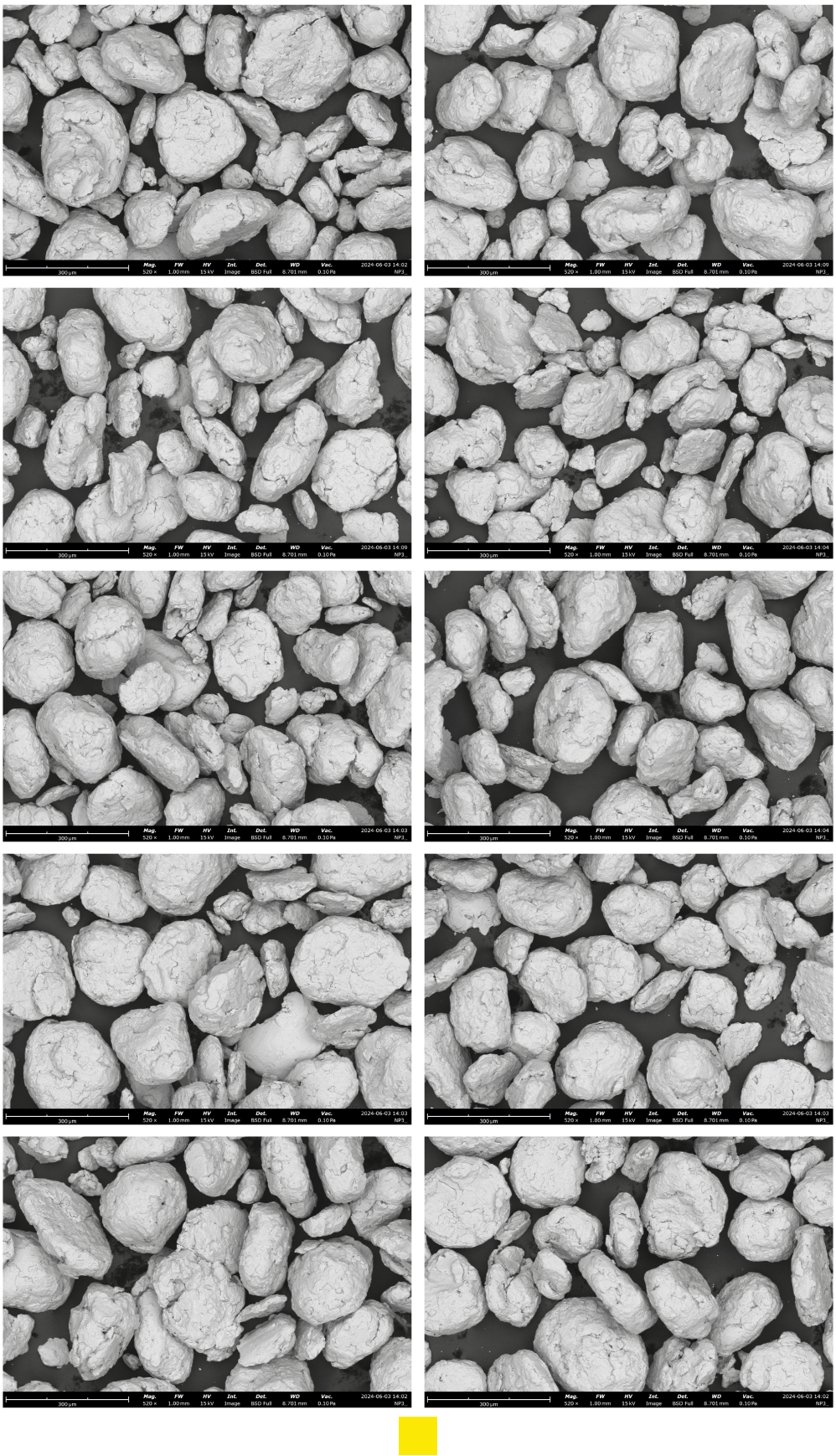

Figure 5.9: SEM micrographs of powder produced in the NP3 ball milling conditions.

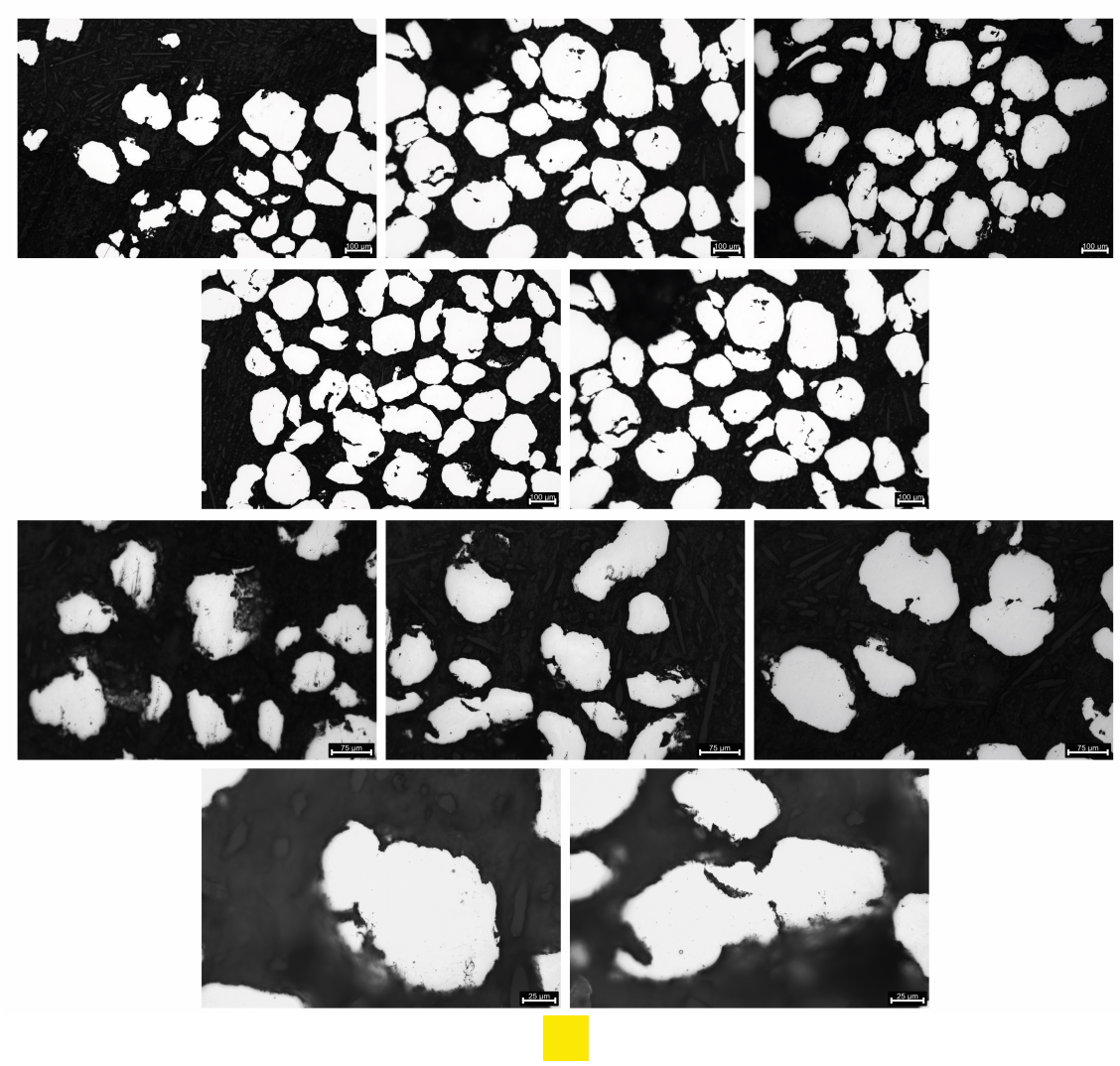

Figure 5.10: Micrographs of powder produced in the NP3 ball milling conditions (polished sample observed under optical microscopy).

Annex E - Micrographs of the DED printed thin wall with upcycled powder

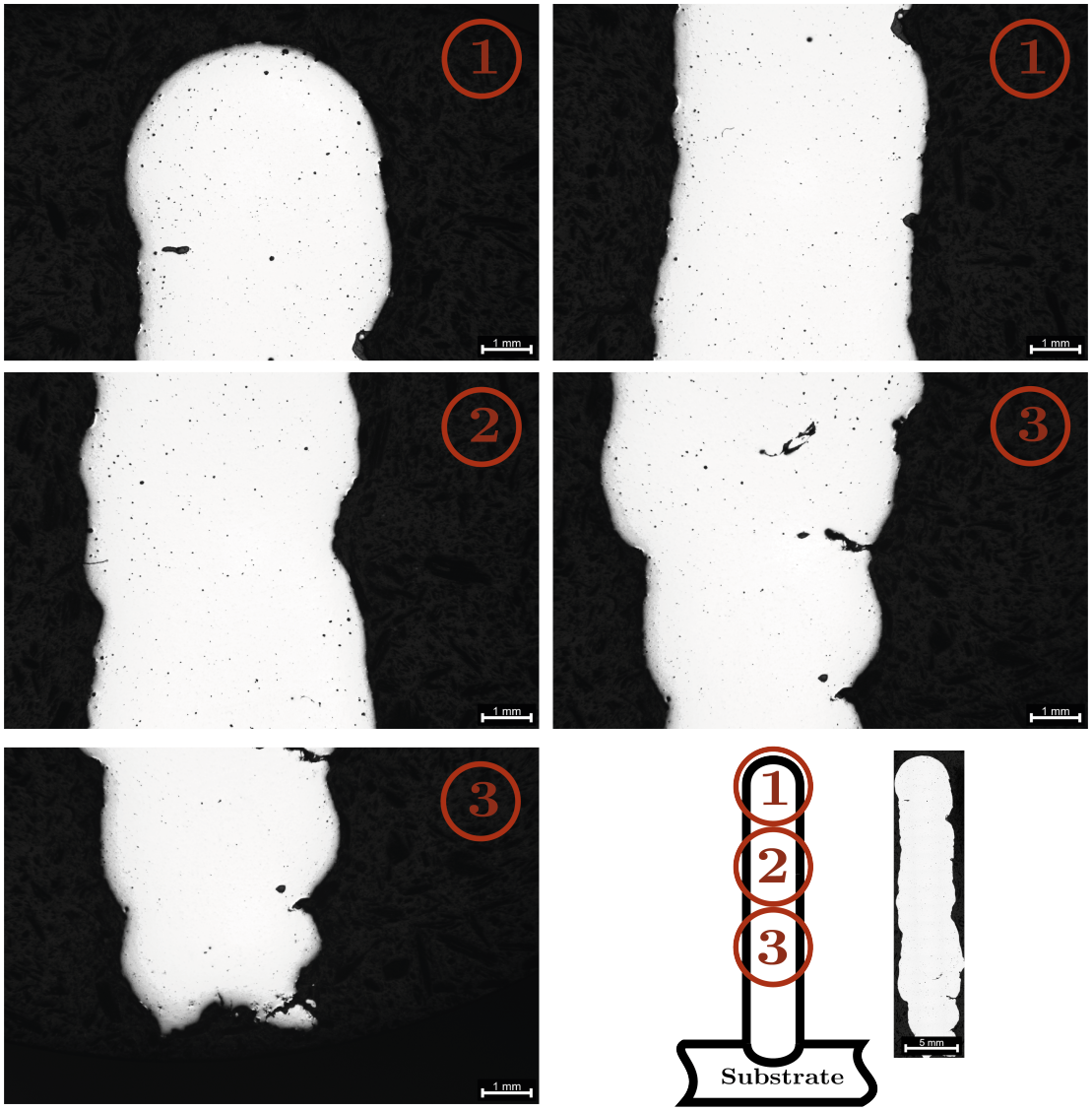

Figure 5.11: Micrographs of the DED printed thin wall with upcycled powder (observed under optical microscopy) and schematic of the 3 different zones observed.

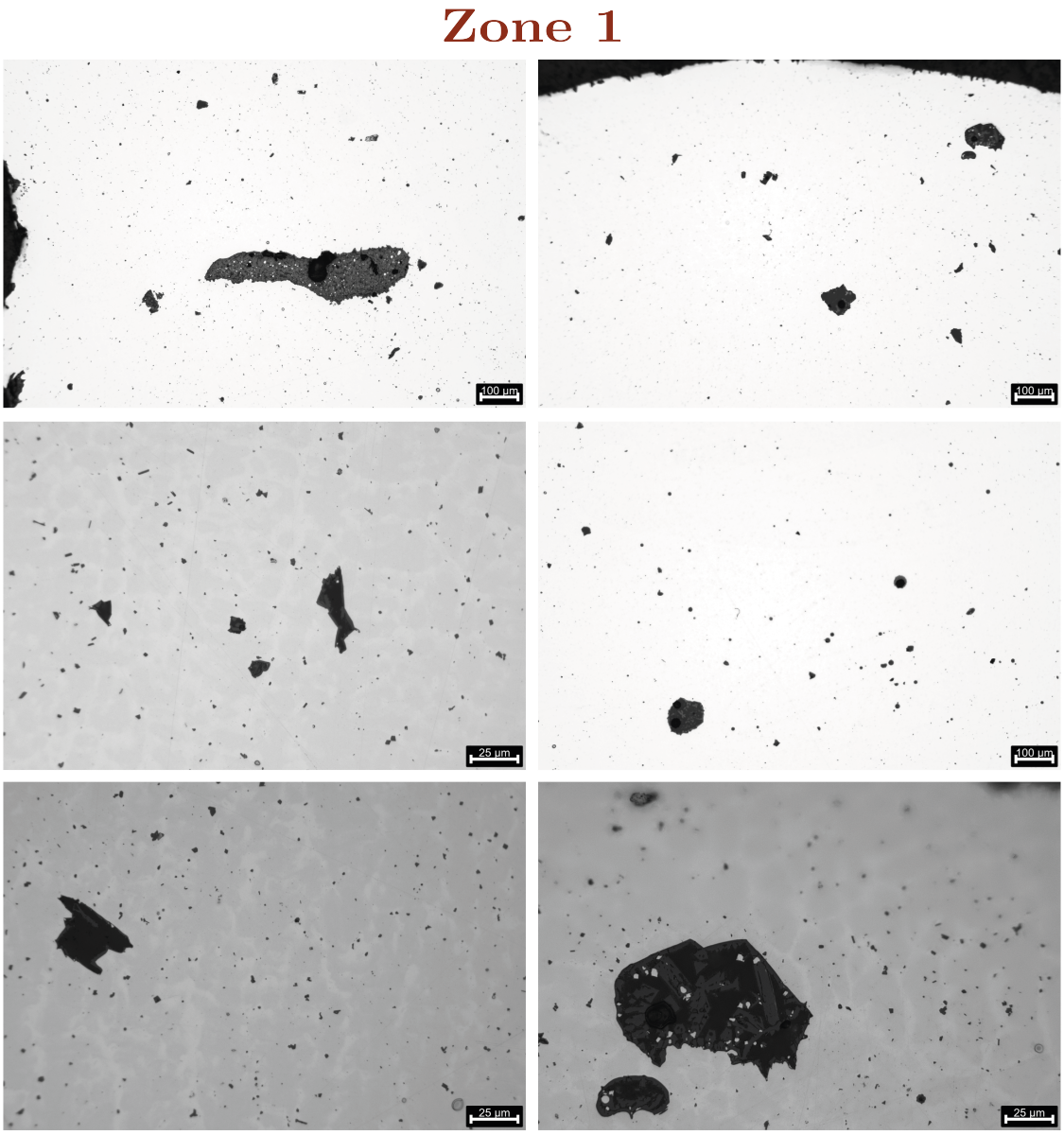

Figure 5.12: Micrographs of the DED printed thin wall with upcycled powder (observed under optical microscopy) - Zone 1

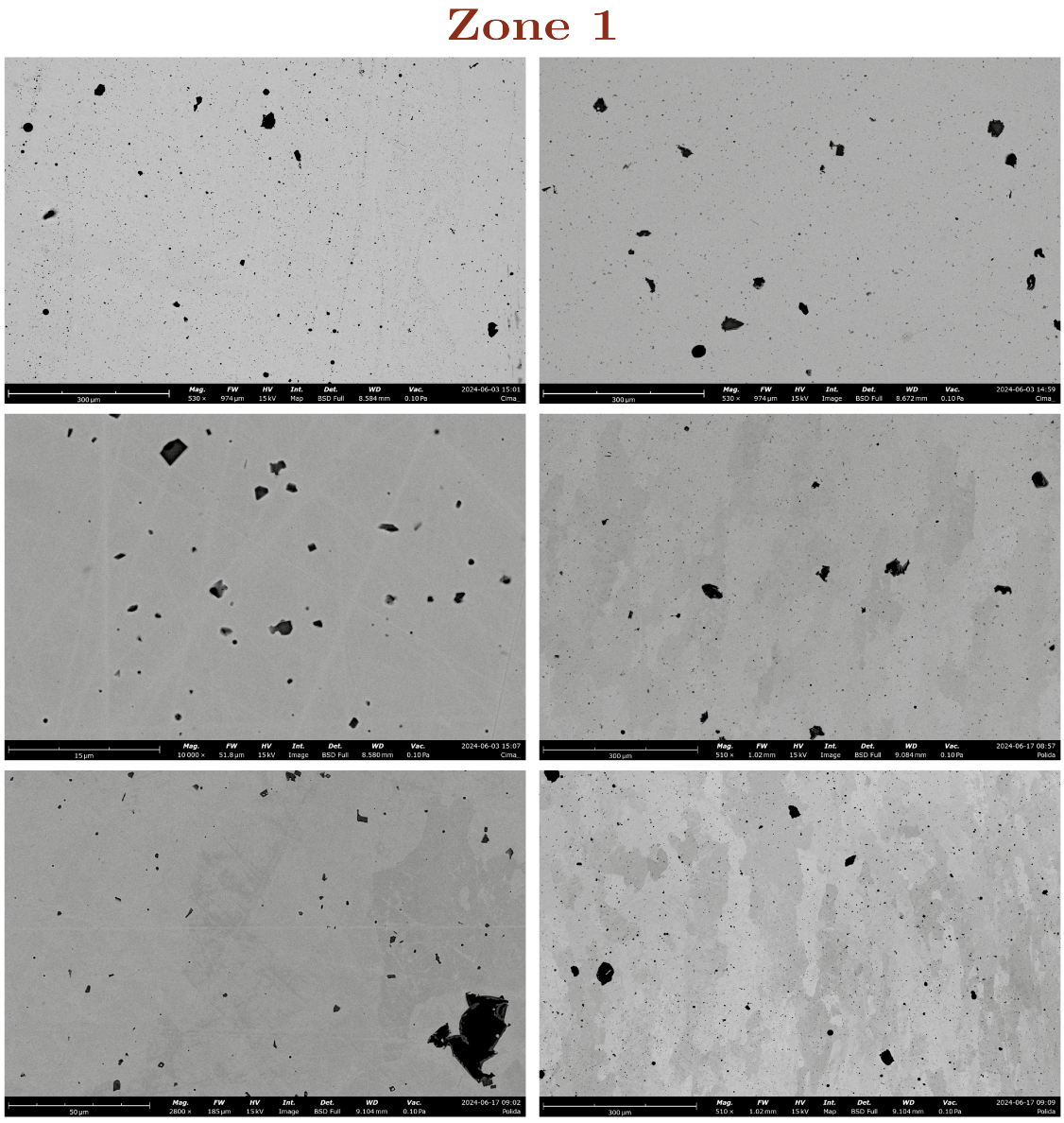

Figure 5.13: Micrographs of the DED printed thin wall with upcycled powder (observed in SEM) - Zone 1

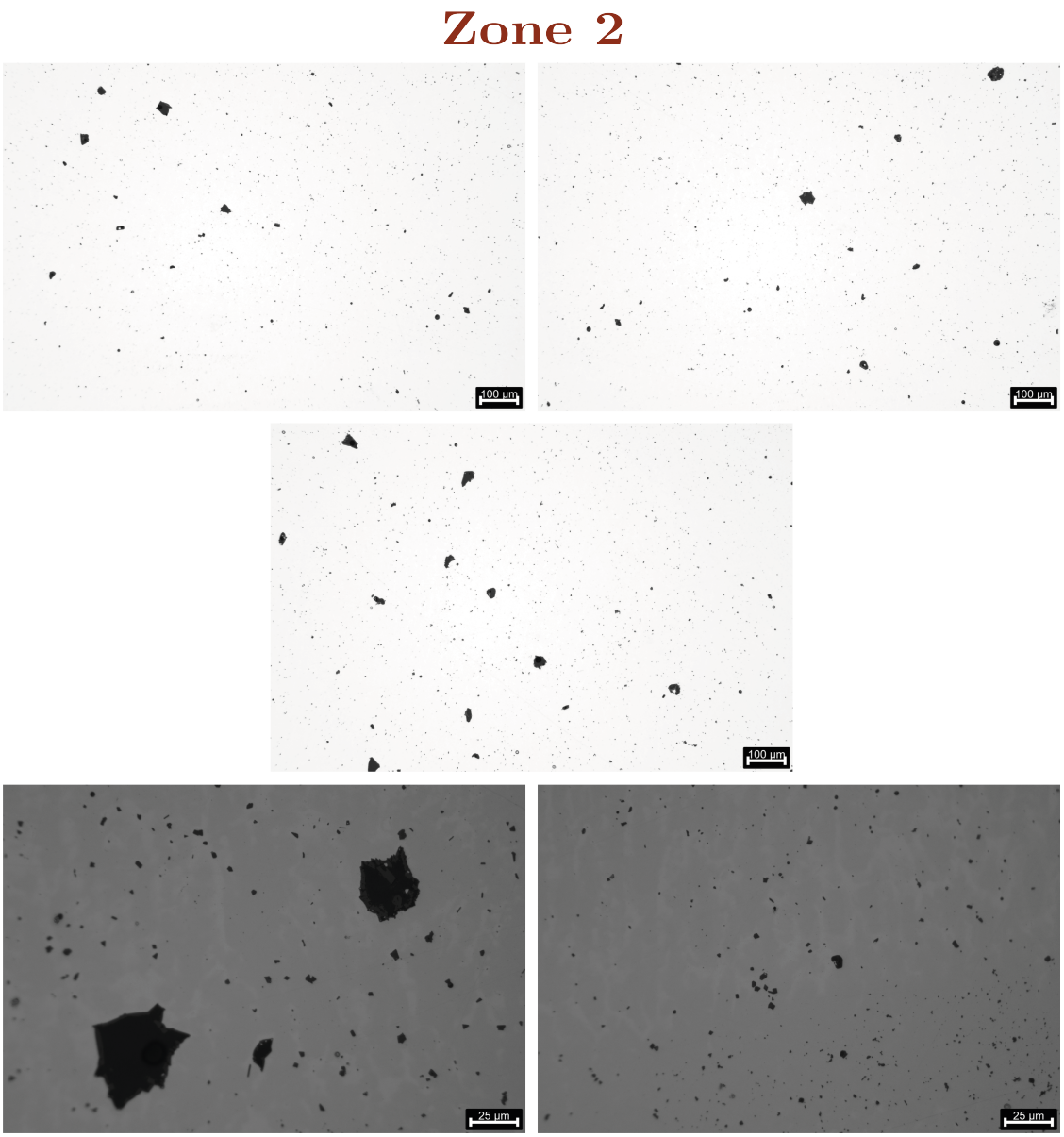

Figure 5.14: Micrographs of the DED printed thin wall with upcycled powder (observed under optical microscopy) - Zone 1

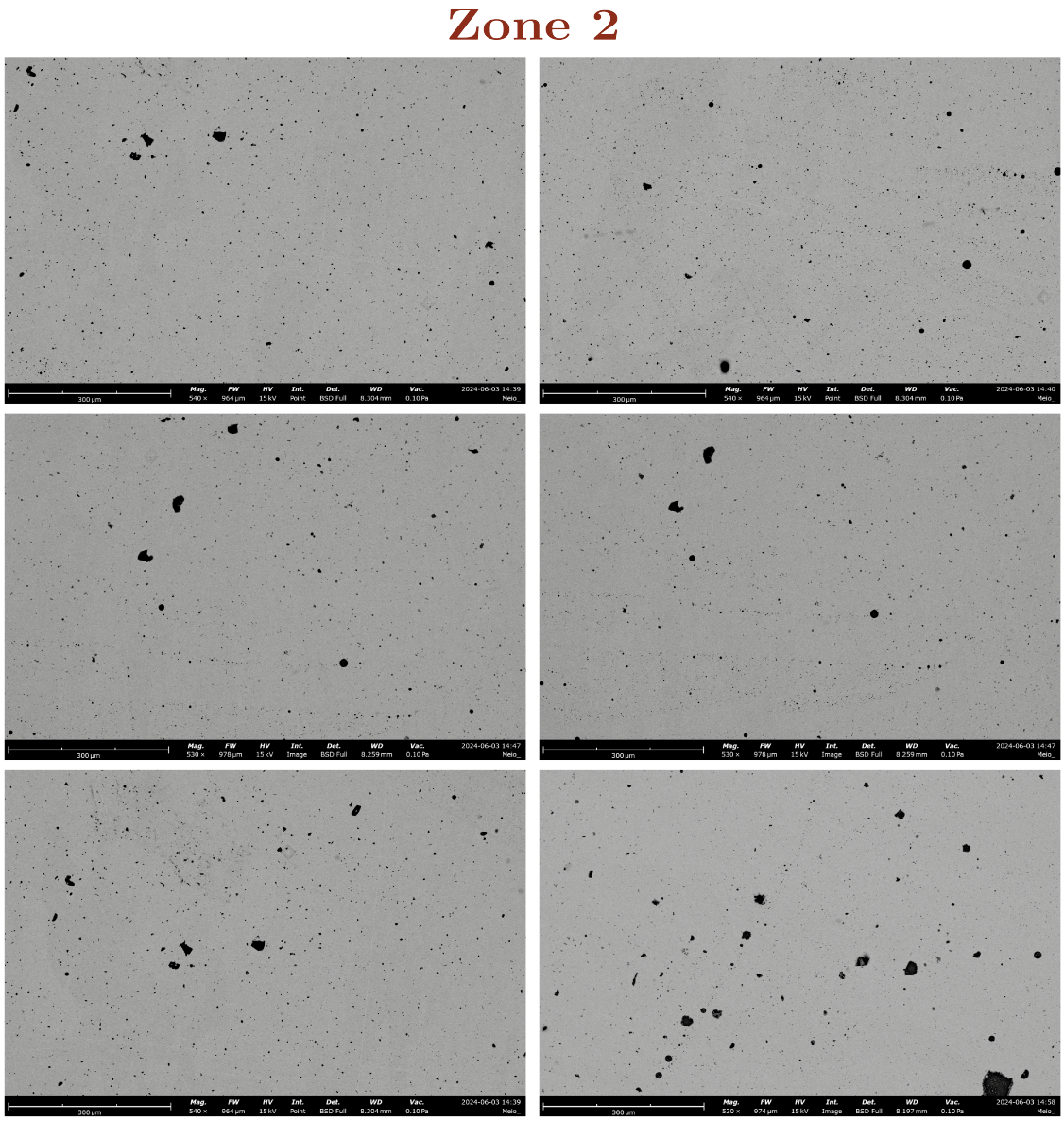

Figure 5.15: Micrographs of the DED printed thin wall with upcycled powder (observed in SEM) - Zone 2

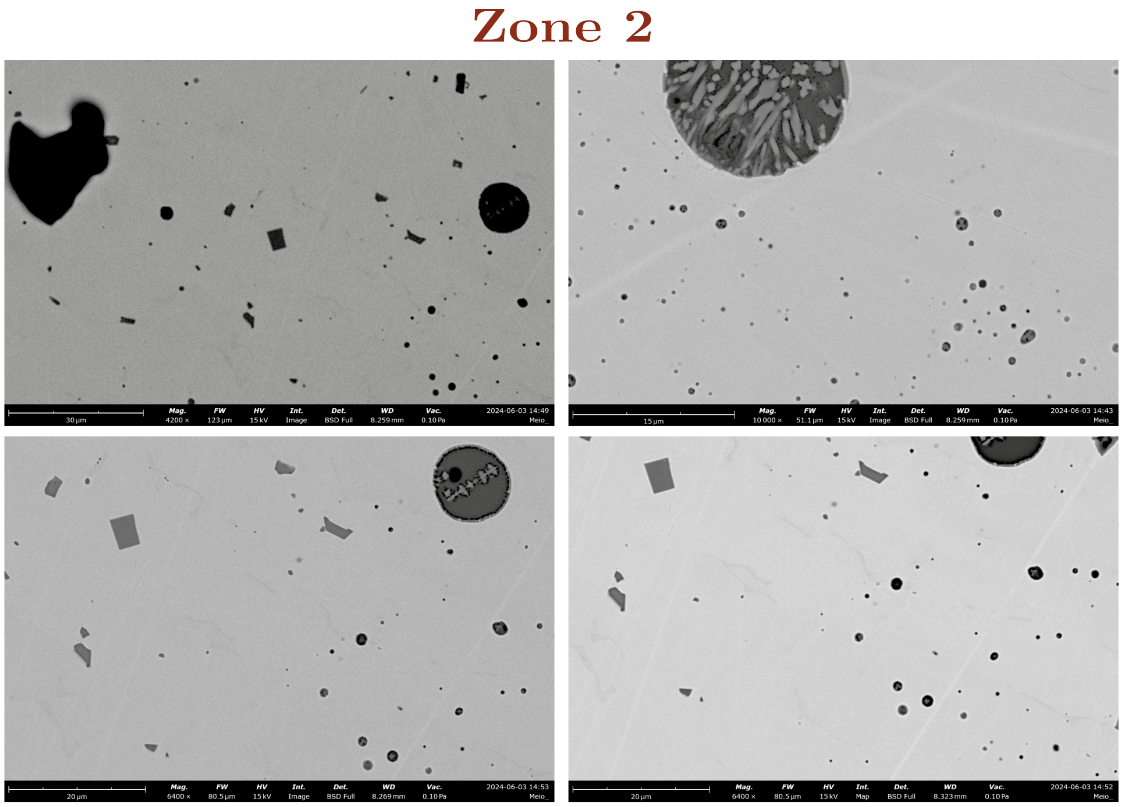

Figure 5.16: Micrographs of the DED printed thin wall with upcycled powder (observed in SEM) - Zone 2

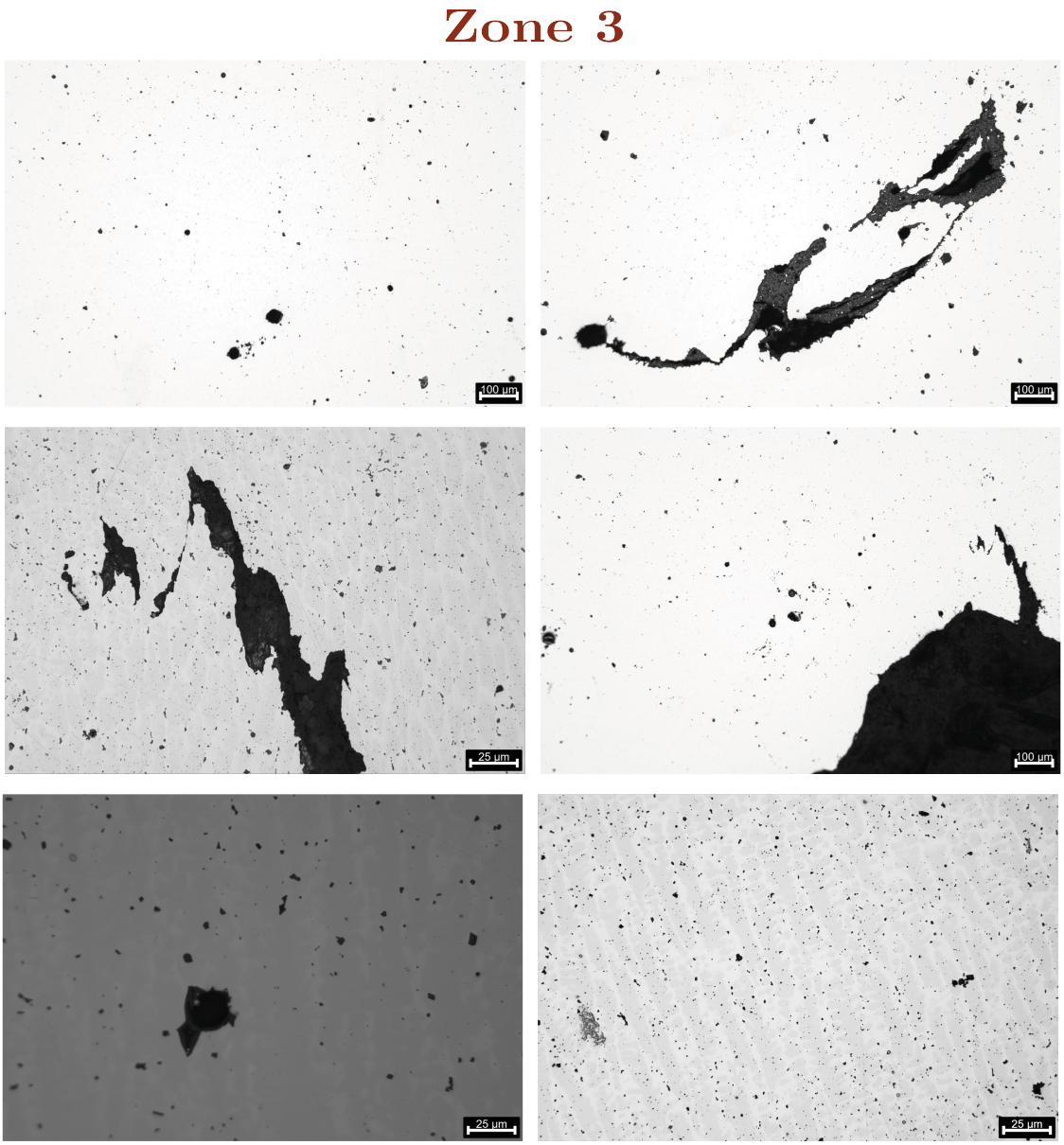

Figure 5.17: Micrographs of the DED printed thin wall with upcycled powder (observed under optical microscopy) - Zone 1

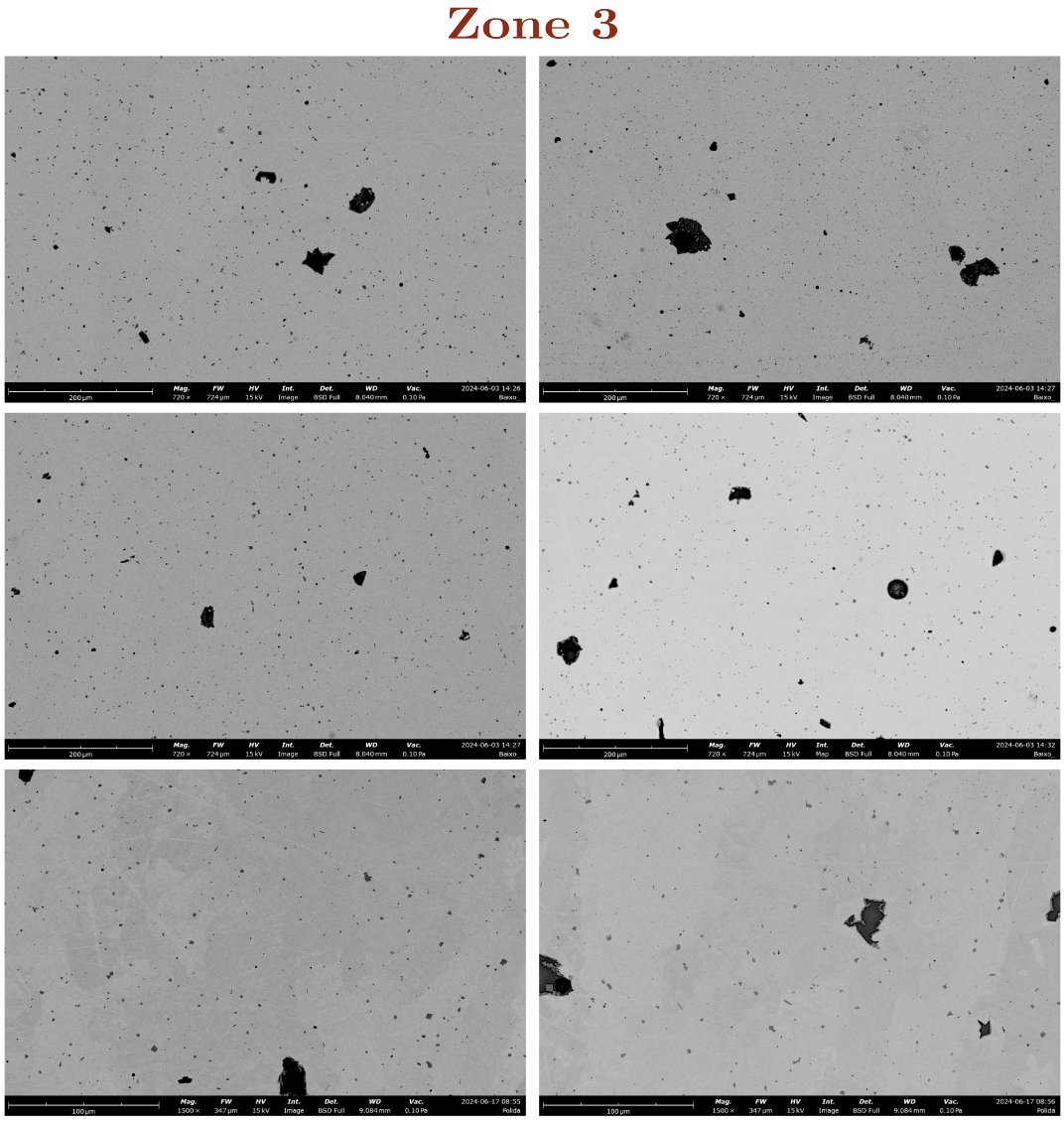

Figure 5.18: Micrographs of the DED printed thin wall with upcycled powder (observed in SEM) - Zone 3

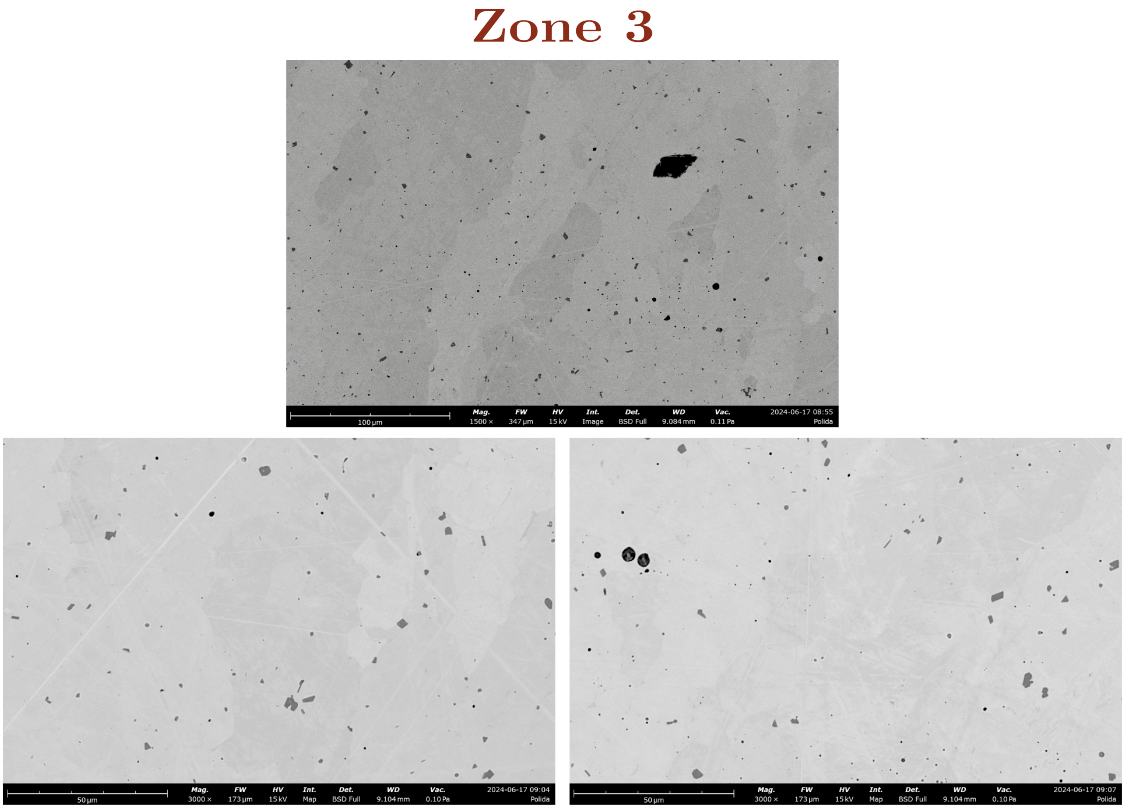

Figure 5.19: Micrographs of the DED printed thin wall with upcycled powder (observed in SEM) - Zone 3

Annex F - Semi-quantitative chemical composition of a thin wall printed with upcycled powder - Matrix measurements

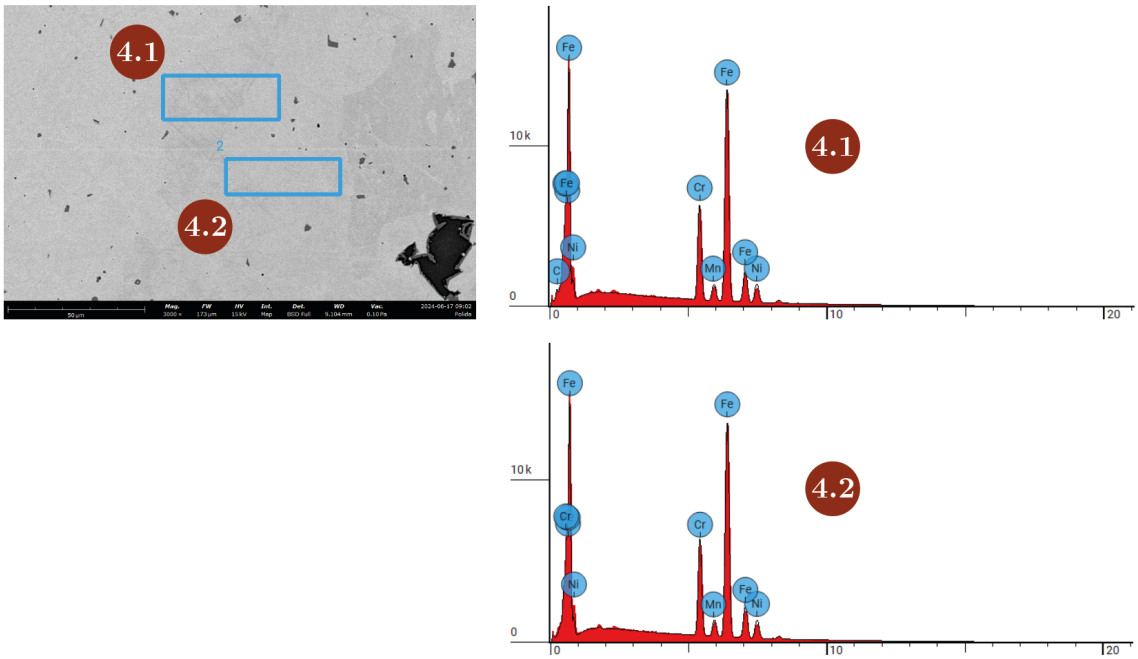

Figure 5.20: Semi-quantitative chemical composition of a thin wall printed with upcycled powder - Matrix measurement.

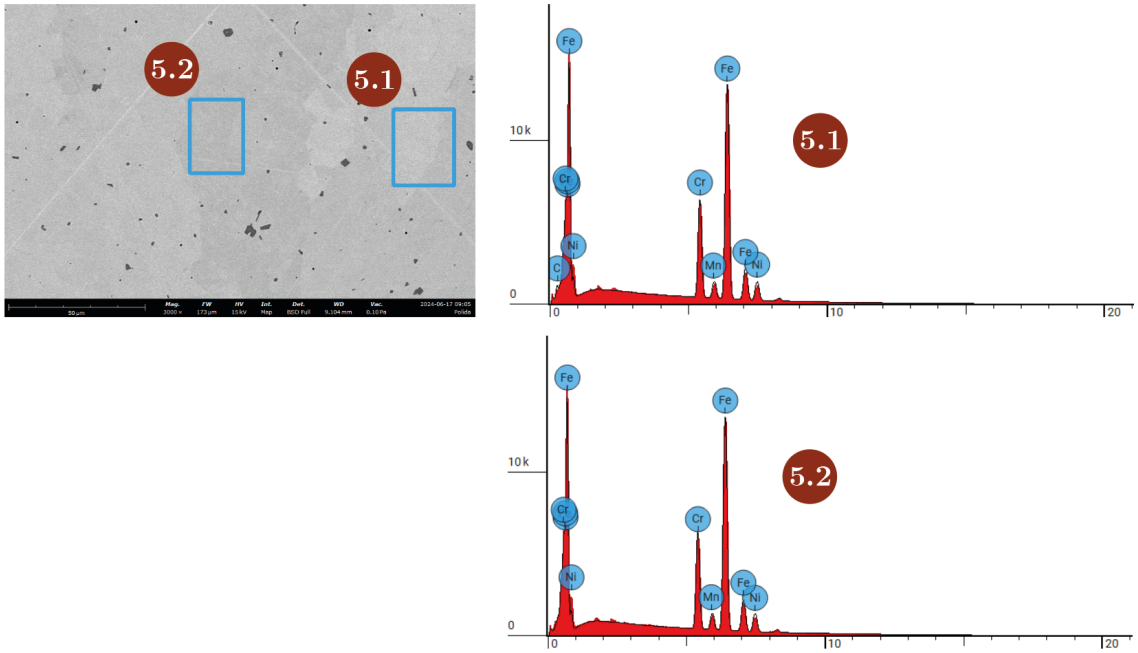

Figure 5.21: Semi-quantitative chemical composition of a thin wall printed with upcycled powder - Matrix measurement.

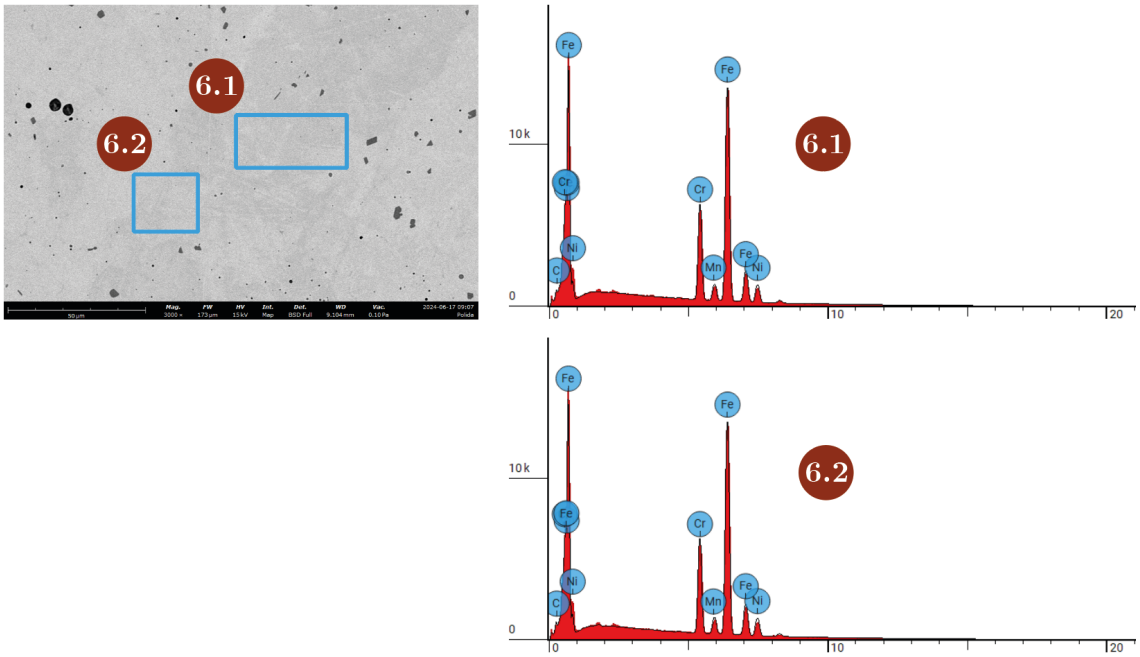

Figure 5.22: Semi-quantitative chemical composition of a thin wall printed with upcycled powder - Matrix measurement.

Annex G - Semi-quantitative chemical composition of the original block (as supplied) - Matrix measurements

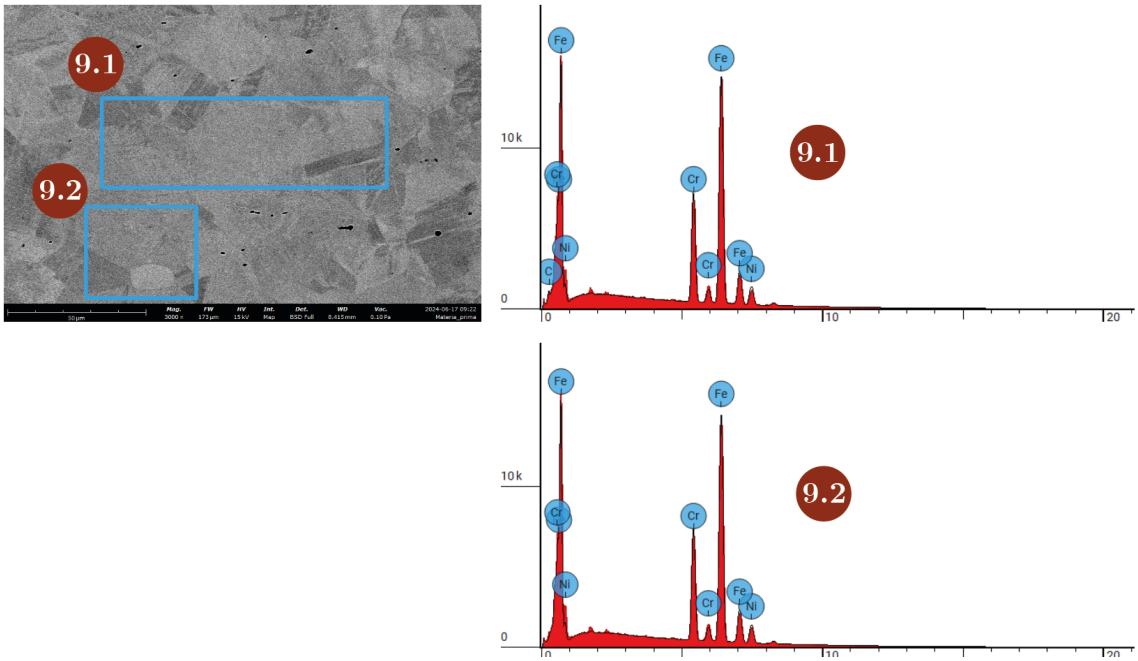

Figure 5.23: Semi-quantitative chemical composition of the original block (as supplied) - Matrix measurement.

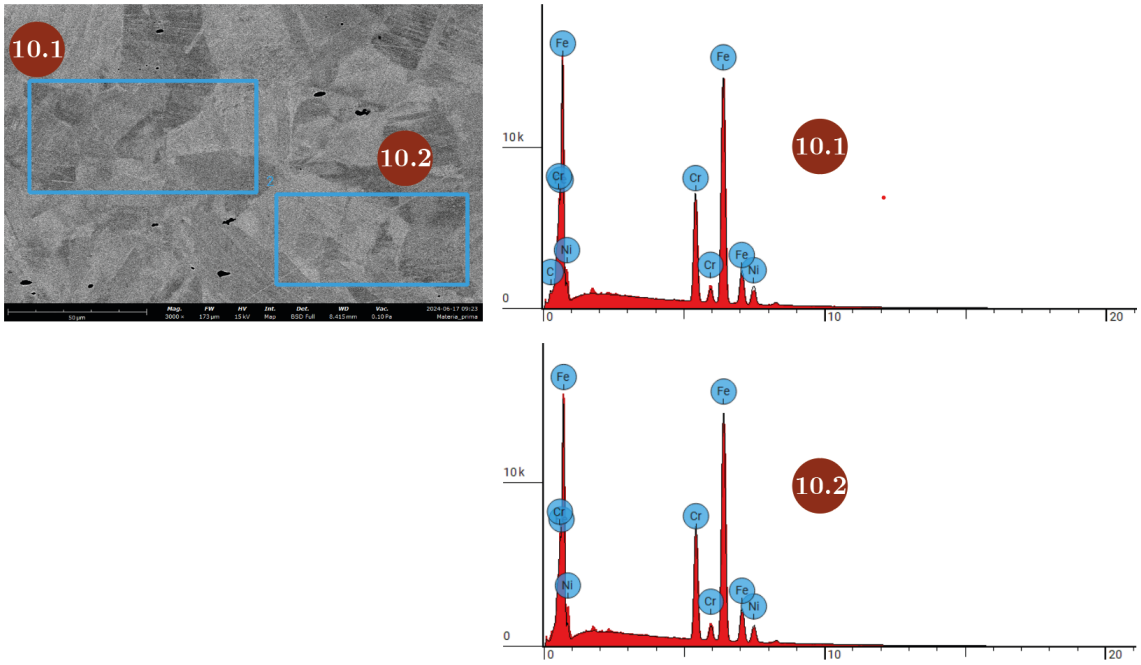

Figure 5.24: Semi-quantitative chemical composition of the original block (as supplied)r - Matrix measurement.

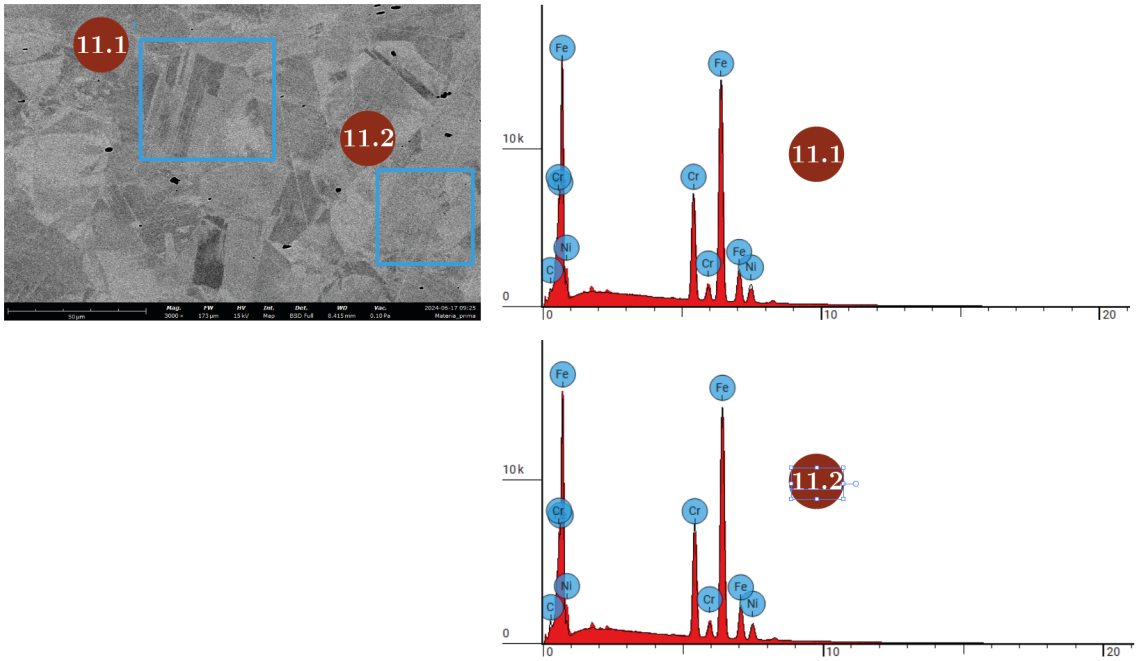

Figure 5.25: Semi-quantitative chemical composition of the original block (as supplied) - Matrix measurement.

Annex H - Semi-quantitative chemical composition measurements on a thin wall printed with upcycled powder

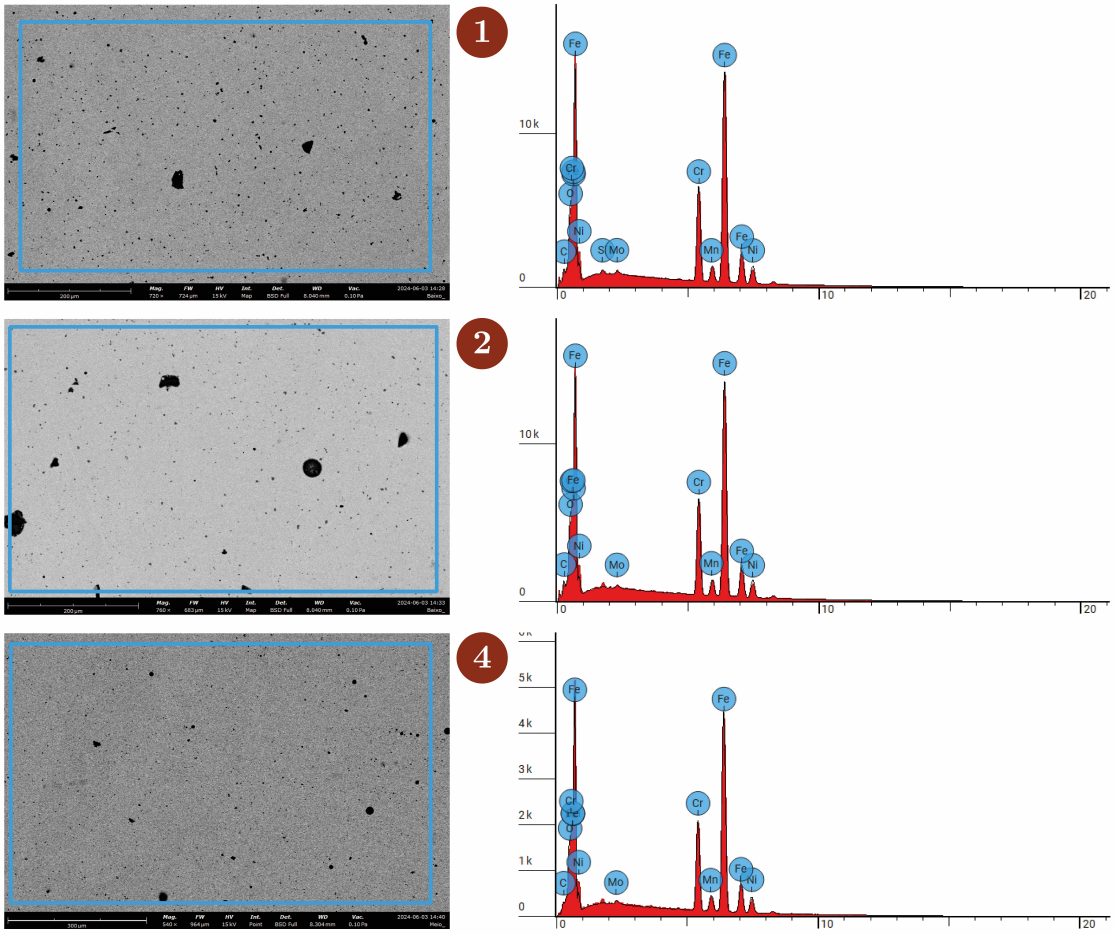

Figure 5.26: Semi-quantitative chemical composition of a thin wall printed with upcycled powder.

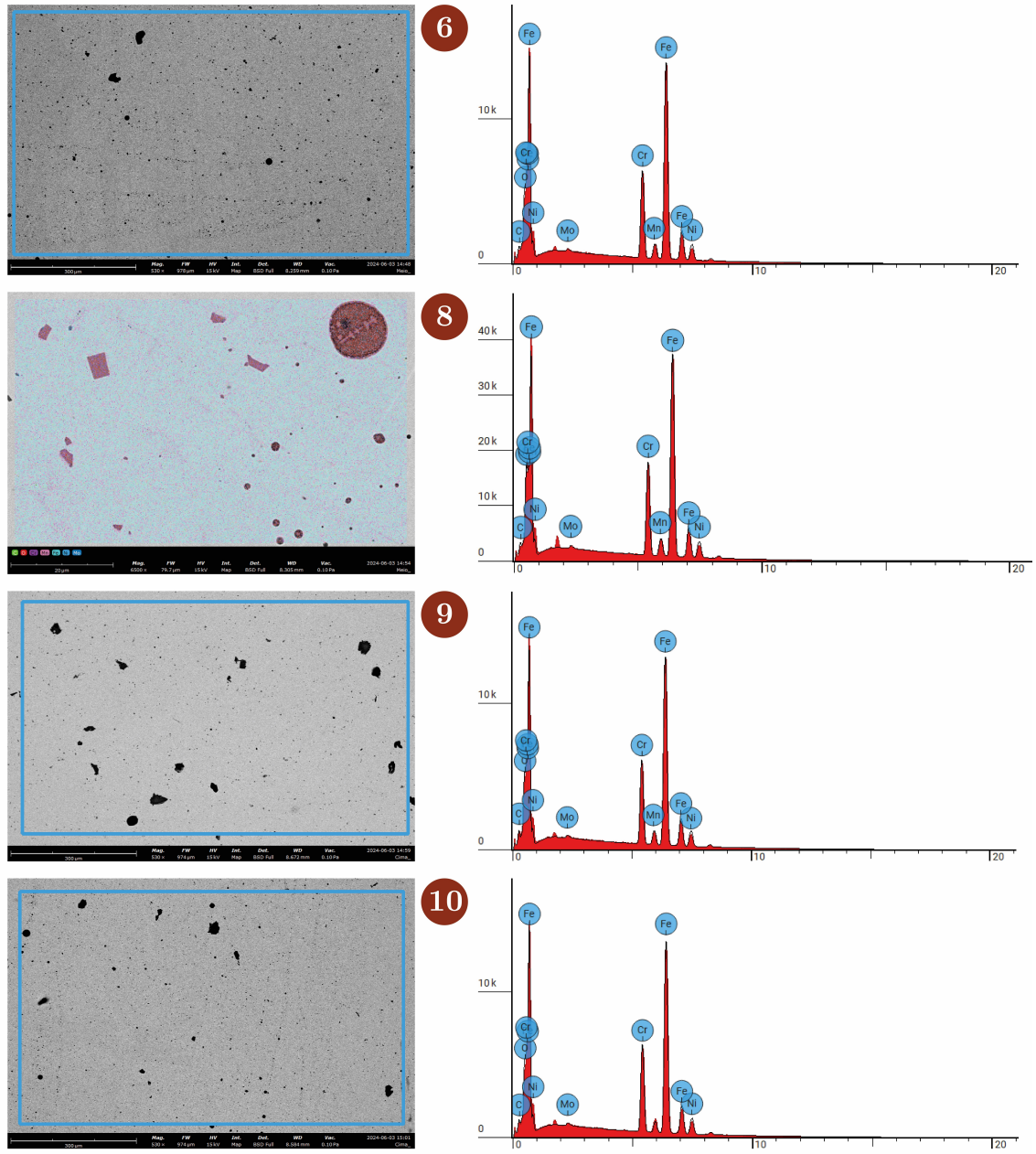

Figure 5.27: Semi-quantitative chemical composition of a thin wall printed with upcycled powder (continuation).

Annex I - Semi-quantitative chemical composition of inclusions observed in the DED printed thin wall (with upcycled powder)

Table 5.4: Semi-quantitative chemical composition (wt%) of inclusions observed in the DED printed thin wall (with upcycled powder).

Semi-quantitative chemical composition (wt%) of the inclusions														
Inclusion number	**Fe**	**Tl**	**Cr**	**Si**	**Mn**	**Al**	**Ni**	**S**	**Ti**	**V**	**Cl**	**Ca**	**O**	**C**
3.1	-	-	11,912	19,620	22,923	3,203	-	0,701	-	-	-	-	41,642	-
3.2	-	-	10,400	22,800	21,600	3,400	-	-	-	-	-	-	41,800	-
5.1	-	-	22,478	12,188	21,578	4,096	-	-	1,299	-	-	-	38,362	-
5.2	30,319	-	23,330	6,372	13,669	0,925	1,233	0,925	-	-	-	-	23,227	2,7
5.3	35,766	-	19,917	6,465	11,887	1,147	2,190	0,938	-	-	-	-	21,689	4,1
5.4	47,692	-	19,590	3,795	7,590	0,615	4,923	0,821	-	-	-	-	14,974	2,5
5.5	34,532	-	24,153	5,858	13,977	0,822	2,980	-	-	-	-	-	17,677	2,797
7.1	0,000	-	13,400	17,400	27,600	1,700	-	1,300	-	-	-	-	38,600	-
7.2	0,000	-	43,944	-	17,317	1,702	-	-	-	2,402	-	-	34,635	-
7.3	17,017	-	17,317	12,412	19,620	2,102	-	3,504	-	-	-	-	28,028	-
11.1	4,426	-	34,352	4,109	15,174	4,109	-	-	-	-	0,632	1,370	35,827	5,195
112	13,641	-	38,090	-	15,950	1,784	-	-	-	2,099	-	-	28,437	4,7
11.3	10,114	0,522	40,147	-	16,163	0,625	1,043	-	-	2,190	-	-	29,197	4,196
11.4	41,240	-	28,846	-	12,394	-	3,525	4,167	-	-	-	-	9,829	6,306
11.5	24,843	-	35,535	-	14,465	-	2,201	1,153	-	-	-	-	21,803	4,6

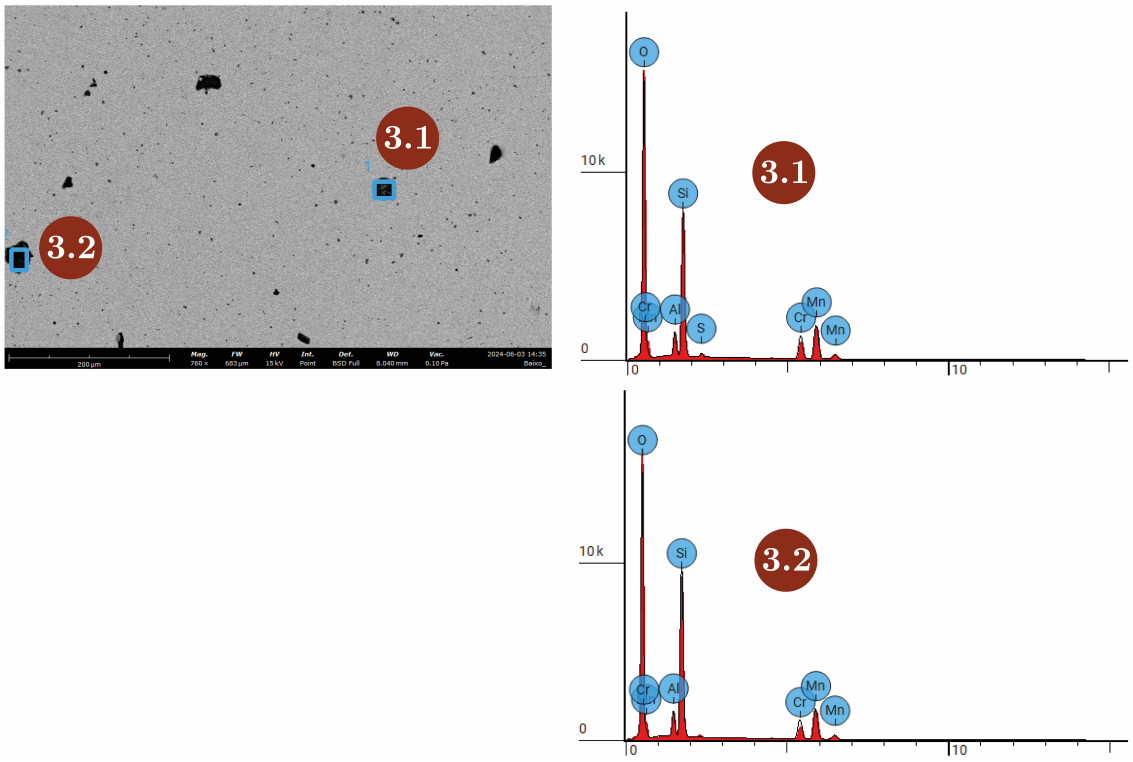

Figure 5.28: Semi-quantitative chemical composition of the inclusions numbered 3.1 and 3.2.

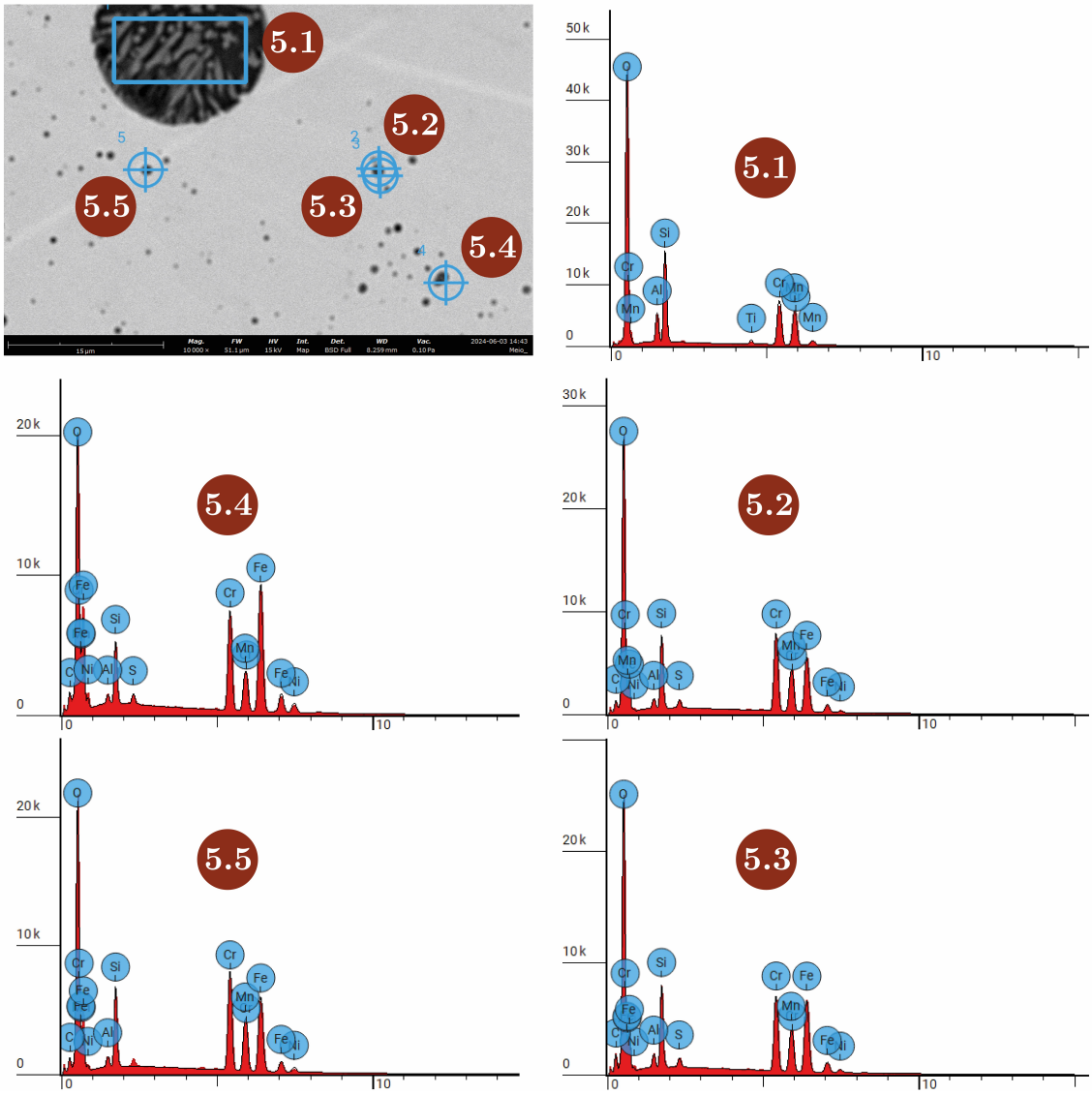

Figure 5.29: Semi-quantitative chemical composition of the inclusions numbered 5.1, 5.2, 5.3, 5.4 and 5.5.

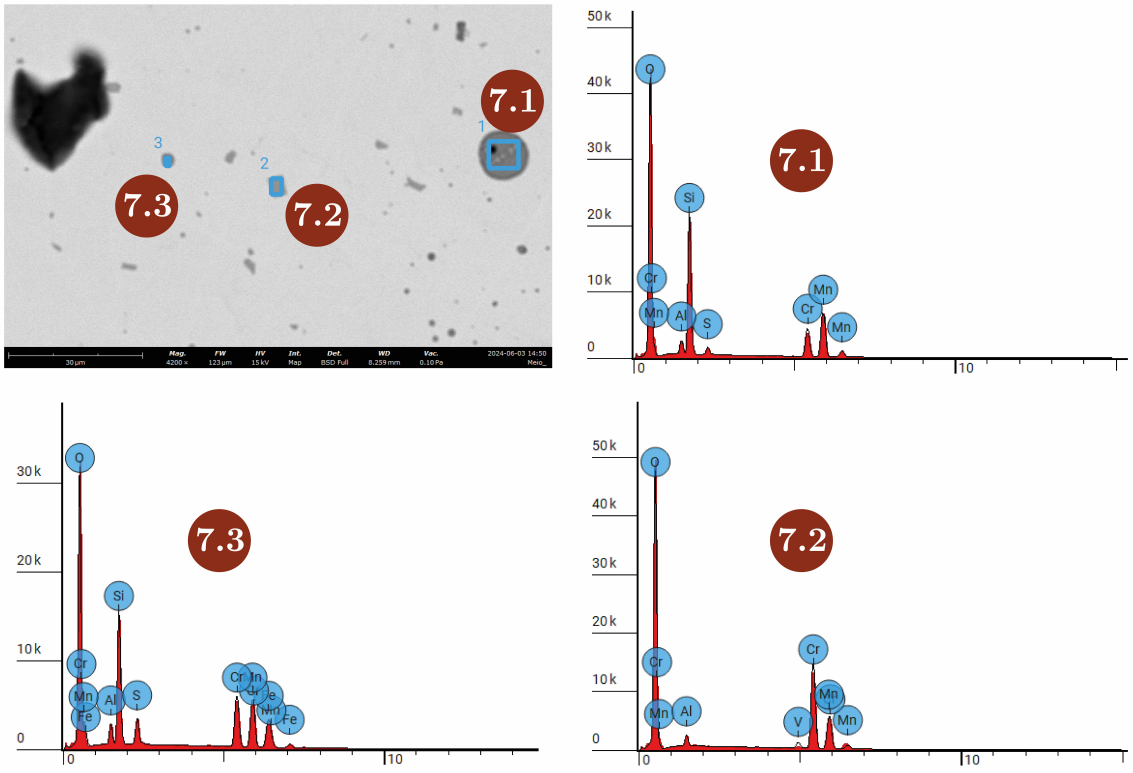

Figure 5.30: Semi-quantitative chemical composition of the inclusions numbered 7.1, 7.2 and 7.3

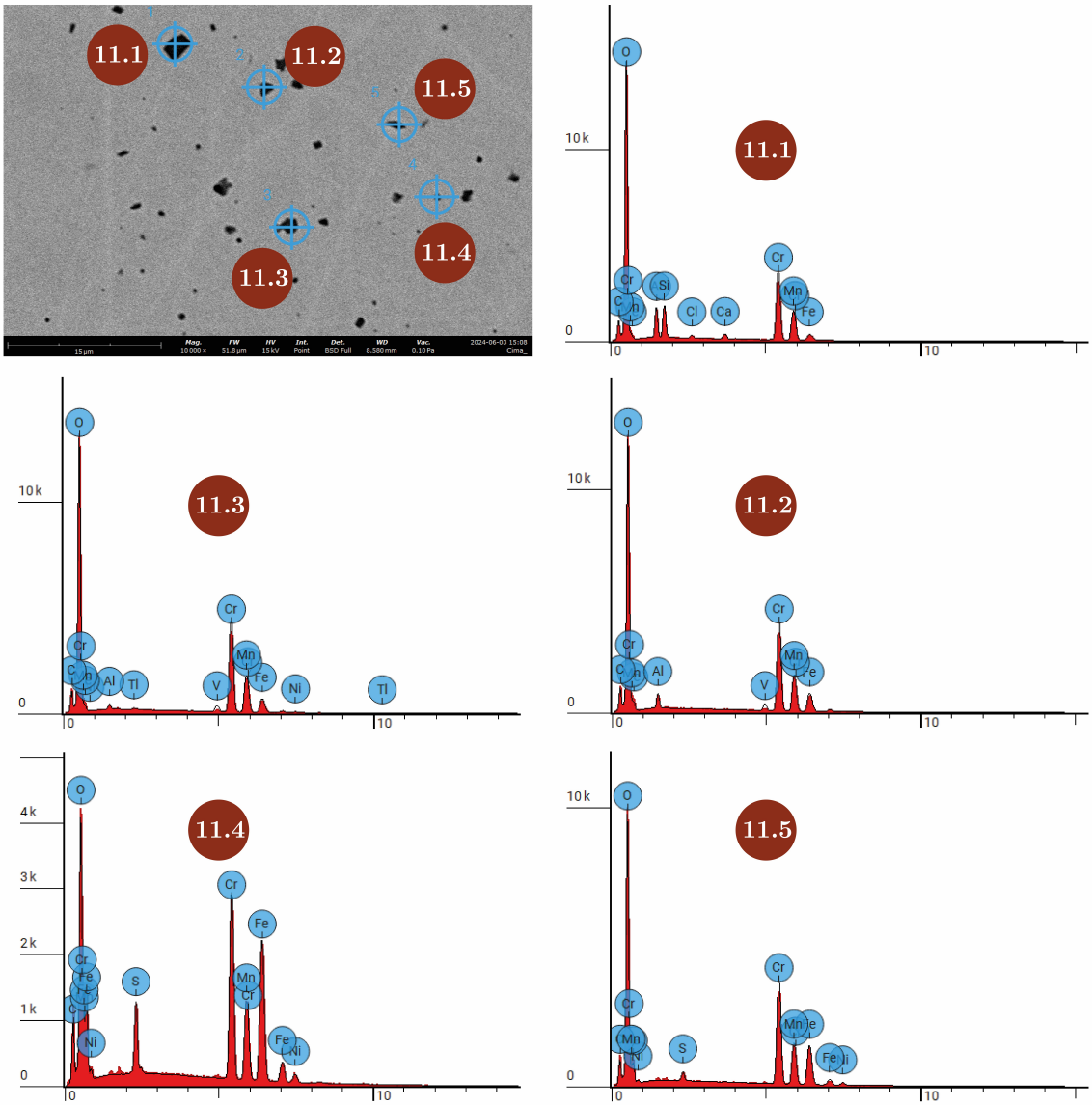

Figure 5.31: Semi-quantitative chemical composition of the inclusions numbered 11.1, 11.2, 11.3, 11.4 and 11.5.

Annex J - Micrographs of the original block (as supplied)

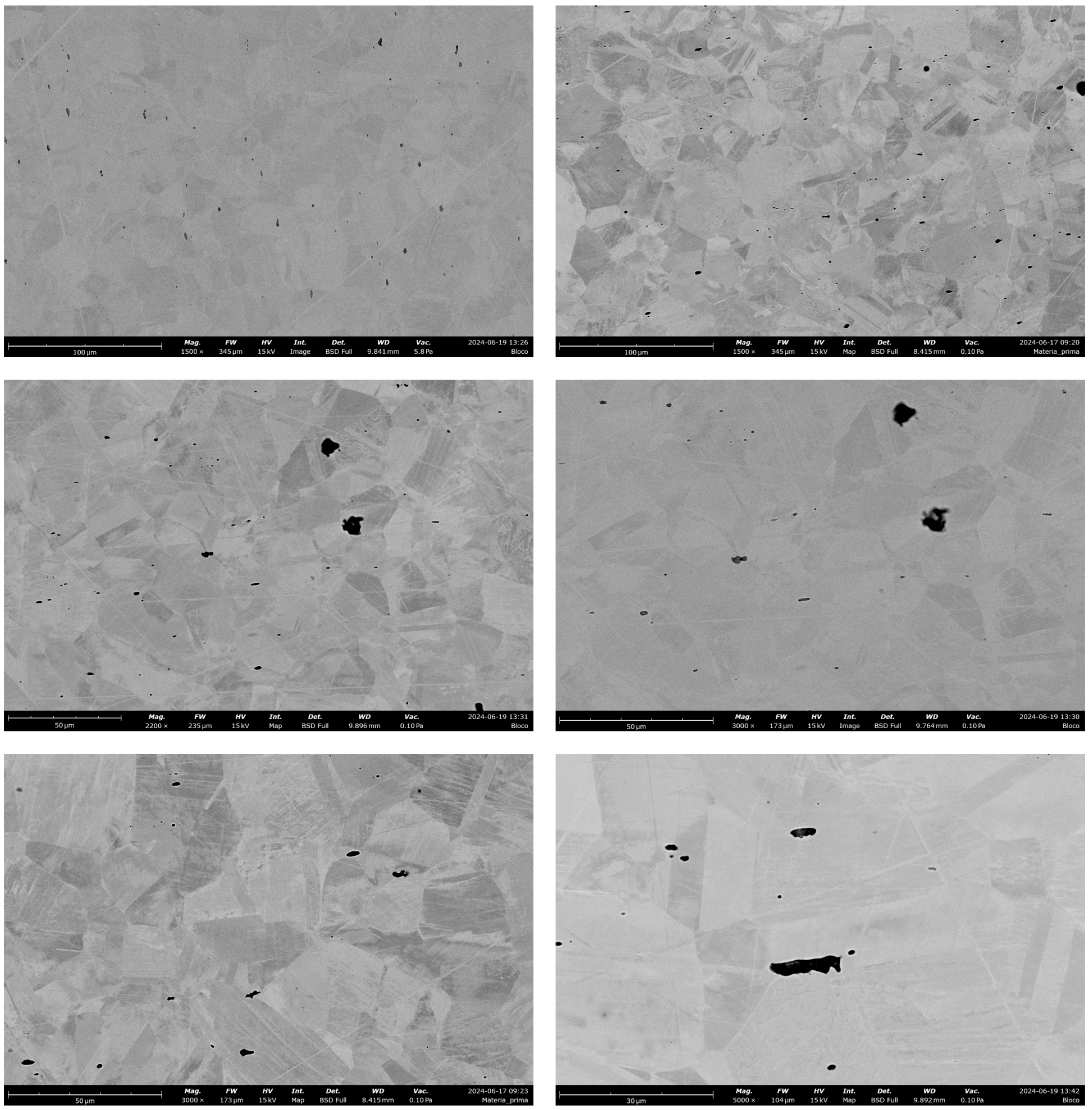

Figure 5.32: Micrographs of the original block (as supplied) (observed under optical microscopy).

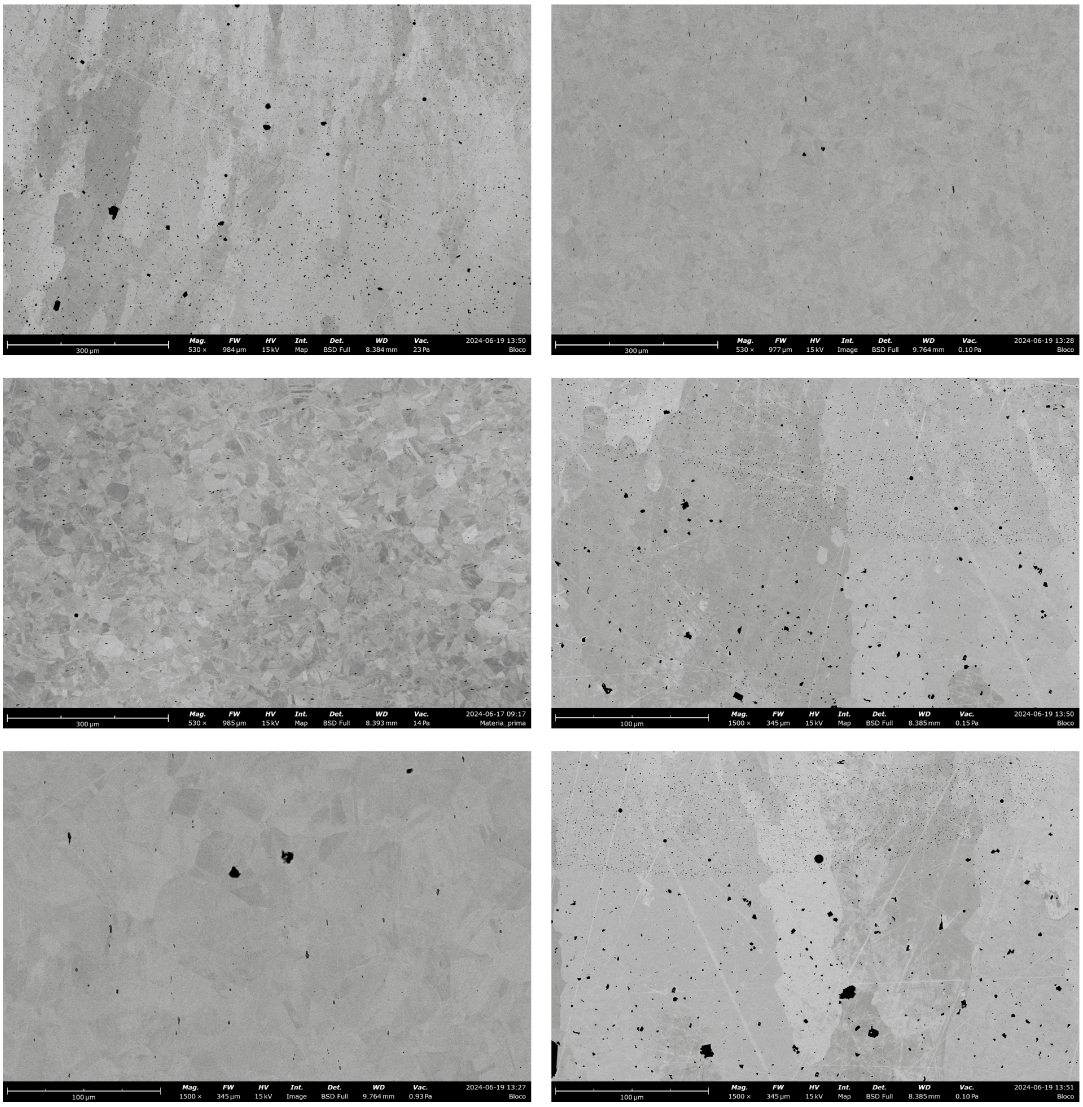

Figure 5.33: Micrographs of the original block (as supplied) (observed under optical microscopy).

Annex K - Semi-quantitative chemical composition measurements of inclusions observed in the original block (as supplied)

Table 5.5: Semi-quantitative chemical composition (wt%) of inclusions observed in the original block (as supplied).

Semi-quantitative chemical composition (wt%) of the black spots															
Spot number	**Fe**	**Cr**	**Ni**	**Mn**	**Si**	**C**	**O**	**N**	**Al**	**Cl**	**Ca**	**Zn**	**S**	**Na**	**Ti**
1.1	51,652	15,516	5,305	-	1,301	18,619		2,402	0,701	0,901	3,604	-	-	-	-
1.2	42,986	11,523	4,609	-	-	36,874	2,305	-	-	-	-	1,703	-	-	-
1.3	-	26,104	-	33,333	-	5,020	23,394	-	-	-	-	-	12,149	-	-
1.4	3,600	8,600	-	50,600	-	5,400	-	-	-	-	-	-	31,800	-	-
1.5	7,000	2,100	1,300	-	-	11,700	49,200	-	-	-	28,700	-	-	-	-
2.1	19,081	10,589	1,099	39,461	-	3,596	-	-	-	-	-	-	26,174	-	-
2.2	39,740	11,211	3,403	-	1,301	18,482	15,015	-	0,701	0,901	7,901	-	-	1,401	-
2.3	32,232	12,112	1,201	29,329	-	6,607	-	-	-	-	-	-	18,519	-	-
2.4	31,795	17,151	2,307	20,160	-	6,419	11,635	-	-	-	-	-	10,532	-	-
2.5	41,667	12,851	3,715	19,980	-	9,438	-	-	-	-	-	-	12,349	-	-
3.1	-	27,046	0,599	23,253	3,493	-	34,431	-	4,491	-	2,395	-	3,194	-	1,098
3.2	11,948	20,080	0,602	15,462	7,731	-	34,538	-	3,815	-	5,823	-	-	-	-
3.3	12,751	21,084	-	30,221	1,104	-	19,478	-	0,803	-	1,104	-	13,454	-	-
3.4	13,914	31,431	0,501	19,820	-	4,204	27,027	-	-	-	-	-	3,103	-	-
3.5	14,700	24,400	1,100	28,700	-	6,000	13,600	-	-	-	-	-	11,500	-	-
3.6	23,600	20,900	1,500	22,900	-	6,000	14,700	-	-	-	-	-	10,400	-	-

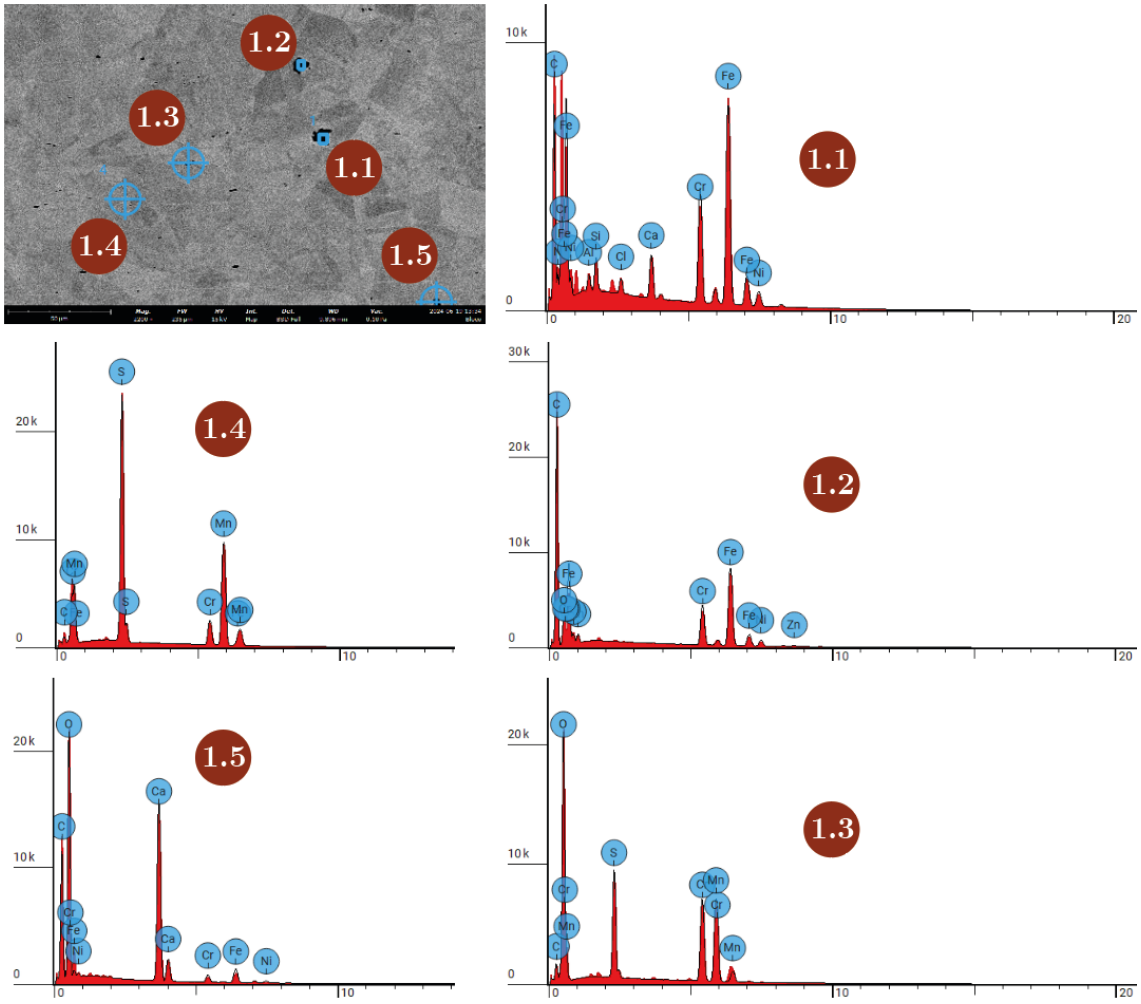

Figure 5.34: Semi-quantitative chemical composition of the inclusions numbered 1.1, 1.2, 1.3, 1.4 and 1.5

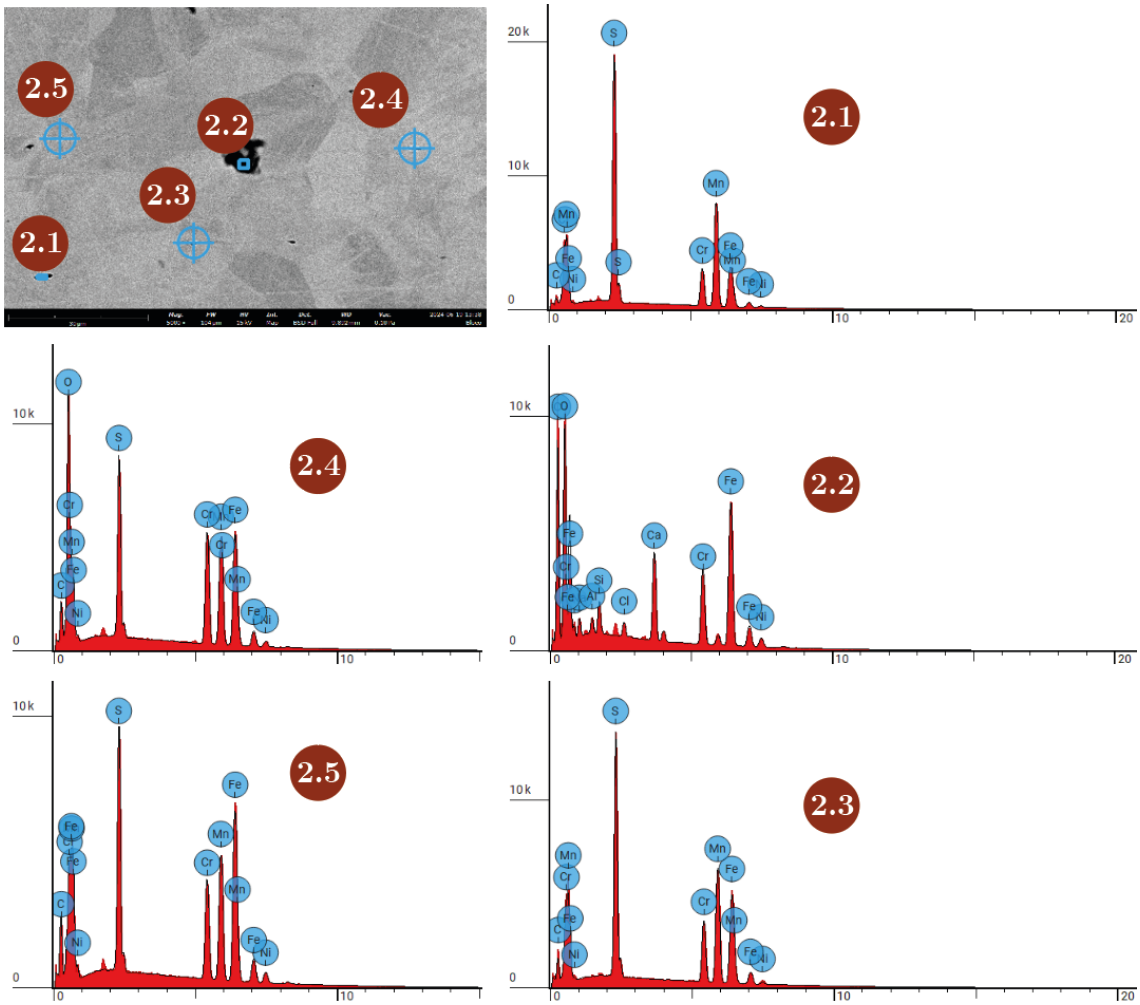

Figure 5.35: Semi-quantitative chemical composition of the inclusions numbered 2.1, 2.2, 2.3, 2.4 and 2.5

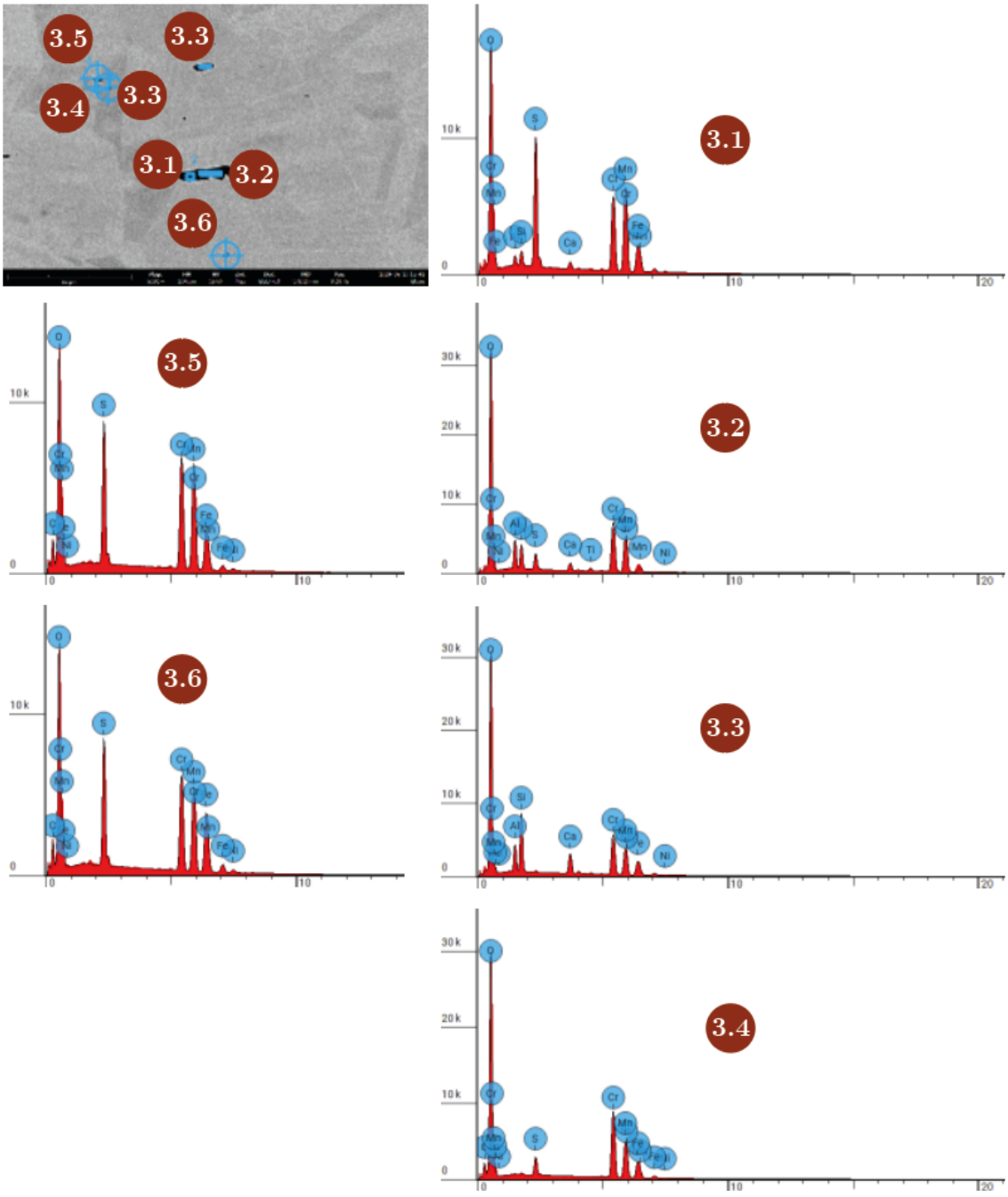

Figure 5.36: Semi-quantitative chemical composition of the inclusions numbered 3.1, 4.2, 5.3, 5.4, 5.5 and 5.6

Annex L - Microhardness measurements along the height of a DED printed thin wall with upcycled powder

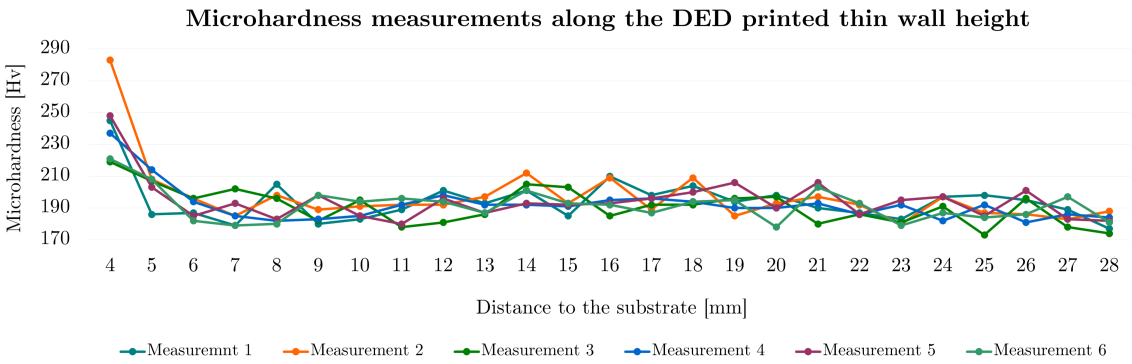

Figure 5.37: Microhardness measurements along the height of a DED printed thin wall with upcycled powder.

Table 5.6: Microhardness measurements along the height of a DED printed thin wall with upcycled powder

Microhardness Measurements along the DED printed thin wall height [HV]								
Distance to the substrate [mm]	**Measurement number**							
	1	**2**	**3**	**4**	**5**	**5**	**Average**	**Standard Deviation**
4	245	283	219	237	248	221	242,2	21,3
5	186	208	207	214	203	208	204,3	8,8
6	187	196	196	194	185	182	190,0	5,6
7	179	185	202	185	193	179	187,2	8,1
8	205	198	196	182	183	180	190,7	9,4
9	180	189	182	183	198	198	188,3	7,4
10	183	191	195	185	185	194	188,8	4,7
11	189	192	178	192	180	196	187,8	6,6
12	201	192	181	198	196	194	193,7	6,3
13	193	197	186	192	187	187	190,3	4,0
14	201	212	205	192	193	201	200,7	6,8
15	185	193	203	191	192	193	192,8	5,3
16	210	209	185	195	193	192	197,3	9,1
17	198	189	192	196	196	187	193,0	4,0
18	204	209	192	194	200	194	198,8	6,1
19	194	185	196	190	206	195	194,3	6,4
20	198	193	197	190	190	178	191,0	6,6
21	190	197	180	193	206	203	194,8	8,6
22	187	192	186	186	186	193	188,3	3,0
23	183	180	181	192	195	179	185,0	6,2
24	197	197	191	182	197	187	191,8	5,8
25	198	187	173	192	185	184	186,5	7,7
26	195	186	196	181	201	186	190,8	7,0
27	189	183	178	186	183	197	186,0	5,9
28	177	188	174	184	182	181	181,0	4,5

Annex M - Engineering and true curves obtained from the tensile tests

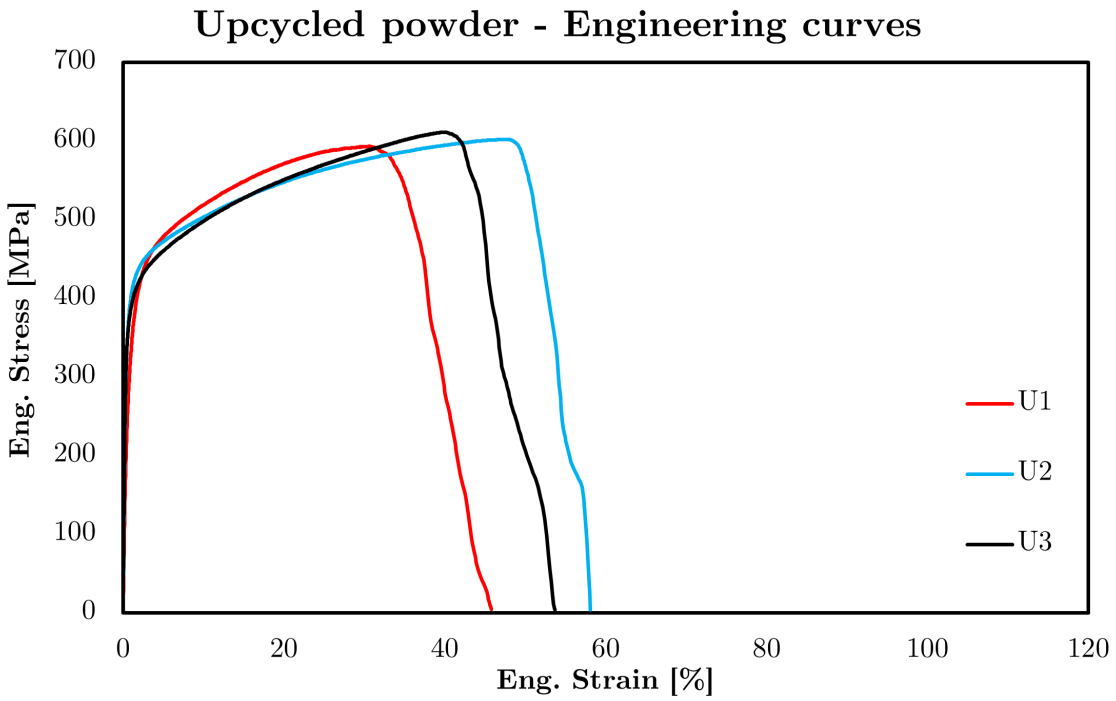

Figure 5.38: Engineering curve obtained from the tensile testing of the specimens DED printed with upcycled powder.

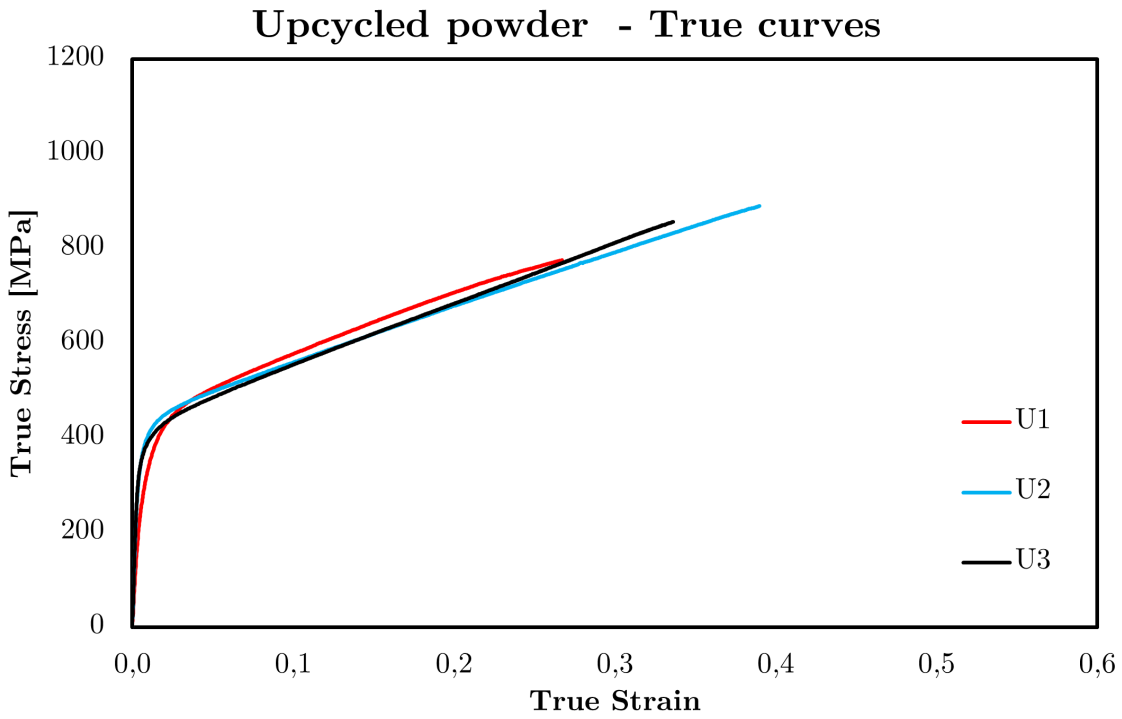

Figure 5.39: True curve obtained from the tensile testing of the specimens DED printed with upcycled powder.

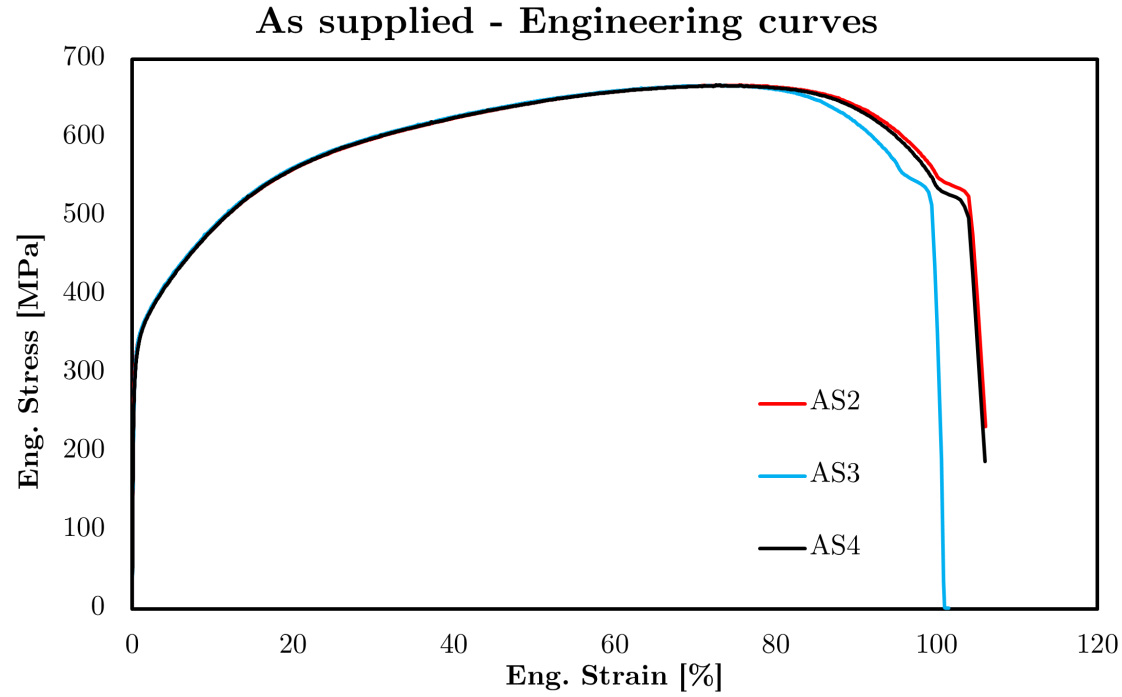

Figure 5.40: Engineering curve obtained from the tensile testing of the specimens taken from the original block (as supplied).

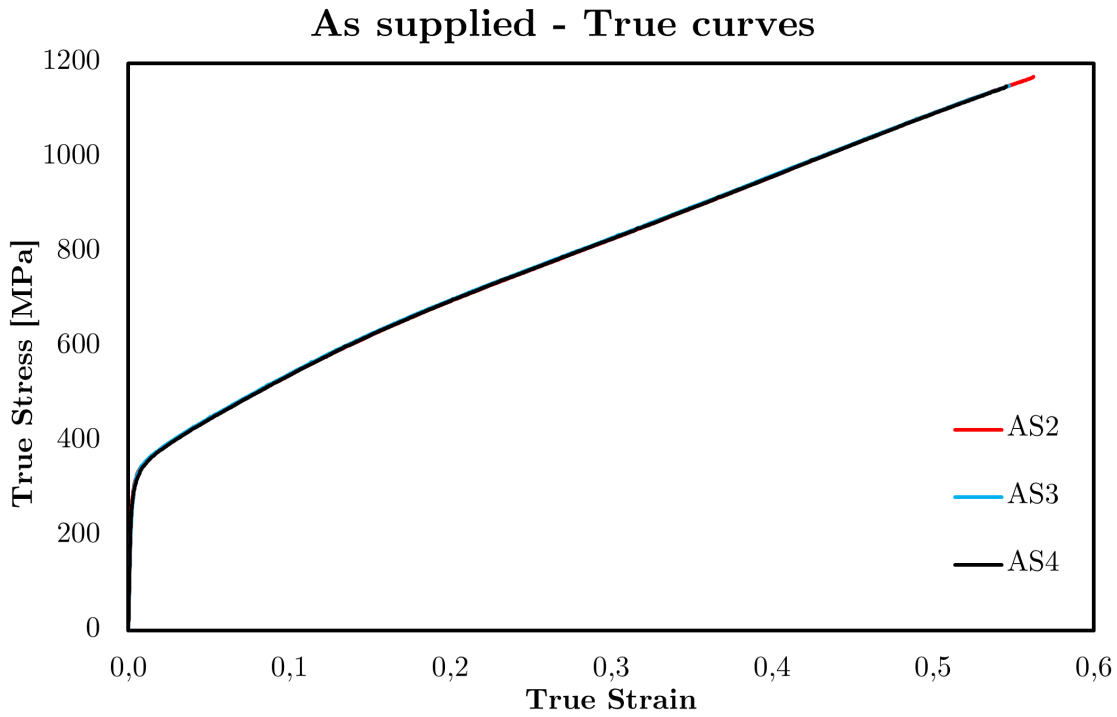

Figure 5.41: True curve obtained from the tensile testing of the specimens taken from the original block (as supplied)

Annex N - Images of the deformation field during the tensile tests obtained though DIC

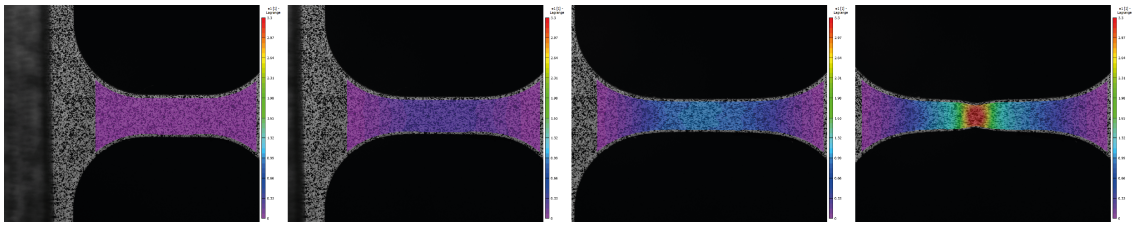

Figure 5.42: Images of the deformation field during the tensile tests obtained though DIC: specimen AS2; from the left to the right, 1st, 1000th, 2000th and 2557th (immediately prior to the fracture) images.

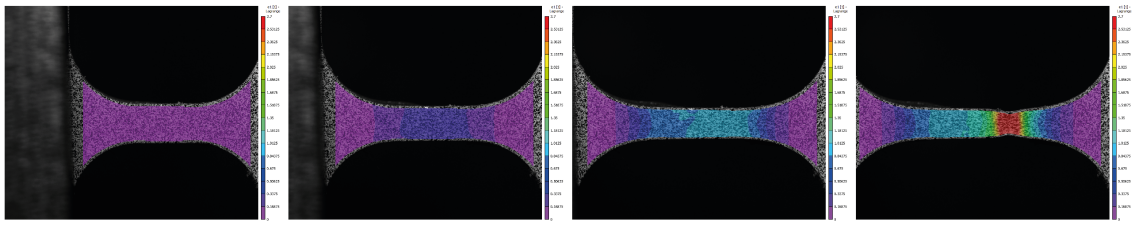

Figure 5.43: Images of the deformation field during the tensile tests obtained though DIC: specimen AS3; from the left to the right, 1st, 1000th, 2000th and 2515th (immediately prior to the fracture) images.

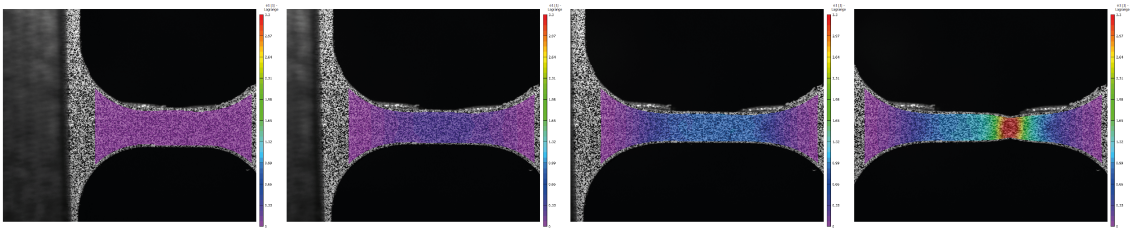

Figure 5.44: Images of the deformation field during the tensile tests obtained though DIC: specimen AS4; from the left to the right, 1st, 1000th, 2000th and 2619th (immediately prior to the fracture) images.

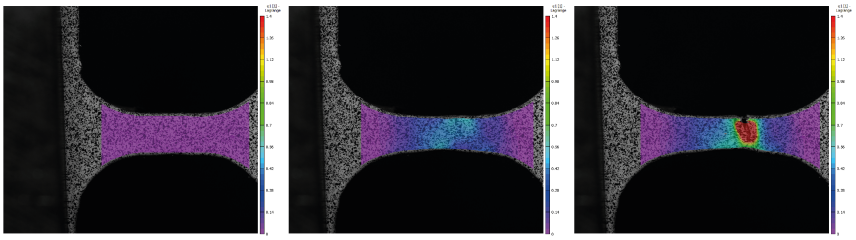

Figure 5.45: Images of the deformation field during the tensile tests obtained though DIC: specimen U1; from the left to the right, 1st, 850th and 1000th (immediately prior to the fracture) images.

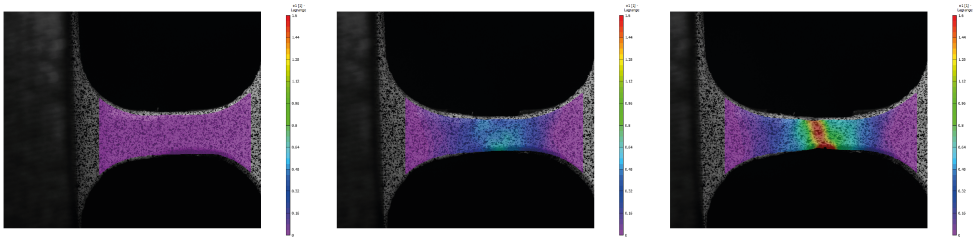

Figure 5.46: Images of the deformation field during the tensile tests obtained though DIC: specimen U2; from the left to the right, 1st, 900th and 1313th (immediately prior to the fracture) images.

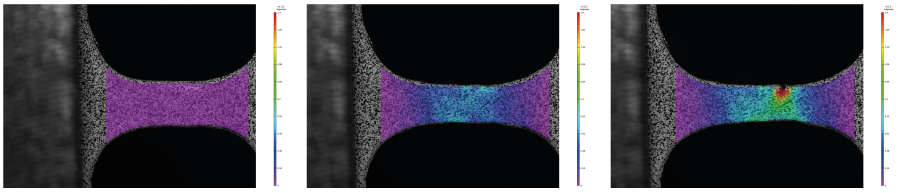

Figure 5.47: Images of the deformation field during the tensile tests obtained though DIC: specimen U3; from the left to the right, 1st, 1000th and 1300th (immediately prior to the fracture) images.

Annex O - Tensile specimens dimensions measurements

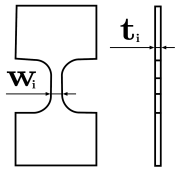

Figure 5.48: Schematic of the tensile specimens dimensions measured prior to the tensile testing.

Table 5.7: Tensile specimens measurements and parameters involved in the tensile testing and image acquisition.

Sample			Thickness [mm]				Width [mm]			
Type	**Number**	**ID**	**t1**	**t2**	**t3**	**ti**	**w1**	**w2**	**w3**	**wi**
DED printed with upcycled powder	**1**	**U1**	1,124	1,102	1,068	**1,098**	2,028	2,064	2,061	**2,051**
	2	**U2**	0,989	0,98	0,983	**0,984**	2,408	2,343	2,354	**2,368**
	3	**U3**	1,104	1,102	1,09	**1,099**	2,418	2,394	2,429	**2,414**
From the original block (as supplied)	**1**	**AS1**	1,004	1,001	1,007	**1,004**	2,037	2,03	2,054	**2,040**
	2	**AS2**	0,98	0,978	0,977	**0,978**	2,047	2,032	2,02	**2,033**
	3	**AS3**	0,983	0,98	0,978	**0,980**	2,042	2,045	2,036	**2,041**
	4	**AS4**	0,975	0,978	0,974	**0,976**	2,039	2,049	2,029	**2,039**
	5	**AS5**	0,974	0,971	0,977	**0,974**	2,035	2,029	2,017	**2,027**
	6	**AS6**	0,985	0,987	0,976	**0,983**	2,045	2,027	2,047	**2,040**

Annex P - Micrographs of the tensile specimens fracture surfaces

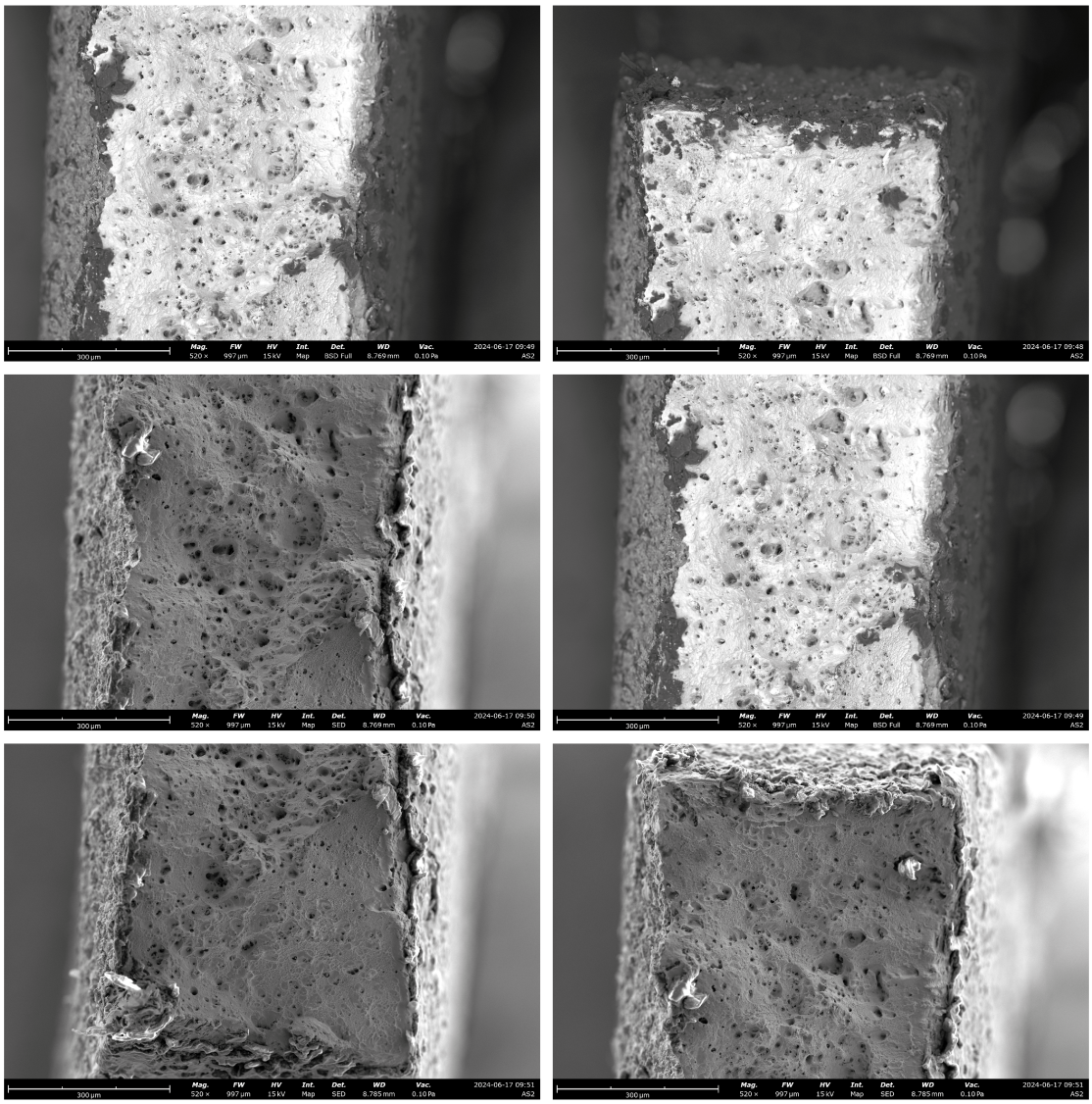

Figure 5.49: Fracture surface micrographs of specimen AS2 (observed in SEM).

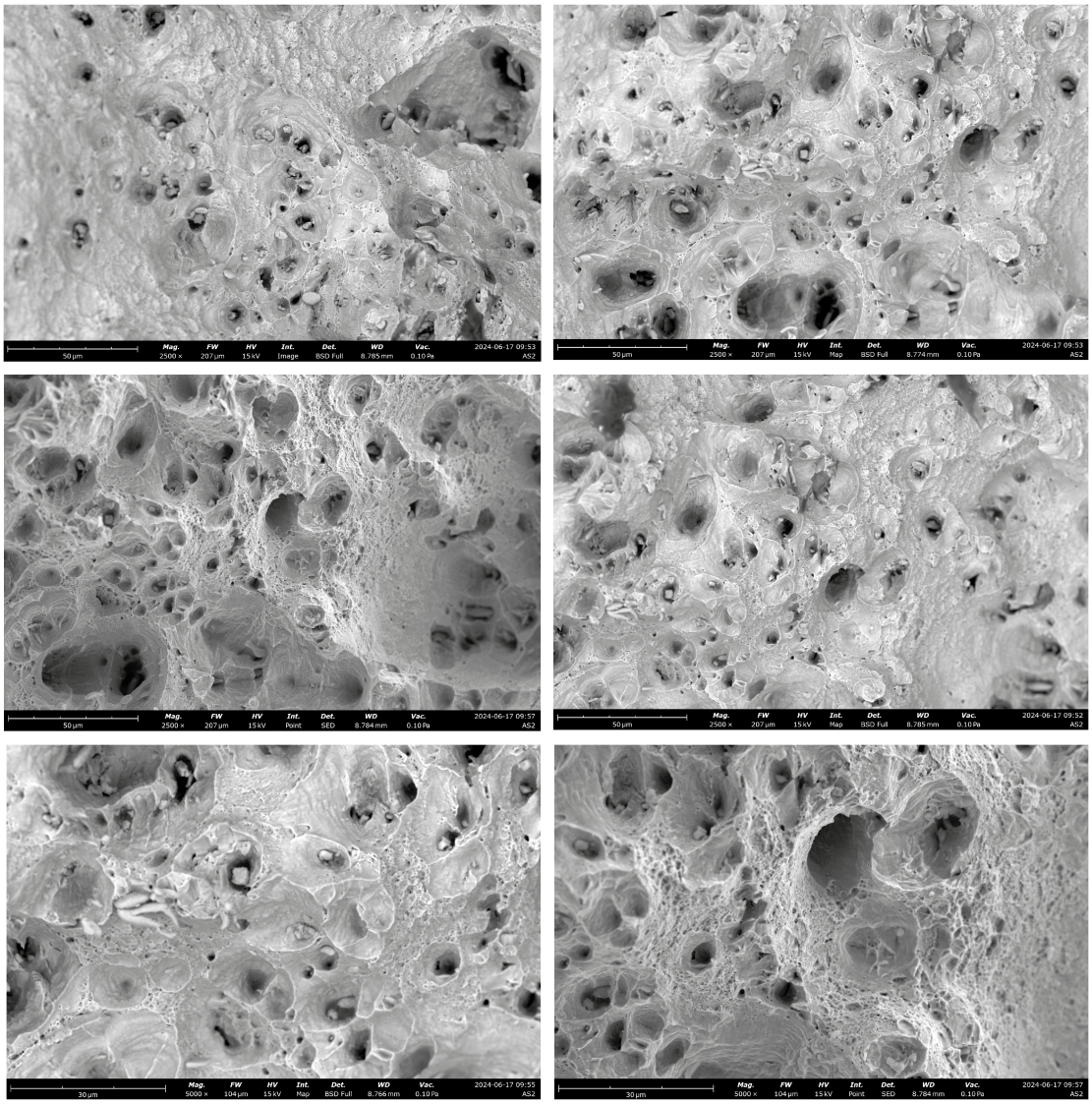

Figure 5.50: Fracture surface micrographs of specimen AS2 (observed in SEM).

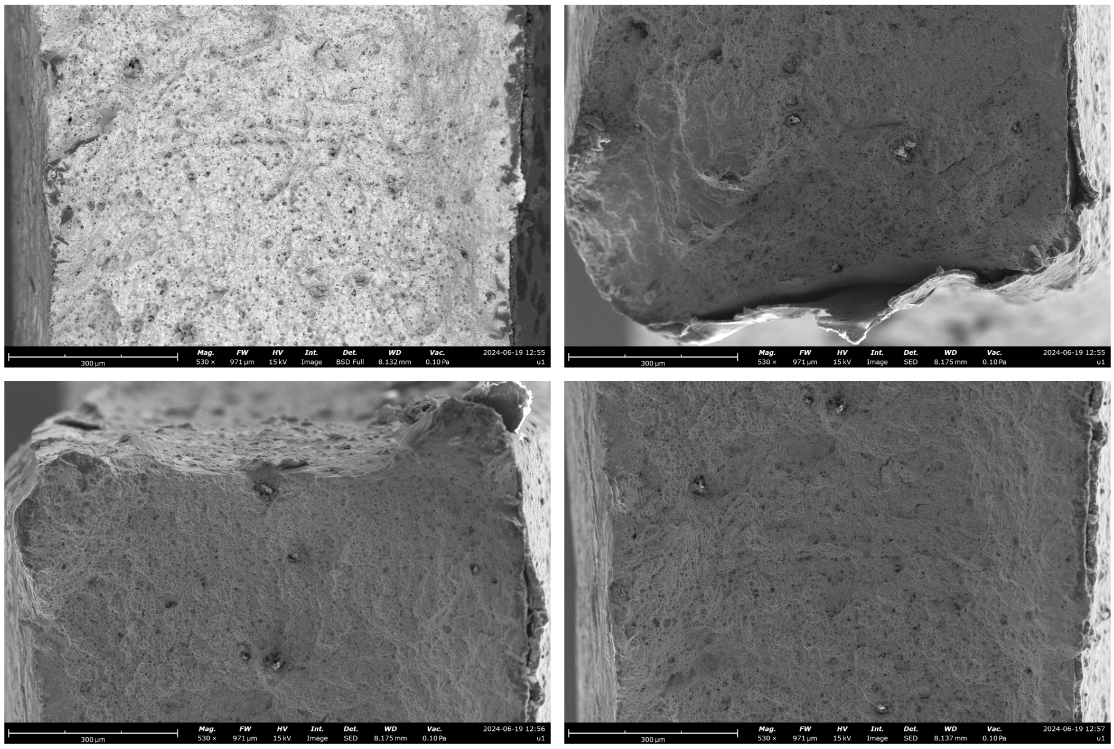

Figure 5.51: Fracture surface micrographs of specimen U1 (observed in SEM).

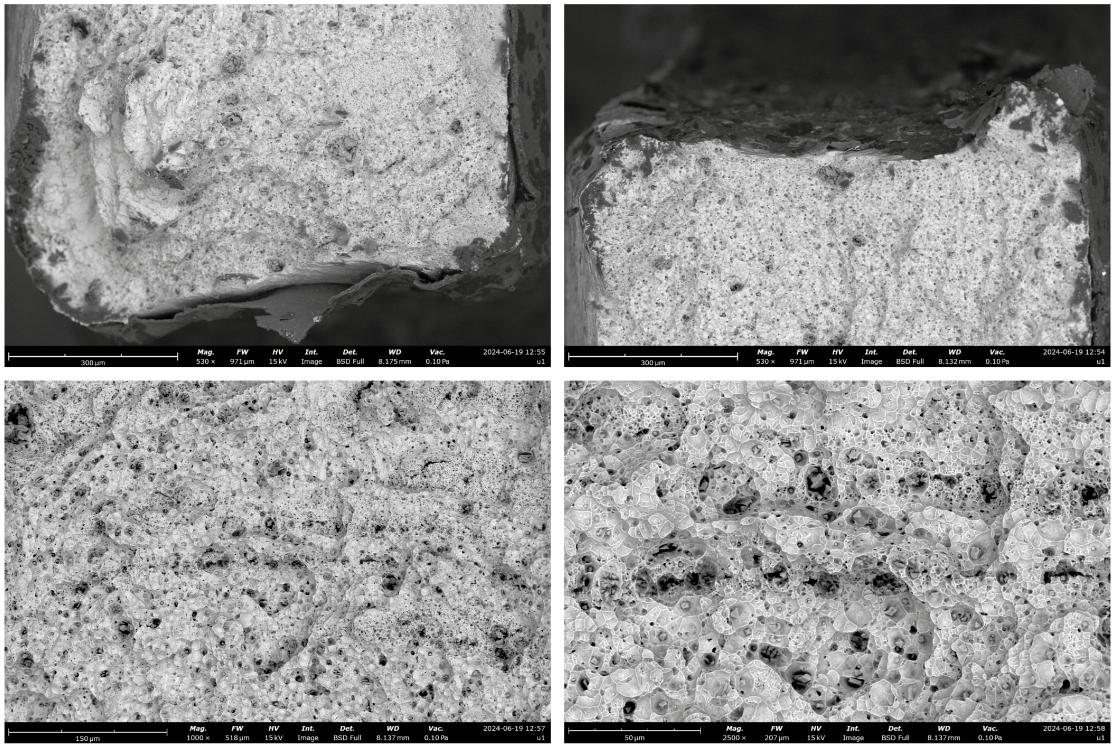

Figure 5.52: Fracture surface micrographs of specimen U1 (observed in SEM).

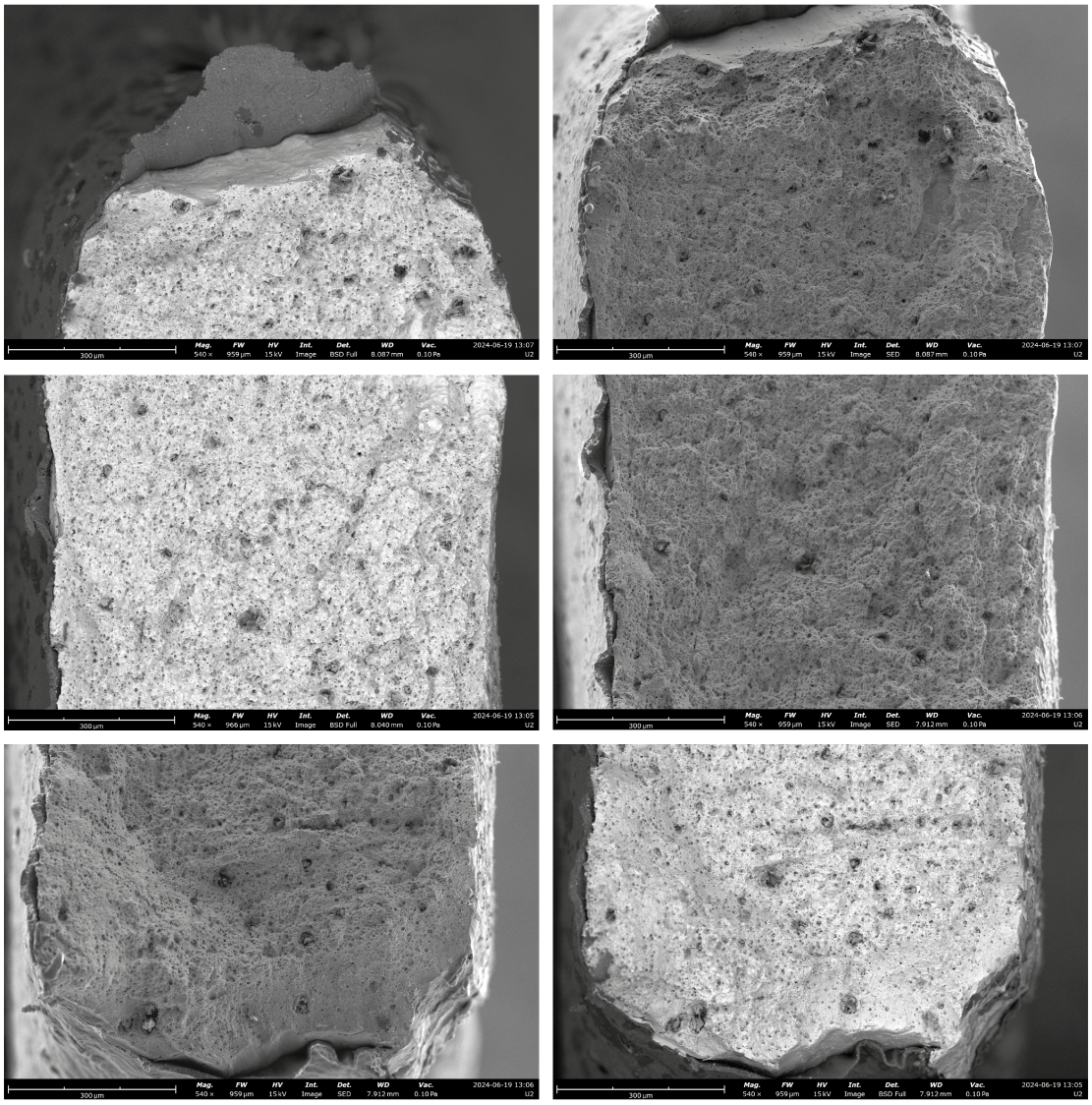

Figure 5.53: Fracture surface micrographs of specimen U2 (observed in SEM).

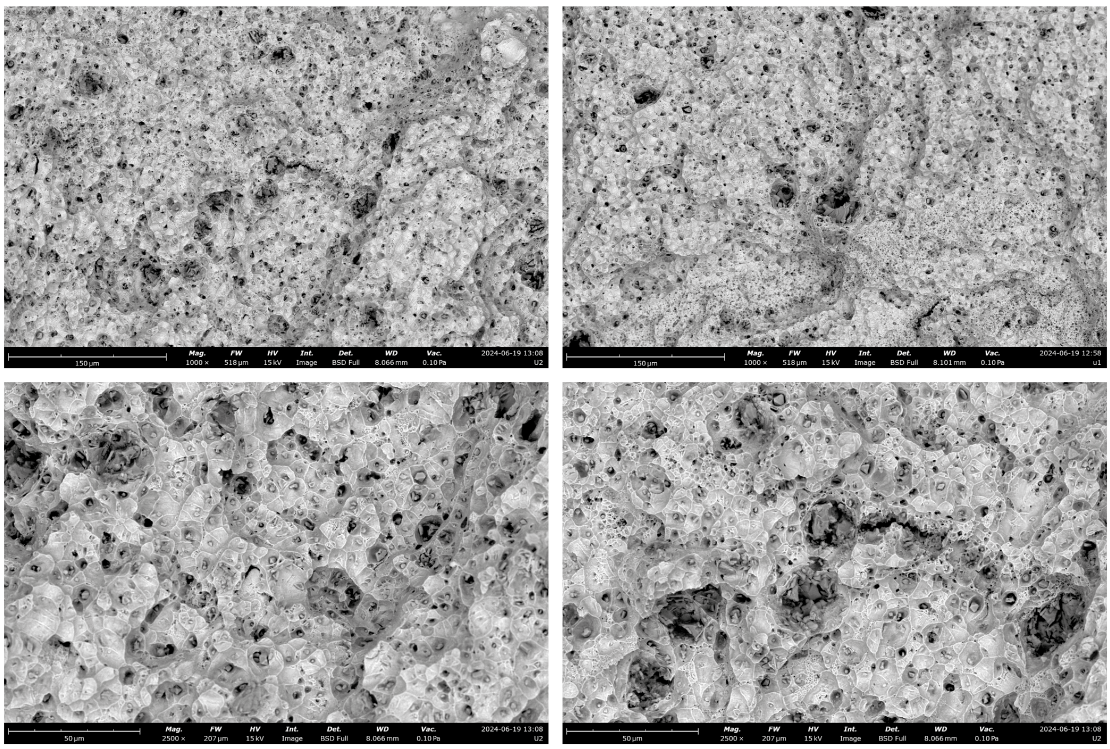

Figure 5.54: Fracture surface micrographs of specimen U2 (observed in SEM).